On the Feasibility of Photoacoustic Guidance of High Intensity Focused Ultrasound

Arik Funke

PHD THESIS OF THE
UNIVERSITY PIERRE AND MARIE CURIE

Speciality: Biomedical Engineering, Physics
Graduate School 389: P2MC

presented by

M. Arik Raffael FUNKE

in fulfillment of the requirements for the degree of

DOCTOR OF PHILOSOPHY OF THE
UNIVERSITY PIERRE AND MARIE CURIE

Topic of the thesis:

On the Feasibility of Photoacoustic Guidance of High Intensity Focused Ultrasound

Defended on September 22nd, 2010 before the jury composed of:

Paul Beard	Referee
Claude Boccara	PhD Adviser
Emmanuel Bossy	Co-Adviser
Cyril Lafon	Referee
Agnès Maître	President of the Jury
Wiendelt Steenbergen	Examiner

The work for this thesis was carried out at:

Institut Langevin
10 rue Vauquelin
75231 Paris CEDEX 05
France

A laboratory of:

ESPCI ParisTech
CNRS UMR 7587
INSERM Unit 979
University Pierre and Marie Curie
University Denis Diderot

Amendments as per September 21$^{\text{st}}$, 2011.

Abstract

An extensive summary in French is available in Appendix E on page 189.

The aim of this work is to investigate the possibility of automatic guidance and focussing of therapeutic ultrasound in complex media with photoacoustic waves. Possible applications exist in the field of non-invasive surgery, in particular for brain tumour therapy.

It is demonstrated in this work that a spectrally selective optical contrast agent can be used to isolate the photoacoustic signal of a target from a non-selective photoacoustic background in an optically tissue-mimicking phantom up to a depth of 6 cm with commercially available ultrasonic imaging probes. It is furthermore demonstrated that using purpose-built ultrasound probes, weak photoacoustic signals can be detected and therapeutic ultrasound emitted with the same probe. This ability was used to demonstrate the feasibility of guiding therapeutic ultrasound by use of a spectrally selective optical contrast.

Over the course of the work for this thesis the theoretical basis of photoacoustics was explored as foundation for a detailed analysis of noise sources and the development of novel noise reduction strategies. Proof of principle experiments demonstrating the possibility of guiding therapeutic ultrasound with photoacoustics were completed by work on vectorised contrast agents, in particular gold nanorods and Indocyanine green.

Keywords: photoacoustics, therapeutic ultrasound, HIFU, time-reversal, focusing, vectorised, gold nanorods, Indocyanine green

Résumé Français

Un résumé substantiel en français est disponible en Annexe E en page 189.

Le but de ce travail de thèse est d'étudier la possibilité d'une guidage et focalisation automatique d'ultrason thérapeutique dans des milieux complexes avec des ondes photoacoustiques. Des applications dans le domaine de la chirurgie non-invasive peuvent être envisagées, en particulier pour la thérapie des tumeurs cérébrales.

Il est démontré dans ce travail qu'un agent de contraste à sélectivité spectrale optique peut être utilisé pour isoler le signal photoacoustique d'une cible d'un fond photoacoustique non-sélectif dans un fantôme imitant les propriétés optiques des tissus jusqu'à une profondeur de 6 cm avec des sondes ultrasonores disponible commercialement. En outre, il est démontré qu'utilisant de sondes ultrasonores construites avec les contraintes de l'expérience à l'esprit, des signaux photoacoustique faibles peutvent être détecté et de l'ultrason thérapeutique émis avec la même sonde. Cette capacité a été utilisée pour démontrer la faisabilité d'un guidage d'ultrason thérapeutique par un contraste optique à sélectivité spectrale.

Au cours des travaux de cette thèse les bases théoriques de la photoacoustique ont été étudiées en tant que fondement d'une analyse détaillée des sources de bruit et d'un développement de nouvelles stratégies de réduction de bruit. Des expériences de preuve de principe démontrant la possibilité de guider de l'ultrason thérapeutique par photoacoustique ont été complétées par des travaux sur des agents de contraste vectorisé, en particulier des nano-bâtonnets d'or et de vert d'indocyanine.

Titre francais: Sur la faisabilité d'un guidage photoacoustique d'ultrasons focalisés de haute intensité

Mots-clés: photoacoustique, ultrason thérapeutique, HIFU, renversement temporel, focalisation, véctorisation, nano-bâtonnets d'or, vert d'indocyanine

Contents

Part I

Introduction

Chapter 1

Introduction

Contents

Over the last decades industrialised societies have experienced a steady increase in life expectancy and a shift in the age structure from a pyramid at the beginning of the 20^{th} century to a constricted pyramid or even inverse pyramid in some cases. One consequence of this process is a continuous increase in the cancer incidence rates, since three quarters of the cases of cancer are diagnosed in people aged 60 years and older. (See also Figure 1.1.) According to the World Health Organisation (2009), cancer is the leading cause of death world wide. In 2004 it accounted for 7.4 million or 13% of deaths.

As is the case for many age-related diseases, research into novel methods for cancer diagnosis and treatment has been particularly active over the last two decades. With cancer incidence rates on the increase for the foreseeable future, a treatment modality with lower complication rates and no need for a sterile operating environment would be very beneficial. One emerging method, High Intensity Focused Ultrasound (HIFU), is at the cusp of commercialisation and has proven itself to be an efficient, effective and most importantly non-invasive treatment modality. Unfortunately, at present the indications that can be treated with this new procedure are fairly limited due to technological limitations.

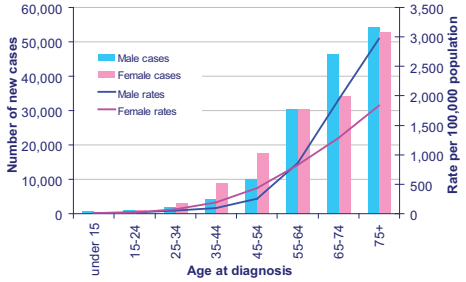

(a) Number of new cases and rates, by age and sex, all malignant neoplasms (excluding non-melanoma skin cancer), UK, 2007

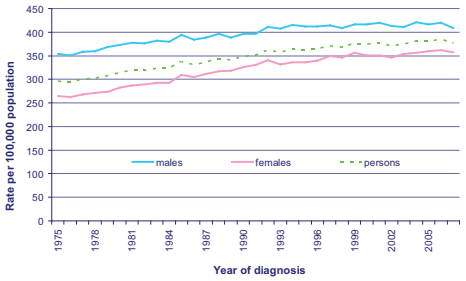

(b) Age-standardised (European) incidence rates, all cancers excluding non-melanoma skin cancer, by sex, Great Britain, 1975-2007

Figure 1.1: Statistics on cancer incidence by Cancer Research UK (2010)

Over the course of the work for this thesis, the feasibility of one method that may ultimately allow to broaden the range of indications that can be treated by HIFU was explored: more specifically the possibility of guiding HIFU by use of photoacoustic signals from exogenous contrast agents. This method may allow innovations to HIFU such as fully automatic motion compensation during treatment, treatment of tumours whose position is only approximately known, selective molecular targeting and targeting of tumours in acoustically complex environments such as the brain.

1.1 Structure of this Document

This document consists of three main parts.

Part I serves as an introduction to the subject matter:

- Chapter 1 provides a brief historical overview of the technologies employed and the state of the art of the methods used to motivate a more detailed explanation of the objectives of this work.
- Chapter 2 provides a theoretical foundation of the most pertinent topics. The choice of detail in which various topics are presented is heavily influenced by the existing know-how of the laboratory in which this work was carried out. While work on light propagation and time-reversal has been the subject of research for a considerable time, photoacoustics for biomedical applications is a new research topic. While the former topics are treated in sufficient detail to allow a reader not familiar with these subjects to understand the main part of this thesis, the

latter topic is treated in more detail to contribute to the knowledge base of the laboratory.

Part II is the main section of the document:

- Chapter 3 provides a detailed description of the materials and methods used in the course of the work for this thesis.
- Chapter 4 introduces the principle of the method proposed in this thesis. It presents early experimental results and identifies problem areas to be further investigated during this thesis.
- Chapter 5 focuses on methods for noise control & filtering and methods for signal extraction.
- Chapter 6 presents experimental results demonstrating the feasibility of photoacoustically guided HIFU.
- Chapter 7 presents some of the progress that has been made towards applying the proposed method in biological tissue and *in vivo*, it focuses in particular on the validation of exogenous targeted contrast agents that were developed by our collaborators for use with the proposed method.

Part III contains a brief review of the principal conclusions of the work presented in this document and presents some perspectives for future work.

Part IV contains some appendices. Material that the reader may find useful for the comprehension of this thesis but could also be found in specialised textbooks is presented here. It is inteded primarily as a pedagogic aid for the non-specialist reader, supporting the theoretical and mathematical sections of this thesis. Where appropriate, reference is made to sections of the appendix in the body of the main parts of this thesis.

For the convenience of the reader some specialist terms of which the meaning cannot easily deduced from the context are explained in a nomenclature at the end of this document. Expressions for which an explanation is provided are marked with a star* when first used in this document.

1.2 State of the Art

History of Medical Ultrasound

Woo (1998) provides an excellent overview of the history and the development of ultrasound technology. Some milestones with regard to the methods and technologies employed in this thesis shall be highlighted in the following.

19th Century: Establishing the Foundations for Modern Acoustics

The first systematic experiments in underwater acoustics were carried out by the Swiss scientist Jean-Daniel Colladon in 1826 when he investigated in Lake Geneva with an underwater bell the speed of sound in water. The theoretical foundations for modern acoustics were established by Lord Rayleigh with his seminal work "The Theory of Sound" (Rayleigh (1877)) in which he presented the first mathematical description of a sound wave.

Investigations in high-frequency acoustics were enabled by the discovery of the piezo-electric effect by Jacques and Pierre Curie in 1880 at ESPCI in Paris. (Curie and Curie (1880)) In combination with the discovery of the diode and triode which allowed the development suitable power amplifiers, the piezo-electric effect permitted the generation and detection of sound in the megahertz regime, paving the way for underwater sonar detection.

Motivated by the Titanic disaster and the necessities of the first world war, the first high-frequency ultrasonic echo-sounding device was developed in 1916 by Paul Langevin at ESPCI in Paris and the Swiss-Russian inventor Constantin Chilowsky who was working in France at the time. (Chilowsky and Langevin (1916)) This technological breakthrough was made possible by the development of the first quartz-sandwich transducers which the inventors named "hydrophone". The technology was then further developed in classified research.

1940s and 1950s: Towards Medical Applications for Ultrasound

The 1940's saw a rapid development of RADAR technology which stimulated further developments in ultrasonics. Also in the 1940's ultrasonic metal flaw detection was developed simultaneously in most industrialised nations.

Already during the development of the hydrophone, Paul Langevin noted the first hints at the bio-effects of ultrasound when fish in the ultrasonic beam of his devices were killed. In 1938 the German physician Raimar Pohlman introduced ultrasonic physiotherapy at Charité Berlin. He proposed using intensities below than $5\,\mathrm{W/cm^2}$, noting that the transducer needed to be kept in motion and that insonication of the bone had to be avoided.

The first suggestion of ultrasonic medical imaging was made in 1940 by Gohr and Wedekind of the Hospital of the University of Köln. (Gohr and Wedekind (1940)) They proposed to use an echo-reflection mode similar to the one used in metal flaw detection to detect tumours but were unable to produce convincing experimental results.

In 1942 Lynn and Putnam began investigating the use of ultrasound to destroy brain tissue in animals and noted that predominantly tissue close to the skull bone was destroyed. They discovered that for the destruction of deep tissue the skull bone needed to be removed. (Lynn and Putnam (1944))

The 1950s saw the first wide-spread applications of ultrasound to medical applications: William Fry at the University of Illinois (Fry et al. (1954)) and Russell Meyers at the University of Iowa (Meyers et al. (1959)) performed craniotomies* and used the overlapping fields of four ultrasonic transducers to destroy parts of the basal ganglia in Parkinson patients without damage to overlaying tissue. This revolutionary use of focused ultrasound to destroy deep-seated tissue lead to them being regarded today as the founding fathers of the field of high-intensity focused ultrasound (HIFU) for surgical applications. However the development of the drug L-dopa as a less invasive treatment for Parkinson led to the end of their experiments.

Petter Lindström of the University of Pittsburgh used ultrasound in palliative care to alleviate pain from carcinomatosis* by treatment of the frontal lobe. (Lindstrom (1954)) Numerous researchers applied ultrasound to rehabilitation. Jerome Gersten at the University of Colorado explored the use of ultrasound for the treatment of rheumatic arthritis. Peter Wells at Bristol University, Douglas Gordon at West End Hospital for Neurology and Neurosurgery in London and Mischele Arslan at the University of Padua applied ultrasound to the treatment of Ménière's disease*. (Woo (1998))

During the 1970s interest in therapeutic ultrasound waned while diagnostic ultrasound technology flourished with the development of piezo-ceramic and piezo-composite transducers. A notable exception is the work of Frederic Lizzi at the Riverside Research Institute, New York exploring the use of high-intensity focused ultrasound for sealing retinal scars and treatment of glaucoma. (Lizzi et al. (1978, 1981); Coleman et al. (1985)) Until recently, Lizzi's approach had been abandoned in favour of the emerging LASER technology.

High Intensity Focused Ultrasound

Principles of High Intensity Focused Ultrasound

High Intensity Focused Ultrasound, or HIFU, is an umbrella term for surgical methods employing strongly focused ultrasonic fields to destroy a target region in depth without damage to overlaying or surrounding tissues. Generally it is used for thermal ablation of tissue, but non-thermal modes of use are possible. HIFU is generally regarded as one of the methods of thermal ablation among microwave-, radio-frequency, laser and cryo-ablation.

HIFU is unique in that there is no need to insert a probe, making it the only potentially non-invasive ablative technique which does not depend on ionising radiation. In the context of tumour treatment this is of particular significance as it eliminates the risk of seeding tumour cells along the insertion track.

The frequencies of HIFU generally range from several 100 kHz to about 1.5 MHz. At lower frequency, ultrasound cannot be sufficiently focussed while at higher frequencies the attenuation before reaching the target is too large.

Depending on the transducer geometry and frequency used, the ultrasonic focus is typically a rice corn-shaped region with dimensions $1\,\mathrm{mm} \times 10\,\mathrm{mm}$. If the region to be destroyed is larger, the focus is typically scanned sequentially to cover the entire target region.

A successful HIFU treatment regime depends on three key components: firstly the reliable identification of the target region, secondly the selective delivery of thermal energy to the target region and lastly the monitoring of the treatment progress. While the problem of energy delivery was already mastered during the very first experiments in HIFU, such as the experiments by William Fry in the 1950s, the lack of imaging technology for the reliable identification of the target region stalled progress.

The significant progress that has been made over the last two decades in medical imaging has led to a resurgent interest in the idea of non-invasive surgery via HIFU. This is evidenced by a rapidly expanding number of publications on the topic in the 1990s. Research has been focused primarily on improving energy delivery and treatment monitoring. In the following the progress in the field of HIFU shall be illustrated with a few selected publications.

For treatment monitoring, several approaches are still being actively explored in parallel. While MRI-guided HIFU treatment has become a reliable procedure as evidenced by the development of commercial HIFU devices by Chongqing HAIFU in China, Insightec in Israel and Supersonic Imagine in France, research is still ongoing to achieve reliable treatment monitoring with acoustic waves. This would allow a significant reduction in the procedure's cost by reducing the complexity of HIFU devices.

Ultrasonic Methods for Treatment Control and Monitoring

Since delivery of efficient energy to tissue at depth is no longer a problem in many cases for HIFU, research has been very active with regard to controlling the use of this energy to selectively destroy a target region and avoid damage to surrounding tissue. Futhermore approaches for monitoring of the treatment progress are increasingly beeing investigate. In the following some illustrative examples of ultrasonic approaches to solving these problems are provided.

One of the earliest approaches to treatment monitoring is the idea of ultrasonic temperature imaging. In Simon et al. (1998) a method was presented that exploited the shift of the ultrasonic speckle grains due to the thermal expansion of tissue to determine the *in situ* temperature. This was followed by Vaezy et al. (2001) who demonstrated that the thermal imaging sequences could be interleaved with the HIFU therapy sequences. Even though the method can today be realised in real-time (Liu and Ebbini (2010)) and has good spatial and temperature resolution, it is limited to a relative temperature elevation of about 10 K which at present still severely limits its usefulness for HIFU monitoring. Another weakness of the method is its sensitivity to tissue motion which may prohibit some applications.

Another approach for monitoring HIFU treatment is to exploit the fact that tissue elasticity and geometry changes in response to heating and or thermal necrosis. (Sapin-de Brosses et al. (2010)) Arnal et al. (2010) demonstrate that the combination of elastographic* temperature imaging and strain imaging can be used for the detection of lesion formation. One possible advantage of elastographic temperature imaging in contrast to traditional ultrasonic temperature imaging is that it is insensitive to tissue motion.

Significant effort has also been invested in detection of cavitation and heating during HIFU treatment to avoid the creation of an uncontrolled bubble clouds which can cause the point of maximum energy deposition to migrate from the ultrasonic focal point towards the transducer surface, thereby leading to inadvertent tissue damage.

However as was suggested very early by Hynynen (1991) and later demonstrated by Thomas et al. (2005), the presence of bubbles can greatly increase the efficacy of heating, in part due to the strong resonance behaviour of gas bubbles in ultrasonic fields which leads to harmonic conversion and increased energy absorption by tissues. To avoid the risk of the previously mentioned migration of the point of heat deposition, a high level of control over the cavitation activity was found to be essential. (Coussios et al. (2007))

HIFU & Vascular Occlusion

Apart from ablating tissue, HIFU can also be used to occlude blood vessels to alter the vascularisation of tissue. This may be useful as a preparation for extensive surgical procedures as well as to reduce blood flow to some tissue areas for as therapy.

Vaezy et al. (1997) showed that using ultrasound it was possible to all but arrest hemorrhaging from rabbit livers in less than two minutes by thermally inducing coagulation. Denbow et al. (2000) showed it was possible in animal models to thermally occlude the femoral artery in 5 seconds with the perspective of using the technique to treat twin-twin transfusion syndrome in foetal therapy. Vaezy et al. (2007) investigated the use of HIFU to seal air leaks following parenchymal* lung injury as an alternative to lung resection. Zderic et al. (2007) demonstrated a novel surgical method for liver resection on a pig model to minimise hemorrhaging during the procedure. HIFU was used to cauterise a wall in the liver occluding all but the largest blood vessels prior to incision. The method is of particular interest as uncontrolled bleeding is today still one of the most difficult complications during liver resection.

Another area of active research is the efficiency of energy delivery. Work has included research into optimal HIFU scanning patterns to exploit the natural heat diffusion in tissue but also into reducing the heat loss from the target region through blood flow. An example for the latter is the provided by Leslie and Kennedy (2007) who reduced heat-loss from the target region during HIFU

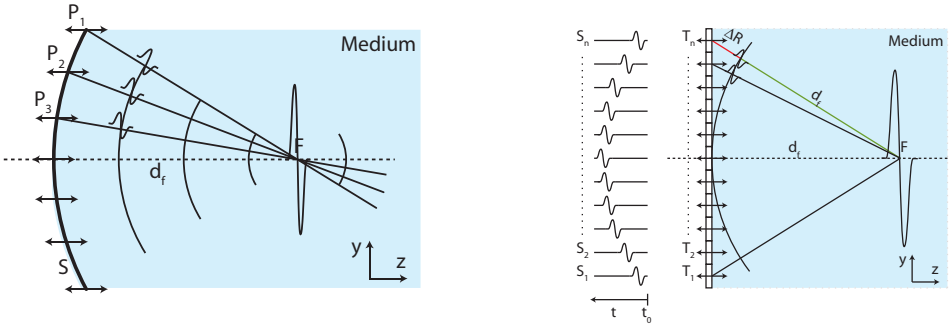

(a) geometrically focused surface

(b) phased array with spherical delay law

Figure 1.2: Focusing via a shaped surface or with a phased array

by reducing the blood perfusion of the target region by trans-arterial chemoembolisation prior to HIFU.

Development of Specialised HIFU Devices

With the development of minimally invasive operative technology over the last two decades, another option of improving energy delivery to the target region has become available. Lafon et al. (1998) developed an interstitial HIFU transducer for treating tumours of the digestive tract which is a difficult location for extra-corporeal HIFU due to the possibility of the presence of gas and ultrasonic aberrations due to overlaying tissue structures. Delabrousse et al. (2010) demonstrated in a pig liver model that using closed-loop temperature control reproducible lesions can be produced with an interstitial HIFU device with the perspective of treating hepatocellular carcinoma* and colorectal metastases in liver.

Intracavity HIFU devices for the treatment of prostate cancer have reached commercial stage with several competing devices available such as Ablatherm and Sonablate.

Another example of a highly specialised HIFU device at the cusp of commercialisation is the development of a HIFU device for the treatment of glaucoma by EyeTechCare in France with which HIFU can be seen to have come full circle since the first attempts to use HIFU for this purpose in the 1970s by Frederic Lizzi.

Time-Reversal

On the Need for Time-Reversal Focusing and its History

Just as was the case with the earliest attempts at using HIFU for medical purposes, most commercialised HIFU devices today use mono-element

transducers with a spherically curved surface vibrating in sync as illustrated in Figure 1.2a which produce an ultrasonic focal spot at the geometric centre of curvature. These transducers are then scanned mechanically such that the ultrasonic focus covers the target region during therapy. For acoustically homogeneous media, such a geometrically determined focus is an inexpensive and easily controlled approach as it requires only a single signal generator and power amplifier to drive the therapeutic transducer.

Unfortunately, the regions of the human body that can be approximated as an acoustically homogeneous medium are limited: the speed of sound in in fatty tissues is 1440 m/s, in blood 1540 m/s, in muscular tissue 1600 m/s and in bone 3000 m/s. An abdominal fat layer of different thickness at different locations would for example delay some parts of the spherically focused wavefront relative to others: the wavefront is aberrated. As a result, the apparent geometric focus of different regions of the wavefront is located at different positions and consequently, different regions of the wavefront focus at different positions. This results in a widening of the extent of the ultrasonic focus and a reduction in the maximum pressure.

While for most patients the aberrations due to the abdominal fat layer are modest at the HIFU frequencies, Lynn and Putnam (1944) already noted that the aberrations due to the skull bone lead to a complete loss [1] of ultrasonic focusing and that treatment of deep tissues required a craniotomy to remove the aberrating layer. The aberrating effects of the skull bone were further investigated in White et al. (1968, 1969); Fry and Barger (1978).

Phillips et al. (1975) suggested applying phase corrections to signals acquired with a phased array in the context of diagnostic imaging through the skull. Thomas et al. (1996) proposed ultrasonic focusing by time reversal of therapeutic ultrasound and were able to demonstrate a 10 dB improvement at the focus.

Principles of Time-Reversal Focusing

Focusing with a time-reversal mirror is an adaptive focusing technique that allows among others automatic correction of wavefront aberrations. The aim of the method is to emit a wavefront carefully distorted such that after traversing an aberrating layer a spherically focused wavefront results.

The basic idea of time-reversal focusing stems from the realisation that the linear wave equation of a non-dissipative inhomogeneous medium

$$\left[\rho_0(\mathbf{r})\,\nabla\cdot\left(\frac{1}{\rho_0(\mathbf{r})}\nabla\right)-\frac{1}{c_s(\mathbf{r})^2}\frac{\partial^2}{\partial t^2}\right]p(\mathbf{r},t)=0 \tag{1.1}$$

1. The loss of ultrasonic focussing at MHz frequencies is among others due to the fact that the diploë* of the skull bone is structured with a characteristic length scale similar to the ultrasonic wavelength at MHz frequencies. To avoid this problem, it has been suggested to work at lower frequencies, which however brings new challenges with regard to cavitation control and treatment safety.

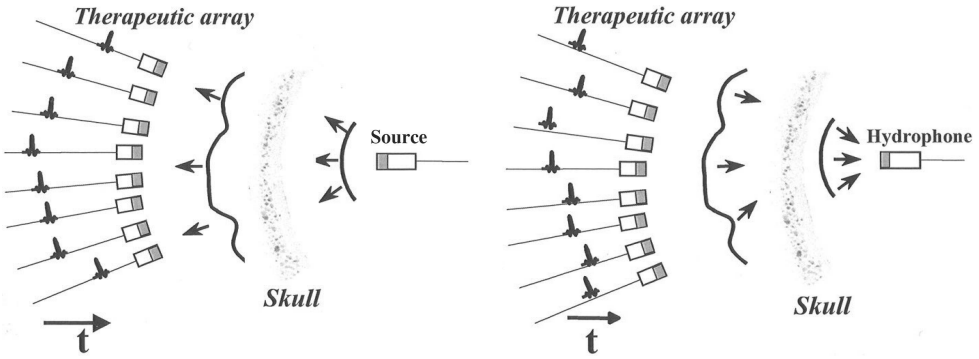

(a) Step 1: recording the causal solution $g_{causal}(\mathbf{r}, t)$

(b) Step 2: re-emitting the time-reversed causal solution with a delay t_0: $g_{causal}(\mathbf{r}, t_0 - t)$

Figure 1.3: Principle of focusing with by time-reversal. Illustration (slighly adapted): Pernot et al. (2007)

is satisfied mathematically by two solutions due to the fact that the temporal derivative is of second order: a causal solution $g_{causal}(\mathbf{r}, t)$ of which the form depends on the inhomogeneities of the medium and an anti-causal solution which is given by $g_{anti-causal}(\mathbf{r}, t) = g_{causal}(\mathbf{r}, -t)$. The notion of "time-reversal" in this context results from the fact that the causal and the anti-causal solutions are symmetrical with respect to time: the anti-causal solution behaves as if the causal solution was "played" in reverse. To provide a mode intuitive picture: if g_{causal} is a wave diverging from a point source, e.g. the ripples on the surface of a lake after a stone was dropped in the water, $g_{anti-causal}$ represents a solution in which rings "magically" appear at the boundary of the lake, converge towards a point and end by expelling a stone from the lake. Even though time-reversal in its stric form requires a loss-less medium, focussing by time-reversal produces optimal focussing for a given energy even in lossy media due to the fact that the time-reversal operation corresponds to a matched filter. (Tanter et al. (2001); Aubry et al. (2001))

Due fundamental physical considerations, i.e. that the effect cannot precede the cause, the anti-causal solution is generally discarded as un-physical. However, as (1.1) exhibits translational invariance with respect to time, by shifting the anti-causal solution an arbitrary time t_0 from the origin of time by the substitution $t \to t - t_0$, the anti-causal solution becomes $g_{anti-causal}(\mathbf{r}, t - t_0) = g_{causal}(\mathbf{r}, t_0 - t)$ which is physical as long as $t \leq t_0$.

In the context of focusing by time-reversal the wavefront diverging from a point source (i.e. the causal solution) is recorded on an array of transducers as illustrated in Figure 1.3a. Due to the fact that the anti-causal and thus converging solution is given by the time-reversed causal solution, it is sufficient to play the recorded wave front in reverse at a late time (i.e. after t_0) to

Figure 1.4: Therapeutic ultrasound array used by Pernot et al. (2007). Photos: Pernot (2004)

recreate a wave field that converges towards the position of the point source as illustrated in Figure 1.3b. Inspired by its effect, the array of transducers recording and re-emitting the wave fronts is sometimes called a time-reversal mirror.

The great advantage of focusing by time-reversal is that the acoustic medium needs not be acoustically homogeneous but may exhibit an arbitrary degree of inhomogeneity. It therefore allows focusing acoustic waves in situations where geometric focusing is impossible. One of the downsides of this approach is that an acoustic point source needs to be present at the position of the desired focus at least for the first step of the process.

Methods for Creating an *in Situ* Acoustic Point Source

At first glance the need for an *in situ* acoustic point source that can be used for time-reversal focusing may appear to severely limit the method. However, numerous approaches exist to create such a source with minimally invasive methods as well as non-invasively.

The first approach, and to date still the gold-standard in terms of focusing power, was demonstrated *in vivo* by Pernot et al. (2007) with the perspective of treating brain tumours. Skulls of sheep were placed against a therapeutic ultrasonic array consisting of 200 mono-element transducers distributed in a semi-random manner on a hemi-spherical dome-like surface. (See Figure 1.4 and Figure 1.5.) A skin incision was made and a hole 10 mm in diameter was drilled in the skull bone to insert a 4 mm trocar*. The trocar allowed the insertion of a 3 mm needle hydrophone which was positioned at the target

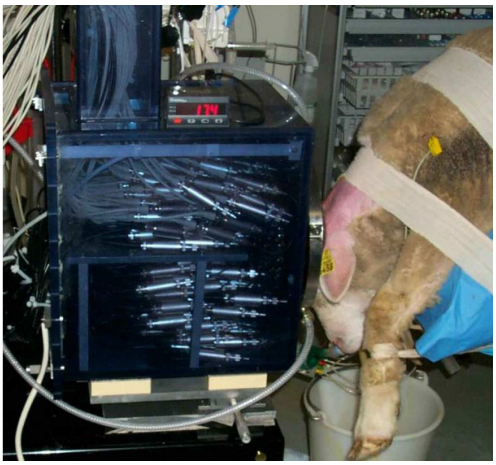

Figure 1.5: Sheep skull placed against the therapeutic ultrasound array in Pernot et al. (2007). Photo: Pernot (2004)

location deep in the brain of the animal. The first step of the time-reversal procedure is then carried out. In practice the procedure used it equivalent to emitting an ultrasonic pulse with the hydrophone and recording it by the transducers of the array after having propagated through the skull bone.

In a second step, the needle hydrophone and trocar were removed. The acquired signals were time-reversed and used to target HIFU at the position of the needle hydrophone. It was shown, by MRI imaging and histology that a well-defined lesion could be produced at the location of the hydrophone without performing a craniotomy. In this particular experiment, the acoustic energy at the focus could be increased 25-fold by using time-reversal focusing compared to traditional focusing.

Even though insertion of a trocar does not compare unfavourably in terms of collateral damage to existing methods such as the Gamma Knife - and may even be required independently of the HIFU procedure for a tissue biopsy, it prevents HIFU from offering an indisputable advantage over existing surgical methods for the treatment of brain tumours. Research has therefore been focused on creating the required acoustical point source *in situ* non-invasively.

Marquet et al. (2009) demonstrate the feasibility of replacing the first step of the procedure, i.e. the acquisition of the signals diverging from a point source, with a numerical simulation. Monkeys were fitted with a stereotactic frame* and the structure of the skull bone measured with a CT scan. The data of the CT scan served as the basis for the creation of a numerical model of the acoustic properties of the brain and skull bone. A virtual source was then created in a finite difference time-domain simulation at the position of the desired focus and the propagation of the virtual acoustic pulse through the skull bone simulated.

Once the simulation was completed, the monkeys were positioned with the stereotactic frame in front of the HIFU array and the simulation results used to target the ultrasonic beam. It was demonstrated that well-defined lesions could be produced at the desired location deep in the brain of monkeys.

Unfortunately, errors in positioning and the practical limits to the spatial resolution of the finite difference time-domain simulation result in a 20% drop of the intensity at the focal spot compared to the intensity that can be obtained with a hydrophone. Gateau et al. (2010) proposed a method which uses the approximate focusing obtained by simulation to induce a single cavitation bubble in the focus region. Using time-reversal of the ultrasonic signature of the created bubble it was possible to recover 17±1% of the missing 20% of the intensity at the focus.

It is clear that with the combination of the methods presented in Marquet et al. (2009) and Gateau et al. (2010) HIFU can now provide a unique alternative to existing surgical methods: an entirely non-invasive method for brain surgery. However, the method still required a significant effort in equipment, time and know-how. It requires a detailed computed tomography of the skull, two hours of simulation at the present time and use of a stereotactic frame to guarantee a common frame of reference for the simulation and the time-reversal. While the time needed for the simulation can be expected to rapidly become negligible in about six years time due to the increase in processing power of computers, the need for a CT scan and the stereotactic frame will remain.

One of the perspectives of the methods developed in this thesis is to eliminate the need for the simulation of the virtual source presented in Marquet et al. (2009) by creating a physical point source at the desired target location that can be recorded on a traditional therapeutic array and used for time-reversal: CT scan, expensive simulation and stereotactic frame would no longer be needed and the procedure therefore significantly simplified thus rendering a routing clinical application more feasible.

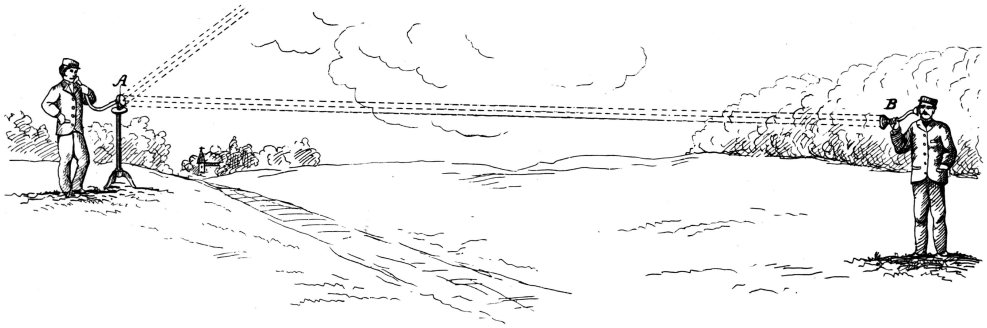

Figure 1.6: Bell's Photophone. Illustration: Bell (1881b)

Photoacoustics

Discovery and Early Investigations

The PHOTOACOUSTIC EFFECT [2], or alternatively the THERMOACOUSTIC EFFECT [3], describes the conversion of electromagnetic radiative energy into acoustic energy in a medium, e.g. the generation of sound from the absorption of light. The effect was first discovered by Alexander Graham Bell in 1880 in his search for wireless communication while working on an invention he called the photophone. (Bell (1881a); see Figure 1.6.)

The photophone comprised a transmitter consisting of a voice-modulated mirror which reflected a beam of sunlight towards a receiver with a selenium cell connected to a loudspeaker. The invention allowed wireless communication over a distance of 400 m but Bell realised that the range would be difficult to extend due to the lack of appropriate light sources. (Bell (1881b)) During his experiments however Bell noted that an audible sound was emitted from the selenium cell itself.

The discovery of the photoacoustic effect was followed by a flurry of research investigating the phenomenon in detail. Bell himself investigated how different solids responded when exposed to a beam of modulated light and quickly concluded that a membrane blackened with soot produced the loudest sound. Röntgen and Tyndall investigated liquids and gases while Lord Rayleigh provided in Rayleigh (1881) the first attempt at a theoretical unders-

2. Especially in early literature, the PHOTOACOUSTIC EFFECT was referred to as the OPTO-ACOUSTIC EFFECT. Rosencwaig (1976) proposed referring to the effect as the photoacoustic effect to avoid confusion with the acousto-optic effect which describes the acoustic modulation of light. While the term photoacoustic effect today dominates in literature, optoacoustic effect is still used by some research groups.

3. The term THERMOACOUSTIC EFFECT is generally used when the source of energy is not provided by ultraviolet, visible or near-infrared light but for example by microwaves or x-rays to emphasise this difference to the vast body of work using light as energy source. It emphasises a distinction of technology and experimental context rather than of physical principle.

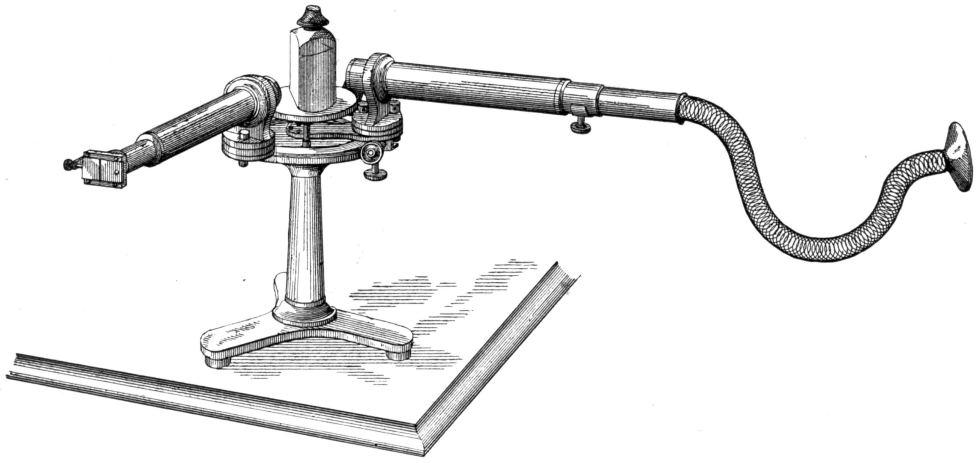

Figure 1.7: Bell's Spectrophone. Illustration: Bell (1881b)

tanding of the phenomenon. Rayleigh's paper also introduced what has since become known as thermal confinement, as the condition for optimal sound production. With his intuition for innovative technologies Bell (1881b) introduced a practical application for the photoacoustic effect, the Spectrophone. The spectrophone is essentially a spectroscope with a hearing tube for detection. (See Figure 1.7.) With the spectrophone spectroscopy could be extended beyond the visible range.

Development of the Photoacoustic Effect as a Tool for Spectroscopy

Due to the lack of suitable light sources and a way to quantify sound intensities, interest in the photoacoustic effect rapidly waned following the initial excitement until 1938 when Viengerov introduced a gas spectrometer based on the photoacoustic effect which allowed him to detect CO_2 in a concentration of $0.2\,\%_{vol}$ in N_2 gas. (Viengerov (1938)) However it was not until the 1970s with the introduction of the laser as a high-intensity modulated light source and the theoretical models for the effect by Rosencwaig and Gersho (1975); Rosencwaig (1976) that photoacoustic spectroscopy became a routine method for chemical analysis. An early example is the investigation of Patel et al. (1974) using a balloon-born photoacoustic detector to measure the temporal variations of nitric oxide in the stratosphere that provided the crucial data for the understanding of the ozone hole: the depletion of ozone in the stratosphere by man-made nitric oxide. Today photoacoustic detectors are widely used for pollution monitoring, smoke detection and trace gas detection with sensitivities of the order of parts per trillion.

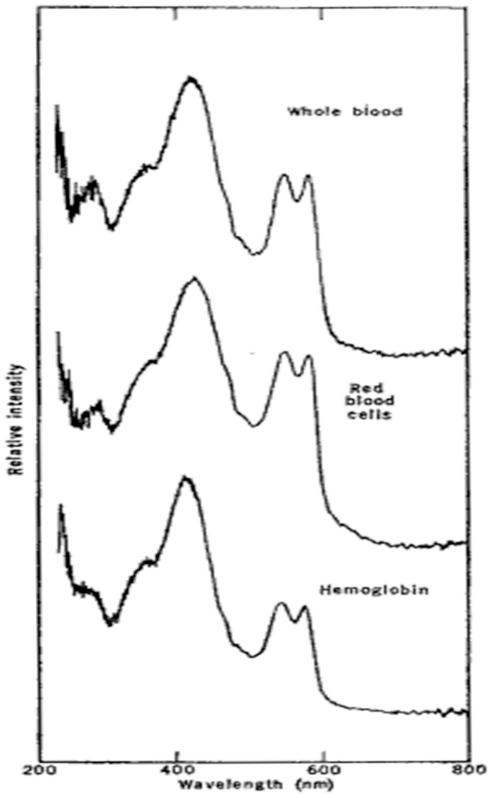

Figure 1.8: Photoacoustic absorption spectra of haemoglobin, red blood cells and whole blood (all dried). Illustration: Rosencwaig (1973)

Photoacoustic Effect for Optical Sensing in Diffusive Media

Applications of photoacoustic spectroscopy are first suggested by Rosencwaig of Bell Laboratories in 1972. In a series of ground-breaking experiments in the early 1970s Rosencwaig demonstrated numerous applications to photoacoustic spectroscopy, among others the measurement of molecular concentrations of membrane proteins, the measurement of the band gap of semiconductors in powder or amorphous form. In Rosencwaig (1973) he presented the photoacoustic absorption spectrum of haemoglobin measured in its natural environment of whole blood - at a time when the spectrum of haemoglobin was generally measured after a lengthy isolation process. Rosencwaig proposed photoacoustics as a method to monitor the haemoglobin content of blood. The varied work of Rosencwaig was reviewed by Maugh (1975) but progress was slow until the spread of digitising oscilloscopes facilitated research by allowing to time-resolve the photo-acoustic signals.

It was Oraevsky (1994) and Kruger (1994) who introduced the idea of using time-resolved photoacoustic signals for imaging the optical absorption in optically diffusive media independently. Kruger (1994) used a phantom

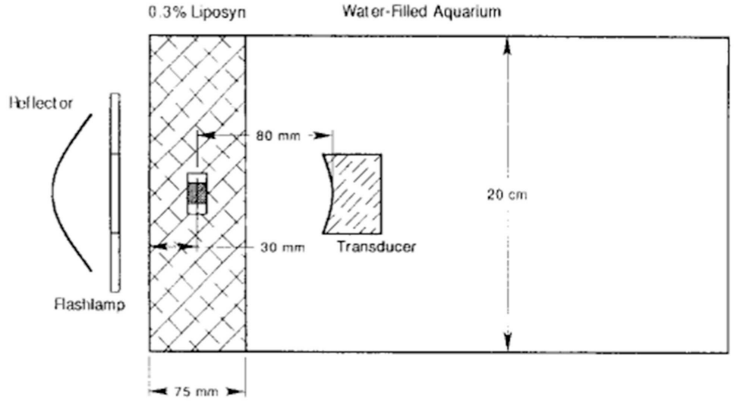

(a) Experimental setup.

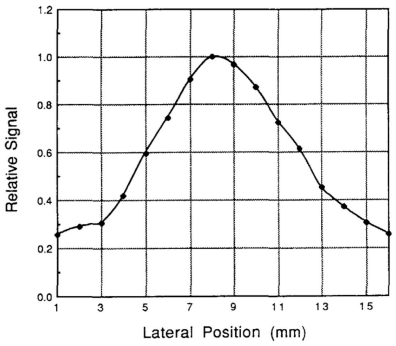

(b) Lateral position of the optical contrast.

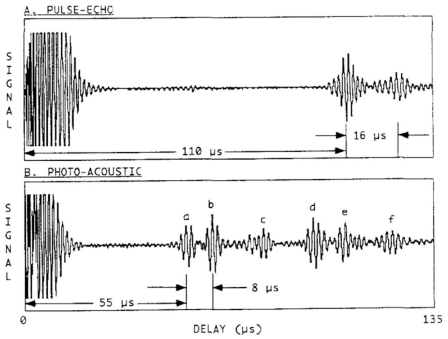

(c) Axial position of the optical contrast.

Figure 1.9: Experiment to localise an optical contrast in a diffusive medium. Illustrations: Kruger (1994)

consisting of 0.3% Liposyn solution, a Xenon lamp with a flash duration of 1 µs and a focused 0.5 MHz ultrasound transducer to localise a single optical absorber. (See also Figure 1.9.) He realised that the resolution was limited by the bandwidth of the transducer used and more importantly the duration of the flash. He also proposed considering microwave pulses as a source of energy.

The theory of photoacoustic signal generation and ultrasonic wave propagation in liquid media was developed by Karabutov et al. (1996). In 1996 in a patent application Oraevsky, Jacques and Esenaliev proposed using time-resolved photoacoustic signals in analogue to echographic imaging as a medical diagnostic imaging tool. (Oraevsky et al. (1998)) However, the technological challenges put this aim out of reach for the time being. In Oraevsky et al. (1997) they demonstrated that it was possible to use the temporal profile of photoacoustic signals to obtain estimates of the average optical properties of different biological tissues that were of the correct order of magnitude: e.g. for

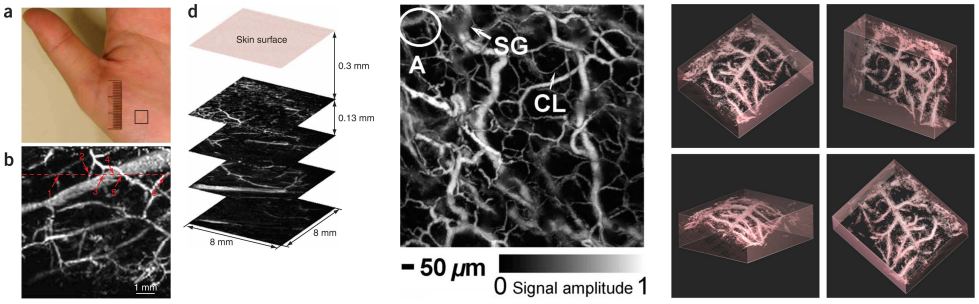

(a) Photoacoustic microscopy. Illustration: Zhang et al. (2006)

(b) Optical resolution photoacoustic microscopy of a nude mouse ear. Illustration: Maslov et al. (2008)

(c) Non-invasive photoacoustic tomography of the vasculature of the mouse brain. Illustration: Laufer et al. (2009)

Figure 1.10: Examples of photoacoustic microscopy & photoacoustic tomography

beef liver $\mu_a = 0.3\,\mathrm{cm}^{-1}$, $\mu_s' = 4.13\,\mathrm{cm}^{-1}$ at 1064 nm. Kruger et al. (1999) and Wang et al. (1999) were among the first to present thermoacoustical images using microwave excitation of a sample.

Contemporary Photoacoustic Imaging Modalities for Biomedical Applications

Today there are mainly three competing photoacoustic imaging modalities; photoacoustic microscopy, optical resolution photoacoustic microscopy and various tomographic methods:

Photoacoustic microscopy refers to methods employing large-scale illumination and detection using a focused ultrasonic transducer. The advantage of this method is that the envelope of the temporal photoacoustic signal can be used directly for the formation of a line in a photoacoustic image. A complete image is acquired by mechanically scanning the transducer focus over the region of interest. (See Figure 1.10a.) The resolution of the method is limited by the duration of the light pulse and the absorption of high-frequency ultrasound in tissue. To achieve a resolution of 5 µm a frequency of about 300 MHz would be required. Given that the attenuation of tissue can be as high as $80\,\mathrm{dB.mm}^{-1}$ for these frequencies, the photoacoustic signal can only be detected at a distance of 500 µm or less. (Li and Wang (2009))

An evolution of photoacoustic microscopy attempting to overcome this limitation is photoacoustic microscopy with optical resolution. With this method light is focused in the medium and scanned in the region of interest. Due to the diffusion of light in biological tissue, this method is limited to a depth of about 100 µm. However, optical transverse resolution can be obtained. (See

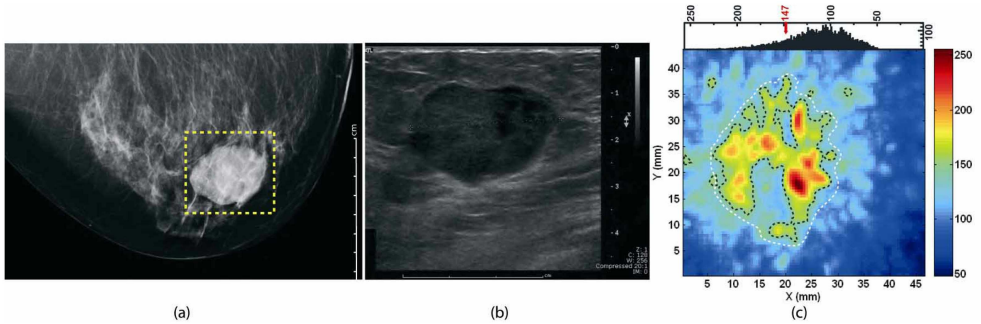

Figure 1.11: (a) x-ray image, (b) echography, (c) tomographic photoacoustic image of a tumorous region in a human breast. Illustration: Manohar et al. (2007)

Figure 1.10b.)

For tomographic photoacoustic imaging methods the entire region of interest is illuminated and the photoacoustic signals detected using unfocused detectors for acoustic waves, which may be piezo-electrical, optical, etc. These may be point-like or small surface area detectors, line or large plane detectors. Depending on the detection type and measurement geometry different reconstruction algorithms are used to create an optical image from the detected photoacoustic signals. E.g. for a 1-D linear acoustic array as commonly used in echographic imaging photoacoustic beamforming similar to echographic beamforming may be used. For line detectors, Radon inversion schemes similar to those used in x-ray CT are used.

Apart from the work presented above, photoacoustics has been used for a number of other imaging or sensing methods. Among them are small animal imaging (Laufer et al. (2009), see also Figure 1.10c), photoacoustic spectroscopy for functional imaging (Wang et al. (2003)) and molecular imaging (Li et al. (2008); De La Zerda et al. (2008)). Due to the fact that the efficacy of the conversion of luminous energy to acoustic energy depends on the temperature, photoacoustics may also be used for temperature monitoring, for example during HIFU treatment (Wang et al. (2009)). A near-comprehensive review of the applications of photoacoustics in biomedical imaging and sensing is provided by Li and Wang (2009).

Generally speaking, photoacoustic imaging has been limited to depths of several millimetres. This can be attributed in part to the need for high-power tunable lasers to penetrate deeper in tissue and in part to additional challenges arising from severe variations of the local light spectrum as a function of penetration depth. However, some authors have already demonstrated that photoacoustic sources can be detected several centimeters in depthin biological tissue. (Esenaliev et al. (1999); Manohar et al. (2007))

Time-Reversal Using Photoacoustic Signals

Our group demonstrated in Bossy et al. (2006) that it is possible to use photoacoustic waves from a single optical contrast in an acoustically complex medium to correct acoustic aberrations. The experimental setup used was similar to that of the first experiments exploring the use of photoacoustics for imaging diffusive media by Kruger (1994) (see Figure 1.12a): a single optical contrast (AS) in the form of a transparent sphere with an absorption coefficient of $\mu_a = 10\,\mathrm{cm}^{-1}$ was suspended is a 0.4% Intralipid solution (IL) at 3 cm in depth relative to the point of light injection. A frequency-doubled Nd:YAG laser was used to generate 85 mJ, 5 ns pulses at 532 nm. The photoacoustic signals were acquired with an ultrasonic linear array (UA) in front of which a strong acoustical aberrator (RS) could be placed. Figure 1.12a illustrates the photoacoustic waveforms received in a homogeneous and an aberrated medium.

After replacing the optical contrast with a needle hydrophone (HGL) it was shown that by emitting the photoacoustic wave form in reverse time from the linear array, an ultrasonic focus could be obtained at the position of the optical contrast agent even in the presence of a strong acoustical absorber. In Figure 1.12b the dashed line corresponds to the focus obtained by time-reversal in an aberrated medium and the dotted line the pressure distribution obtained in an aberrated medium without time-reversal. The dashed line respresents the optimal focus obtained in a homogeneous medium. It clearly demonstrates that time-reversal of photoacoustic waves can be used to obtain a quality of the focus in an aberrated medium equivalent to that obtained by conventional techniques in homogeneous media.

To demonstrate one application for time-reversal of photoacoustic waves, two nylon wires hidden behind a strong acoustical absorber to be imaged echographically. (See Figure 1.12d.) On one of the wires an optical contrast was suspended with was could be used to compensate for the aberration by time-reversal of the photoacoustic waves.

1.3 Objective and Motivation for this Thesis

The primary objective of the work for this thesis was to explore the opportunities for photoacoustics in the context of HIFU. While photoacoustics and HIFU have both seen significant developments over the last decade, very little research explored possible interactions between the two fields. It was suspected due to known changes to the optical properties of biological tissues as a result of heating that photoacoustics might be useful for treatment monitoring as well as to provide an *in situ* acoustic source.

While at the beginning of this thesis the state of knowledge made it premature to aim for the implementation of a specific practical application of photoacoustics in the context of HIFU, the explorations of the subject matter during the course of the work for this thesis were inspired by two prospective

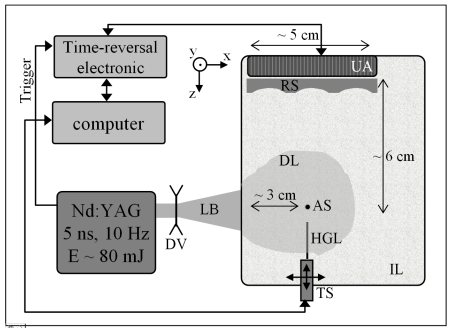

(a) Experimental setup

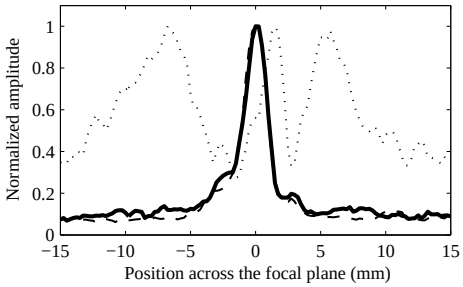

(b) Focus obtained by time-reversal (solid line).

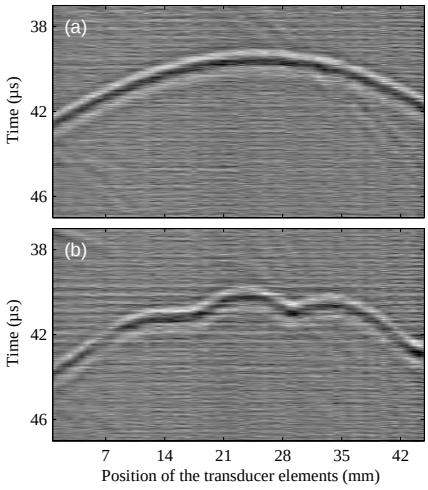

(c) Typical photoacoustic wave forms without (upper figure) and with acoustical aberrator (lower figure).

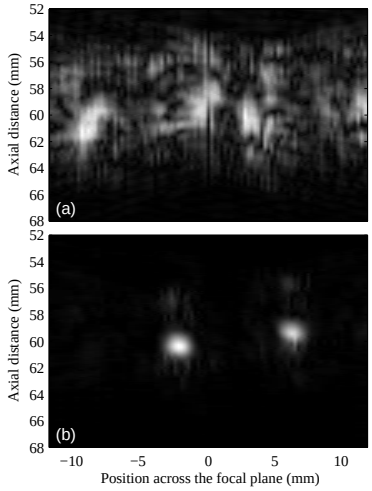

(d) Echographic image without and with aberration correction

Figure 1.12: Experiments by Bossy et al. (2006) on time-reversal of photoacoustic waves. Legend for (b):
—— Focus obtained by time-reversing the photoacoustic waves measured in the presence of an aberrator.
· · · Focus obtained by time-reversing the photoacoustic signal measured without aberrator, but time reversed in the presence of an aberrator.
−− Focus obtained by time-reversing the photoacoustic waves measured without aberrator, i.e. optimal focussing in a homogeneous medium for the given transducer geometry.

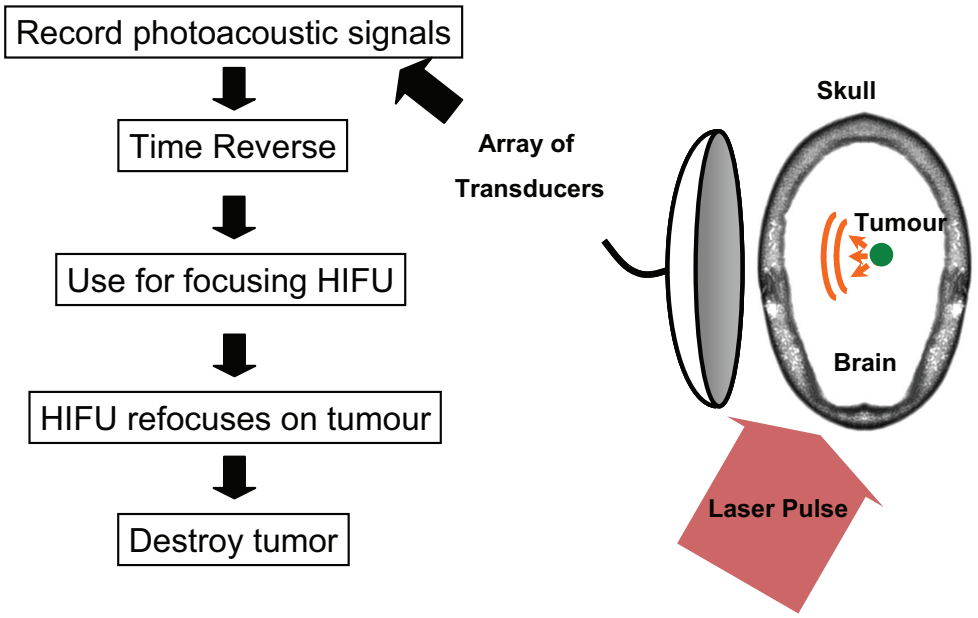

Figure 1.13: Schema of a proposed application combining photoacoustics and HIFU. Sequence: laser illumination, ultrasound emission by the tumour, recording of the signals produced.

applications both of which would use photoacoustic to provide an acoustic source *in situ*.

Photoacoustics for HIFU Aberration Correction

The first application for photoacoustics in the context of HIFU that was envisaged was for aberration correction during the treatment of tumours in acoustically complex media, such as behind the skull bone. (See Figure 1.13.) For this the tissue containing the tumour would be illuminated with a short light pulse which would diffuse through the tissue and be partially absorbed by the tumour. The tumour would then emit acoustic waves via the photoacoustic effect which would propagate through the skull bone and be recorded on an array of therapeutic transducers. The photoacoustic signals could then be time-reversed and used to focus HIFU back on the tumour from which the photoacoustic waves originated.

The challenges arising in the context of this application are primarily due to the fact that the presence of endogenous optical contrasts in tissues results in the generation of photoacoustic signals from various tissue structures. To achieve selective targeting of the tumour, it was explored whether an optically selective contrast agent could be used to discriminate the photoacoustic signals of the tumour from those of the endogenous photoacoustic background. Furthermore the need to detect extremely faint acoustic signals on an array

of detectors that is able to withstand the energy densities for HIFU treatment poses unique technological and signal processing challenges.

Targeting of Tumours at Unknown Locations

Today tumour treatment is generally an invasive surgical procedure. To be certain that the benefit of the procedure outweighs the risk and discomfort to the patient, tumours are generally allowed to reach a certain size, e.g. of the order of a centimetre, to allow reliable diagnosis: millimetre-sized tumours are very difficult to target reliably with a biopsy needle, cannot be palpated or imaged with current technologies in sufficient detail to observe the evolution of pathological changes to the tissue. Furthermore they are difficult to locate during a surgical procedure.

The combination of photoacoustics and HIFU may allow tumours to be treated at an earlier stage: due to the non-invasiveness of the procedure the risk and discomfort to the patient is likely to be very low which would allow a more pro-active approach to treatment of tumours.

If the presence of millimetre-sized tumours was confirmed, it could be envisaged that the patient be injected with a non-toxic optical contrast agent that was chemically targeted to allow predominant accumulation in the tumour. The physician would then orient the therapeutic array towards the approximate location of the tumour and allow the system to automatically target the tumour by using the photoacoustic source due to the contrast agent in the tumour as a guide.

Furthermore, a portable therapy system similar to today's portable echography devices could be envisaged that would allow the free-hand treatment of tumours, e.g. in the breast, as a routine out-patient procedure such as echographic imaging is today. Since breast cancer is the most common type of cancers in women (Cancer Research UK (2010)), this would considerably reduce the financial burden of routine tumour therapy on health care systems and free operating theatres as well as hospital beds for other procedures. Furthermore the risk to patients due to secondary infections acquired during post surgery care in hospital could be minimised.

The challenge for the free-hand HIFU with photoacoustic targeting lies primarily in the need for real-time updating of the focusing parameters. Since photoacoustic signals are very faint and since there are limits to the permissible repetition rate for laser illumination of the human body, the signal detection electronics and signal processing routines must allow the detection of the photoacoustic signals with sufficient signal to noise ratio such as to not require the averaging over multiple acquisitions.

Chapter 2

Theoretical Background

Contents

2.1 Light Propagation in Tissues

The origins of the idea of using light to investigate the interior of the human body lie in the 19^{th} century. While the human body is clearly not transparent, the magical red glow of a hand held in front of a lamp in the dark shows that some light can penetrate.

The implementation of routine optical imaging of biological tissue *in vivo* has proven evasive. This is mainly due to one highly disadvantageous property of biological tissue: tissue is not a homogeneous medium but a complicated mixture of materials and structures of all sizes. While light absorption in tissue is relatively low, if appropriate wavelengths are chosen, biological tissue is highly scattering to light. As a result a significant proportion of the light used to illuminate tissue is reflected and the effective path lengths of photons in the medium significantly increased. In combination this leads to a very limited

penetration depth of light in tissue of the order of millimetres for ballistic light and of the order of centimetres for multiply-scattered light.

In the field of optical imaging of biological tissues, methods are generally differentiated by the type of photons that are used as a source of information. The photons in a scattering medium can be loosely classified into three categories:

Ballistic photons have not been scattered by the medium. In tissue these are very scarce at useful depths due to an exponential decrease of their number with depth.

Multiply scattered photons have undergone several scattering events and can be, depending on the absorption coefficient of the tissue, still relatively numerous even at greater depths. However, due to the probabilistic nature of scattering they have lost all geometric information about their path and are thus in their raw form of little use for traditional optical imaging based on ray-tracing.

Snake-like photons is a category for the boundary cases between above two categories. Generally photons that have undergone little scattering and follow an near-ballistic path are considered snake-like photons. These may be used to achieve a slightly blurred optical image.

For photoacoustics, photons themselves do not act as carriers of information about the medium but merely serve as a source of energy for the photoacoustic effect. The information about the medium is carried by the generated acoustic waves. Therefore, the complexity of the paths of the photons in the medium is of importance only in so far as it is related to the distribution of luminous energy in the medium. In the following a short introduction to the factors determining the distribution of luminous energy in biological tissue is provided.

Absorption Coefficient

Absorption in tissues arises at the molecular scale. The energy of photons is absorbed by the molecules and the electrons of atoms. Absorption at visible wavelengths is dominated by atomic absorption while at infrared wavelengths molecular absorption dominates.

On a macroscopic scale, the efficiency of absorption is spatially averaged. An absorption coefficient μ_a is defined such that for a collimated beam in a homogeneous, non-scattering medium, an infinitesimal change of the intensity of light dI results from the propagation of the light of intensity I by an infinitesimal length of path dL:

$$dI = -\mu_a \, I \, dL \tag{2.1}$$

Integration of (2.1) over a path length L gives the Beer-Lambert attenuation law:

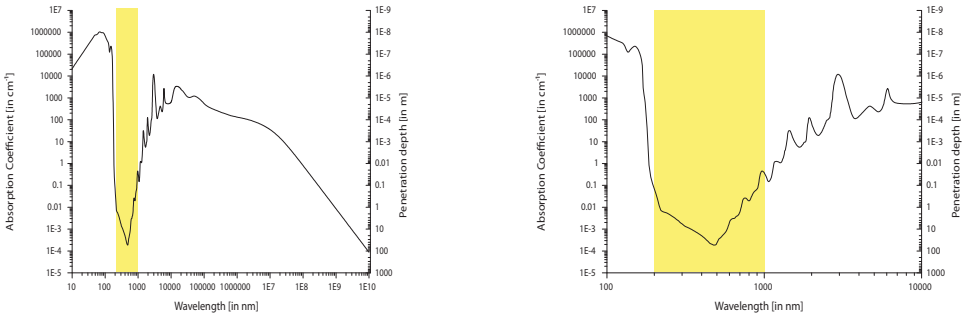

(a) (b)

Figure 2.1: Absorption spectrum of water. The yellow shaded region identifies the window with relatively low absorption. Data: Segelstein (1981)

$$I(L) = I_0\, exp\,(-\mu_a\, L) \tag{2.2}$$

where I denotes the beam intensity after path length L and I_0 the initial beam intensity.

As biological tissue consists of various materials its absorption spectrum is a combination of the absorption spectra of its components such as water, lipids, haemoglobin and melanin.

Water as the most abundant matter in most biological tissues absorbs principally in the infrared, as well as in the ultraviolet. This leaves a window where little of the energy is absorbed for wavelengths between 200 and 1000 nm as can be seen in Figure 2.1b. For medical diagnostics this defines a first set of boundaries for the permissible wavelengths.

Haemoglobin as another important component of many biological tissues absorbs strongly in the ultraviolet to red. The fact that biological tissue appears red on trans-illumination is due to the absorption of light at lower wavelengths by haemoglobin. The absorption of haemoglobin therefore imposes a new lower boundary for permissible wavelengths for therapeutic applications at about 700 nm. (See Figure 2.2.) The "therapeutic window" is identified in all following absorption spectra by turquoise shading. It is notable that there is a significant divergence of the absorption spectra for haemoglobin in its oxygenated (HbO_2) and de-oxygenated state (Hb) for wavelength greater than 600 nm. Of particular interest are the wavelength about 800 nm where the absorption spectra cross with opposite gradients. This is exploited by spectroscopic approaches to measuring the oxygenation of blood. (Prahl (1999))

Lipids do not contribute significantly to the total absorption of light in biological tissue over the relevant range of wave lengths.

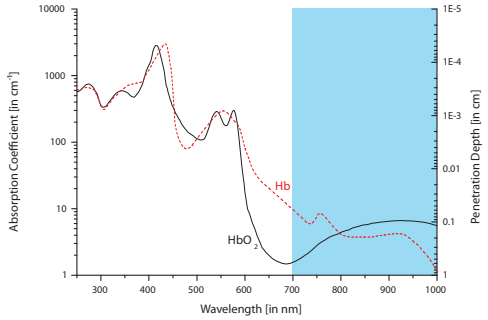

Figure 2.2: Absorption spectra of oxygenated and de-oxygenated haemoglobin. The turquoise shaded region identifies the therapeutic window. The absolute values for the absorption coefficient depend on the concentration of haemoglobin in the blood. This spectrum was calculated on the typical assumption of a molar concentration $c = 2.33 \times 10^{-3}\,\mathrm{M}$ of haemoglobin in blood. Data: Prahl (1999)

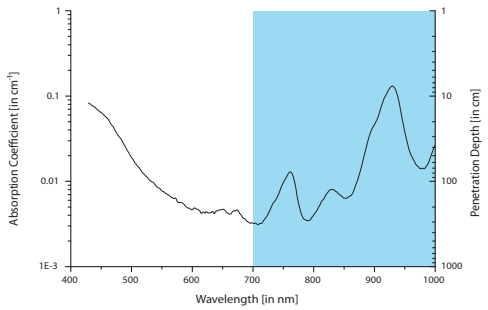

Figure 2.3: Absorption spectrum of mammal lipids measured at 37°C. The turquoise shaded region identifies the therapeutic window. Data: van Veen et al. (2004)

(See Figure 2.3.) However, since the refractive index of lipids differs significantly from that of water, lipids contribute heavily to scattering. (van Veen et al. (2004))

Melanin as other proteins in the body absorb principally in the ultraviolet. The melanin responsible for the absorption is found in micron-sized organelles called melanomas. (See Figure 2.4.) Melanomas are present mainly in the epidermal layer of the skin. The absolute absorption values depend on the tanning of the skin. The volume concentration of melanomas in the epidermis varies between 1-3% for light skinned Caucasians and between 18-43% for dark-pigmented Africans. (Jacques (1998))

The effective absorption coefficient of biological tissue results from the addition of the absorption coefficients of its components. Some typical assumptions

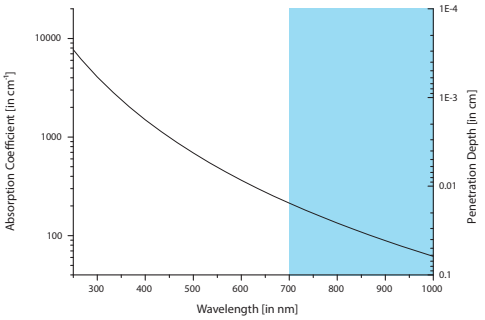

Figure 2.4: Absorption spectrum of the interior of a skin melanoma by melanin. Data: Jacques (1998)

for the proportions for above mentioned components are:

- the body consists to 75% of water and to 7% of blood
- the total haemoglobin concentration of blood is relatively constant in adults at a molar concentration of $c = 2.33 \times 10^{-3}\,\mathrm{M}^{-1}$ (Prahl (1999))
- the haemoglobin oxygen saturation $SO_2 = {}^{c_{HbO_2}}/_{c_{Hb}+c_{HbO_2}}$ depends on the metabolism of the tissue but values of 95% for arterial and 65% for venous blood are commonly assumed

The absorption coefficient of tissue depends heavily on wavelength, but according to Durduran et al. (2002) in breast tissue, a value of $\mu_a = 0.05\,\mathrm{cm}^{-1}$ appears to be a reasonable estimate in the range of $750 - 830\,\mathrm{nm}$.

Scattering Coefficient

Scattering occurs when any wave encounters inhomogeneities in the parameters of its medium. For the scattering of light, the electromagnetic wave is generally scattered by inhomogeneities of the medium's refractive index, e.g. by lipid vesicles in an aqueous environment.

The phenomena of scattering in biological tissues relevant to this document are modelled depending of the size of the scattering particles. All of them are of elastic nature, conserving the energy and thus wavelength of the wave incident.

Rayleigh Scattering applies to particles that are small compared to the wavelength of the light [1]. Suffice it here to say that Rayleigh scattering results in a near-isotropic re-emission of the energy.

Mie Scattering is used to predict the behaviour of light in the presence of larger particles. Here the re-emission of the energy is no longer isotropic but follows a complex function dependent on wavelength, particle size and geometry and the refractive indexes of the particle and the surroundings. The complex form of the re-emission can be understood as

1. A typical assumption is that the particle is smaller than $\lambda/10$.

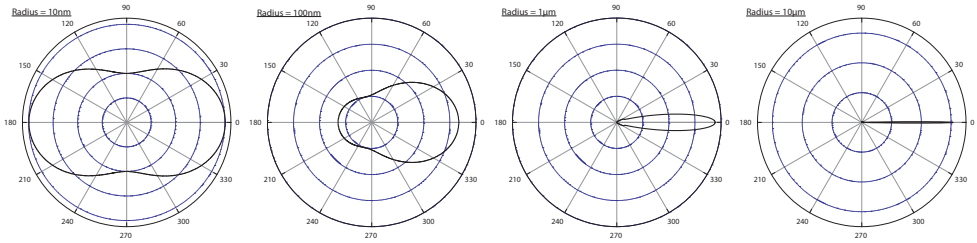

Figure 2.5: Linear-scaled polar intensity plots for the scattering of light with wavelength of 785 nm by four spherical air bubbles at 37°C in water of sizes 10 nm, 100 nm, 1 µm and 10 µm. The series visualises how the scattering tends from fairly isotropic for 10 nm to principally forward for 10 µm-sized inclusions.

a superposition of de-phased light emitted from different parts of the particle. For an illustration of the effect of particle size please refer to Figure 2.5.

Geometrical Optics suffices to describe scattering by particles that are large compared to the wavelength such as raindrops in sunlight, etc.

A spatially averaged parameter for the scattering of light is defined in analogue to the absorption coefficient. The scattering coefficient μ_s is defined such that for a collimated beam in a homogeneous, non-absorbing medium an infinitesimal change of the intensity of unscattered light dI results from the propagation of the light of intensity I by an infinitesimal length of path dL:

$$dI = -\mu_s \, I \, dL \tag{2.3}$$

Integration of (2.3) over a path length L gives the intensity of unscattered light (or ballistic photons):

$$I = I_0 \, exp\,(-\mu_s \, L) \tag{2.4}$$

where I denotes the unscattered beam intensity after path length L and $I_0$the initial beam intensity. For human breast tissue $90\,\mathrm{cm}^{-1}$ is a typical value. (Durduran et al. (2002))

The mean free path $l = {}^1/_{\mu_s}$ is the mean distance a photon travels between two scattering events. In biological tissue a typical value is 100 µm.

Anisotropy Factor

As illustrated by Figure 2.5 the scattering of light by small particles depends on the particles' sizes. While small particle scatter light fairly isotropically, the directionality of the scattered light increases with particle size. It thus becomes necessary to introduce a parameter to take this directionality

into account. A factor of anisotropy g for a medium is defined as the mean cosine of the diffusion angles:

$$g = \int_{-1}^{+1} f(\cos\theta)\, \cos\theta \;\, \mathrm{d}\,(\cos\theta) \tag{2.5}$$

where θ denotes the angle between the photon's direction vector before and after the scattering event. $f\,(\cos\theta)$ is the polar probability distribution function of the scattering direction of a photon scattered in the media.

For isotropic scattering g is zero as the probability of scattering forward and backwards is equal. For forward scattering g tends to +1, for backward scattering it tends to -1. In biological tissue the coefficient of anisotropy is of the order of 0.8 to 0.98 (Gelebart (1998)), and it thus relatively directional.

Henyey and Greenstein (1941) developed an expression for f to model a fitting angular dependence of scattering by small particles in interstellar clouds which satisfies (2.5) for any given g,

$$f\,(\cos\theta) = \frac{1}{4\pi} \frac{1-g^2}{(1+g^2-2g\cos\theta)^{\frac{3}{2}}}, \tag{2.6}$$

which has proven invaluable for simulations as often the factor of anisotropy is known but the exact form of f is not.

By combining g and μ_s a new parameter called the reduced scattering coefficient μ_s' can be introduced that takes into account the directionality of the scattering in a medium.

$$\mu_s' = \mu_s\,(1-g) \tag{2.7}$$

Analogously to l an $l^* = (\mu_s')^{-1}$ can be defined which has been named the transport mean free path. It is generally best understood as the length of path after which a photon has lost its memory of direction in the given medium. (Wang and Wu (2007)) Typical values for μ_s' and l^* are $9\,\mathrm{cm}^{-1}$ and $0.1\,\mathrm{cm}$ in the range of $750-830\,\mathrm{nm}$.

Coefficients Combining Absorption and Scattering

The total attenuation including absorption and scattering effects of collimated light is given by the extinction coefficient μ_t (or total attenuation coefficient) defined by:

$$\mu_t = \mu_a + \mu_s \tag{2.8}$$

It follows that the total intensity of ballistic, or collimated, light is given by:

$$I = I_0\, exp\,(-\mu_t\, L) \tag{2.9}$$

Using diffusion theory, it is furthermore possible to define an effective transport coefficient μ_{eff} that gives the intensity of scattered at a certain depth in the medium:

$$\mu_{eff} = \sqrt{3\mu_a \left(\mu_a + \mu_s'\right)} \text{ valid if } L > l^* \tag{2.10}$$

The effective transport coefficient serves to solve the common problem of determining the illumination intensity of a material at depths exceeding a millimetre where effectively no ballistic light remains. Its inverse gives the effective penetration depth of light for depths beyond the ballistic regime. It is typically of the order of a centimetre for near-infrared wavelengths.

2.2 Medical Limits on Illumination

When using lasers in a diagnostic context, it is of particular importance to ensure that the illumination does not cause damage to the tissue. According to Mordon (2007) there are three main types of laser-tissue interaction mechanisms that need to be considered.

- **Electromechanical effects** describe the mechanical damage to tissue due to acoustic shock waves induced by laser pulses. The shock waves may result from plasma generation, explosive vaporisation or induced cavitation. For very high irradiances of the order of 10^{10}-$10^{12}\,\mathrm{W\,m^{-2}}$ atoms are ionised. The pressure gradient at the boundary of the plasma induces a propagating shock wave. Alternatively for irradiances of a duration shorter than the characteristic time scale for thermal diffusion in the tissue, e.g. $< 500\,\mu\mathrm{s}$, the heating is thermally confined. This results in heat accumulation without diffusion and explosive vaporisation. This effect may be used to mechanically break up particles in tissue to facilitate re-absorption, e.g. for de-pigmentation of removal of tattoos. The third alternative results from the combination of thermal confinement with mechanical confinement. Here no explosive vaporisation is possible and a gas bubble forms during the laser pulse which collapses violently after the end of the laser pulse.
- The **photoablative effect** describes a vaporisation of the tissue components without thermal lesioning of the surrounding tissue. Typically the photoablative effect occurs when the energy of the photons exceed the inter-molecular binding energy resulting in a breakup of molecules and a direct vaporisation. This effect is beneficially exploited in laser surgical techniques such as the LASIK technique for corneal reshaping. The effect typically occurs for ultraviolet wavelengths, e.g. $200 - 300\,\mathrm{nm}$. Alternatively the effect can also occur for low-energy photons, e.g. $2900\,\mathrm{nm}$, for which water presents significant absorption. In this case, a short pulse can heat the tissue locally and leads to vaporisation. Heat diffusion is avoided if the duration of the pulse is of the order of $100\,\mu\mathrm{s}$ or less.

– **Photothermal effects** describe modification of tissue due to heating induced by the absorption of light energy. They include hyperthermia for moderate rises in temperature, e.g. $41 - 44$°C, for a duration of the order of tens of minutes. This results in apoptosis due to interference with the enzymatic processes in the cell. For temperatures between 45°C and 100°C proteins and collagen are denatured leading to coagulation by thermal necrosis. Tissue desiccates, blanches*, shrinks and is eventually re-absorbed by the body. For temperatures above 100°C components of tissue volatilise or carbonise rapidly. Around the volatilised zone where the temperature was more moderate a region of thermal necrosis forms.

The European Norm NF EN 60825-1/A2 of January 2006 [2] regulates safe exposure levels for users of lasers to avoid any of the harmful effects described above. In the following the safe exposure levels as defined by the norm for skin shall be explored. Ocular exposure levels can be neglected assuming that the patient will use protective eye-wear during any photoacoustic procedure. Even though the norm EN 60825-1 explicitly does not apply to intentional exposure of the human body for medical treatment it should provide a good indication of the acceptable exposure levels.

For pulsed lasers, as are used in photoacoustic applications, the norm defines two criteria to be met for safe exposure levels for the skin:

– The exposure due to a single pulse in a train of pulses must not exceed the maximum permissible exposure for a single pulse.
– The mean exposure due to a train of pulses of a certain duration must not exceed the maximum permissible exposure for a single pulse of the same duration.

Table 8 of the norm EN 60825-1/A2 defines the following maximum permissible exposures for skin for lasers in the visible wavelength range $400 - 700\,\mathrm{nm}$ ($\mathrm{MPE_{vis}}$) for different pulse durations t:

– t between 1 ns and 100 ns: $200\,\mathrm{J\,m^{-2}}$
– t between 100 ns and 10 s: $1.1 \times 10^4\, t^{0.25}\,\mathrm{J\,m^{-2}}$ (or equivalently $1.1 \times 10^4\, t^{-0.75}\,\mathrm{W\,m^{-2}}$)
– t between 10 s and 3×10^4 s: $2000\,\mathrm{W\,m^{-2}}$

For near-infrared wavelengths between 700 nm and 1400 nm the values for the maximum permissible exposure $\mathrm{MPE_{NIR}}$ are multiplied by a factor C_4, such that $\mathrm{MPE_{NIR}} = \mathrm{MPE_{vis}} C_4$, where

$$C_4 = \begin{cases} 10^{0.002(\lambda - 700)} & \text{for } 700 < \lambda < 1049.485 \text{ nm} \\ 5 & \text{for } 1049.485 < \lambda < 1400 \text{ nm.} \end{cases} \tag{2.11}$$

The laser to be used in our experiments operates between 670 nm and 1064 nm with a pulse repetition rate of 10 Hz and a pulse duration of typi-

2. This norm has now been superseded by the norm EN 60825-1 of May 2008. Due to the limited availability of the new norm, the previous revision is used in this work. Since light sources with the relevant characteristics have been wide-spread for several decades, the changes to the relevant sections are assumed to be negligible.

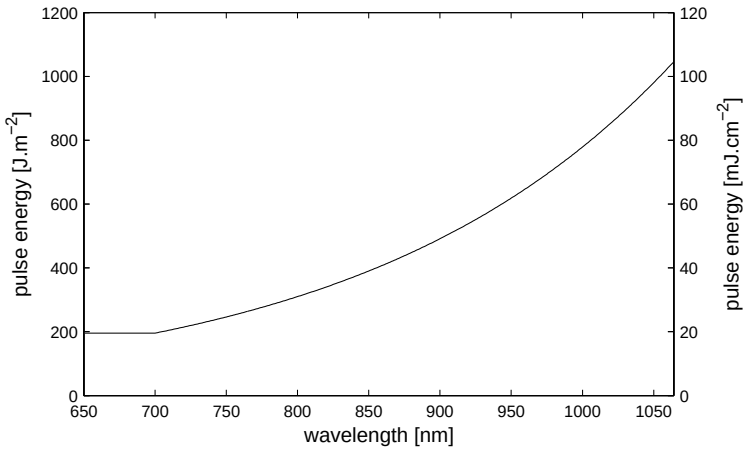

Figure 2.6: Maximum permissible exposure for a laser with nano-second pulse duration operating at 10 Hz.

cally 5 ns. The first criterion thus defines a maximum permissible exposure of $200\,\mathrm{J\,m^{-2}}$ for wavelengths between 400 nm and 700 nm.

For the second criterion for pulse trains of durations between 100 ns and 10 s, the most restrictive conditions occurs for a duration of $T = 10\,\mathrm{s}$, which leads to a maximum permissible exposure of $19561\,\mathrm{J\,m^{-2}}$ over a period of $T = 10\,\mathrm{s}$, or equivalently $1956\,\mathrm{W\,m^{-2}}$. For a laser operating at 10 Hz this translates to a maximum permissible exposure with respect to a single pulse of $196\,\mathrm{J\,m^{-2}}$. For pulse trains of durations between 10 s and 3×10^4 s the limit of $2000\,\mathrm{W\,m^{-2}}$ translates for a 10 Hz laser to $200\,\mathrm{J\,m^{-2}}$ which is identical to the value obtained for the first criterion.

For a laser with a repetition rate of 9.78 Hz, the maximum permissible exposures for a single pulse and for the mean exposure of a train of pulses are identical. For lasers with lower repetition rates, the first criterion dominates by capping the maximum permissible pulse energy. For lasers with higher repetition rates the second criterion dominates by capping the maximum permissible power. A laser operating at 9.78 Hz therefore maximises at the same time the total energy that can be deposited in tissue over time periods of 10 s and above and the pulse energy. The maximum permissible exposure for our application as a function of wavelength is illustrated in Figure 2.6.

In the therapeutic windows at 800 nm the maximum permissible exposure for skin is $31\,\mathrm{mJ\,cm^{-1}}$. A 130 mJ pulse must therefore be spread over a circular region at least 2.3 cm in diameter to stay within permissible exposure limits.

2.3 Photoacoustic Effect

While thermoacoustic imaging can be implemented in many cases without consideration for the intricacies of the thermoacoustic effect, it will become clear in the course of this document that the use of photoacoustic signal from deep in the human body is a challenging endeavour. A successful implementation of such a system depends on the careful optimisation of the various parameters of the system. An awareness of the dominating factors and of the physical assumptions made in the derivations of the mathematical description of the thermoacoustic effect is therefore indispensable.

The objective of this section (in conjunction with Appendices A and B on page 167) is to provide a complete derivation of the thermoacoustic problem in fluids from first principle and some exemplary solutions. It represents an attempt to provide a statement of the theoretical background of thermoacoustics using valid physical assumptions, explicit statement of the assumptions made and consistent mathematical notation.

Many yet unresolved questions that were encountered in the course of the work for this thesis, require a detailed understanding of the thermodynamic processes involved in the thermoacoustic effect. Apart from providing the reader with an understanding of the photoacoustic effect, this section and the corresponding appendices are intended to serve as a basis for further work. With regard to the results presented in this thesis, the most immediate applications were to gain a better understanding of the frequency spectrum of thermoacoustic waves, the conditions for efficient illumination and the energy balance of the photoacoustic effect.

Fundamental Principles

The theoretical framework used to describe the spatio-temporal evolution of pressure and density fields in fluids is based on four fundamental principles:

Conservation of momentum in a fluid, as stated by the Navier-Stokes equation:

$$\rho\left[\frac{\partial \mathbf{v}}{\partial t}+\mathbf{v}\nabla\mathbf{v}\right]=-\nabla p+\mu\nabla\mathbf{v}+\left(\zeta+\frac{1}{3}\eta\right)\nabla\left(\nabla\mathbf{v}\right)+\mathbf{f}, \tag{2.12}$$

where $p(\mathbf{r},t)$ denotes the acoustic pressure field, $\mathbf{v}(\mathbf{r},t)$ the particle velocity field, $\rho(\mathbf{r},t)$ the mass density field, μ and ζ the shear and bulk coefficients of viscosity and $\mathbf{f}(\mathbf{r},t)$ the density of external forces.

Conservation of mass in a fluid, as stated by the continuity equation

$$\frac{\partial \rho}{\partial t}+\nabla\left(\rho\mathbf{v}\right)=0. \tag{2.13}$$

A thermodynamic statement describing the relation of changes in the three variables of state, density ρ, absolute pressure P and entropy per unit

mass s,

$$d\rho = \left(\frac{\partial \rho}{\partial P}\right)_s dP + \left(\frac{\partial \rho}{\partial s}\right)_P ds. \tag{2.14}$$

Conservation of energy expressing that the change in energy of a fluid element results from a combination of heating and and thermal diffusion

$$\frac{\partial Q}{\partial t} = V\,H - k \oint \nabla T\, d\mathbf{S} \tag{2.15}$$

$$\rho T \frac{\partial s}{\partial t} = H + k\nabla^2 T, \tag{2.16}$$

where $T(\mathbf{r}, t)$ it the temperature field, $H(\mathbf{r}, t)$ is the field of absorbed heat per unit volume per unit time and k is the heat conductivity of the medium.

Linear Acoustics without Sources

Let us begin by recalling that the simplest form of a linear acoustic equation in fluids is based on the following assumptions:

- There are no acoustic sources.
- The medium is assumed to be acoustically homogeneous with negligible viscosity.
- The fluid undergoes only adiabatic transformations on the acoustic time scale, i.e. $ds = 0$, and $d\rho = \left(\frac{\partial \rho}{\partial P}\right)_s dP$, in the entire medium.
- All equations are linearised to first order variations.

Under these assumptions, the homogeneous linear wave equation describing the evolution of a pressure field as a function of time and space can shown to be

$$\left(\nabla^2 - \frac{1}{c_s^2}\frac{\partial^2}{\partial t^2}\right) p(\mathbf{r}, t) = 0, \tag{2.17}$$

where $p(\mathbf{r}, t)$ denotes the acoustic pressure field (i.e. the time-varying part of the absolute pressure field $P(\mathbf{r}, t)$) and $c_s^2 = \left(\frac{\partial \rho}{\partial P}\right)_s^{-1}$ the adiabatic speed of sound.

For convenience, above equations may also be expressed in terms of the velocity potential $\phi(\mathbf{r}, t) = \nabla \mathbf{v}(\mathbf{r}, t)$. Re-expression of two fundamental principles in terms of ϕ,

- conservation of momentum in a fluid

$$\rho_0 \frac{\partial \phi}{\partial t} = -p \tag{2.18}$$

- and conservation of mass in a fluid

$$\frac{\partial \rho}{\partial t} + \rho_0 \nabla^2 \phi = 0, \tag{2.19}$$

leads to an expression of the homogeneous linear wave equation in terms of the velocity potential

$$\left(\nabla^2 - \frac{1}{c_s^2}\frac{\partial^2}{\partial t^2}\right)\phi(\mathbf{r},t) = 0. \tag{2.20}$$

At this point the reader may find it useful to skim through the detailed derivation provided in Appendix B on page 173 as reference to details of the derivation of the homogeneous, linear wave equation will be made during the derivation of the photoacoustic problem.

The Linear Thermoacoustic Problem

The linear theory of thermoacoustics is based on the same assumptions as the theory of linear acoustics without sources with one exception: heating of the medium acts as a source of acoustic waves - and thus the process is no longer isentropic with $ds \neq 0$ at the location of the heating. However, it is still presumed that wave propagation is adiabatic.

The expressions for the conservation of momentum and mass remain unchanged, but the thermodynamic statement describing the dependence of a change in density on a change in pressure and entropy can no longer be simplified as in section A.4 on page 169. Instead, the partial derivative $\left(\frac{\partial\rho}{\partial s}\right)_P$ in the general expression

$$d\rho = \frac{1}{c_s^2}dP + \left(\frac{\partial\rho}{\partial s}\right)_P ds \tag{2.21}$$

must be related to known physical constants or measurable quantities. However, given that entropy is related to heat flow, an intuitive relation to the measurable quantity temperature suggests itself. The differential may be split accordingly leading to the equivalent expression

$$d\rho = \frac{1}{c_s^2}p + \left(\frac{\partial\rho}{\partial T}\right)_P \left(\frac{\partial T}{\partial s}\right)_P ds, \tag{2.22}$$

where T denotes the temperature.

Using the isobaric thermal expansion coefficient β and the isobaric specific heat capacity c_P , which are measurable physical constants of materials defined as $\beta = \frac{1}{V}\left(\frac{\partial V}{\partial T}\right)_P = -\frac{1}{\rho}\left(\frac{\partial\rho}{\partial T}\right)_P$ and $c_P = T\left(\frac{\partial s}{\partial T}\right)_P$, one obtains

$$d\rho = \frac{1}{c_s^2}dP - \frac{\beta\rho T}{c_P}ds, \tag{2.23}$$

which (2.23) may equivalently be written in terms of temporal derivatives

$$\frac{d\rho}{dt} = \frac{1}{c_s^2}\frac{dP}{dt} - \frac{\beta\rho T}{c_P}\frac{ds}{dt}. \tag{2.24}$$

Given the definition of entropy per unit mass $ds = \frac{\delta q}{T}$, where δq denotes the infinitesimal absorbed heat per unit mass, one may express the rate of change of entropy as a function of a heat source term. If $H(\mathbf{r},t) \equiv \frac{1}{V_0}\frac{\delta q}{dt}$ is defined as the rate of absorbed heat per unit volume, under the assumption that heat diffusion is negligible on the relevant temporal and spatial scales, from (2.16) one obtains $\rho T\frac{\partial s}{\partial t} = H$. As discussed in section A.5 on page 169, under the assumption of subsonic flow (2.24) can be approximated by

$$\frac{\partial \rho}{\partial t} = \frac{1}{c_s^2}\frac{\partial P}{\partial t} - \frac{\beta}{c_P}H. \tag{2.25}$$

Similarly to section A.5 on page 169, one then obtains the thermoacoustic wave equation

$$\left(\nabla^2 - \frac{1}{c_s^2}\frac{\partial^2}{\partial t^2}\right)p(\mathbf{r},t) = -\frac{\beta}{c_P}\frac{\partial H}{\partial t}, \tag{2.26}$$

where the right-hand side of the equations serve as source term for the homogeneous wave equation. Using the first Grüneisen coefficient defined by $\Gamma = \frac{\beta c_s^2}{c_P}$, the thermoacoustic wave equation ma be written as

$$\left(\nabla^2 - \frac{1}{c_s^2}\frac{\partial^2}{\partial t^2}\right)p(\mathbf{r},t) = -\frac{\Gamma}{c_s^2}\frac{\partial H}{\partial t}. \tag{2.27}$$

This illustrates that the efficiency of the generation of acoustic waves by heat absorption is fully defined by the coupling coefficient Γ.

It is useful to note that when wave propagation is expressed in terms of the velocity potential ϕ, the source term is directly proportional to the heating function $H(\mathbf{r},t)$:

$$\left(\nabla^2 - \frac{1}{c_s^2}\frac{\partial^2}{\partial t^2}\right)\phi(\mathbf{r},t) = \frac{\beta}{c_P\rho_0}H(\mathbf{r},t) \tag{2.28}$$

Solution of the Thermoacoustic Problem

Solution for an Infinite Medium

Expressions (2.27) and (2.28) are inhomogeneous differential equations. A Green's function approach to finding a solution is thus well-suited. Given above Green's function solutions for the inhomogeneous wave equation (see Appendix B on page 173), the solution to the thermoacoustic problem (2.27)

$$\left(\nabla^2 - \frac{1}{c_s^2}\frac{\partial^2}{\partial t^2}\right)p = -\frac{\Gamma}{c_s^2}\frac{\partial H}{\partial t}, \quad (\mathbf{r},t) \in \mathbb{R}^3\times]-\infty,+\infty[\tag{2.29}$$

with the medium initially at rest, $p = 0$ and $\frac{\partial p}{\partial t} = 0$, is therefore given by

$$\begin{aligned} p(\mathbf{r}, t) &= \left[G \underset{\mathbf{r}}{\otimes} \underset{t}{\otimes} \frac{\Gamma}{c_s^2} \frac{\partial H}{\partial t} \right] (\mathbf{r}, t) \\ &= \left[\frac{\partial G}{\partial t} \underset{\mathbf{r}}{\otimes} \underset{t}{\otimes} \frac{\Gamma}{c_s^2} H \right] (\mathbf{r}, t) \\ &= \frac{\partial}{\partial t} \left[G \underset{\mathbf{r}}{\otimes} \underset{t}{\otimes} \frac{\Gamma}{c_s^2} H \right] (\mathbf{r}, t) , \end{aligned} \tag{2.30}$$

where $G(\mathbf{r} - \mathbf{r_s}, t - t_s)$ is the Green's function for an infinite three-dimensional medium.

Solutions Under Stress Confinement

Stress Confinement Condition During the work for this thesis, as for most biomedical applications of photoacoustics, we were concerned with the use of nanosecond laser pulses to produce acoustic waves.

Expressed in three dimensional form, the solution to the photoacoustic problem in an infinite homogeneous medium provides further insights into the waves generated by a "short" heating function: Using the three dimensional Green's function given in Appendix B on page 173, one obtains the three dimensional solution for the generated pressure wave:

$$p_{3D}(\mathbf{r}, t) = \frac{\Gamma}{c_s^2} \frac{\partial}{\partial t} \int d\mathbf{r_s} \, \frac{1}{4\pi \|\mathbf{r} - \mathbf{r_s}\|} H \left(\mathbf{r_s}, t_s - \frac{\|\mathbf{r} - \mathbf{r_s}\|}{c_s} \right) \tag{2.31}$$

This expression shows that each heated point at location $\mathbf{r_s}$ emits a spherical wave with temporal dependence given by the time derivative of the heat source term. Each spherical wave emitted at a point $\mathbf{r_s}$ is delayed due to acoustic propagation by $\frac{\|\mathbf{r}-\mathbf{r_s}\|}{c_s}$ when arriving at an observer at $\mathbf{r}$.

If $t_{heating}$, the duration of the heating terms over the whole source region is short compared to the maximum difference between the propagation delays $\frac{\|\mathbf{r}-\mathbf{r_s}\|}{c_s}$ for different heated points $\mathbf{r_s}$, the heating can be considered to be instantaneous with regards to the generation of the acoustic wave. This situation is mathematically stated via the stress confinement condition, i.e. $t_{heating} \ll t_{acoustic}$, where $t_{stress} \sim {}^{d}/_{c_s}$ defines the stress relaxation time and d is the characteristic length scale of the absorbing region as viewed by an observer at $\mathbf{r}$.

Applied to heating with laser pulses, it is thus required that the pulse duration t_{pulse} satisfies $t_{pulse} \ll t_{stress}$. Moreover, in optically scattering media such as biological tissues, the initial laser pulse duration may be broadened by the diffusion of light within the medium. Assuming that light obeys a diffusion equation with diffusion constant $D_{light} = v \left[3 (\mu_a + \mu_s') \right]^{-1}$, the pulse broadening due to diffusion $t_{diffusion}$ is given by $t_{diffusion} \sim {}^{L^2}/_{D_{light}}$, where L

is the characteristic depth of the sources in the scattering medium. For L on the order of a few centimetres, and for D_{light} on the order of $10^5\,\mathrm{m^2 s^{-1}}$, $t_{diffusion}$ is of the order of tens of nanoseconds. For nanosecond pulses, $t_{heating}$ is therefore never longer than tens of nanoseconds in typical tissues at centimetric length scales. The stress confinement condition $d \gg t_{heating}\, c_s$ therefore requires a typical dimensions of the absorbing region $d \gg 10\,\mu\mathrm{m}$.

In the previous section it was assumed that heat transfer is negligible during the heating by the laser pulse. The corresponding heat confinement condition states that the characteristic time for heat transfer must be much larger than that of the heating duration. As for the diffusion of light intensity, the characteristic time scale for diffusion is given by $t_{heat} \sim {}^{d^2}/_{D_{heat}}$, where D_{heat} is the thermal diffusion coefficient. In tissue, D_{heat} can be approximated by that of water, i.e. $D_{heat} \simeq 1.5 \times 10^{-7}\,\mathrm{m^2 s^{-1}}$. For $d \gg 10\,\mu\mathrm{m}$, as derived from the stress confinement condition with heating duration of tens of nanosecond, t_{heat} is of the order of milliseconds and thus much longer that the heating duration.

For heating by nanosecond pulses, with absorbers larger than a few tens of µm, both stress and heat confinement conditions hold.

Expression for the Solutions Under Stress Confinement Under stress confinement, the source term $H(\mathbf{r}, t)$ may be separated as

$$H(\mathbf{r}, t) = E_{abs}(\mathbf{r})\, \delta(t - t_0), \tag{2.32}$$

where t_0 is the time of the laser pulse, and $E_{abs}(\mathbf{r})$ is the energy per unit volume absorbed during heating. The solution given in (2.30) therefore simplifies to

$$p(\mathbf{r}, t) = \frac{\Gamma}{c_s^2} \frac{\partial}{\partial t} \left[G(\mathbf{r}, t - t_0) \underset{\mathbf{r}}{\otimes} E_{abs}(\mathbf{r}) \right] \tag{2.33}$$

or equivalently

$$p(\mathbf{r}, t) = \frac{\Gamma}{c_s^2} \frac{\partial}{\partial t} \int d\mathbf{r_s}\, E_{abs}(\mathbf{r_s})\, G(\mathbf{r} - \mathbf{r_s}, t - t_0), \tag{2.34}$$

which illustrates that the photoacoustic signals are proportional to the temporal derivative of the sum of impulse responses generated in the source region weighted by the density of absorbed energy.

In the three dimensional case, using

$$G(\mathbf{r} - \mathbf{r_s}, t - t_s) = \frac{1}{4\pi \|\mathbf{r} - \mathbf{r_s}\|}\, \delta\left(t - t_s - \frac{\|\mathbf{r} - \mathbf{r_s}\|}{c_s} \right), \tag{2.35}$$

the field may be expressed as

$$p_{3D}(\mathbf{r}, t) = \frac{1}{4\pi c_s^2} \frac{\partial}{\partial t} \int d\mathbf{r_s}\, \Gamma E_{abs}(\mathbf{r_s})\, \frac{1}{\|\mathbf{r} - \mathbf{r_s}\|}\, \delta\left(t - t_0 - \frac{\|\mathbf{r} - \mathbf{r_s}\|}{c_s} \right), \tag{2.36}$$

which shows that in three dimensions only sources distributed on a sphere of radius $\|\mathbf{r}-\mathbf{r_s}\| = c_s\,(t-t_s)$ contribute to the photoacoustic pressure at location $\mathbf{r}$ and time t. A simple way to reconstruct the absorbed energy distribution is therefore to apply a simple delay and sum algorithm, analogous to that used in conventional ultrasound. All the photoacoustic images shown in the following chapters were obtained in this way.

Note that the solution may also be written equivalently as

$$p_{3D}\,(\mathbf{r},t) = \frac{1}{4\pi c_s^2}\frac{\partial}{\partial t}\left[\frac{1}{c_s(t-t_s)}\int d\mathbf{r_s}\,\Gamma E_{abs}\,(\mathbf{r_s})\;\delta\left(t-t_0-\frac{\|\mathbf{r}-\mathbf{r_s}\|}{c_s}\right)\right], \tag{2.37}$$

where the integral term is a spherical Radon transform. This formulation shows that the temporal integral of the photoacoustic pressure is directly proportional to the spherical Radon transform of the absorbed energy. Since a spherical Radon transform is invertible, an exact reconstruction of the absorbed energy can be obtained under appropriate conditions.

Recasting the Source Term Problem as an Initial Value Problem. It can be shown that under the stress confinement, the initial pressure field is simply related to the absorbed energy. Equation (2.34) may be rewritten as

$$p\,(\mathbf{r},t) = \frac{1}{c_s^2}\int d\mathbf{r_s}\,\Gamma E_{abs}\,(\mathbf{r_s})\,\frac{\partial G}{\partial t}\,(\mathbf{r}-\mathbf{r_s},t-t_0)\,.$$

As shown in section B.2 on page 176, this expression corresponds to the solution of the pressure wave equation without source but with initial conditions:

$$\left(\nabla^2-\frac{1}{c_s^2}\frac{\partial^2}{\partial t^2}\right)p=0,\quad (\mathbf{r},t)\in\mathbb{R}^n\times]t_0;+\infty[,$$

with an initial pressure distribution $p(\mathbf{r},t=t_0)=p_0=\Gamma E_{abs}\,(\mathbf{r})$ and not initial movement $\frac{\partial p}{\partial t}\,(\mathbf{r},t=t_0)=0$.

The initial pressure field at the end of the impulse heating is therefore given directly by the absorbed energy density multiplied by the first Grüneisen coefficient. This formulation of the photoacoustic problem is often encountered in the literature, in addition to the formulation using the inhomogeneous thermoacoustic wave equation.

Solution for Spherically Symmetrical Sources

In the case of a spherically symmetric problem where $H\equiv H\,(r,t)$ with $r\in\mathbb{R}^+$, the Laplacian operator of the general case simplifies to $\nabla^2=\frac{\partial^2}{\partial r^2}+\frac{2}{r}\frac{\partial}{\partial r}$. It may be shown that the thermoacoustic wave equation can therefore be expressed as the problem

$$\left(\frac{\partial^2}{\partial r^2}-\frac{1}{c_s^2}\frac{\partial^2}{\partial t^2}\right)(r\phi)=\frac{\Gamma}{c_s^2\rho_0}\,r\,H\,(r,t)\,,\quad (r,t)\in\mathbb{R}^+\times]t_0;+\infty[. \tag{2.38}$$

Since in polar coordinates translational symmetry with respect to position no longer applies, (2.38) can no longer be solved via simple convolution as in the general case (2.30). Nevertheless a Green's function for this problem may be constructed from the one-dimensional Green's function

$$G_{sph}\left(r,t|r_s,t_s\right)=\frac{c_s}{2}\left[u\left(t-t_s-\frac{r-r_s}{c_s}\right)-u\left(t-t_s-\frac{r+r_s}{c_s}\right)\right], \quad (2.39)$$

where $u\left(x\right)$ is the Heaviside function. The solution to (2.38) is thus given by

$$r\phi=-\frac{\Gamma}{c_s^2\rho_0}\int_{t_0}^{t}dt_s\int dr_s\, G_{sph}\left(r,t|r_s,t_s\right)\, r_s H\left(r_s,t_s\right) \quad (2.40)$$

$$\phi=-\frac{\Gamma}{c_s^2\rho_0 r}\int_{t_0}^{t}dt0\int dr_s\, G_{sph}\left(r,t|r_s,t_s\right)\, r_s H\left(r_s,t_s\right). \quad (2.41)$$

Substituting (2.41) into $p=-\rho_0\frac{\partial\phi}{\partial t}$, and evaluating over the extent of the heating function, one obtains the photoacoustic pressure waveform for spherically symmetric source terms valid outside the spatial extent R of the photoacoustic source

$$p_{sph}\left(r,t\right)=\frac{\Gamma}{2r}\int_0^R dr_s\, r_s\left[H\left(r_s,t-\frac{r-r_s}{c_s}\right)-H\left(r_s,t-\frac{r+r_s}{c_s}\right)\right]. \quad (2.42)$$

In the case of an impulse heating function $H\left(r,t\right)\equiv E_{abs}\left(r\right)\delta\left(t\right)$, (2.42) reduces to

$$p_{sph}\left(r,t\right)=\frac{\Gamma}{2}\frac{c_s t-r}{r}E_{abs}\left(|c_s t-r|\right). \quad (2.43)$$

It is instructive to express this solution in terms of the retarded time $t_-=t-\frac{|r|}{c_s}$ for an observer at a distance r:

$$p_{sph}\left(r,t\right)=\frac{\Gamma}{2}\frac{c_s t_-}{r}E_{abs}\left(|c_s t_-|\right)\quad \forall r>R \quad (2.44)$$

Temporal Wave Form When looked at from a fixed distance r from the absorber, the photoacoustic wave form is therefore proportional to a line function $c_s t_-$ in retarded time. The spatial distribution of the absorbed energy density $E_{abs}\left(|c_s t_-|\right)$ defines temporal extent of this infinite line through the limited spatial extent of the spatial distribution of absorbed energy density.

Frequency Spectrum Since the temporal wave form is given by an expression of the form

$$p_{sph}\left(t_-\right)=\frac{\Gamma}{2}\frac{c_s}{r}t_-\,E_{abs}\left(|c_s t_-|\right), \quad (2.45)$$

the Fourier transform takes the form

$$\mathcal{F}\left[p_{sph}\left(t_-\right)\right]\left(f\right)\equiv\hat{p}_{sph}\left(f\right)=\frac{\Gamma}{2}\frac{c_s}{r}\mathcal{F}\left[t\right]\left(f\right)\otimes\mathcal{F}\left[E_{abs}\left(|c_s t_-|\right)\right]\left(f\right). \quad (2.46)$$

If $\hat{E}_{abs}(f) \equiv \mathcal{F}[E_{abs}(|c_s t_-|)](f)$, the Fourier transform of the pressure wave form may be re-expressed as

$$\hat{p}_{sph}(f) = \frac{\Gamma}{2}\frac{c_s}{r}\frac{1}{2\pi i}\,\delta'(f) \otimes \hat{E}_{abs}(f) \tag{2.47}$$

$$= \frac{\Gamma c_s}{4\pi r i}\frac{\partial}{\partial f}\hat{E}_{abs}(f), \tag{2.48}$$

as it is known [3] that $\mathcal{F}[t](f) = (2\pi i)^{-1}\,\delta'(f)$ and
$\int f(x)\,\delta^{(n)}(x)\,dx \equiv -\int f'(x)\,\delta^{(n-1)}(x)\,dx$.

Solutions for Specific Geometries

To illustrate the wave forms obtained via the thermoacoustic effect, analytic expressions for two idealised distributions of absorbed energy density are derived for a temporal impulse heating function by evaluating (2.44) and (2.48).

Uniform, Spherically Symmetric Energy Density Assuming the energy density is given in terms of the Heaviside function $u(x)$

$$E_{abs}(r) = u(a - |r|), \tag{2.49}$$

equation (2.43) is given by

$$p_{sph}(r,t) = \frac{\Gamma}{2}\frac{c_s}{r}\,t_-\,u(a - |r|) \tag{2.50}$$

$$= \frac{\Gamma}{2}\frac{c_s}{r}\,t_-\,\Pi\left(\frac{1}{a}\,c_s t_-\right), \tag{2.51}$$

where $\Pi(x)$ is the rectangle function. The Fourier transform then takes the form

$$\hat{p}_{sph}(f) = \frac{\Gamma c_s}{4\pi r i}\frac{\partial}{\partial f}\mathcal{F}\left[\Pi\left(\frac{1}{a}\,c_s t_-\right)\right](f) \tag{2.52}$$

$$= \frac{\Gamma c_s}{4\pi r i}\frac{\partial}{\partial f}\mathrm{sinc}\left(\frac{a}{c_s}\pi f\right). \tag{2.53}$$

The frequency of highest energy density is given by $f_{max} = 0.663\frac{c_s}{R}$. The temporal waveform, the magnitude of its Fourier transform and the squared magnitude of the Fourier transform for the case of a uniform, spherically symmetric distribution of the density of absorbed energy are illustrated by Figure 2.7.

3. This identity may be proven by integrating the Fourier integral by parts.

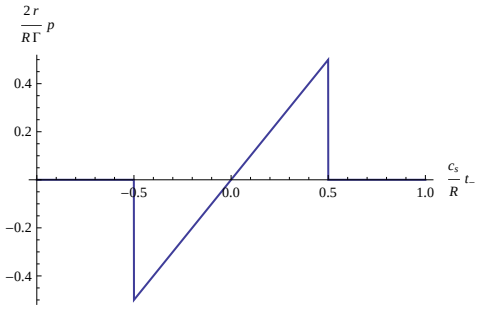

(a) Pressure from a UD

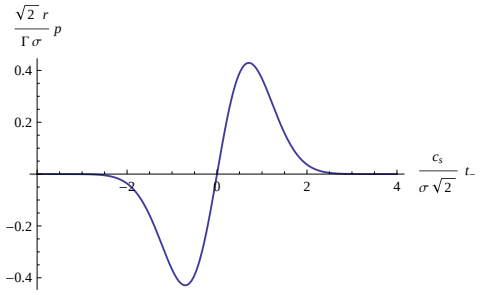

(b) Pressure from a GD

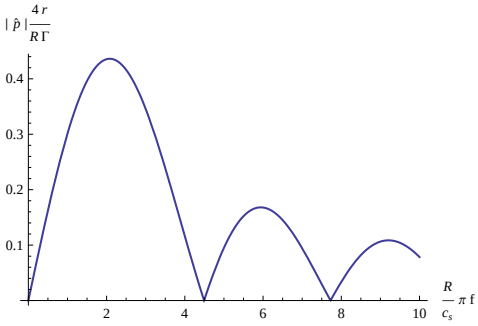

(c) Magnitude of the Fourier Transform of the Pressure from a UD

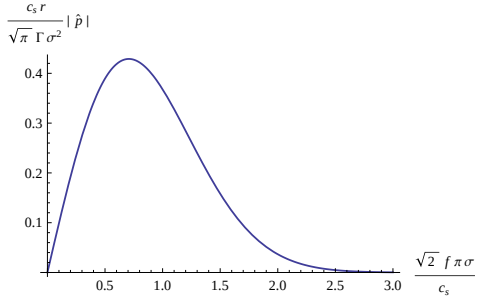

(d) Magnitude of the Fourier Transform from a GD

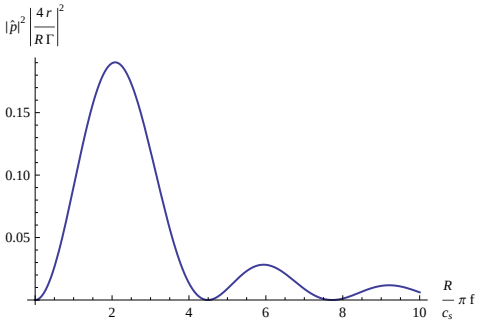

(e) Squared magnitude from a UD

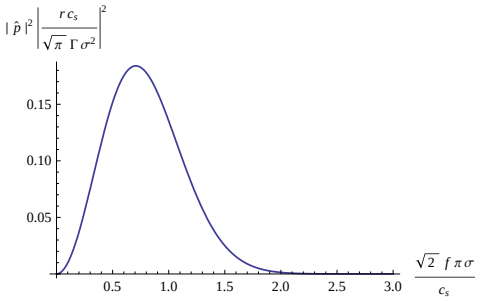

(f) Squared magnitude from a GD

Figure 2.7: Temporal waveform, magnitudes of the Fourier transform and squared magnitude of the Fourier transform of the photoacoustic signals produced by (a, c, e) a uniform spherically symmetric energy density distribution (UD) and (b, d, f) a Gaussian spherically symmetric energy density distribution (GD)

Gaussian, Spherically Symmetric Energy Density Assuming the energy density is given in terms of Gaussian apodisation function

$$E_{abs}(r) = e^{-\frac{(c_s t_-)^2}{2\sigma^2}}, \tag{2.54}$$

equation (2.43) is given by

$$p_{sph}(r,t) = \frac{\Gamma}{2}\frac{c_s}{r} t_- \, e^{-\frac{(c_s t_-)^2}{2\sigma^2}}. \tag{2.55}$$

The Fourier transform then takes the form

$$\hat{p}_{sph}(f) = \frac{\Gamma c_s}{4\pi r i}\frac{\partial}{\partial f}\mathcal{F}\left[e^{-\frac{(c_s t_-)^2}{2\sigma^2}}\right](f) \tag{2.56}$$

$$= \frac{\Gamma c_s}{4\pi r\, i}\frac{\partial}{\partial f}\left(\frac{\sqrt{2\pi}\sigma}{c_s}\, e^{-\left(\frac{\sqrt{2}\pi\sigma f}{c_s}\right)^2}\right) \tag{2.57}$$

The frequency of highest energy density is given by $f_{max} = \frac{c_s}{2\pi\sigma}$. The temporal waveform, the magnitude of its Fourier transform and the squared magnitude of the Fourier transform for the case of a Gaussian, spherically symmetric distribution of the density of absorbed energy are illustrated by Figure 2.7.

Concluding Remarks

With regard to the work presented in this thesis it is sufficient to be aware of two fundamental results.

- The frequency of the highest energy density of photoacoustic waves is given by $f_{max} \sim {}^{c_s}/_{d}$, where d is the characteristic size of the optical absorber. If absorbers of different sizes are to be detected, a transducer with a wide bandwidth is required.
- Since the absorbed luminous energy is given by $E_{abs}(z) = \mu_a I_{light}(z)$, and the acoustic intensity $I_{ac} \propto p^2$, the intensity of photoacoustic signals I_{PA} behaves as $I_{PA} \propto I_{light}^2$. A decrease in light intensity therefore leads to an disproportional loss in the intensity of the photoacoustic signal generated.

Part II

Experimental Section

Chapter 3

Instruments

Contents

The objective of this chapter is to describe in detail the principal components of the experimental setup used during the work for this thesis. A particular emphasis is put on the generation and delivery of light suitable for *in vivo* photoacoustics deep in tissue. It summarily presents some of the technological difficulties encountered and solutions developed during the work for this thesis.

The contents of this chapter are not indispensable for the comprehension of the results presented in the remainder of this documents, however an awareness of the technological limitations will be assumed.

3.1 Light Source

To generate the energy needed for the photoacoustic effect, a combination of a laser and an optical parametric oscillator was chosen. This allows illumi-

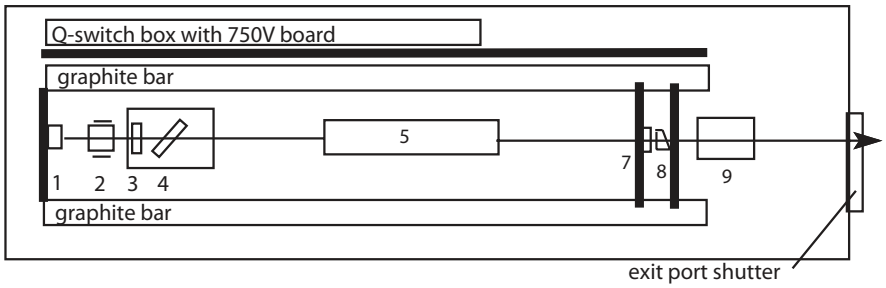

Figure 3.1: Surelite optical layout. Source: Continuum (2002)

nation of samples in a wide range of different wavelengths, in particular in the diagnostic window.

Continuum Surelite II-10

The pump laser used for this work was a Surelite II-10 laser by Continuum, CA, USA. The Surelite II-10 is a flashlight-pumped, Q-switched Nd:YAG laser.

The optical layout of the Surelite II-10 is illustrated in Figure 3.1. The cavity is defined by the rear mirror (1) and the output coupler (7). The laser comprises a Nd^{3+}-doped YAG rod (5) as gain medium which is pumped by a flash lamp driven by $-1800\,\mathrm{V}$ electrical pulses resulting in a flash with a duration of approximately $200\,\mu\mathrm{s}$. The primary transition in Nd:YAG crystals emits light at a wavelength of $1064\,\mathrm{nm}$.

Q-Switch

Generally the cavity is blocked by a Q-Switch: a combination of a polariser (4), a $\lambda/4$ plate (3) and a Pockels cell (2). The Pockels cell exploits the Pockels electro-optic effect to induce birefringence in a non-linear optical medium with an electric field to create an electrically controlled wave plate. At approximately $3600\,\mathrm{V}$ this results in a $\lambda/4$ rotation of the phase of photons at $1064\,\mathrm{nm}$ while at $0\,\mathrm{V}$ no rotation is induced. The polariser is transparent for horizontally polarised light and reflective for vertically polarised light.

When the Pockels cell is not electrically polarised, a photon generated in the Nd:YAG rod (5) travelling towards the rear mirror (1) is polarised horizontally by the polariser (4). Its polarisation is then changed to circular by the wave plate (3) and passes unaffected through the inactive Pockels cell (2). After being reflected by the rear mirror, the photon passes the inactive Pockels cell a second time and its polarisation is changed from circular to vertical by the wave plate. It is therefore reflected by the polariser (4) and oscillation in the cavity is prevented.

On the other hand, when the Pockels cell is electrically polarised, on each pass through the active Pockels cell a photon's polarisation is changed an

additional time from circular to linear or vice versa. A photon's polarisation is therefore identical upon completion of the entire path between the first and second pass through the polariser. In other words, the photon now has horizontal polarisation when it encounters the polariser a second time and passes unimpeded, permitting oscillation in the cavity.

By pumping the gain medium with closed cavity, energy can be stored through population inversion since the life-time for spontaneous emission is much greater than for stimulated emission, the later being only possible with an open cavity. By carefully selecting the delay between activation of the flash lamp and the opening of the cavity with respect to the life-time for spontaneous emission, an optimal degree of population inversion can be achieved and the stored energy be released in a very short but intense light pulse.

After passing the output coupler (7), the light has a wavelength of 1064 nm, a pulse energy of approximately 650 mJ, a pulse width of $5 - 7$ ns and is horizontally polarised.

Second Harmonic Generation

As illustrated in Section 2.1, at 1064 nm light absorption in water is non-negligible. To achieve maximum penetration depth in biological tissues, wavelengths between 700 nm and 900 nm would be desirable. The wavelength of the photons generated by the Nd:YAG crystal is therefore transformed in two steps, the first of which is second harmonic generation, also known as frequency doubling.

Second harmonic generation describes a non-linear optical process in which two photons interacting with a non-linear medium are effectively combined, resulting in a doubling of the energy (and thus frequency) of the photons in a beam.

The second harmonic generation assembly (9) implements a Type I second harmonic generation resulting in a rotation of the polarisation of the beam by 90°. It operates with a maximum efficiency of approximately 50%. Phase matching is achieved by automated temperature control and manual angular fine-tuning of the Crystal orientation.

The light exiting the Surelite II-10 therefore consists to 50% of light at 1064 nm horizontally polarised (300 mJ) and to 50% of light at 532 nmvertically polarised (300 mJ) with $4 - 6$ ns pulse duration. According to Continuum (2002) the beam is approximately 7 mm in diameter and has a divergence of 0.3 mrads [1].

One effect of the angular fine-tuning of the crystal for second harmonic generation is that its interfaces are not perpendicular to the optical axis of the laser cavity as illustrated in Figure 3.2. Part of the primary beam is reflected at the (uncoated) interfaces of the crystal and undergoes internal

1. Half angle for 86% of the energy. For a Gaussian beam, 86% of the energy are contained within 2σ.

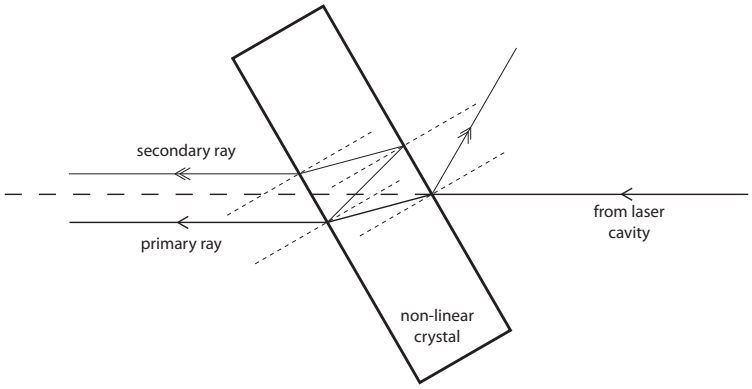

Figure 3.2: Illustration of origin of secondary ray due to SHG

reflection leading to a secondary, less energetic, ray emerging from the laser. Furthermore a slight non-parallelism of the two interfaces of the crystal causes the secondary ray to emerge at a slight angle with respect to the primary ray. The energy in the secondary ray was verified to be of the order of 0.5% compared to the energy in the primary ray [2].

Output Stability

Continuum (2002) specifies an average power drift of ±6.0% over 8 hours and a shot-to-shot energy stability of ±3.5% with an RMS shot-to-shot error of ±0.8% for 1064 nm.

Measurements revealed long-term power drifts of the order of 10% over one hour for 532 nm and thus significantly larger than specified. Five independent measurements have revealed two types of behaviour. As can be seen in Figure 3.3, in three cases there is a quasi-linear decrease of the power as a function of time, while in two other cases there was a transitory period during which the power increased significantly over a period of 10 minutes before beginning to slowly decrease from this higher value. It is unclear what triggers these two regimes. They appear to occur at random.

An estimate of the RMS error for the shot-to-shot energy was found to be of the order of 1.4% which is also higher than specified.

The noise in the output power and the shot-to-shot energy translates into noise in the amplitude of the generated photoacoustic signals. Depending on the quantity investigated, measurements obtained from the photoacoustic signals may therefore need to be normalised by instantaneous output power or even by the energies of the individual pulses.

2. The measurements were carried out with a primary ray pulse energy of 599 mJ (532 nm & 1064 nm). Due to the non-linearity of second harmonic generation, a slightly different ratio might be observed at lower pulse energies.

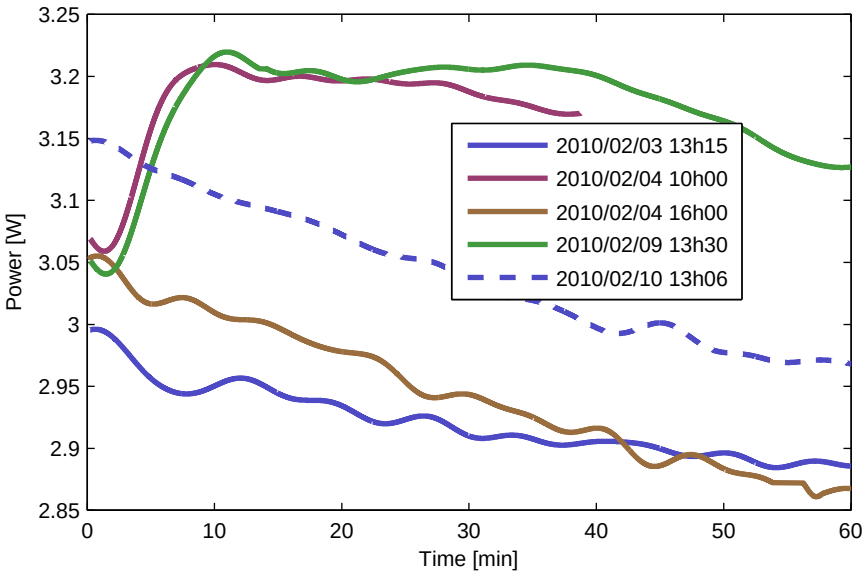

Figure 3.3: Output power (low-frequency filtered with $f_{cutoff} = 1/200\,\mathrm{s}$)

Control of the Surelite II-10

The Surelite II-10 can be operated either with internal triggering of the flash-lamp and the Q-Switch or with externally supplied triggers. It also allows to access the flash-lamp and Q-Switch triggers to serve as the master device for triggering other devices. In the experiments presented in this thesis, the Lecoeur Open System time-reversal electronics was triggered on the Q-Switch trigger output of the Surelite II-10 with coincides at nanosecond resolution with the laser output.

If internal triggering is used, the flash-lamp trigger exhibits a significant but to a large degree deterministic jitter of the order of µs. Without post-processing, ultrasonic signals acquired using the flash-lamp trigger can therefore not be averaged over multiple acquisitions.

Apart from triggering, the Surelite II-10 allows all operations to be remote controlled via a serial port by a computer. In particular, the Q-Switch delay and opening of the cavity via serial port allows fully automated photoacoustic acquisitions.

Optical Parametric Oscillator

At the outset of the work presented in this document, it was unclear which wavelengths would be most practical for photoacoustic generation in depth in biological tissues and which contrast agents would be employed. It was therefore decided to work with an optical parametric oscillator (OPO) that allows

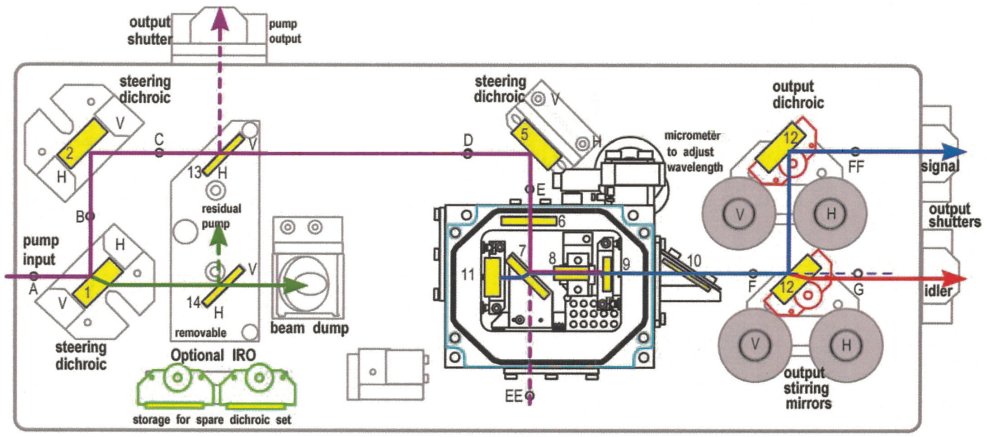

Figure 3.4: Layout of the Surelite OPO Plus. Illustration: Continuum (2002)

the generation of light in the entire range of wavelengths in the diagnostic window.

The physical principles at work in an OPO and the factors determining its operating characteristics are described in Appendix C on page 179. For the comprehension of the results presented in this thesis it is sufficient be aware that an OPO is a non-linear optic device that converts a pump beam at frequency ω_P to two output beams: a beam of less energetic photons named the idler beam at frequency ω_I, and beam of more energetic photons named the signal beam at frequency ω_S. Optical parametric processes conserve energy and the frequencies of the beams are thus related by $\omega_P = \omega_I + \omega_S$. Different approaches exist that allow continuous tuning of the output wavelengths. In the OPO used over the course of the work for this thesis tuning was achieved by changing the angle of of the non-linear crystal with respect to the axis of the cavity. In the remainder of this work, the signal beam of the OPO which can be tuned in the range $670 - 1000\,\text{nm}$ is used to illuminate the samples.

Surelite OPO Plus

The Surelite OPO Plus is an idler-resonant double-pass computer-controlled BBO [3] OPO system.

The OPO cavity is defined by the mirror 11 and output coupler 9 between which the non-linear crystal 8 is mounted on a motorised stage allowing for phase-matching by tilting the crystal.

The pump beam from the Surelite II-10 enters the device at point A. The dichroic 1 strips the pump beam if necessary of any remaining fundamental at 1064 nm which is then absorbed in the beam dump. The pump beam at

3. β-BaB_2O_4 is a popular crystal in nonlinear optics due to is transparency range from $200 - 2600\,\text{nm}$

532 nm is coupled into the cavity by use of the mirrors 1, 2 and 5 and the dichroic 7, which provide the necessary degrees of freedom to align the pump beam with the OPO cavity and centre the beam in the non-linear crystal for maximum efficiency. After traversing the non-linear crystal, the pump beam is reflected by the output coupler 9, re-traverses the crystal a second time in the inverse direction and exits the cavity back towards the pump laser by dichroic 7 and mirrors 5, 2 and 1. This double-pass of the pump beam increases the interaction length of the pump beam with the non-linear crystal without requiring the OPO cavity to be resonant for the pump beam which would severely complicate wavelength adjustment [4].

Since BBO crystals are hygroscopic, the entire cavity is contained in an hermetically sealed enclosure [5]. The pump beam enters through the window 6 and exits through window 10. Since the pump beam is monochromatic, window 6 may be treated with anti-reflection coating and used at right angles to the beam, while the output wavelengths are variable which requires window 10 to be used at Brewster angle to minimise reflections.

Finally the idler and signal beams are separated by dichroic 12 and exit through separate output ports. Mirrors 13 and 14 are optional and can be used to recover the 532 nm or 1064 nm components of the pump beam respectively for diagnostic purposes.

When pumped by a Surelite II-10 with 300 mJ at 532 nm and a pulse duration of $4-6$ ns, the Surelite OPO Plus produces approximately 130 mJ combined in the idler and the signal beam, corresponding to a power conversion factor of 43%. Due to the above mentioned factor of pulse shortening, the signal pulse has a duration of $2-4$ ns and the idler pulse a duration of $3-5$ ns.

As is the case for second harmonic generation in the Surelite II-10, Type I phase matching in the OPO results in a rotation of the polarisation of the signal and idler beams with respect to the pump beam by 90°. The vertically polarised pump beam at 532 nm therefore leads to horizontally polarised signal and idler beams.

Beam Characteristics and Control

To characterise the signal beam of the optical parametric oscillator, it was projected onto a semi-transparent paper with a millimetre grid and the scattered light was imaged with a commercial digital camera. The wavelength was set to 690 nm so as to allow it to pass through the infrared filter found in all consumer digital cameras.

4. In a single-resonant OPO, the output wavelengths are determined solely by the phase-matching condition of the crystal. With double-resonant or triple-resonant OPOs, the output wavelengths are additionally influenced by the geometry of the cavity. Such devices have lower oscillation thresholds but are delicate to operate. For further details please refer to Boyd (2008, §2.9, in particular p. 113) and Duarte (2008, §2.4).

5. If left in ambient air, a BBO crystal "fogs" up due to the humidity in the air and becomes unusable.

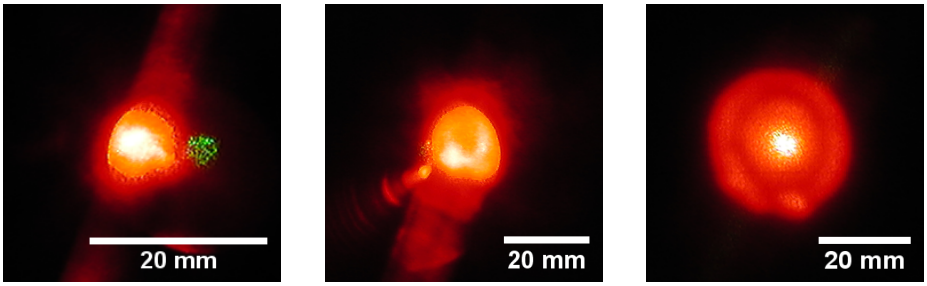

(a) at 0 cm (b) at 14 cm (c) at 85 cm

Figure 3.5: Shape of the signal beam as a function of position of distance from the signal output port.

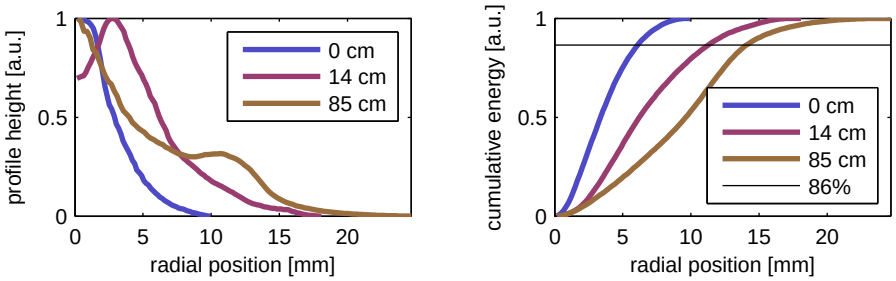

(a) Angular-averaged beam profile (b) Cumulative energy

Figure 3.6: Radial beam profile characteristics at different distances.

The millimetre grid was used for focusing the objective under daylight illumination and to correct for perspective distortion [6]. The results are illustrated in Figure 3.5.

To quantify the divergence of the beam, angular-averaged radial profiles of the perspective-corrected beam spots were calculated [7] as well as the cumulative beam energy as a function of radius. (See Figure 3.6). 86% of the energy are contained within radii of 6.1 mm, 11.2 mm and 14.0 mm at the positions 0 cm, 14 cm and 85 cm from the signal exit port respectively. Excluding the data at 14 cm due to insufficient radial symmetry, the divergence [8] is determined to be $\theta = 9.2$ mrad or 0.53° at 690 nm.

When collimating the signal beam, two competing criteria need to be ba-

6. Perspective correction was carried out by overlaying the image of the signal beam spot with the image of the millimetre grid and compensating the distortion by the "Perspective Transformation" of a popular commercial image processing software package.

7. The radial profile was calculated using the "Radial Profile Extended" plug-in for ImageJ by Philippe Carl.

8. Half angle for 86% of the energy.

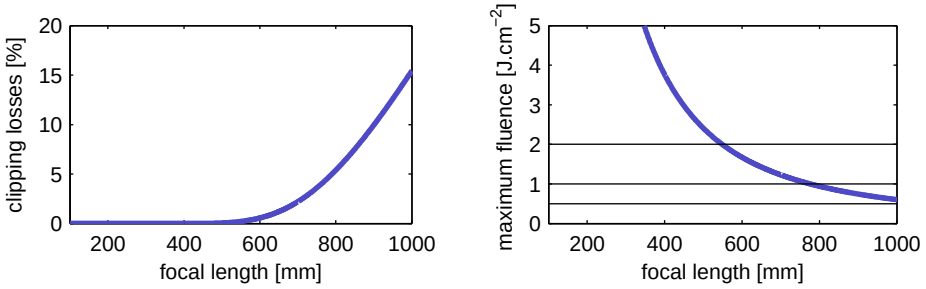

(a) estimated clipping losses (b) estimated maximum fluence

Figure 3.7: Beam characteristics as a function of the focal length of the collimating lens.

lanced. A low maximum fluence permits the use of less expensive optical components while a small beam diameter reduces geometric losses due to beam clipping. Assuming an aperture size of 1" used at 45°[9] for the optics in use and a Gaussian beam shape[10], one may estimate the clipping losses and peak fluence as a function of the focal length used to collimate the beam.

Since the focal plane of any collimating lens must coincide with the plane of the beam waist, the size of the beam σ as a function of focal length f is given by

$$\sigma(f) \approx f \tan(\theta), \tag{3.1}$$

where θ is the divergence angle corresponding to 86% of the energy. At an angle of incidence of 45°, the effective aperture diameter is given by $^{25.4\,\mathrm{mm}}/_{\sqrt{2}}$ the clipping losses are given by

$$L \approx 1 - 2\pi \int_0^{^{25.4\,\mathrm{mm}}/_{2\sqrt{2}}} dr\, \mathcal{N}_{2D}(r, \sigma(f))\, r, \tag{3.2}$$

where $\mathcal{N}_{2D}(r, \sigma)$ is the normalised two-dimensional Gaussian function. Similarly, assuming a total pulse energy of $E_{tot} = 130\,\mathrm{mJ}$, the maximum fluence Φ_{max} is given by

$$\Phi_{max}(f) \approx E_{tot}\, 2\pi\, \mathcal{N}_{2D}(r = 0, \sigma(f)). \tag{3.3}$$

As illustrated in Figure 3.7, clipping losses remain negligible up to focal lengths of 600 mm. Typical damage thresholds for different commercial optical coatings are 0.5 J cm^{-2}, 1 J cm^{-2}, 2 J cm^{-2} and 10 J cm^{-2}, which correspond to focal lengths of 1100 mm, 775 mm, 550 mm and 245 mm. Considering the readily commercially available focal lengths, a collimating lens with

9. Typical configuration for high-fluence dielectric mirrors.
10. In practise, the beam shape varies as a function of wavelength.

$f = 500\,\text{mm}$ was chosen resulting in a $\Phi_{max} = 2.4\,\text{J cm}^{-2}$ which was found to be acceptable for optics with a guaranteed damage threshold of $2\,\text{J cm}^{-2}$.

To control the beam intensity a combination of an achromatic $\lambda/2$-wave plate with a polarising cube and beam dump was investigated. However, it was found that in a laboratory context a control of the beam intensity was more easily realised by increasing the Q-Switch delay of the pump laser on an *ad hoc* basis.

3.2 Beam Shaping and Beam Delivery

It has been observed that the spatial form of the signal beam of the optical parametric oscillator is heavily dependent on the choice of wavelength [11]. In particular, for wavelengths below approximately 685 nm, the angular distribution of the energy is much more narrow than for longer wavelength. Above, the angle of divergence remains fairly constant but the form of the angular distribution varies from a Gaussian-like shape to a ring-shape with hot-spots appearing at different wavelengths within the beam.

As the method explored in this work is fundamentally based on extracting the difference in the photoacoustic signals acquired at different wavelengths, it is of little surprise that problems arise if the form of the illumination changes as a function of wavelength.

Furthermore, to make the method presented in this work clinically viable, methods for delivering the illumination beam to the patient need to be found. The elevated energy densities of pulsed lasers make this a non-trivial endeavour.

Beam Homogenisation

Theoretical Background for Beam Shaping with Microlens Arrays

One method for shaping the illumination spot that was explored makes use of arrays of microlenses. The arrays of microlenses consist of lenses with diameters of the order of tens of micrometres that are molded in a lattice-structure onto the surface of a glass slide. Using an appropriate optical setup such arrays may be used to produce spatially homogeneous fields from almost arbitrarily shaped input-beams as shall be shown below.

Given an array of microlenses as illustrated schematically in Figure 3.8a, where h denotes the position of the centre of the microlens, $2r$ the diameter of the microlenses, f their focal length and α the angle of a plane wave [12]

11. This is due to the fact that the Surelite OPO Plus cavity is resonant for the idler and not for the signal beam.

12. Given the small diameter of the microlenses, any well-behaved field incident of the array of microlenses may be approximated as a plane wave at the scale of an individual microlens.

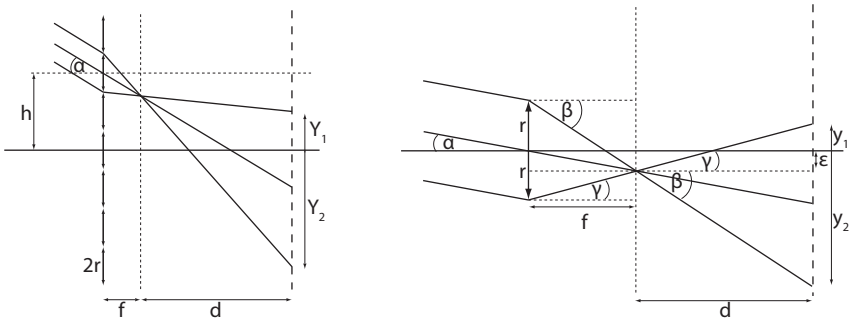

(a) Geometry of an array of microlenses.

(b) Geometry of a single microlens.

Figure 3.8

incident with respect to the normal of the microlens array, we shall investigate the shape of the field a distance d from the focal plane of the microlenses. It is assumed that the angle of incidence α is sufficiently small to allow a thin lens approximation on the scale of an individual microlens.

Figure 3.8b illustrates in more detail the case of an individual microlens. It is trivial to deduce that the angles on the figure are related to the physical dimensions as follows:

$$\tan(\alpha) = \frac{\epsilon}{f} \tag{3.4}$$

$$\tan(\beta) = \frac{r+\epsilon}{f} \tag{3.5}$$

$$\tan(\gamma) = \frac{r-\epsilon}{f}. \tag{3.6}$$

The positions y_1, y_2 of the edge of the spot created by an individual microlens with respect to the centre of the microlens is given by

$$y_1 = \quad d\tan(\gamma) = d\left[\frac{r}{f} - \frac{\epsilon}{f}\right] \tag{3.7}$$

$$y_2 = -d\tan(\beta) = d\left[-\frac{r}{f} - \frac{\epsilon}{f}\right]. \tag{3.8}$$

Assuming a divergence angle θ is provided for a collimated beam incident on the array of microlenses as defined in Figure 3.9a, the positions y_1, y_2 may be expressed as

$$y_1 = \quad d\tan(\theta) - d\tan(\alpha) \tag{3.9}$$

$$y_2 = -d\tan(\theta) - d\tan(\alpha). \tag{3.10}$$

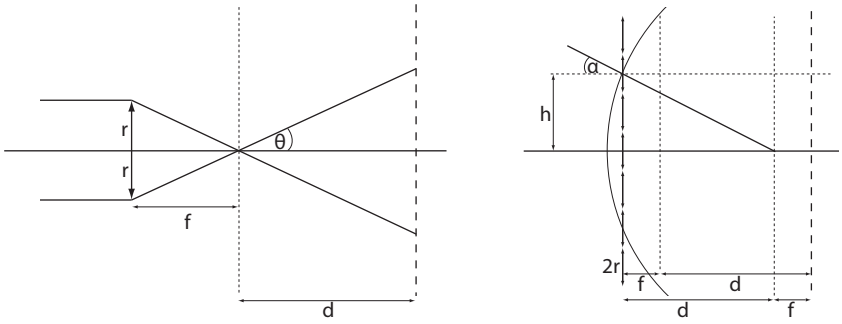

(a) Definition of the divergence angle. (b) Geometry of focusing.

Figure 3.9

Given that the centre of an individual microlens is at h, the positions Y_1, Y_2 of the edge of the spot created by an individual microlens with respect to the coordinate system for the entire array are given by

$$Y_1 = y_1 + h = \quad d\tan(\theta) - d\tan(\alpha) + h \tag{3.11}$$
$$Y_2 = y_2 + h = -d\tan(\theta) - d\tan(\alpha) + h. \tag{3.12}$$

This shows that each individual microlens produces a spot of size $2d\tan(\theta)$, of which the position is determined by the position of the centre of the microlens h and the angle of incidence α.

It is possible to find angles of incidence α for each individual microlens such that each individual microlens illuminates the same spot. This occurs if $-d\tan(\alpha) + h = 0$, or simply

$$\tan(\alpha) = \frac{h}{d}. \tag{3.13}$$

As can easily be deduced from Figure 3.9b, this condition is satisfied if the curvature of the incident wavefront is shaped such that it converges in the plane at a distance d from the microlens array. Positions Y_1, Y_2 of the edge of the spot are then given by

$$Y_1 = \quad d\tan(\theta) \tag{3.14}$$
$$Y_2 = -d\tan(\theta). \tag{3.15}$$

In conclusion, if an initially collimated beam of any shape is focused in a plane at a distance d from an array of microlenses, each microlens illuminates the same region of space in a plane at a distance $d + f$ from the array. This plane shall be referred to in the following as the "sharp plane" due to the fact that the beam has sharp boundaries in this plane. In any other plane, the boundaries are smeared due to convolution effects. Note that under the

assumption of small α made above, $f \ll d$ and the sharp plane is effectively located at a distance d from the array of microlenses.

The size of the region illuminated is determined only by the angle of divergence θ of the microlens array and the distance d between the sharp plane and the focal plane of the array of microlenses [13]. The shape of the region illuminated in the sharp plane is identical to the aperture shape of the microlenses: circular lenses result in circular spots, square lenses result in square spots. An incident field with a spatially inhomogeneous intensity but spatially homogeneous angle of incidence (before focusing), is converted into a field with spatially homogeneous intensity but spatially inhomogeneous angle of incidence in the sharp plane.

It should be pointed out that if the beam incident on the array of microlenses would not focus to an ideal point in the sharp plane in the absence of the array, the spot produced by the array in the sharp plane is convoluted by the shape of the hypothetical focus spot.

Geometry of the Microlens Array Used

The microlens array used in this work was fabricated by RPC Photonics, NY, USA under the trademark "Engineered Diffusers". More specifically, the product EDC-10 with circular lenses, a divergence angle $\theta = 5°$ and a typical feature size $r = 80\,\mu m$ was used . The microlenses are realised as polymer replicated on a glass substrate. Divergence angle and feature size allow to deduce the focal distance of the microlenses to be $f = 914\,\mu m$. It follows that the focal spot produced by each microlens is located within the glass substrate.

This fact also explains the motivation for using polymer on glass substrate: the highest energy densities occur in the focal plane of the microlens array. If the substrate was made from polymer, the damage threshold for the composite would be defined by the permissible energy densities in the focal plane. Since for glass the damage threshold vastly exceeds that of polymer, the damage threshold of the compound element is limited by the comparatively lower energy density incident on the polymer surface of the microlenses.

Energy Balance for Microlens Arrays

For any beam shaping solution, the transmission loss is a critical performance criterion. Experimentally it was found that the transmission coefficient of EDC-10 is approximately 70%. An effort was made to investigate the origin of this non-negligible loss. It was found that three factors contribute to similar degree: reflection at material interfaces, maximum packing density of the lens shape in compact packing and the sparsity of the packing of the microlenses.

13. A noteworthy implication of this fact is that a homogeneous spot smaller in size than the input beam can be achieved as is illustrated in Figure 3.11 on page 66.

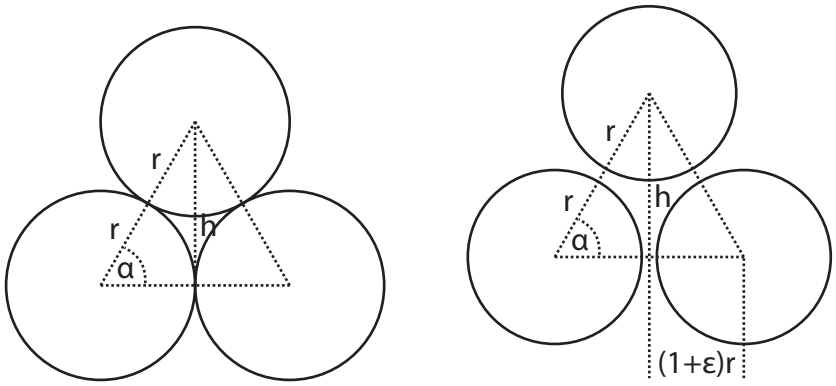

(a) Compact packing. (b) Sparse packing.

Figure 3.10: Packing of disks on a hexagonal lattice.

The exact materials used for the microlens array are unknown but for an order of magnitude calculation one may assume PMMA ($n_{PMMA} = 1.492$) on BK7 glass ($n_{BK7} = 1.517$) surrounded by air ($n_{air} = 1.000$). There are thus three material interfaces to reflect energy: air-PMMA, PMMA-glass, glass-air. The transmission coefficient of an interface between two materials with refractive indexes n_1 and n_2 is given by

$$T_{1\to 2} = \frac{4n_1n_2}{(n_1+n_2)^2}. \tag{3.16}$$

It follows that the combined interface transmission coefficient of the microlens array to the first approximation is given by

$$T_{int} = T_{air\to PMMA}\ T_{PMMA\to BK7}\ T_{BK7\to air} \tag{3.17}$$

$$\approx 0.920. \tag{3.18}$$

Furthermore geometric losses arise due the packing density that can be obtained with a compact packing of the shape of the lenses. The highest packing density for circular lenses may be obtained in a compact hexagonal lattice as illustrated in Figure 3.10a. It may be found by comparing the area contained within the sections of the disks $A_{section}$ contained within the triangle with the area of the triangle $A_{triangle}$,

$$\eta_h = \frac{3\,A_{section}}{A_{triangle}}. \tag{3.19}$$

Since $h = \sqrt{(2r)^2 - r^2} = \sqrt{3}r$, $A_{triangle} = \sqrt{3}r^2$. It thus follows that $A_{section} = \frac{1}{6}\pi r^2$. The hexagonal packing density for compactly packaged disks is thus gi-

ven by

$$\eta_h = \frac{\pi}{2\sqrt{3}} \tag{3.20}$$

$$\approx 0.907. \tag{3.21}$$

Since only light that has passed through the circular lenses contributes to the sharp beam in the "sharp plane", the light incident on the region between the microlenses is typically absorbed or reflected by masks. Alternatively it may be scattered widely such as to make in no appreciative contribution to the intensity distribution in the sharp plane by filling the space with small scattering structures. In any case, the light is effectively lost and the optimal transmission coefficient for the microlens array with circular lenses is given by

$$T_{int}\,\eta_h \approx 0.835. \tag{3.22}$$

These two effects however, do not explain all the losses observed experimentally. It is interesting to note that due to limitations in the fabrication process, most microlens array are not realised in compact packing. It may be shown that if the microlens radius is given by r and the length of one side of the triangle by $2\,r\,(1+\epsilon)$ as illustrated in Figure 3.10b, the packing density is given by

$$\eta_{sparse} = \eta_h \frac{1}{(1+\epsilon)^2}. \tag{3.23}$$

If $T_{int}\,\eta_{sparse} = 0.7$, $\epsilon = 0.0918$. A transmission coefficient of 70% may thus be explained if the distance between the centres of the microlenses are separated by a distance 9% larger than the diameter of the microlenses.

To achieve loss-less beam shaping with microlenses, several conditions need to be satisfied:

1. The shape of the microlenses used must be packageable with a density of $\eta = 1$: i.e. only triangular, rectangular or hexagonal lenses are permissible.
2. The fabrication process must allow the realisation of compact packing.
3. Anti-reflection coatings must be used to eliminate interface losses.

As illustrated by Figure 3.11, despite their limitations microlens arrays are an excellent solution for wavelength-independent beam shaping, beam homogenisation and hot-spot control. However, the transmission coefficient of the low-cost microlens array used in this work left to be desired.

Choice of Light Guides

For ease of use in clinical applications, beam delivery via a flexible system would be desirable. An obvious choice would be beam delivery by light-guides such as fibre optics but telescopic systems with free-space propagation of the

(a) Collimated OPO beam before beam shaping.

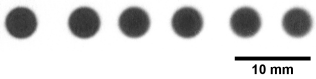

(b) Spot in the sharp plane after beam shaping.

Figure 3.11: Burn-paper impacts of the OPO signal beam at 700 nm to 950 nm in steps of 50 nm.

beam between mirrors are an interesting alternative. In context of this work, the possibility of fibre light-guide beam delivery was explored due to the greater flexibility in use and the difficulty of constructing sufficiently flexible telescopic systems. Furthermore light-guides present the advantage of homogenising the beam over the propagation path, potentially eliminating the problem associated with varying beam shape as a function of wavelength.

Beam Delivery by Thick Glass Fibre

A first series of attempts was made with a 900 µm fibre with polymer cladding. Unfortunately despite significant effort, practically no energy could be transmitted. One of the problems encountered was that the polymer cladding did not withstand the energy densities and blackened rapidly. This may have been compounded by the fact that the surface quality of the ends of the fibres was less than optimal as they had to be polished by hand. Scattering off surface defects is well known to be a major contributor to fibre degradation in high power optics. Attempts to shield the cladding with a stainless steel aperture did not result in a significant improvement.

The attempt of using single fibres appears to have been doomed to failure considering the energy densities involved and was abandoned in favour of innovative light-guide solutions: assuming a pulse with Gaussian temporal and spatial profiles, a 130 mJ pulse with a FWHM-duration of 4 ns has a peak power of 31 MW. If focused to a spot with a 2σ-diameter of 900 µm, a maximum energy density of 10 GW cm^{-2} is reached. According to Said et al. (1995), the energy density is therefore of the same order of magnitude as the damage threshold for fused silica.

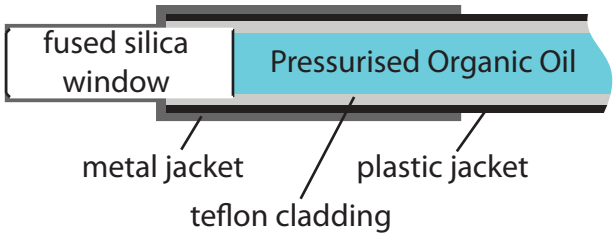

Figure 3.12: Structure of a Lumatec liquid core fibre.

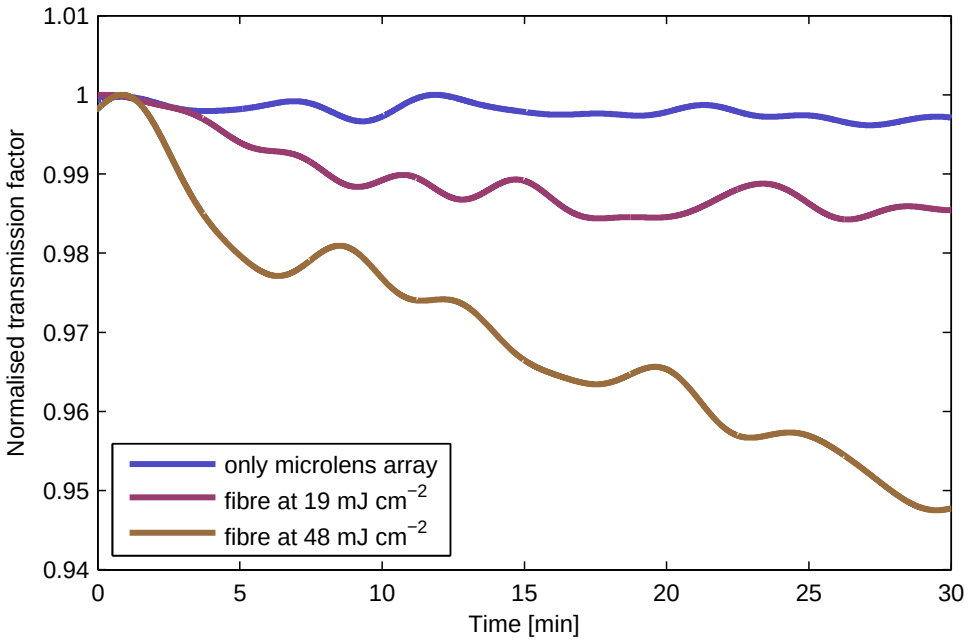

Figure 3.13: Normalised transmission factor of the liquid core fibre as a function of exposure time. (low-frequency filtered with $f_{cutoff} = 1/200\,\mathrm{s}$)

Liquid Core Light Guides

Given that the energy density is inversely proportional to the square of the radius of the beam, it is clear that if the aperture of the light guide can be increased, the energy densities involved quickly fall to more moderate levels. For a beam with a 2σ-diameter of 8 mm, the energy density is only of the order of 120 MW cm^{-2}.

For mechanical reasons, this is not an option with silica cores. One alternative is to use liquid-core light-guides. In the course of the work for this thesis, the suitability of the Lumatec 2000 series liquid-core light-guide was tested.

The Lumatec 2000 series, manufactured by Lumatec, Germany, consists

of core of a pressurised proprietary organic oil compound with a diameter of 8 mm surrounded by a Teflon cladding. The entry and exit ports consist of fused silica cylinders with a length of 30 mm and a diameter of approximately 9 mm. The outward facing edged of the windows are cleaved at 45° to leave a useful aperture of 8 mm. (See Figure 3.12.)

Unfortunately, after extensive testing on multiple fibres it had to be concluded that despite the large diameter of the fibre it lacked long-term stability at the required energy densities. To ensure optimal illumination of the fibre and avoid any eventual hot-spot in the laser beam, an optical setup was devised using an array of microlenses that allowed to project a homogeneous illumination spot at the interface between the fused silica window and the organic oil 30 mm deep in the fibre. The configuration ensured that all parameters such illumination spot diameter on the silica-oil interface and the most extreme angles of incidence remained well within operating limits of the fibre. Nevertheless at an energy density of merely 48 J cm^{-2}, corresponding to 25 mJ for our fibre, a loss of approximately 8%/h in the transmission factor could be observed. (See Figure 3.13.)

The exact process of fibre degradation remains unclear and will be difficult to ascertain since the manufacturer is willing to provide only very limited information on the proprietary organic oil used as core. In some fibres, especially in cases where the injection configuration did not ensure a homogeneous illumination, grey-black clouds could be observed in the oil after exposure. Other fibres experienced significant loss in the transmission factor without any visible damage.

Fused-End Fibre Bundle

An alternative to liquid core light-guides are fibre bundles consisting of a large number of small diameter individual fibres. Originally this approach was avoided as the packing density in typical fibre bundles is low; which implies low transmission coefficients. On the other hand since the individual fibres are made from silica, the energies densities that can be incident on a fibre bundle are generally much higher than those tolerated by liquid core light-guides.

The research engineer of our laboratory, Jean-Marie Chassot, carried out extensive tests on an innovative type fibre bundles: CeramOptec, Germany, manufactures fibre bundle where the fibres are fused at the ends of the bundle. Each individual fibre in the bundle consists of a core of pure fused silica with a diameter of 179 µm. The core is surrounded by a first cladding of lightly fluorine doped fused silica with a diameter of 186 µm, which in turn is surrounded by a second cladding of fluorine doped fused silica with a diameter of 200 µm.[14] The second silica cladding is then protected by a silicon jacket

14. Standard optical fibres have a single cladding which is silica, doped with fluorine to produce the necessary step in the refraction index. However, the typical fluorine content of fibre cladding is incompatible with the manufacturing process of fused-end fibre bundles as

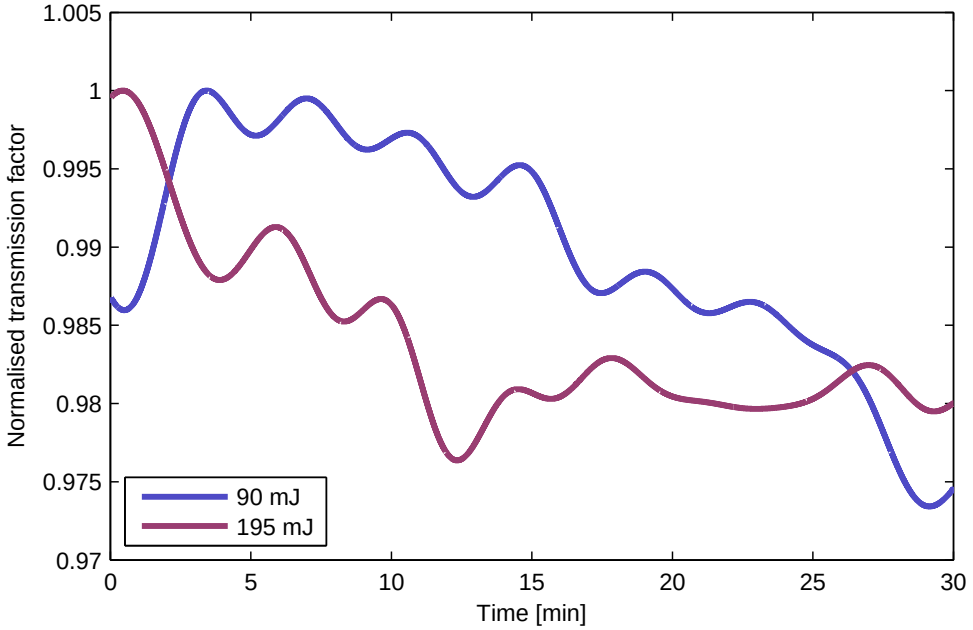

Figure 3.14: Normalised transmission factor of the fused-end fibre bundle as a function of exposure time at 532 mJ. (Low-frequency filtered with $f_{cutoff} = 1/200\,\mathrm{s}$). Data: Jean-Marie Chassot

with a diameter of 250 µm.

At the end of the fibre, the silicon cladding is removed and the silica part of the fibres fused on a length of the order of tens of millimetres. The major part of the light is guided in the core of the fibre, but the several layers of cladding contribute to the light-guiding.

For initial tests of the stability of the fibre bundles by CeramOptec, the manufacturer supplied a returned fibre. Jean-Marie Chassot carried out differential measurements of the transmission coefficient as a function of exposure time. At energy densities comparable to that used to illuminate the liquid core light-guide, no damage to the fibre could be observed. The fibre was therefore exposed directly to the beam of the Surelite II-10 at 532 nm with has a diameter of the order of a few millimetres. The results are shown in Figure 3.14

the fluorine leads to the formation of bubbles during the fusion process.

The fluorine content is therefore reduced in the first cladding to allow fusing the cores surrounded by the first cladding. This however results in a smaller refractive index step between fibre core and first cladding, which in turn implies in an inconveniently narrow acceptance angle of the fibre bundle.

To mitigate this limitation, a second cladding with high fluorine content surrounds the first cladding beyond the region where the ends of the fibres are fused. The result of this construction is a fibre bundle with wide acceptance angle. Light which leaks from the core into the first cladding during propagation is contained therein by the second cladding.

.

The normalised transmission factor can be observed to decrease slightly over time with approximately $4\%/h$. However, it is not entirely certain that this is indeed due to damage to the fibre, as the rate of decrease appears to be independent of the energy density used. Furthermore, the fluctuations due to noise in the measurement are of the order of a few percent and may therefore be responsible for the apparent decrease. Even if the decrease in transmission factor is due to fibre damage, the energy densities in the beam from the Surelite II-10 are much higher than those that would occur if the fibre was used with the beam of the OPO. At present, it would therefore appear that the fibre bundle by CeramOptec will withstand the energy densities occurring when used with the beam of the OPO.

A custom-built fibre bundle with a diameter of 5.5 mm consisting of approximately 756 individual fibres was ordered. Only one end of the fibre bundle was fused while at the other ends the fibres were individually polished. This allows a great degree of flexibility to change the illumination of a sample by re-arranging the loose fibre ends to suit the application. While no potentially destruconly tive test were undertaken on this bundle, the absolute transmission factor was measured and found to be $(81.3 \pm 0.1)\,\%$.

To interpret this transmission factor, it is important to note that a typical individual fibre in a fused-end fibre bundle responsible for guiding light has two distinct parts. The non-fused part of the fibre and the fused part of the fibre. The non-fused part is always significantly longer than the fused part and thus contributes most to the light propagation path.

In the non-fused part, the fibre has a circular cross-section and corresponding "circular" modes which can propagate. In the fused part, the fibre has a hexagonal cross-section and corresponding "hexagonal" propagating modes.

While it is possible to pack "hexagonal" modes with a packing factor of 1, "circular" modes can at best be packed with a factor of 0.907. (See Section 3.2.) Combining this maximum packing factor for "circular" modes with interface losses of 4% on injection and exit of the light into and from the fibre leads to a total transmission factor of a bundle fibrs with compactly packed "circular" modes of $0.96^2 \times 0.907 = 83.6\%$.

Comparison with the measured transmission factor of 81.3% suggest that the "hexagonal" modes do not couple perfectly into the "circular" modes of the fibre. The fusing of the individual fibres merely seems to ensure compact packing of the "circular", propagating modes of the fibre.

3.3 Ultrasound Electronics

The experiments presented in this document were realised with two different ultrasound time-reversal electronics. For all photoacoustic acquisitions a Lecoeur Open System was used. As this system cannot sustain the energies

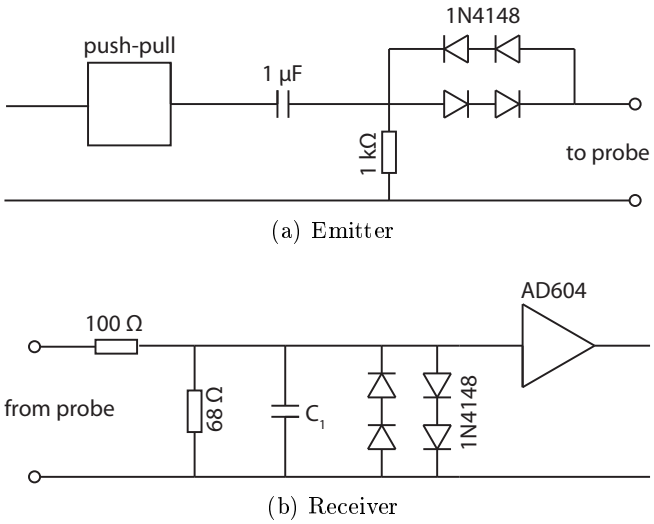

(a) Emitter

(b) Receiver

Figure 3.15: Lecoeur Open System circuit diagrams

needed for high-intensity focused ultrasound, the Supersonic Imagine Brain Therapy prototype system at CIERM Paris was employed for all HIFU experiments.

Lecoeur Open System

The Lecoeur Open System used in this work was a sequencer/signal generator/digitiser system with 64 independent, fully programmable channels controlled via USB by a computer. It may be used to control a 64-element ultrasonic array on emission and reception. The Lecoeur Open System can be operated either as trigger master or as a slave.

The circuit diagrams for the emitter and receiver circuits are shown in Figure 3.15. In the emitter circuit, the push-pull is a power amplifier circuit that provides the necessary current to drive a connected probe with a given potential difference waveform.

In the receiver circuit the AD604 is a low-noise, variable gain amplifier by Analog Devices for the potential difference waveforms created by an ultrasound probe. As used in the Lecoeur Open System, it allows adjusting the reception gain between 0 and 79 dB. The diodes are blocking current below the threshold voltage of silicon, i.e. 0.6 V. For a voltage of less than 1.2 V on the terminals of the amplifier, the diodes therefore do not contribute to the circuit. If the voltage however exceeds the threshold voltage of 1.2 V, the diodes short circuit, thereby providing over-voltage protection for the high-sensitivity amplifier.

Ultrasound probes may be connected in two modes, either in pulse-echo mode or transmission mode. In the first case, the emission and reception electronics are wired to the same physical connector, allowing the same probe to be

used for emission and reception. In the transmission mode, the emission and reception electronics are wired to separate connectors. In this configuration, typically two different ultrasound probes are used for emission and reception.

In this work, signals detected by the Open System were normalised such that the maximum emittable/detectable amplitude at a given amplification corresponded to a value of 1. In the following this will be referred to as "device units". For emission, as signals are processed by an 8-bit digital-to-analog converter providing digitisation of the pressure amplitude on 128 levels or at a resolution of 42 dB. The detection circuit comprises a 12-bit analog-digital converter which provides digitisation of the pressure amplitude on 2048 levels or at a resolution of 66 dB. On reception, one level corresponds to 4.88×10^{-4} device units.

The system used during the work for this thesis went through several revisions with the manufacturer to iron out various hardware and software related bugs.

Supersonic Imagine Brain Therapy System

The Supersonic Imaging brain therapy system is a prototype 512-channel time-reversal electronics developed by Supersonic Imagine, France, primarily for HIFU procedures targeting the brain. The technical details of this system are outside the scope of this chapter, however its principle of operation is analogue to the Lecoeur Open System. In the context of our experiments, the principal difference to the Lecoeur Open System is, that the Supersonic Imagine brain therapy system was designed specifically to withstand HIFU energy densities.

The system we used for our HIFU experiments is located at the Paris research hospital Kremlin-Bicêtre. The photoacoustic data were therefore acquired in our laser laboratory with the Lecoeur Open System and time-reversed in a separate experiment on the Supersonic Imagine brain therapy system.

3.4 Ultrasound Probes

During the work for this thesis, two different ultrasound probes were used. The first was a commercially readily available imaging probe for use with the Lecoeur Open System, the second a custom HIFU compatible ultrasonic probe that was built during the course of the work primarily for use with a yet to be delivered HIFU time-reversal electronics.

Diagnostic Ultrasound Probe

The diagnostic ultrasound probe used for almost all photoacoustic experiments was built by Vermon, France. It is a 64-element probe, with a central frequency of 1.5 MHz and a -6 dB pulse-echo bandwidth of 65%. The probe

has a pitch of 0.7 mm and an elevation of 13 mm. It is elevation focused at 60 mm.

Preliminary measurements indicate that when connected to the Lecoeur Open System, the pressure on reception can be approximately estimated by

$$P\,[\mathrm{MPa}] = 0.38 \frac{\text{amplitude [device units]}}{\text{reception gain}}. \tag{3.24}$$

Imasonic HIFU-Compatible Probe

The second ultrasound probe used was developed during the course of the work for this thesis with Imasonic, France, to be a compromise between the requirements for a HIFU probe and the bandwidth requirements for the detection of photoacoustic signals. It is the expanded version of the Imasonic prototype transducer discussed in Chapter 6 on page 117.

The probe has 128 elements with a central frequency of 1.65 MHz and a −6 dB pulse-echo bandwidth of 45%. It has elements with a width of 0.45 mm and an elevation of 20 mm arranged with a pitch of 0.7 mm. It is elevation focused at 64 mm.

Chapter 4

Proof of Principle & Identification of Challenges

Contents

The objective of this chapter is to explain the fundamental principles of focusing ultrasound by photoacoustic signals and present the basic experimental setup. The description of an early approach to the problem and the results obtained lead to an identification of the problem areas with respect guiding HIFU with photoacoustics. The challenges identified during the implementation and analysis of this early approach inspired the choice of topics that was explored in the following work.

4.1 Guiding Ultrasound with a Selective Optical Contrast

As has been shown in Section 2.1, numerous endogenous chromophores are present in biological tissue. Upon exposure of the tissue to light pulses, acoustic waves are generated by various different tissue structures via the photoacoustic effect. These photoacoustic waves are generally exploited for photoacoustic

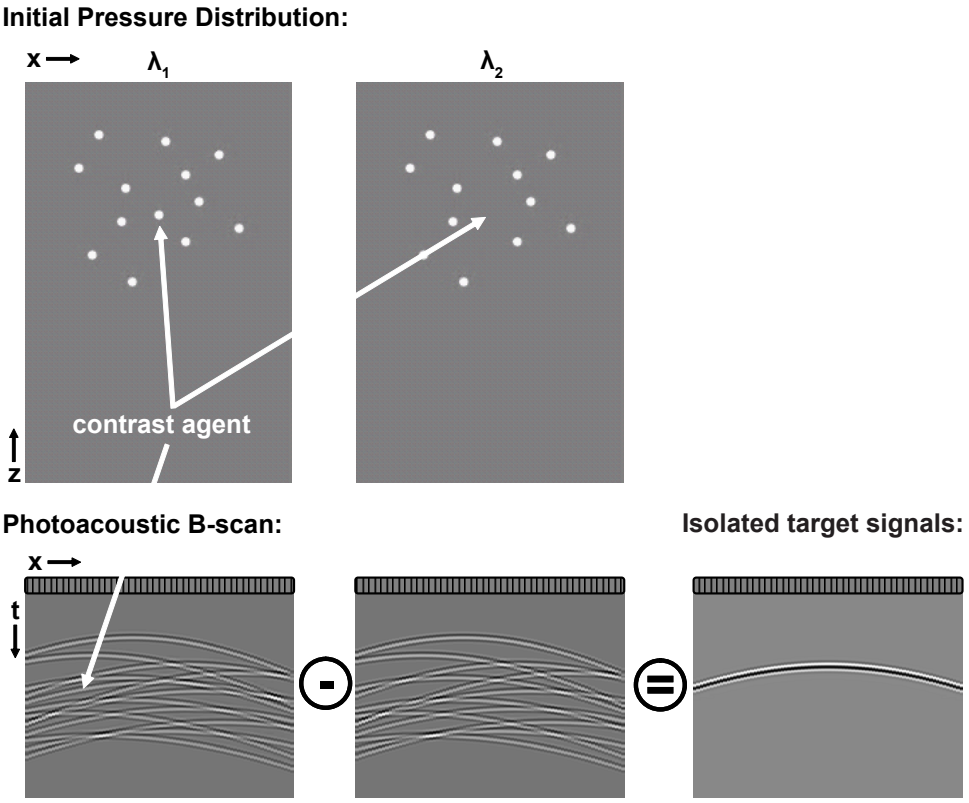

Figure 4.1: Principle of using spectral selectivity to isolate the signals from a target. The initial pressure distributions (upper part of the figure) were propagated with a finite-difference time-domain algorithm and the signals incident on a virtual linear array recorded (lower part of the figure). Illustration adapted from Bossy et al. (2008).

imaging of tissue but in the context of this work, where a single discrete region in the tissue is to be targeted, this "photoacoustic background" is a deleterious effect.

To use the photoacoustic signals for targeting ultrasound, the signals originating from the target area need to be isolated from this photoacoustic background. Over the course of this work, it was investigated whether a spectrally selective optical contrast agent could be used to isolate the signals of a target from those of a spectrally non-selective background.

At its most basic, the idea of using an optically selective target in a non-selective background is illustrated schematically by Figure 4.1: Supposing a medium contains a number of discrete optical absorbers, of which one only absorbs light at a wavelength λ_1, while all others absorb light at all wavelengths. If this medium is then illuminated by with two different wavelengths, λ_1 and

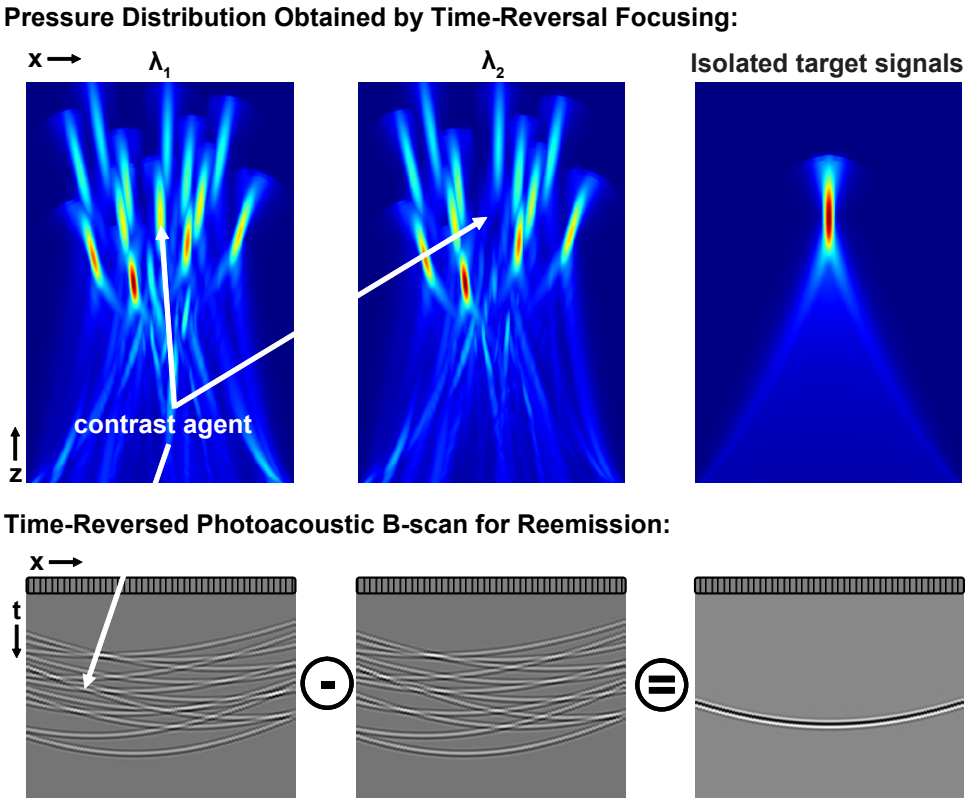

Figure 4.2: Simulation of the pressure distribution obtained with focusing by phase conjugation. The time-reversed photoacoustic signals (lower part of the figure) were convolved with a continuous wave, reemitted from a virtual ultrasound transducer and propagated by a finite-difference time-domain algorith. The envelope of the resulting pressure field in the medium is shown in the upper part of the figure. Illustration adapted from Bossy et al. (2008).

λ_2, an initial pressure distribution as shown in the upper part of the figure results. This initial pressure distribution then propagates as acoustic waves through the medium which can be recorded, e.g. on a linear array, resulting in photoacoustic B-scans as those shown in the lower part of the figure.

The two B-scans are identical but for a missing wavefront corresponding to the target in the B-scan recorded at λ_2. Subtraction of the signals recorded at λ_2 from those recorded at λ_1 therefore allows to isolate the photoacoustic signals of the target which may then be used to focus ultrasound; either by using them to determine the position and extent of the target and using conventional beamforming or by using them for focusing via time-reversal.

Figure 4.2 shows the pressure fields obtained is the photoacoustic signals shown in Figure 4.1 are time-reversed and used to target continuous-wave

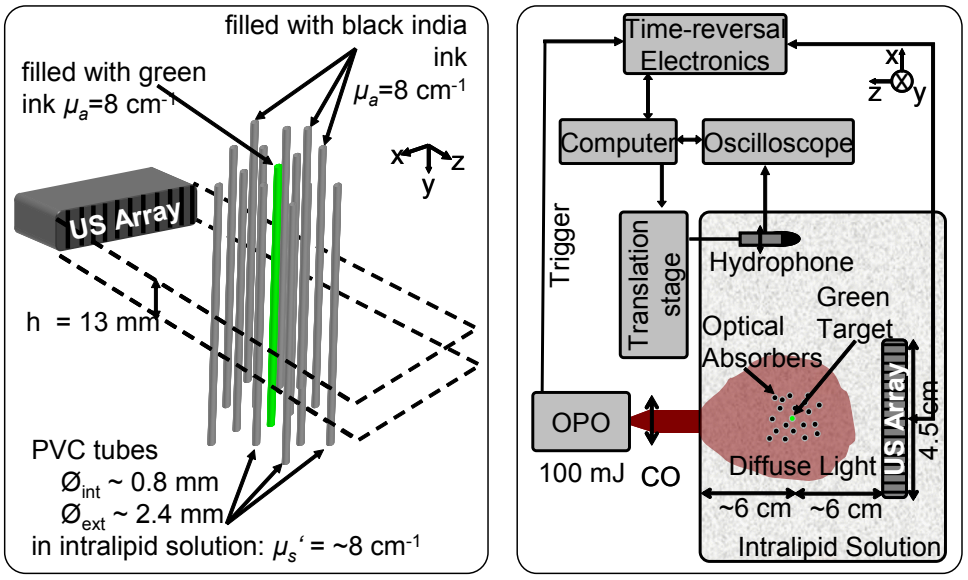

(a) (b)

Figure 4.3: Basic experimental setup used for the work for this thesis

ultrasound. It illustrates that if acoustic energy is to be concentrated on a single target photoacoustic target, it is essential to isolate the photoacoustic signals from the target from the photoacoustic background.

4.2 Experimental Setup

The principle of using a spectrally selective contrast agent to isolate the photoacoustic signal of a target and focus ultrasound, was tested with an academic phantom using the experimental setup illustrated by Figure 4.3.

The phantom consisted of a set of PVC tubes distributed quasi-randomly over an area of approximately 50 mm × 80 mm. All tubes but one were filled with a black ink solution with an absorption coefficient of $\mu_a\,(\lambda_1{=}672\,\mathrm{nm}) = 8.0\,\mathrm{cm}^{-1}$ and $\mu_a\,(\lambda_2{=}730\,\mathrm{nm}) = 7.3\,\mathrm{cm}^{-1}$. One of the tubes was filled with a green ink solution with an absorption coefficient $\mu_a\,(\lambda_1{=}672\,\mathrm{nm}) = 8.0\,\mathrm{cm}^{-1}$ and $\mu_a\,(\lambda_2{=}730\,\mathrm{nm}) = 0.2\,\mathrm{cm}^{-1}$. The set of tubes was immersed in an aquarium filled with a $0.8\%_{vol}$-Intralipid solution which has a reduced scattering coefficient of $\mu_s'\,(\lambda_1{=}672\,\mathrm{nm}) = 8.9\,\mathrm{cm}^{-1}$ and $\mu_s'\,(\lambda_2{=}730\,\mathrm{nm}) = 8.1\,\mathrm{cm}^{-1}$ and serves as a tissue-mimicking environment [1]. The "target tube" filled with green ink

1. The reduced scattering constants quoted are derived from the Intralipid concentration used and the results obtained by van Staveren et al. (1991). During the work for this thesis however it was found that low-concentration Intralipid solutions are thermodynamically unstable at room temperature resulting in a progressive separation of the aqueous and lipid

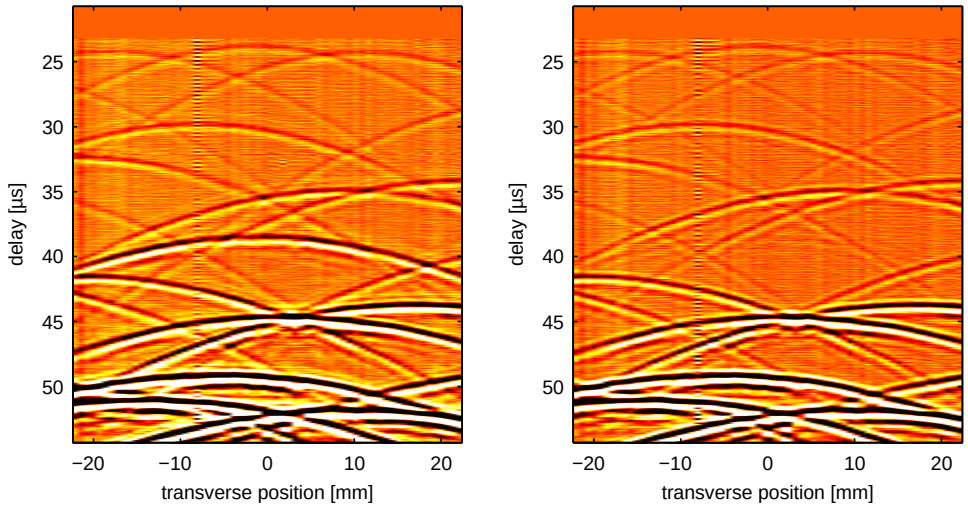

(a) $\lambda_1 = 672\,\mathrm{nm}$ (b) $\lambda_2 = 730\,\mathrm{nm}$

Figure 4.4: Photoacoustic B-scans of the phantom. Colour bar limits: ± 0.05 device units

was positioned 6 cm from the aquarium wall as well as 6 cm from the ultrasound array. It was illuminated from one side with light pulses from an OPO and the photoacoustic signals were recorded on a linear array from the opposite side.

The phantom was illuminated with a collimated but otherwise unmodified beam from the OPO with a diameter of approximately 1 cm with pulses of the order of 125 mJ. The diagnostic ultrasound array by Vermon described in Chapter 3 on page 51 was used for the detection of the photoacoustic signals. The Lecoeur Open System time-reversal electronics was operated as a slave controlled by the Q-Switch trigger of the Surelite II-10.

It should be kept in mind that some of the methods presented in the previous chapter, in particular with regard to beam shaping and beam delivery, were developed after the experiment presented in this chapter.

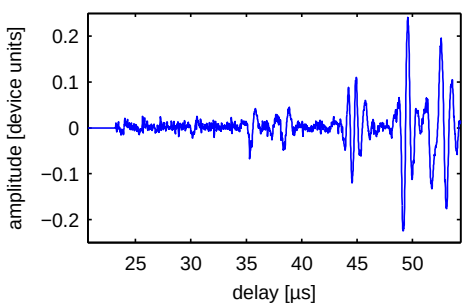

(a) A-scan on channel 32.

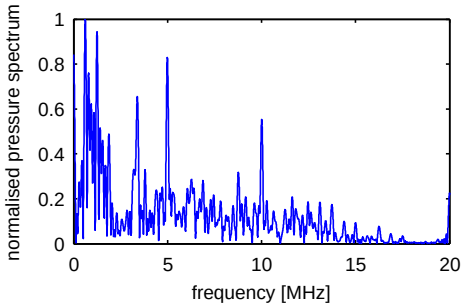

(b) Fourier transform of the deepest third of the signals on channel 32.

Figure 4.5: Photoacoustic signals at 672 nm averaged over 86 acquisitions.

4.3 Photoacoustic Results & Target Signal Isolation

It was observed that photoacoustic signals originating from sources at centimetric depths were comparable to the noise level of the detection electronics. To increase the signal-to-noise ratio (SNR), 86 acquisitions were averaged. The increase in SNR for acquisition with a significantly larger number of repetitions was found not to justify the increase in the transfer time of the signals from the detection electronics to the computer. The photoacoustic B-scans obtained are shown in 4.4. The colour bar was chosen to saturate for signal from shallow absorbers to allow visualising the photoacoustic signals from deep absorbers.

From the B-scans it is obvious that the amplitude of the photoacoustic signals decreases rapidly as function of the depth of the optical absorber in the scattering medium. This is expected due to the reduction in the local light intensity due to optical scattering and absorption as discussed in section 2.1 on page 27.

One can also observe that despite the averaging of a number of acquisitions the noise floor of the data is still large especially at depths of the order of 4 cm and more. To illustrate this point an A-scan of the signals on a single channel is plotted in Figure 4.5a. Figure 4.5b shows a normalised frequency spectrum of the deepest third of the pressure signal where noise dominates. It can be seen that the frequency spectrum in regions with little photoacoustic signals is fairly wide-band compared to the bandwidth of the transducer used.

A photoacoustic acquisition identical to the one described above but with

phases. As a consequence, the scattering properties of liquid Intralipid solutions depend heavily on the time elapsed between preparation of the solution and the experiment. The characteristic time scale of the process is estimated to be of the order of one to a few days. The figures for the reduced scattering coefficient quoted in this work as well as in literature are therefore best regarded as order of magnitude estimates unless the age of the solution and storage conditions are explicitly specified.

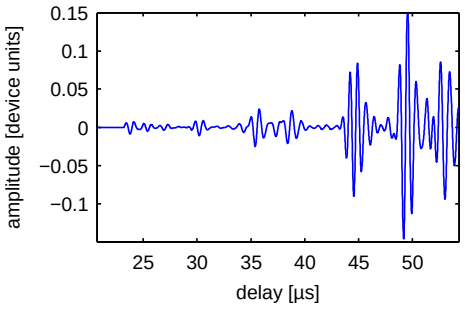

(a) Filtered A-scan on channel 32.

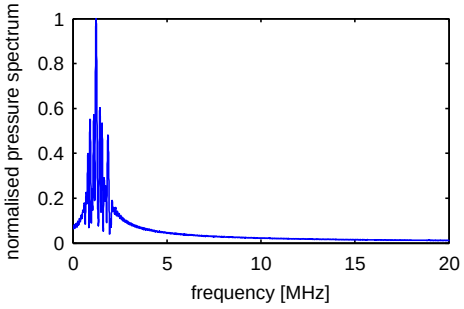

(b) Fourier transform of the deepest third of the filtered signals on channel 32.

Figure 4.6: Filtered photoacoustic signals at 672 nm.

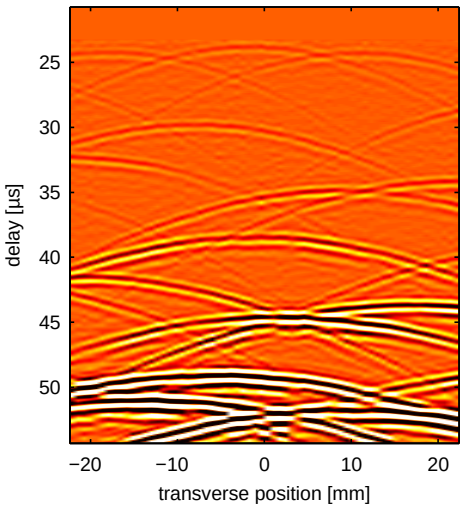

(a) $\lambda_1 = 673\,\mathrm{nm}$

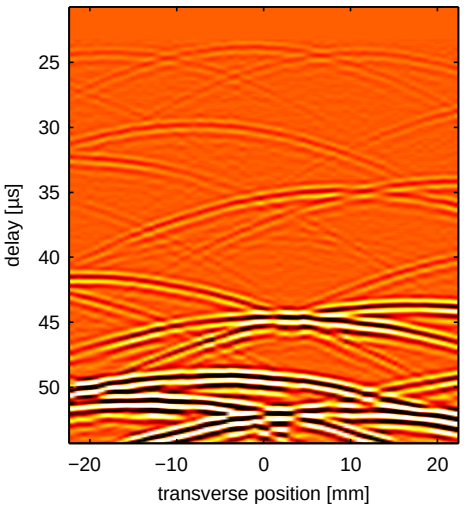

(b) $\lambda_2 = 730\,\mathrm{nm}$

Figure 4.7: B-scans of the filtered photoacoustic signals of the phantom. Colour bar limits: ± 0.05 device units

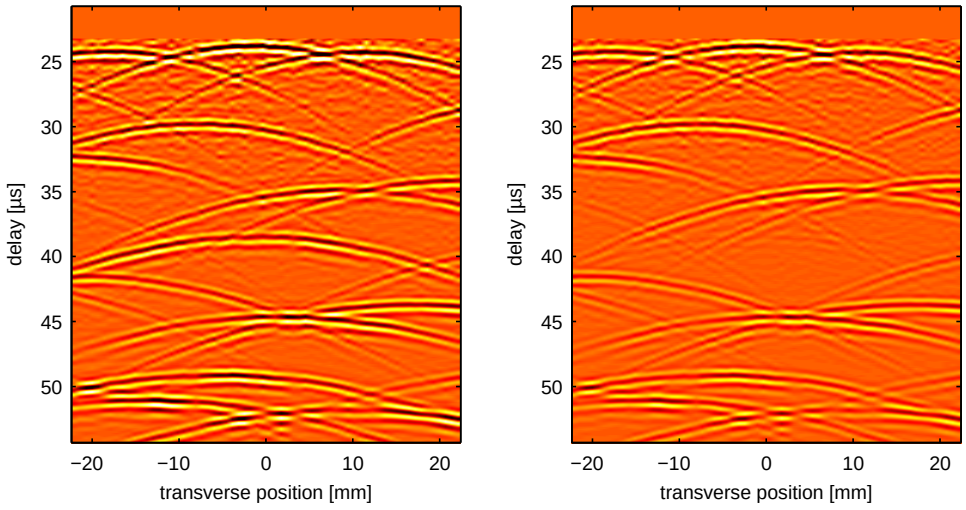

(a) $\lambda_1 = 673\,\mathrm{nm}$ (b) $\lambda_2 = 730\,\mathrm{nm}$

Figure 4.8: Depth-corrected, filtered photoacoustic B-scans of the phantom. The images are plotted with identical colour scales.

the laser remaining closed, was acquired to serve as a measure of the additive noise. By comparison of its frequency spectrum with the bandwidth of the transducer used, a band-pass filter was constructed that allowed to gain access to the signals from deeper optical absorbers. (See Figure 4.6 and Figure 4.7.)

After bandwidth filtering it was attempted to isolate the signals from the photoacoustic target by subtracting the data set obtained at λ_2 from the data set obtained at λ_1. Unfortunately, this simple approach failed due to the fact that it depends on the assumption that the local light intensity in the medium at the two wavelengths is identical. The first problem with this assumption arises from the fact that the energy of the pulses produced by an OPO depends on the output wavelength as explained in Section 3.1. This problem could in principle be mastered by normalising the photoacoustic signal amplitudes by the pulse energy. However, even for the highly idealised phantom this is insufficient. The scattering solution used for our phantom has a slight difference in the reduced scattering constant at λ_1 and λ_2 as was mentioned in the previous section. This leads to a different profile of the light intensity as a function of depth.

To linearise the problem and allow the isolation of the signals from the target by subtraction, the amplitude of the photoacoustic signals had to be normalised by the local light intensity. As the local light intensity is unknown without a near-perfect knowledge of the optical properties of the medium, an exponential law was fitted to the amplitudes of the photoacoustic signals and used as a normalisation function. As can be seen in Figure 4.8, this allows

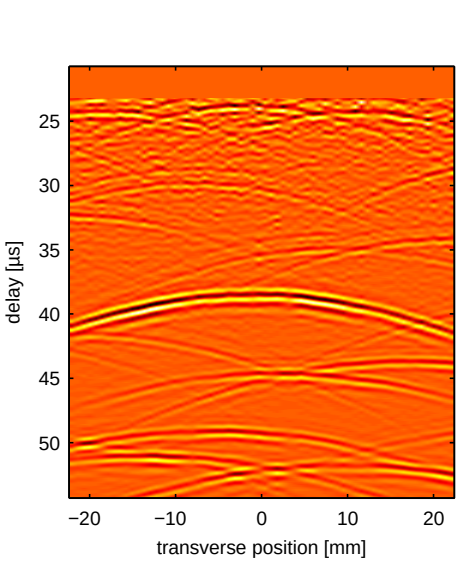

(a) B-scan

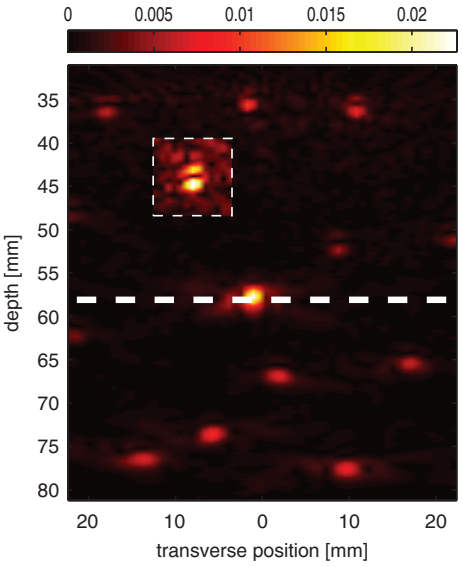

(b) Beamformed image on a linear scale. The dashed horizontal line represents the depth at which the pressure profile shown in Figure 4.11a on page 85 was measured. Within the inset bounded by the dashed rectangle, the values are multiplied by a factor of 10 to illustrate faint details.

Figure 4.9: Isolated photoacoustic signals from the target.

normalising the photoacoustic amplitudes to some degree but an exponential does not model the decrease in light intensity as a function of depth perfectly. This may be due to the finite spatial dimensions of the scattering phantom. Nevertheless as can be observed in Figure 4.9, the approach allowed the isolation of the target to a not insignificant degree. The imperfect separation of the signals of the target is also due to the fact that the tubes containing the ink solutions are not completely transparent but absorb light more strongly at λ_2. This results in the characteristic double-spots that can be observed in the beamformed image at $t = 45 - 50\,\mu s$ where the signal from the ink solution at the interior of the tubes are is eliminated but some of the photoacoustic signals from the tube walls persist.

4.4 Time-Reversal Results

After having "isolated" the target's signals from the photoacoustic background, the signals were time-reversed by flipping the B-scan data matrix in the time dimension. The data was then Fourier-transformed and the phase of the

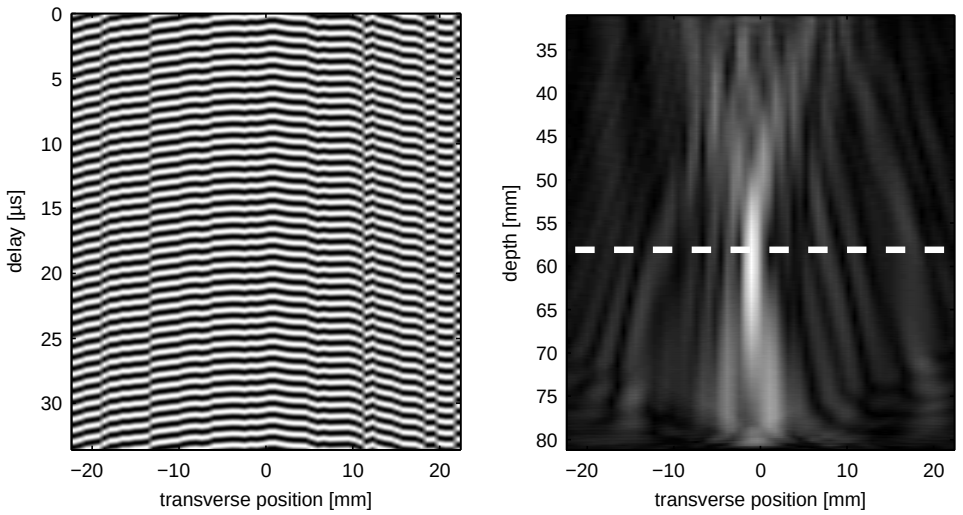

(a) B-scan of the emitted signals

(b) Beamformed image of the emitted signals. The dotted line represents the depth at which the pressure profile shown in Figure 4.11a was measured.

Figure 4.10: Photoacoustically guided continuous wave signals

Fourier component at the frequency of highest energy density $f_{max} = 1.16\,\mathrm{MHz}$ measured. With the phase values of each channel, an emission sequence consisting of a sine wave at f_{max} with a duration of 34 µs was constructed (see Figure 4.10a) and emitted by the time-reversal electronics.

To verify the quality of refocusing, after removing the set of tubes, a hydrophone was scanned across the position of the target tube measuring the pressure amplitude as a function of transverse position. The line along which the hydrophone was scanned is represented by the dashed line in Figure 4.9b and Figure 4.10b. As a basis for comparison, two alternative emission sequences were constructed and the pressure amplitude measured. The first was based on the depth-compensated signals obtained at λ_1, i.e. Figure 4.8a on page 82. The second was focused on the position of the target tube with a traditional delay law based on geometric focussing in a homogeneuos medium. The pressure amplitude distributions obtained in the three cases are shown in Figure 4.11.

In both, Figures 4.11a and 4.11b, the thin line shows the pressure amplitude distribution that would be obtained with traditional delay law focusing for comparison. In Figure 4.11a , the bold line shows the pressure amplitude distribution obtained by focusing via time-reversal (or in the continuous wave case more specifically phase conjugation) of isolated photoactoustic signals of the target. In Figure 4.11b , the bold line show the pressure amplitude

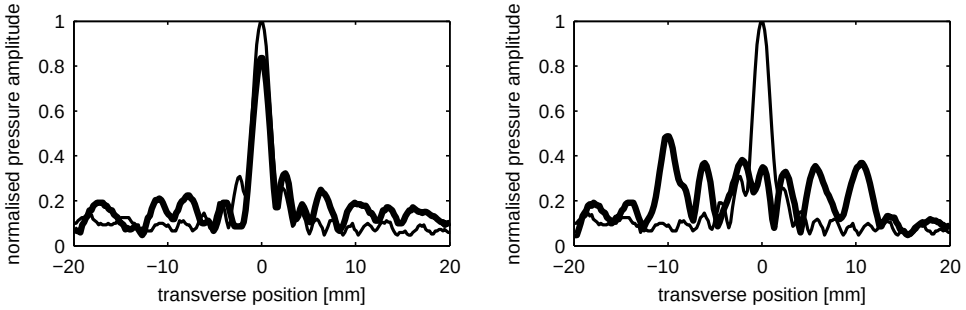

(a) Guided by the isolated signals of the target.

(b) Guided by the signals obtained at λ_1.

Figure 4.11: Pressure amplitude distributions obtained by photoacoustic guidance. The bold line shows the distribution obtained with photoacoustic guidance, the thin line is the distribution obtained by traditional delay law focusing.

distribution obtained by focussing via time-reversal of all photoacoustic signals received without prior isolation of the signals of the target.

Comparison of Figure 4.11a and Figure 4.11b shows that as already discussed at the beginning of this chapter, isolation of the target's photoacoustic signals is essential for focusing by time-reversal. However, even with the imperfect isolation of this experiment, Figure 4.11a demonstrates that a focal spot of the same width as with geometric focussing in a homogeneous medium can be obtained. In contrast to geometric focussing, the quality of a focus obtained by time-reversal does however not degrade in the presence of inhomogeneities in the medium. Nevertheless, Figure 4.11a also shows that the imperfect isolation of the target's signals causes some energy to be directed to the positions of the tubes representing the photoacoustic background.

4.5 Identification of Problem Areas

Over the course of the work presented in this chapter, several problem complexes have become evident and have guided the further work.

Sampling Noise

The first difficulty is related to the detection of photoacoustic waves originating at depths of several centimetres in tissues. The noise level of the detection electronics is the limiting factor for the maximum depth from which useful information can be extracted.

The method of averaging multiple acquisitions allows a significant reduction in the noise level. However, since compensation of respiratory motion

requires updating the focusing with approximately 10 Hz and since the photoacoustic signals of the highest amplitude are obtained in biological tissue with an illumination repetition rate of 10 Hz, averaging over multiple acquisitions puts the possibility of motion compensation by photoacoustics out of reach. Also, since $SNR \propto \sqrt{n}$, where n is the number of averages, the efficiency of this approach to noise reduction decreases with increasing n while the effort, in terms of acquisition time, data transfer time as well as data volume to be processed, increases proportionally with n. For implementations where the time for data transfer is not negligible compared to the time of flight of the ultrasonic signals, the time required for data transfer further compounds the problem. A method of noise reduction that is compatible with real-time motion compensation would be useful.

Similarly to averaging, bandwidth filtering allowed to significantly decrease the noise level. However, it was observed that the noise spectrum has a complicated shape which depends heavily on the acquisition parameters. An algorithm to obtain an appropriate bandwidth filter would facilitate automating the process of guiding HIFU by time-reversal of photoacoustic signals. Furthermore, a better understanding of the origins of the noise in the system may allow the development of novel noise reduction strategies.

Target Signal Isolation

Isolation of the signals of the target from those of the photoacoustic background was non-trivial even in the case of the fairly well controlled phantom used in the work presented in this chapter. It is clear that a different approach to target isolation will be required for biological tissues.

The approach used in this chapter has several weaknesses:

- The subtraction operation used to isolate the target is highly sensitive to motion. A phase shift of more than $\lambda/10$ between the two acquisitions quickly leads to catastrophic failure of the algorithm. Any isolation algorithm should therefore avoid directly subtracting the signals from two acquisitions.
- It was necessary to manually compensate for the decrease of light intensity as a function of depth. Otherwise, residual signal resulting from slight errors in the subtraction of signals from shallow depths drowns the signal of the target. An isolation algorithm should not require knowledge of the light distribution.
- The approach is based on the fact that the absorption spectrum of the photoacoustic background is identical at λ_1 and λ_2. In biological tissues this will not be the case unless the difference between the two wavelengths is less than typically 10 nm. This in turn would require a "magical" contrast agent with a very sharp absorption peak. In practise, it may prove beneficial to use measurements at a number of different

wavelengths and use the form of the spectrum of the contrast agent to isolate the target.

Feasibility with HIFU Compatible Devices

During this chapter the time-reversal electronics and the ultrasonic probe were designed for diagnostic-level ultrasound. It is not obvious that the results translate seamlessly to HIFU compatible devices since during device design the two applications often impose contradictory requirements. Diagnostic level ultrasound generally uses wide bandwidth ultrasound probes to achieve the best image quality. In contrast, bandwidth is of no concern during HIFU device design since HIFU is essentially single-frequency ultrasound. The guiding design challenge with regard to HIFU is the management of heating due to electrical dissipation in the electronic components during HIFU exposure. It remains to be seen whether the results presented in this chapter are reproducible with HIFU compatible devices.

Feasibility in Biological Samples

The results presented in this chapter are based on a highly idealised phantom. It is clear that biological tissue presents a new set of challenges in particular with regard to the light distribution. The realisation of the method *in vivo* will complicate matters further due to the unavoidable motion of the tissue under investigation.

To avoid optimising the method without regard to the true challenges and constraints encountered in any potential application, it will be necessary to develop a better understanding of the dynamics of the photoacoustic background obtained in biological tissue. This is particularly true for the development of a reliable algorithm for target isolation.

Furthermore, since the method is based fundamentally on the use of an optical contrast agent, the feasibility using the available contrast agents for use *in vivo* should be demonstrated.

Technological Challenges for Clinical Applications

The experiment presented in this chapter was realised on an optical table, using fixed mirrors, etc. For any routine clinical application two factors will be crucial:

- Flexible delivery of the light to the patient. For nanosecond pulses of the order of 100 mJ this is a non-trivial task due to the energy densities involved.
- Ensuring a safe exposure: the OPO used in this experiment exhibited a complicated beam shape with hot spots appearing at different wavelength. For safety reasons, as well as for signal processing, a homogeneous or at least well-defined distribution of intensity would be desirable.

Significant effort was invested in the solution of aforementioned problems involving in particular in the characterisation of the performance of various optical components the high energy densities. Since the methods used are common place, only the results of the investigations are presented in Chapter 3 on page 51.

Chapter 5

Methods for Denoising and Target Isolation

Contents

The analysis of the experiment presented in Chapter 4 on page 75 has shown that the feasibility of photoacoustic guidance of HIFU depends crucially on two key factors. It is necessary to be able to firstly detect the weak photoacoustic signals of the target and secondly to isolate the photoacoustic signals of the target from those of the photoacoustic background. Both of these challenges are intrinsically linked. In particular, the best target isolation algorithm is likely to produce unsatisfactory results if the noise content of the data to be processed is too large.

The objective of this chapter is to investigate the origins of the noise in the experiments presented in this thesis, to develop methods for noise reduction and to present some possible algorithms for target isolation.

5.1 Denoising of Photoacoustic Signals

To detect an analog signal by digital sampling, two conditions have to be met. Firstly, the signal amplitude must be large compared to the resolution of

the detection circuit and secondly the signal amplitude must be large compared to the noise level in the experiment.

In the case of photoacoustics, a number of factors that can potentially be optimised influence signal amplitude. Most importantly since the photoacoustic pressure is proportional to the absorbed energy, i.e. $p \propto E_{abs}$, for a given illumination intensity, the energy per laser pulse should be maximised for the best resolution of the sampled signal. However, the safety limits for laser illumination of biological tissue as detailed in section 2.2 on page 34 present a natural limit to the degree to which the signal quality can be optimised with illumination.

Other factors influencing the signal amplitude presented to the analog-digital converter arise from the architecture of the ultrasonic transducer and the impedance matching between the detector, transmission lines and detection circuit. For the moment it shall be assumed that these factors cannot be influenced without significant effort.

During the experiments for this thesis it was found however, that the amplitudes of the photoacoustic signals were generally large compared to the sampling resolution of the detection circuit. It was also found that for the electronics used, the noise level was large compared to the detection resolution. This means that while the information of the photoacoustic signals is contained in the digitised data, the information is drowned by the noise if the photoacoustic sources are located several centimetres in deep in optically scattering media.

To gain access to the information about the photoacoustic signals, it is necessary to develop methods to reduce the noise level of the data compared to the amplitude of the buried photoacoustic signals. All methods for noise reduction presented in this chapter are based fundamentally on the fact that noise exhibits at least a certain degree of randomness while the properties of photoacoustic signals have certain physical constraints. Successful noise reduction thus depends on the identification of universal characteristics that allows to discriminate photoacoustic signals from the noise - and on the development of algorithms exploiting these characteristics.

While the term "noise" is generally understood to describe an inherently random process, in the context of this section, noise shall be used to describe any part of the recorded signal that does not result from the detection of an acoustic wave by an ultrasound transducer.

Note that all experiment and derived figure presented in this section assume a detection of the signals with with the Lecoeur Open System with the maximum receiver amplification of +79 dB. Furthermore, it was found empirically, that the noise level with the Lecoeur Open System is largely independent of the load. It was therefore decided to investigate the noise characteristics with an open detection circuit to reduce the system's complexity.

Analysis of Dominant Noise Sources

Deterministic Noise Contributions

The first type "noise" encountered with the Lecoeur Open System are spikes in the detected signal with deterministic shape and position. They have been identified to correspond to electronic trigger pulses that control the operation of the system.

The Lecoeur Open System allows the programming of complex emission and detection sequences. The individual elements of such sequences are controlled by electronic pulses generated by a number of sequencers, e.g. to start or end emission of a signal with the emitter circuit or to start or end recording of signals with the receiver circuit.

Ideally the circuits used to control the operation of the system and the circuits used for detection of signals should be electronically isolated. However, electrical crosstalk between wires allows a small part of the trigger pulses to bleed into the detection circuit. Typical trigger pulse amplitudes of the order of several volts combined with the detection amplification by four orders of magnitude results in "phantom signals" appearing in the recorded data. If the positions at which these trigger pulses occur are known, it is possible to program the reception sequences which avoid phantom signals occurring at critical positions in the recorded data.

To understand how the spikes in the recorded data depend on the sequence parameters, simple sequences were programmed and the sequence parameters individually varied. The recorded noise data was then averaged over a large number acquisitions. Regions in the data where noise dominates decrease in amplitude with approximately $1/\sqrt{N}$, where N is the number of acquisitions in the average. Regions in the data that are deterministic do not decrease in amplitude or at a slower rate. Note that the emission memory was zero-filled for all sequences.

Close inspection of the noise data (see Figure 5.1) reveals that the following regions in the received data are influenced by trigger pulses:

- First 100 samples relative to the beginning of any recording. (See Figure 5.2b.)
- Last 20 samples of any recording. (See Figure 5.2f.)
- First 300 samples relative to the beginning of any sequence. This may or may not overlap with an actual reception. (See Figure 5.2d.)
- samples $x_{bank} - 2$ to $x_{bank} + 150$ of any recording where x_{bank} gives the size of the emission memory bank size. [1] This may or may not overlap

1. The Lecoeur Open System allows partitioning its emission memory in to multiple "emission banks". Each emission bank can hold a unique emission pattern. This allows the programming of complicated emission/recording sequences with different emission patterns. The standard emission bank size is 4096 samples which results in a phantom signal located at 51.2 µs and a depth of 7.6 cm with photoacoustic beamforming or at a depth of 3.8 cm using echographic beamforming.

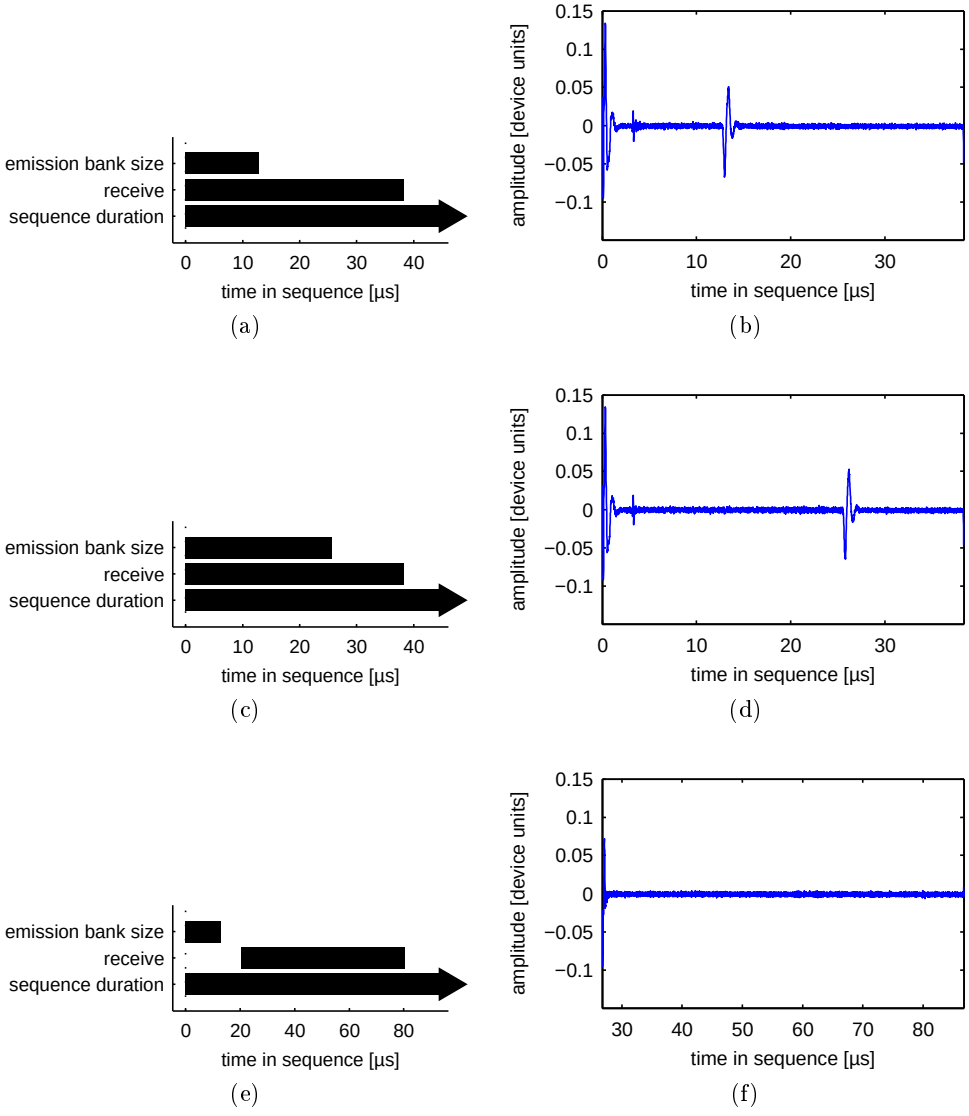

Figure 5.1: Illustration of different sequences and their noise signal averaged over 6272 acquisitions.

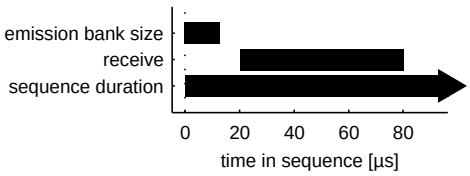

(a)

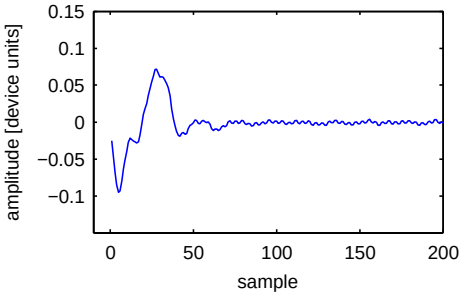

(b) Start of reception trigger.

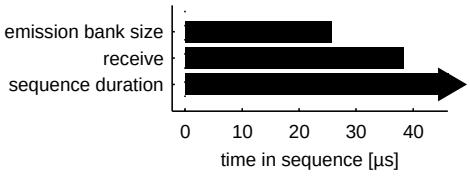

(c)

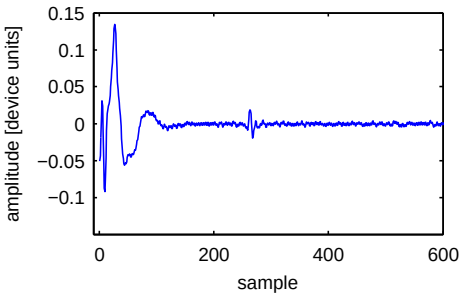

(d) Triggers for start of sequence, emission & reception.

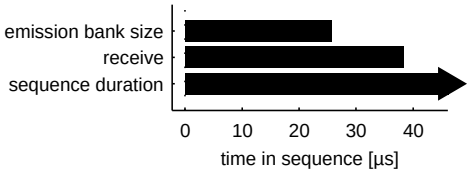

(e)

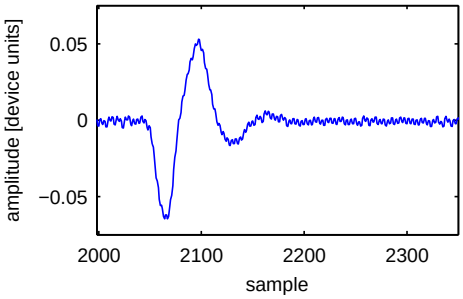

(f) End of emission bank trigger.

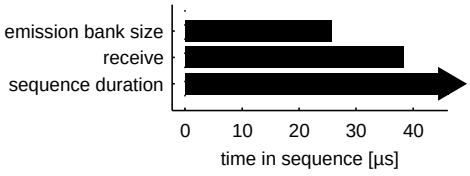

(g)

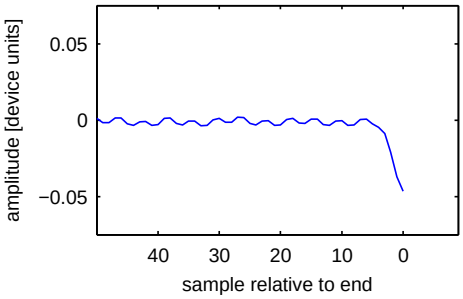

(h) End of reception trigger.

Figure 5.2: Details of different parts of the noise signal averaged over 6272 acquisitions.

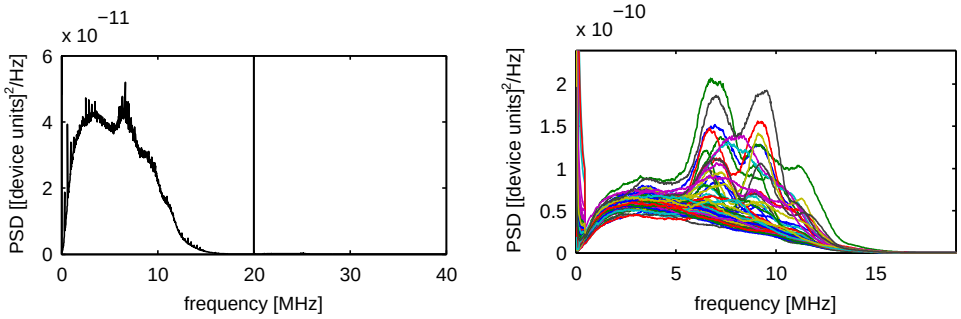

(a) Median power spectral density. Median of 6174 acquisitions. No smoothing.

(b) Median power spectral density per channel. Median of 98 acquisitions per channel, each PSD smoothed with a moving average with a window size of 0.9 MHz prior to calculation of the median.

Figure 5.3

with an actual recording. (See Figure 5.2f.)

Even though these values depend slightly on receiver circuit loading and source of sequence trigger, it was found that this dependence is fairly weak. The values given above are valid whether the receiver circuit it loaded or not and whether the start of the sequence was triggered internally or externally. Please note that these value are only valid for the FPGA processor revision of April 2010. Earlier revisions exhibit additional phantom signals.

A second type of deterministic contribution to the recorded data can be observed in Figure 5.2f. If a large number of acquisitions are averaged, a deterministic regular oscillation emerges from the random noise with an amplitude of approximately 2×10^{-3} device units at a receiver amplification of +79 dB. As can be observed in the noise power spectral density plot shown in Figure 5.3a, this oscillation has a bandwidth only defined by the length of the sample, centred at $f_s = 20$ MHz. The deterministic nature of this noise component combined with its very distinct frequency of 20 MHz suggests that this is a residual signal of the internal clock that synchronises the different sequencers of the Lecoeur Open System which also oscillates at 20 MHz.

Random Noise Contributions

The noise power spectral density[2] of the Lecoeur Open System receiver circuit was estimated from noise acquisitions at a receiver amplification of +79 dB. In open-circuit configuration, the Lecoeur Open System has a noise amplitude $\sigma_N = 2.0 \times 10^{-2}$ device units or equivalently a noise level of −33.9 dB. Figure 5.3a shows that the median PSD averaged over all channels, while Figure 5.3b shows the estimates of the PSD per channel. The median was preferred over the arithmetic mean due to its faster statistical convergence. For Gaussian noise, the difference between the two measures becomes negligible if applied to a large number of samples.

In a well-designed receiver circuit, the noise level is determined by the noise of the signal applied to the circuit, the intrinsic noise of the first amplifier stage and any following filters. To understand the origins of noise in the data recorded by the Lecoeur Open System, it is therefore instructive to consider the design of the receiver impedance matching circuit and the details of the amplifier AD604.

Origins of Random Noise

The AD604 by Analog Devices is a variable-gain low-noise amplifier with two independent channels. Each channel of the AD604 consists of a low-noise pre-amplifier with a programmable gain between +14 dB and +20 dB, a variable attenuator with a gain between −48.4 dB and 0 dB followed by a fixed-gain amplifier of +34.4 dB. Of each channel, the pre-amplifiers and the attenuator with the fixed-gain amplifier can be accessed independently. A single channel allows gains between 0 dB and +54.5 dB, while a combination of two channels allows a useful gain range between 0 dB and +92 dB.

The Lecoeur Open System receiver circuit uses a the pre-amplifier of a single channel operating at +20 dB connected to the two variable attenuators with their fixed-gain amplifiers as shown in Figure 5.4. This results in a gain range between −14 dB and +82 dB as illustrated in Figure 5.5. It appears that for the Lecoeur Open System, the software gain control has been limited to the positive portion of the range where gain is linear to the gain-control voltage, resulting in the known gain range of the system between 0 dB to +79 dB. This simplifies the hardware implementation of the gain-control. The

2. In this thesis, the power spectral density is defined as

$$\mathrm{PSD}\,(f) = \lim_{T\to\infty} \frac{1}{T} \left|\mathcal{F}\left[s\,(t)\right]\right|^2, \tag{5.1}$$

where the Fourier transform of a time-varying signal $s\,(t)$ is defined as $\mathcal{F}\left[s\,(t)\right] \equiv \int_{T/2}^{T/2} s\,(t)\, e^{-2\pi i f t} dt$ and T is the duration of the signal. The energy spectral density is correspondingly defined as

$$\mathrm{ESD}\,(f) = \left|\mathcal{F}\left[s\,(t)\right]\right|^2. \tag{5.2}$$

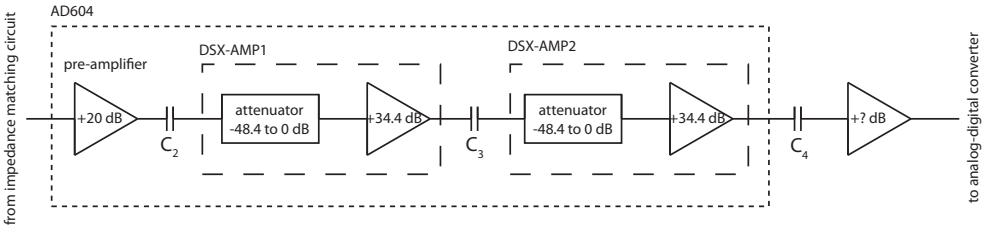

Figure 5.4: Schematic of the amplifier stage of the Lecoeur Receiver Circuit

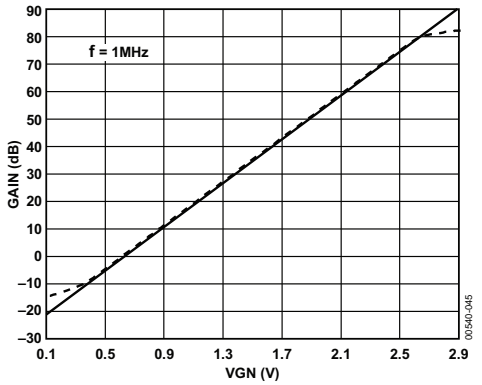

Figure 5.5: Gain of the AD604 amplifier stage of the Lecoeur Open System vs. gain-control voltage. Illustration: Analog Devices (2010)

different elements of the amplifier stage are connected via coupling capacitors $C_1 = 4.7\,\mu\text{F}$, $C_2 = 1\,\text{nF}$ and $C_3 = 20\,\text{pF}$.

According to Analog Devices (2010), the pre-amplifiers of the AD604 have an input voltage noise spectral density of $N_{amp} = 0.76\,\text{nV}/\sqrt{\text{Hz}}$ at $T = 303\,\text{K}$. (See also Figure 5.6a.) In addition, the resistors in the impedance matching circuit in front of the amplifier stage contribute thermal noise with a voltage spectral density[3] of $N_R = (4k_BTR)^{1/2}$ each, where k_B is the Boltzmann constant, T the temperature and R the resistance.

In open-circuit configuration, the noise on the input of the AD604 pre-amplifier due to the impedance matching circuit can be derived from the noise equivalent circuit shown in Figure 5.6b. Even though the value of C_1 is unknown, it must be sufficiently small to avoid attenuating the input signal at ultrasonic frequencies. Since furthermore the input resistance of the pre-amplifier is much larger than the resistance in the impedance matching circuit, it may be assumed that the entire noise voltage due to the 68Ω resistor is applied to the input of the pre-amplifier. The impedance matching circuit therefore contributes an input voltage noise spectral density of $N_{68\Omega} = 1.07\,\text{nV}/\sqrt{\text{Hz}}$ at $T = 303\,\text{K}$.

3. The voltage spectral density is defined as the square root of the power spectral density.

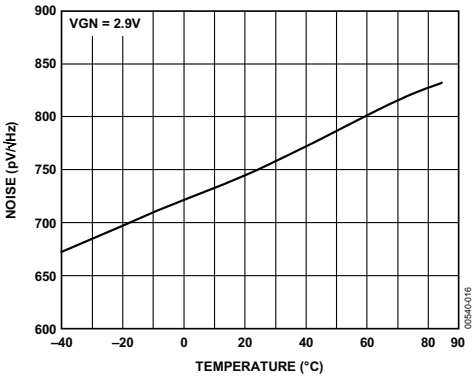

(a) Noise voltage spectral density of the pre-amplifiers of the AD604. Illustration: Analog Devices (2010)

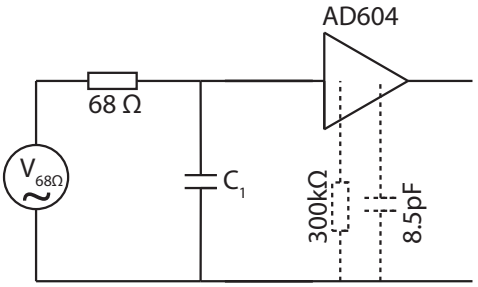

(b) Open-circuit noise equivalent circuit of the Lecoeur Open System receiver circuit. $V_{86\Omega}$ is a voltage noise source equivalent to the noise from a 68Ω resistor. The components drawn in dotted lines represent the input impedance of the AD604.

Figure 5.6

Since the two noise processes are independent, their power may be added, resulting in a total noise input voltage spectral density of

$$N_{tot} = \sqrt{N_{amp}^2 + N_{68\Omega}^2} = 1.31\,\mathrm{nV}/\sqrt{\mathrm{Hz}} \tag{5.3}$$

at $T = 303\mathrm{K}$. Up to at least 20 MHz this spectral density is at worst very weakly dependent on frequency. If a detector were attached to the impedance matching circuit, the noise spectral density would decrease, as some of the noise power would be dissipated in the source resistance. The open-circuit configuration thus represents a worst-case scenario for thermal noise as long as the load impedance is small compared to the input impedance of the AD604.

Device Calibration Factor

Since both amplifier and resistor noise have flat spectral densities, the shape and amplitude of the measured noise power spectral density $\mathrm{PSD}_{\mathrm{meas}}(f)$ can be used to rapidly estimate the bandwidth of the entire receiver chain beginning with the AD604 pre-amplifier input as well as to determine an unit conversion factor c_{conv} relating device units to the voltage applied to the pre-amplifier:

$$\text{Signal [device units]} = c_{conv} \times \text{Signal applied to pre-amplifier [volts]}. \tag{5.4}$$

It follows that the conversion factor is thus given by

$$c_{conv}(f) = \frac{\sqrt{\mathrm{PSD}_{\mathrm{meas}}(f)}}{N_{tot}}. \tag{5.5}$$

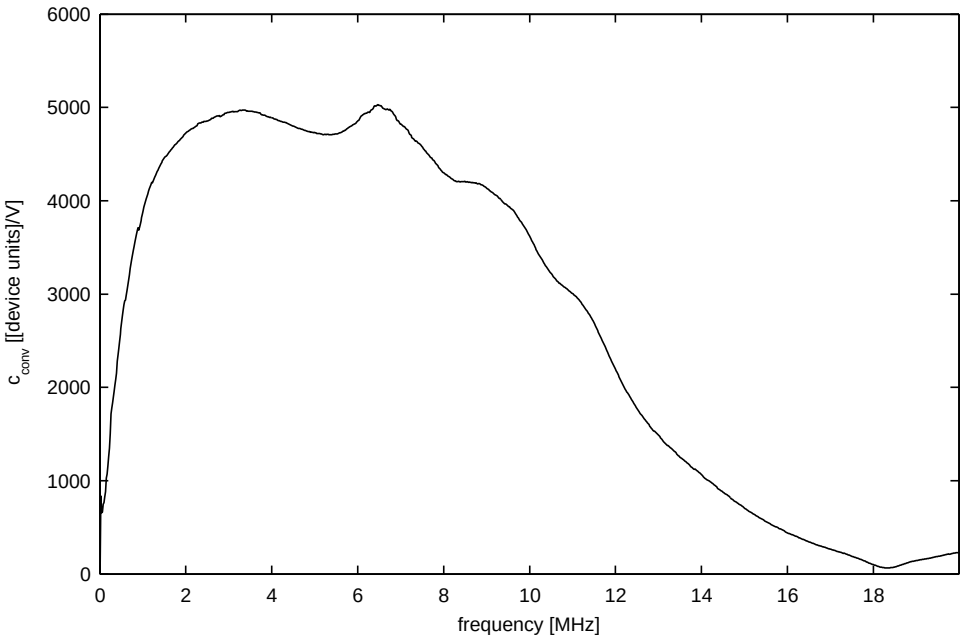

Figure 5.7: Unit conversion factor c_{conv} derived from measured and theoretical noise power spectral density at an receiver amplification of +79 dB. Curve smoothed with a moving average with a window size of 0.5 MHz.

The unit conversion factor for +79 dB receiver gain is illustrated in Figure 5.7.

Combined with the characteristics of the impedance matching circuit, one can find a calibration factor c_{cal} relating device units measured to the voltage applied at the connector of the Lecoeur Open System:

$$\text{Signal [device units]} = c_{cal} \times \text{Signal at the connector [volts]}. \tag{5.6}$$

From the definition of the unit conversion factor it follows that

$$c_{cal} = G_V \, c_{conv}, \tag{5.7}$$

where G_V is the voltage gain of the voltage divider of the impedance matching circuit. (See Figure 3.15b on page 71.)

Unfortunately at present, there is still some uncertainty concerning the true architecture of the impedance matching circuit, preventing the determination of a precise value for this calibration factor. Early preliminary experiments with a single-frequency signal have indicated a calibration factor of $c_{cal} = {}^{1}/_{5}\,\text{V}\times\text{Gain} \approx 1782\,\text{device units}/\text{Volt}$. Neglecting the capacitor C_1 with yet undetermined value, the voltage gain of the impedance matching circuit is $G_V \approx 0.40$. It follows that the calibration factor derived from the noise power spectral density is with $c_{cal} \approx 2000\,\text{device units}/\text{Volt}$ comparable to the value of the preliminary measurements.

Methods for Denoising

Optimal Bandwidth Filtering

In sections 4.3 and 5.1 it has become clear that the photoacoustic signals are not only filtered by the system's impulse response but generally also contain a significant proportion of added random noise. The noise of the Lecoeur Open System receiver circuit has a $-6\,\mathrm{dB}$ central frequency of $6.1\,\mathrm{MHz}$ and bandwidth of 184% $[0.5\,\mathrm{MHz}, 11.7\,\mathrm{MHz}]$. Comparing this to the typical pulse-echo bandwidth of the transducers used in this experiment of approximately 50% centred at $1.5\,\mathrm{MHz}$ it is clear that most of the noise of the recorded signal is in a frequency range where the detectors used can never detect any acoustic signal.

The question then arises how the signals acquired by the system can be optimally filtered, given the spectral densities of the system impulse response and the spectral density of the additive noise. It is clear that applying a simple windowing method in frequency space will allow to eliminate noise from high and low frequency components that are outside the frequency response of our detection system. It remains to be determined however, whether the is an optimal width for the band-pass filter and whether some windowing functions are more adapted to the problem at hand than others.

Wiener Filters It may be shown (see Appendix D on page 185) that in the case of independent additive random noise $N(f)$ applied to a noise-less signal $X(f)$

$$Y(f) = X(f) + N(f) \tag{5.8}$$

the best estimate $\hat{X}(f)$ of the true signal is given by

$$\hat{X}(f) = W(f)\ Y(f). \tag{5.9}$$

$W(f)$ is known as a Wiener filter and defined as

$$W(f) = \frac{P_X(f)}{P_X(f) + P_N(f)}, \tag{5.10}$$

where $P_X(f)$ and $P_N(f)$ are the power spectral densities of the signal and noise respectively. Since the signal-to-noise ratio SNR is defined as signal power over noise power, the use of a Wiener filter is equivalent to weighing the frequency components of a recorded signal with their SNR as per

$$W(f) = \frac{SNR(f)}{SNR(f) + 1}. \tag{5.11}$$

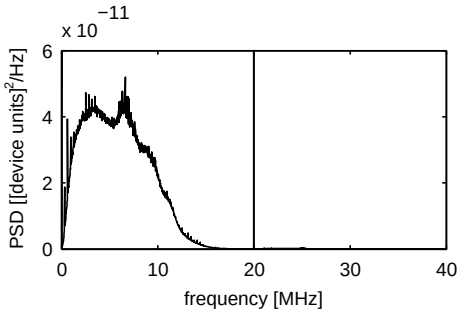

(a) Estimate of the noise power spectral density.

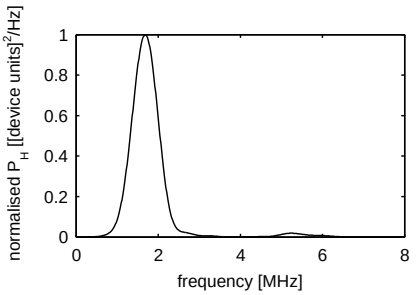

(b) Normalised power spectral density derived detection transfer function of the Lecoeur Open System with the Imasonic HIFU transducer.

Figure 5.8

Definition of a Particular Filter One problem with the application of Wiener filtering to photoacoustic signals is that the precise signal amplitude and shape, and thus $P_X(f)$, are apriori unknown: As shown in Section 2.3, they depend on the geometry of the photoacoustic source and the *in-situ* light intensity at the optical absorber. The next best option is therefore to define a particular Wiener filter in terms of the power spectral density derived transfer function of the detection system $P_H(f)$.

While the determination the precise transfer function is a non-trivial task, for the definition of a Wiener filter it is sufficient to know the gain [4] of the detection system.

The detection gain of the Lecoeur Open System connected to a particular transducer was estimated by illuminating the surface of a transducer immersed in water homogeneously with a laser spot and recording the detected signal. It is clear that the precise shape and amplitude of the photoacoustic signals induced in the acoustic lens by this method are unknown. However, since the acoustic lenses of the transducers used in this work are opaque, the luminous energy is absorbed over a very short length, which results in the production of a photoacoustic wave with a very wide frequency spectral distribution. It shall therefore be assumed that the thus produced photoacoustic signals have a flat frequency response over the relevant frequency range. Nevertheless, to obtain comparable results, the gain curves must be normalised. (See Figure 5.8.)

The normalisation of the system gain curve makes it is necessary to scale the derived power spectral density with respect to the noise power spectral density. If one was to define a total signal to noise ratio in terms of the system transfer function and the system noise as

4. In this section, gain refers to the absolute value of a transfer function.

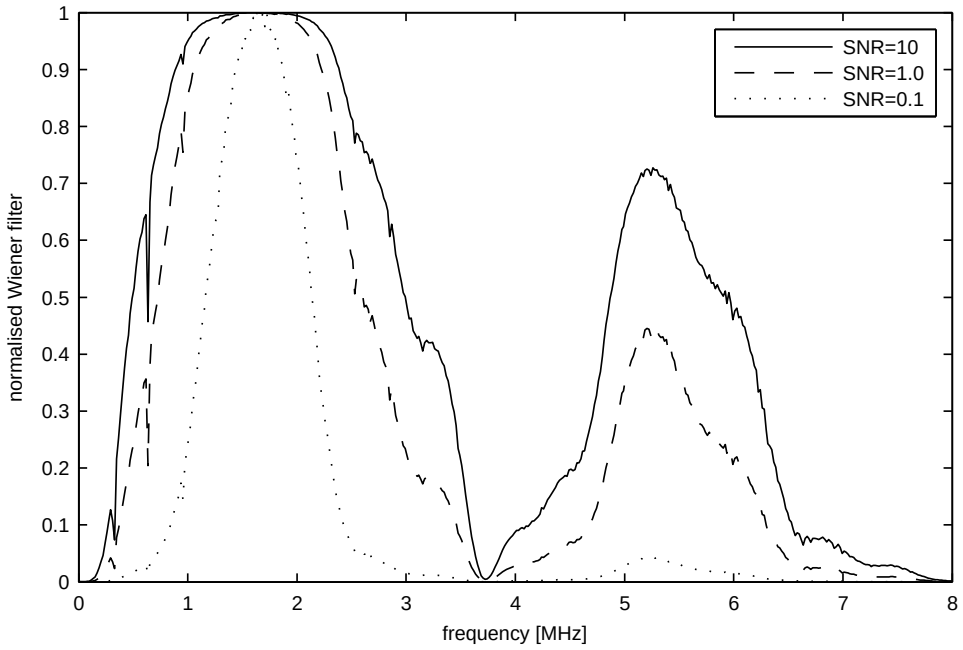

Figure 5.9: Wiener filters defined with different presumed SNR values of the recorded data: a primary "pass-band" is centered on the central frequency of the transducer and a secondary peak arises due to increased detection sensitivity at the second harmonic of the transducer's central frequency.

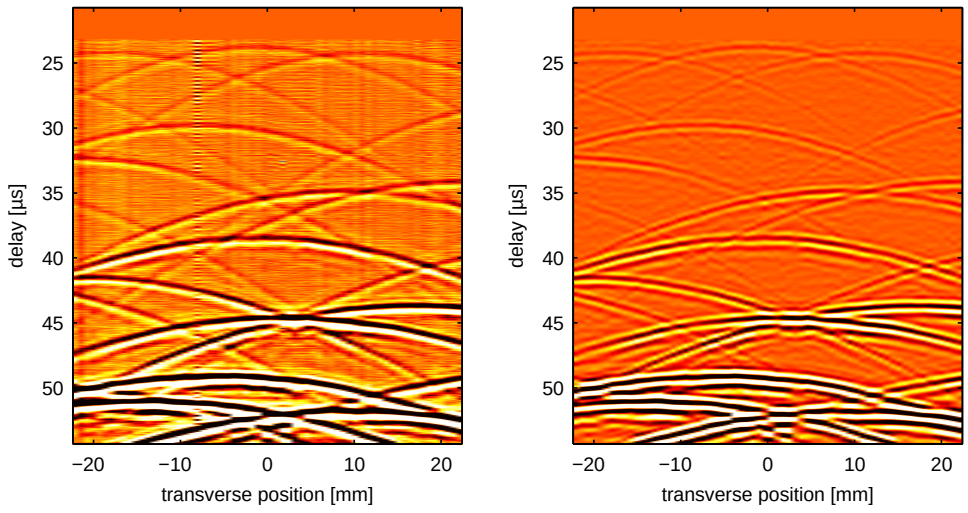

(a) (b)

Figure 5.10: Example of photoacoustic signals filtered with a Wiener filter defined with $SNR_{tot} = 3$.

$$SNR_{tot} = \frac{\int P_H(f)\,df}{\int N(f)\,df}, \tag{5.12}$$

the total signal-to-noise ratio can act as scaling factor. The optimal choice of scaling depends on the intended application for the filtered data, however it was found that a scaling with $SNR_{tot} = 3$ was a good choice for the experiments presented in this thesis.

Figure 5.9 shows three normalised Wiener filters derived from the transfer function with the Imasonic HIFU probe and the Lecoeur Open System. It illustrates how the shape of the filter changes as a function of the presumed signal-to-noise ratio of the recorded data. A "pass-band" is centred on the central frequeny of the transducer. However, a secondary peak of the filter around $f = 5.2$MHz arises due to the transducer's increased detection sensitivity at the second harmonic. This harmonic can be barely identified in Figure 5.8b on page 100 but depending on the SNR assumed when defining the filter, it may make a beneficial contribution to the detected signal. Figure 5.10 illustrated the result of a Wiener filter defined with $SNR_{tot} = 3$ when applied to a photoacoustic B-scan.

Using Parseval's theorem, it may be shown that the rms noise n_{rms} in the recorded data after filtering with is given by

$$n_{rms} = \int W(f)\,N(f)\,df. \tag{5.13}$$

It follows that the noise standard deviation is given by

$$\sigma_N = \int W(f)\,N(f)\,df - \mu_N, \tag{5.14}$$

where μ_N is the DC offset of the noise.

Radon Filtering

Exploiting the knowledge about the possible frequency content of a detected acoustic signal to implement bandwidth filtering allows to realise a significant improvement of the signal-to-noise ration. However, photoacoustic signals have another property that allows to discriminate them from noise: in contrast to noise, photoacoustic signals originate from a physical location. As a result, the form of the wavefronts of photoacoustic waves is not arbitrary but constrained by the physical process from which they arise.

Intuitively the brain of an experienced experimenter exploits this fact: if one knows what a typical signal "looks like" it is possible to identity signals even in the presence of large noise content. This can be illustrated by the data already presented in Chapter 4 on page 75. Comparison the data at $t = 25 - 30\,\mu$s in the B-scan with those in a single A-scan in Figure 5.11 shows

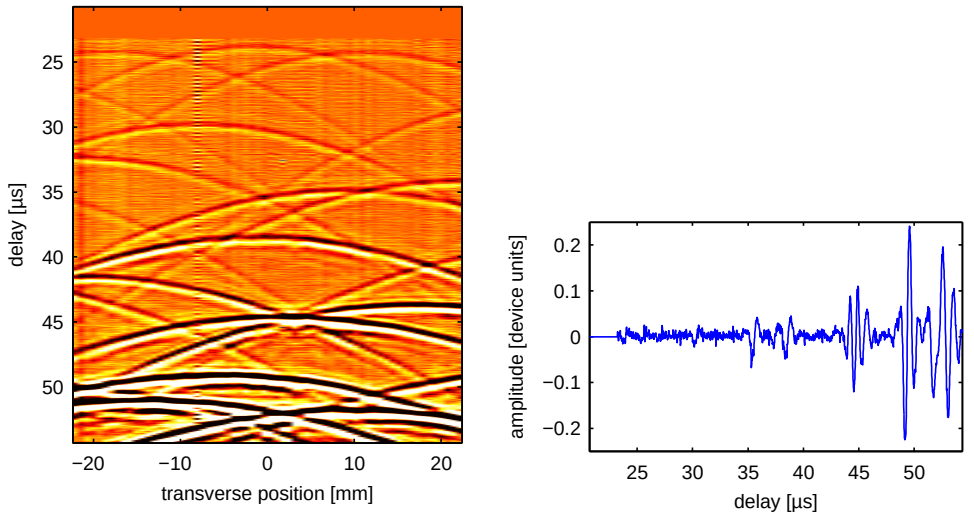

(a) B-scan of photoacoustic signals.

(b) A-scan of the photoacoustic signals at $x = 0\,\mathrm{mm}$.

Figure 5.11

that in the first case the wavefronts are easily identifiable, while in the latter the signals are impossible to locate with certainty.

The physical constraints on the photoacoustic wavefronts may be used for noise reduction as well as to simplify the isolation of the signals of the target from the photoacoustic background. One approach is to use a transformation parametrising the position of the origin of the photoacoustic signals. This is analogous the idea of Radon beamforming in the case of computed x-ray tomography and very closely related to the routine operation of image formation in all echographic imaging devices known in the acoustic community as beamforming. In the following terms Radon Transformation and Beam Forming as well as Radon Transformed Data and Beamformed Image may be regarded as synonymous for the purposes of this section.

The particular challenge in the context of this thesis is that the photoacoustic signals are to be used among others for aberration correction. This requires that the delay law for focusing be derived from signals in B-scan space since it is impossible to extract the information necessary for aberration correction diectly from the beamformed image of aberrated waveforms. It was therefore attempted to find an invertible parametric transformation which allows constraining the origin of the signals in parametric space and transform the result back to B-scan space to extract the information for aberration correction from a dataset with reduced noise content.

Hyperbolic Radon Transform A generalised Radon transform $\mathcal{R}$ operating on data $a\,(t, x_d)$ in two-dimensional space may be defined as a line integral

along a parametrised line $t \equiv t(x, z, x_d)$

$$b(x,z) = \mathcal{R}\left[a(t, x_d)\right](x,z) \tag{5.15}$$

$$= \int_{t=t(x,z,x_d)} a(t, x_d)\, dx_d, \tag{5.16}$$

where $b(x,z)$ is the Radon transformation of $a(t, x_d)$ with the given parametrisation of t .

For an acoustic impulse point source located in a homogeneous medium at position (x, z), the acoustic wave front arrives at a detector located at x_d on the line $z = 0$ with a delay $t(x, z, x_d)$ given by

$$t(x,z,x_d) = \frac{1}{c}\sqrt{z^2 + (x - x_d)^2} \tag{5.17}$$

$$= \sqrt{\left[t_0(z)\right]^2 + \left(\frac{x - x_d}{c}\right)^2}, \tag{5.18}$$

where c is the speed of sound in the medium and $t_o(z) = {}^{z}/_{c}$. One may thus define a hyperbolic Radon transform $\mathcal{R}_h$ as a special case of the generalised Radon transform $\mathcal{R}$ calculated along the set of lines defined by above delay law.

By discretising the Radon operator defined in (5.16) and the position of the detectors, one obtains the well-known beamformer

$$b_{x,z} = \sum_{x_i} a_{x_i,t_i}, \tag{5.19}$$

where x_i is the position of the detector with index i and t_i the corresponding signal delay defined by

$$t_i(x,z) = \frac{1}{c}\sqrt{z^2 + (x - x_i)^2} \tag{5.20}$$

for a linear array of detectors.

Invertability of the Hyperbolic Radon Transform Beylkin (1987) has shown that a wide class of generalised Radon transformations is exactly invertible, in particular if t may be expressed in the form $t = C\, t_0 + \phi(x_d)$, where C is a constant and ϕ and arbitrary function of a single variable. Applied to waveforms generated by acoustic point sources detected by a linear detector, this implies that the Radon transformation is invertible if the curvature of the waveform depends only on the position of the detector; i.e. it is independent of the position of the source.

This condition is approximately satisfied if the depth of the acoustic source is large compared difference between the transverse positions of the source

and the detector $x - x_i$ and all sources lie on a line of constant x.[5] Various existing methods that allow extending the applicability of the result by Beylkin (1987) to hyperbolic lines, such as t^2-stretching proposed Yilmaz (1989), are unfortunately limited to sources with a constrained x coordinate. Neither of these requirements is satisfied in general by photoacoustic signals arising in a biomedical context. However, it was found that under certain conditions the Radon transform is at least approximately invertible by filtered back-projection of the signals with the inverse operation of the discretised Radon operator

$$a_{x_i,t_i} = \sum_x b_{x,z(t_i,x_i,x)}, \tag{5.21}$$

where

$$z\left(t_i, x_i, x\right) = \sqrt{\left(ct_i\right)^2 - \left(x - x_i\right)^2}. \tag{5.22}$$

It is known that any operation involving integration over a finite spatial aperture acts as a low-pass filter for data. (Yilmaz (2001, pp. 485, 943)) It is therefore necessary to apply a filter $\rho\left(t\right)$ to compensate for this redistribution of energy in the frequency spectrum of the data. For the integral form of the Radon transform and 2D-data, the filter is defined in Fourier space as $\mathcal{F}\left[\rho\left(t\right)\right]\left(f\right) = \sqrt{2\pi f}e^{i\pi/4}$. As demonstrated by Beylkin (1987) this filter is not directly discretisable. Nevertheless, it was found that acceptable results could be obtained using the filter for the integral transform at discretised frequencies.

Figure 5.12 demonstrates that by using filtered back-projection of the Radon transform data, the original B-scan data can be recovered for discrete photoacoustic sources in a homogeneous medium even with this approximate inversion procedures. Unfortunately, in the presence of a simulated aberrator, the inversion rapidly fails with increasing degree of aberration.

The underlying data for the illustrations is the data acquired in the experiment presented in Chapter 4 on page 75. (See also Figure 5.12a.) Figure 5.12b is the same set of data, however a sinusodial aberration with an amplitude of approximately 0.37π was applied. Figures 5.12(b&c) show the envelope of the Radon transform of the unaberrated and the aberrated data respectively. It can be observed that the aberration leads to a smearing of the energy in the parameter space, since the sinusodial aberration is not well-parameterised by a hyperbolic delay law. Figures 5.12(d&e) illustrate the filtered back-projection of the Radon transformed data to attempt to recover the original B-scan data of Figures 5.12(a&b).

The decrease in the noise level that can be observed in Figure 5.12e is due to the fact that Figure 5.12c is only a section of the entire parameter space.

5. For $z \gg x - x_i$ (5.20) may be approximated by the first two terms of its series expansion $t_i\left(x, z\right) = {}^{z}/_{c} + {}^{1}/_{2c}z^{-1}\left(x - x_i\right)^2$. Provided that x is a constant, the second term is approximated as being only a function of the positions of the detector x_i if $z \gg x - x_i$. It follows that under the given condition, t_i may approximately be expressed in the form $t = C\,t_0 + \phi\left(x_d\right)$.

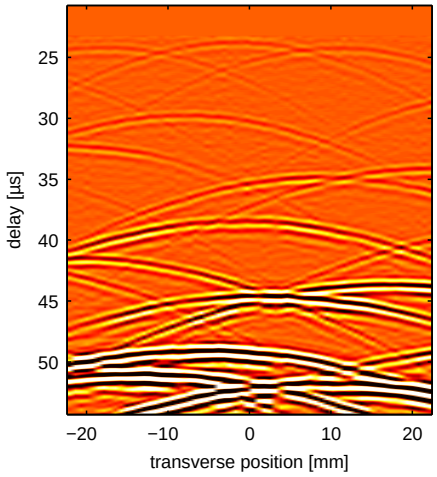

(a) B-scan of unaberrated data

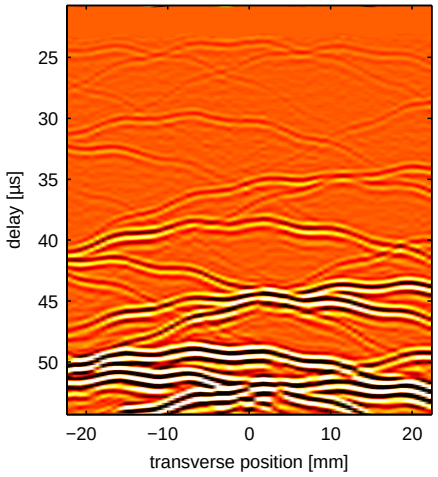

(b) B-scan of aberrated data

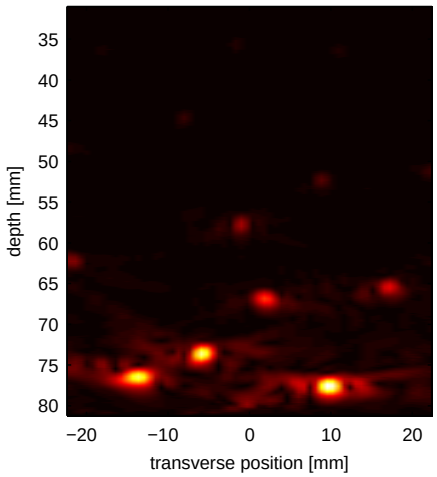

(c) Envelope of the Radon transform of unaberrated data

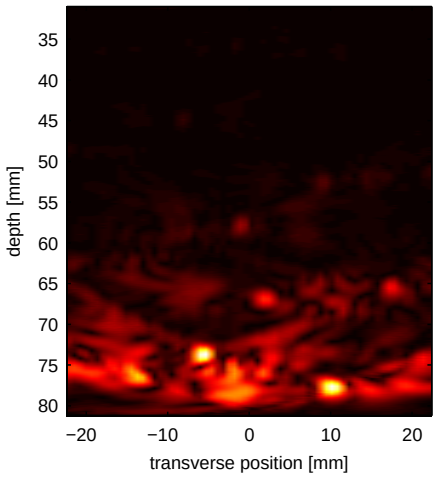

(d) Envelope of the Radon transform of aberrated data

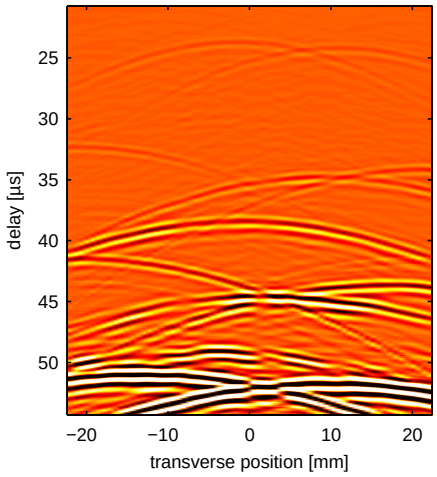

(e) Filtered back-projection of unaberrated Radon transform

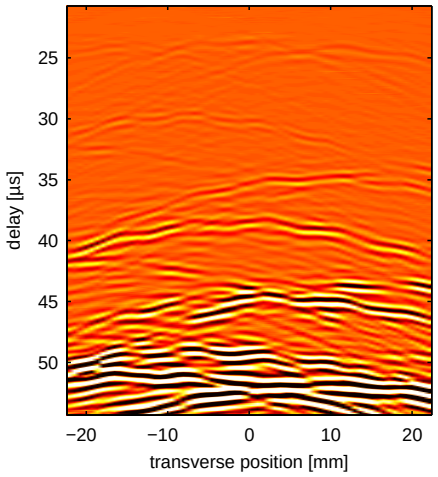

(f) Filtered back-projection of aberrated Radon transform

Figure 5.12: B-scan, Radon transform and filtered back-projection of the Radon transform for unaberrated and aberrated waveforms. Degree of aberration: approximately $\pm 0.36\pi$.

Since the noise content of data is not well-parameterised by the hyperbolic delay law used for the transformation, the noise content is spread over a very large region of the parameter space. Attempting to reconstruct the original dataset from data contained in only a relatively smalll section of the parameter space thus result in a "loss of information" preventing complete reconstruction of the noise content. - In other words: the increase in the signal to noise ratio on reconstruction is a direct consequence of the fact that the noise content and the signal content of the original data are concentrated to different degrees in the paramter space of the Radon transform and the fact that the reconstruction is calculated from a limited section of said parameter space.

On Figure 5.12f it can be observed that with an aberration of $\pm 0.37\pi$, the inversion of the Radon transform begins to diverge significantly from the original data for the given geometry and source configuration. It remains to be seen if a more robust inversion procedure can be obtained in analogy to the work by Beylkin (1987). Despite significant efforts, this has to date remained elusive due to the non-trivial nature of the mathematical problem.

Examples for the Applications of the Radon Transformation For homogeneous media or weakly aberrated waveforms, the Radon transform and its inversion can be used for noise reduction as well as to isolate individual wavefronts. Depending on noise level, Radon transform noise reduction allows to significantly improve the signals-to-noise ratio of the data in B-scan space by imposing a threshold value above the noise level in Radon transform space. Figure 5.13c shows the result of imposing a manually determined threshold on the Radon transformed data prior to inversion by filtered back-projection.

Isolation of individual photoacoustic sources is achieved by applying masks on the Radon transform data which constrain the position of the origin of the desired wavefronts prior to inversion. While with the current implementation of the inversion procedure this application rapidly fails for strongly aberrated data, it nevertheless allows to isolate moderately aberrated wavefronts as illustrated in Figure 5.13d: for this example, a mask was applied manually to the Radon transformed data attemping to select a region of the paramter space containing the data corresponding to the source at $(x = 0\,\mathrm{mm}, z = 58\,\mathrm{mm})$ which was sufficiently large to capture the smeared information about the aberration but small enough to exclude adjacent sources. The ability to isolate individual wavefronts of weakly aberrated data opens the door to diffraction limited focusing on individual photoacoustic sources via time-reversal.

5.2 Isolation of Optically Selective Sources

In the analysis of the experiment presented in Chapter 4 on page 75, several shortcomings of the target isolation algorithm used were highlighted. It was found that the algorithm

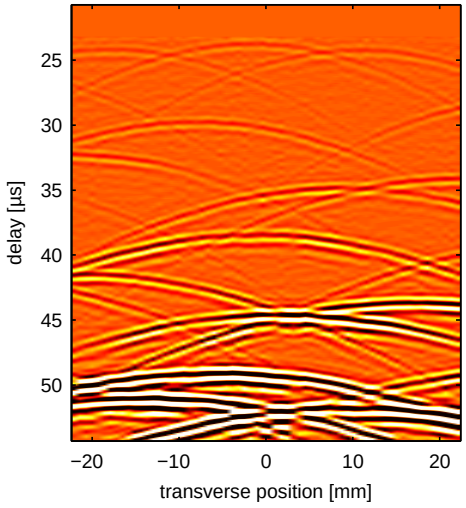

(a) B-scan of unaberrated data.

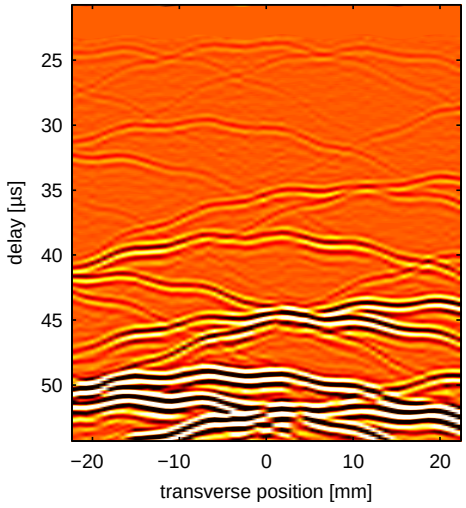

(b) B-scan of aberrated data. Degree of aberration: approximately $\pm 0.36\pi$.

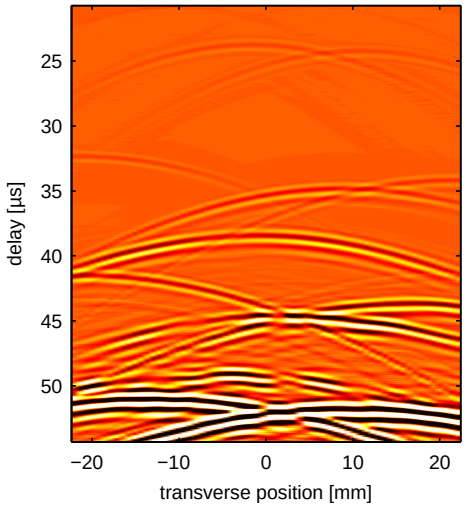

(c) Result of a Radon transform and filtered back-projection used for noise reduction.

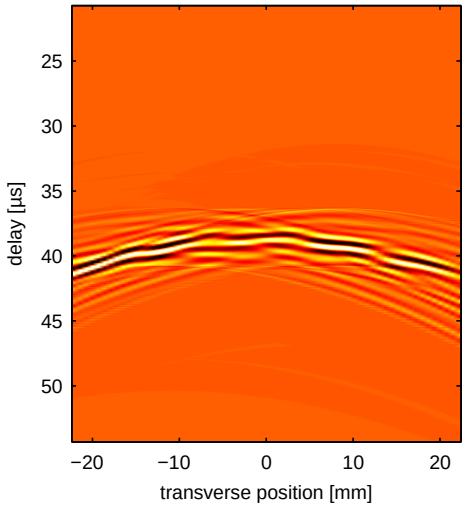

(d) Result of a Radon transform and filtered back-projection used to isolate an aberrated wavefront.

Figure 5.13

- was highly sensitive to motion of the photoacoustic sources between the two acquisitions,
- required a manual compensation for the decrease in illumination intensity as a function of depth,
- did not exploit any apriori knowledge about the absorption spectrum of the optical contrast agent.

Our collaborators, Vincent Jugnon and Habib Ammari of the Department of Applied Mathematics, proposed an algorithm that attempts to alleviate some of these problems.

Basic Target Isolation Algorithm

1. Two sets of two-dimensional data acquired at two different optical wavelength are broken into a number of tiles [6].
2. For each tile, T_1 from data set 1 and T_2 from data set 2:
   a) The data in T_1 and T_2 is re-normalised individually by subtracting the mean of the data.
   b) The data in T_1 and T_2 is rescaled individually by dividing by the standard deviation of the data.
   c) A factor of dissimilarity Q is calculated as $Q = \|T_1 - T_2\|_p$, where $\|x\|_p = \left(\sum_{i=1}^{n} |x_i|^p\right)^{\frac{1}{p}}$ defines the p-norm.
   d) A weight factor W estimating the signal content of the tile is calculated by $W = \|T_1\|_p + \|T_2\|_p$.
3. The map of dissimilarity factors Q is weighted by the map of wight factors W to define a weighted dissimilarity factor map $Q_W = Q\left(W > \widetilde{W}\right)$, where $\widetilde{W}$ is the median of the map of weight factors.
4. The map of weighted dissimilarity factors Q_W is re-normalised by its mean and rescaled with its standard deviation.
5. Q_W is smoothed with a Gaussian blur to remove any sharp transitions and interpolated to the size of the original data sets.
6. A binary mask M is defined by $M = (Q_W > q_{th})$, where q_{th} is a threshold value.

The algorithm thus results in a binary mask that can be used to select the regions of the data that have changed significantly between the two acquisitions.

The algorithm has a number of adjustable parameters:

- size of the tiles

6. The two-dimensional set of data may be for example a B-scan data set or a beamformed image.

- the order p of the norm to use
- the characteristic length scale for the Gaussian blurring
- most importantly the threshold value q_{th} which determines when a difference between two tiles is regarded as significant.

Physical Interpretation of the Algorithm

To the physicist it is instructive to consider an implementation of this algorithm using L_2 norms. Since the square of the L_2 norm is a summation of the squared amplitudes of a signal, the factor of dissimilarity can be understood as

$$Q \propto \sqrt{P_{T_1 - T_2}} \propto \mathrm{rms}\,(T_1 - T_2)\,, \tag{5.23}$$

where P_x is the energy contained in the signal x. Similarly for the weight factor

$$W \propto [P_{T_1} + P_{T_2}] \propto [\mathrm{rms}\,(T_1) + \mathrm{rms}\,(T_2)]\,. \tag{5.24}$$

The quality factor is thus a measure of the energy contained in the difference of T_1 and T_2 while the weight factor is a measure of the total energy contained in tiles T_1 and T_2.

Performance of the algorithm

It was found that by carefully tuning the parameters of the algorithm, a difference between two photoacoustic acquisitions could be extracted fairly reliably. Tile size was not particularly crucial in the majority of applications, but best results were generally achieved with relatively small tile sizes of the order of c/f_c, where c is the speed of sound and f_c the central frequency of the transducer. (See Figure 5.14.)

The most sensitive parameter was found to be the threshold value q_{th} for the binarisation of the mask. It was necessary to adjust this parameter on a case-by-case basis. While this is feasible if the operator can identify the region containing the signals of the target, in highly aberrated case the algorithm could not rely on such user input.

It was found that while the algorithm performs fairly in some situations, it has a number of distinct weaknesses:

1. Any algorithm that relies on the identification of changes between two sets of data is prone to actively select regions of the data where noise dominates. If the two data sets contain only noise or very little signal, step 3 of the algorithm, which intends to deselect regions of the data without significant signal content, still selects half of the tiles due to the use of the median of the weight factors as threshold value.

   A possible improvement to the algorithm would be to use the knowledge of the noise level in the recording to impose an absolute threshold value for step 3 of the algorithm, e.g. using equation (5.14).

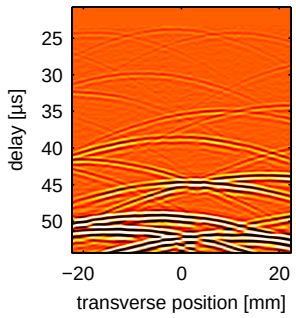

(a) B-scan data of experiment 1 with target

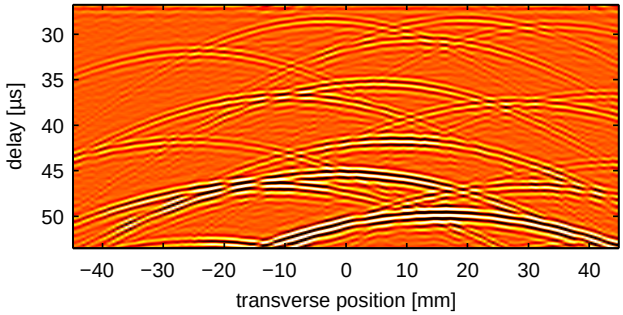

(b) B-scan data of experiment 2 with target

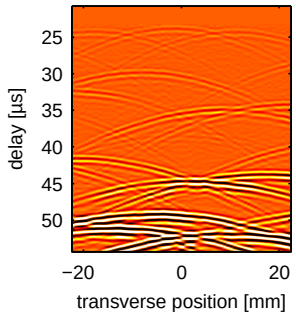

(c) B-scan data of experiment 1 without target

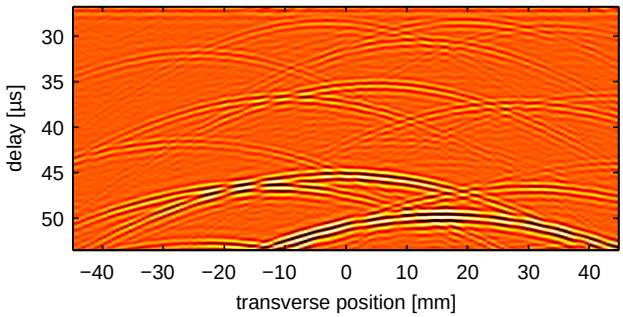

(d) B-scan data of experiment 2 without target

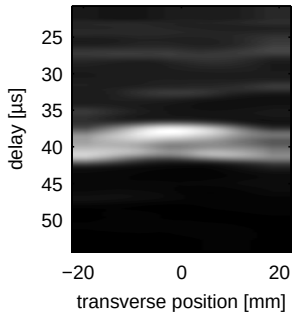

(e) Dissimilarity map Q of experiment 1 with target

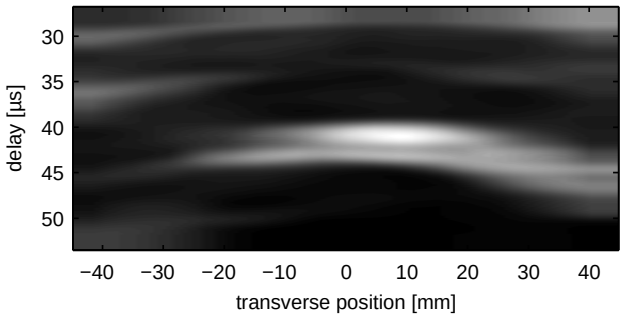

(f) Dissimilarity map Q of experiment 2 with target

Figure 5.14

2. Step 2(b) of the algorithm is very successful for avoiding the need for manual depth correction as was necessary in Chapter 4 on page 75. Unfortunately, if noise in the tiles is negligible and the photoacoustic signals of target does not completely disappear but merely change in amplitude, the rescaling causes the algorithm to detect no appreciable difference between the two signals.

   One method to avoid this effect is to rescale the data in the tiles not by their own standard deviation but by the statistical measures obtained from tiles some distance away. This could allow to rescale the data by the average local illumination intensity, rather than by the intensity of the tile under consideration. - This is a fairly intuitive approach as one looks for tiles that change in energy relative to the surrounding tiles.

3. In Chapter 4 on page 75 it was already mentioned that any algorithm involving a direct subtraction of the signals acquired at the two wavelength is highly sensitive to motion. Step 2(c) of this algorithm still uses a simple subtraction which makes it sensitive to motion - though due to the fact that the difference is limited to tiles, less so than the algorithm used in Chapter 4 on page 75.

   The fact that the algorithm presented here operates on small tiles opens the possibility to translate the tiles relative to one-another to search locally for a relative displacement which results in the lowest value for the dissimilarity factor for a tile.

   Unfortunately while this approach allows to compensate for relative motion of the signals, it does not allow to compensate for slight changes in the geometry of the photoacoustic sources. One approach that may be worth considering is to apply the algorithm to the envelope of the signals in the tiles rather than the signal itself.

4. Finally, if the algorithm is applied to B-scan data, the algorithm suffers from a particularity of the photoacoustic signals: as light intensity increases exponentially as a function of depth, so does the amplitude of the photoacoustic signals generated by optical absorbers. The spherical spreading of the photoacoustic waves then results in the interference of strong photoacoustic signals from shallow absorbers with weak photoacoustic signals from deep absorbers. If the photoacoustic signals from the shallow sources exhibit a large degree of similarity while those from a deep-seated target do not, the tile is not selected by this algorithm.

   In practise this severely limits the applicability of the algorithm *in vivo* since photoacoustic sources are not discrete in this case, resulting in a limiting of the effective aperture over which a focusing law can be ex-

tracted. This effect can be observed in the clipping of the region of dissimilarity on the left in Figure 5.14f on page 111.

The most obvious way to avoid this problem would be to concentrate the energy contained in the waveform originating from a source at a point, i.e. to perform beamforming. For aberrated signals, approximate beamforming would be sufficient for this purpose, under the condition, that the beamforming is a reversible operation. This was one of the driving motivations for the work presented in the preceding section on Radon transformations. An example of the application of the algorithm to filter signals in beamformed space can be found in the following chapter, in particular Figure 6.14a on page 130.

On the Problem of Spectroscopic Approaches

It has been mentioned in the analysis of the experiment presented in Chapter 4 on page 75 that it would be beneficial to exploit the apriori knowledge about the absorption spectrum of the contrast agent attached to the target. It has been shown in Section 2.3 that the photoacoustic pressure is proportional to the absorbed luminous energy

$$p \propto E_{abs} \propto \mu_a I_{light}. \tag{5.25}$$

It may thus appear straight forward to use the photoacoustic signal amplitude to measure the absorption coefficient of the photoacoustic source. - In fact, this is the principle of photoacoustic gas chromatography outlined in the introduction.

The challenge in deep biological tissues arises from the fact, that the local light fluence in depth depends on the optical properties of the medium the light had to traverse to reach the deep location. To illustrate the magnitude of the problem, one may simulate the luminous intensity in a medium consisting of pure water laced with Intralipid resulting in a reduced scattering coefficient of approximately $\mu_s' \sim 8\,\mathrm{cm}^{-1}$ in the diagnostic window. The combination of this scattering which depends only weakly on the wavelength with the absorption coefficient of water results in an effective transport coefficient μ_{eff} which varies significantly as a function of wavelength result in very different local illumination spectra depending on depth as illustrated by Figure 5.15a.

To illustrate the obstacles to implementing spectroscopic approaches deep in biological tissue, a very simple phantom was constructed: four coloured agar-targets were molded into an agar gel phantom with $\mu_s' \sim 8\,\mathrm{cm}^{-1}$. One of the targets was coloured with an India ink solution while the three others were coloured with three different gold nanorod solutions. (The absorption spectra for the gold nanorod solutions are illustrated in Figure 5.15b.)

The phantom was then illuminated at a range of different wavelengths are the amplitude of the photoacoustic signals originating from each of the

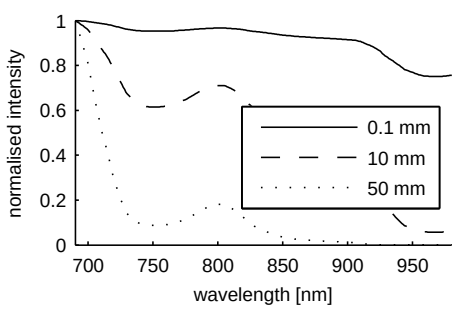

(a) Normalised light intensities in Intralipid/water solution at different depths.

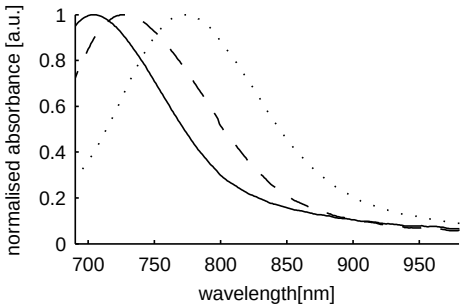

(b) Normalised absorption spectra of three different gold nanorod solutions.

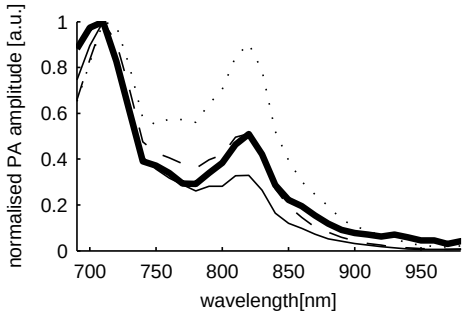

(c) Normalised photoacoustic pressure amplitudes of a black ink solution (in bold) and three gold nanorod solutions.

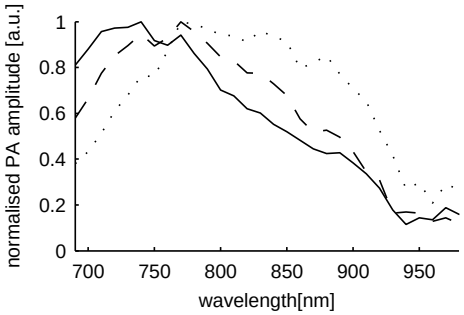

(d) Photoacoustic pressure amplitudes normalised with the pressure amplitude of the black ink target.

Figure 5.15

targets was measured. As can be observed in Figure 5.15c, the photoacoustic amplitude as a function of wavelength is more influenced by the local illumination spectrum than by the absorption spectrum of the targets. This situation changes only, if one uses the target with a black ink solution to estimate the local light intensity and to rescale the photoacoustic amplitudes of the three other targets. The resulting spectra (see Figure 5.15d) resemble much more closely the absorption spectra of the contrast agents used in this experiment.

This experiment illustrates that even in the case of highly idealised phantoms, it is very difficult indeed to measure the absorption coefficient of photoacoustic sources at depths exceeding a few millimetres. Unfortunately, there exist no universal chromophores in the human body that could be used to calibrate the measurement. Methods have been proposed to measure the local light intensity by injecting a known concentration of a contrast agent into the blood stream, e.g. by Rajian et al. (2009). While this approach is intellectually elegant, in practise there are obvious difficulties. To determine the concentration of the injected contrast agent it would be necessary to know the total

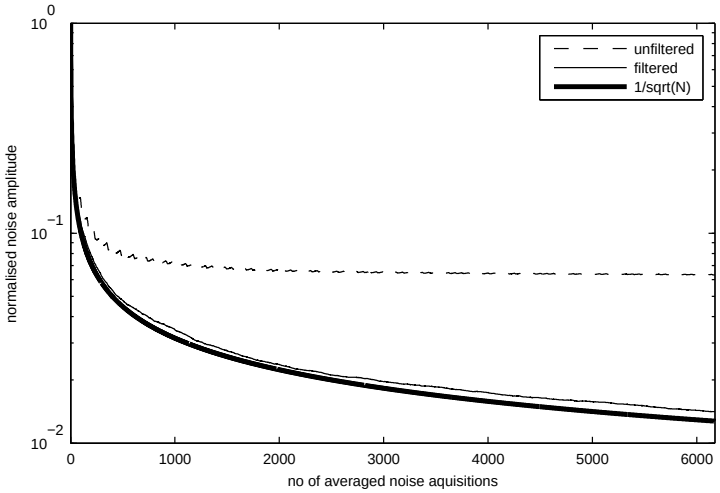

Figure 5.16: Normalised noise amplitude as a function of the number of averaged acquisitions. The bold line shows the theoretically predicted behaviour of the noise amplitude, the dashed line shows the noise amplitude obtained by averaging noise containing a deterministic component.

blood volume of a patient which is all but easy to estimate. Furthermore, the contrast agent would need some time to disperse homogeneously in the body which would make it difficult to make equivalent photoacoustic acquisitions before and after injection. - While these challenges are not insurmountable, they illustrate that even non-quantitative spectroscopy by photoacoustics deep in human tissue is a non-trivial endeavour as will be further illustrated in Chapter 7 on page 135.

5.3 Conclusion

In this chapter, two challenges regarding the processing of photoacoustic signals for guidance of HIFU were explored. With the analysis of the proof-of-concept experiment it has become clear, that the noise level of the recorded data is the limiting factor to the maximum depth from which useful signal can be recovered under optical conditions similar to those in biological tissue.

An analysis of the noise has shown that averaging over multiple acquisitions is an uncomplicated method for noise reduction, provided that the receive sequence is defined to avoid transitory trigger pulses and if a deterministic component due to the internal synchronisation is filtered. Figure 5.16 illustrates this effect: while the average of the noise with deterministic component saturates at the amplitude of this components, the noise with purely random contributions continues with $\sigma_N \propto \sqrt{N}$, where N is the number of averages acquisitions.

Further improvements to the SNR can be achieved with bandwidth filtering. Using the bandwidth of the Imasonic HIFU transducer, the noise power spectral density of the Lecoeur Open System and an assumed $SNR = 1$ for definition of a Wiener filter, the signal-to-noise ration can be improved by approximately 10 dB.

Beamforming with a parametric transformation such as the Hyperbolic Radon transform is of interest for two reasons. Firstly, due to the fact that signals from all transducers are summed, the noise level compared to B-scan space is decreased by a factor of $\sqrt{M}$, where M is the number of channels. This holds whether the medium is homogeneous or aberrating. In the case of a homogeneous medium, the signal amplitude is furthermore increased by coherent summation by a factor of p. By imposing a threshold value $\sigma_{th} = a\,\sigma_W\sqrt{N\,M}$ in beamformed space, the signal-to-noise ratio in B-scan space can be improved dramatically. σ_W is the amplitude of noise in a single-channel, after Wiener filtering, N the number of averaged acquisitions, M the number of channels used for beamforming and a an empirically determined scaling constant.

A second interest of Radon transformation is for isolating the wavefronts corresponding to optically selective photoacoustic sources in a parameter space where the sources energy is concentrated on the smallest possible region of space. This is particularly of interest in the case of aberrating media in which no satisfactory focus can be obtained by traditional focusing. By filtering the signals in beamformed space and inverting the transformation, an optimal focus can be obtained by focusing via time-reversal of the isolated wavefront. It was found however that significant work is still needed to obtain an inversion procedure that is more robust in the case of aberrating media.

A second signal processing challenge for photoacoustic guidance of HIFU is the extraction of photoacoustic sources which are optically selective. While some progress has been made in particular with regards to the problem of inhomogeneous illumination with an algorithm proposed by our collaborators, it has become clear that further work requires a more detailed understanding of the photoacoustic signals arising *in vivo*. The work presented in Chapter 7 on page 135 represents the first steps to establishing this knowledge base with *in vitro* and *in vivo* experiments.

Chapter 6

Photoacoustic Guidance of HIFU

Contents

6.1 Evaluation of Transducer Prototypes

In Chapter 4 on page 75, the photoacoustic signals used to guide ultrasound were detected with a diagnostic ultrasound imaging array. When attempting to translate the method to HIFU ultrasound arrays, care must be taken that three crucial parameters do not deteriorate. The HIFU transducer should be comparable to or better than the diagnostic array with regards to detection sensitivity and bandwidth to ensure that photoacoustic signals can be detected with the new array. In addition however, the HIFU array needs to be able to withstand HIFU energies.

Generally it cannot be assumed that these parameters are comparable in diagnostic and therapeutic ultrasound arrays. Detection sensitivity and bandwidth depend on the construction of the array, in particular on the choice of

piezo-electric material, electrical and mechanical impedance matching as well as transducer backing. The ability to withstand HIFU energies is typically limited in diagnostic arrays by poor evacuation of the waste heat dissipated in the transducer during the HIFU procedure.

Over the course of the work for this thesis, two transducer prototypes attempting to satisfy the specific requirements of photoacoustically guided HIFU were developed and evaluated independently in cooperation with Vermon, France, and Imasonic, France. These prototypes were transducers with elements of the same dimensions as the intended final array but with a lower number of active elements. In the case of the Vermon transducer, an array with 16 elements was provided while for the Imasonic prototype, only 8 elements of a 128-element array were connected.

Reception Characteristics

The bandwidth and sensitivity of transducers is generally measured by exciting a transducer with a short pulse and detecting the reflection from an acoustic reflector. The figures for these parameters given in data sheets are therefore derived from measurements resulting from the convolution of emission impulse response and reception impulse response. For the purposes of photoacoustic detection however, only the reception impulse response comes into play. To reliably compare transducers, the reception impulse response alone should be used.

Unfortunately this not a trivial endeavour since a wide-bandwidth acoustic source of known properties is required. One method for calibrating hydrophones is therefore to excite a layer of optically absorbing medium. Given the optical properties of the medium and the parameters of illumination, the theory of photoacoustics presented in Section 2.3 allows to predict the photoacoustic wave generated which may then be compared to the signals detected. Unfortunately, this method of calibration is limited to non-focused or plane transducers.

The transducer prototypes we evaluated were cylindrically focused linear arrays. To avoid convolving the shape of the acoustic signal incident on the transducer surface with a possibly complicated spatial impulse response, the signals used for calibration need to originate from a point where the spatial impulse response of the transducer approaches a Dirac function. For focused transducers this condition is satisfied if the signals appear to originate from the focus of the transducer. In this case, when impacting on the transducer surface, the wavefronts have the same radius of curvature as the transducer surface.

The transducer reception impulse responses were compared as follows. A small lead sphere, approximately $1 - 2\,\mathrm{mm}$ in diameter, was suspended on a nylon wire in an aquarium filled with an optically scattering solution with $\mu_s' \approx 9\,\mathrm{cm}^{-1}$ and illuminated at a depth of a few centimetres with laser pulses

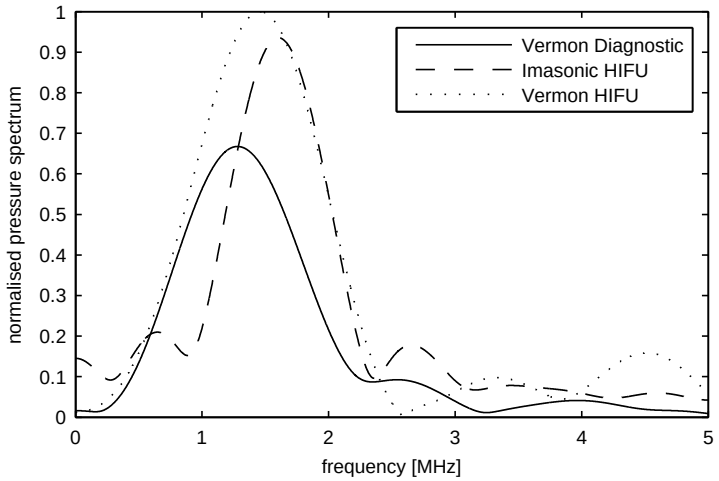

Figure 6.1: Comparison normalised pressure spectra of two HIFU prototype transducers with a diagnostic transducer.

with an energy of approximately 130 mJ. The photoacoustic signals generated were detected with the transducer to be tested. To ensure optimal positioning of the transducer with respect to the photoacoustic source, the amplitude of the photoacoustic signals were maximised by adjusting the positioning of the transducer in three dimensions.

The photoacoustic waves generated by the lead sphere are detected as signals with the following parameters on the three transducers [1]:

Vermon Diagnostic Probe: central frequency $f_c = 1.30\,\text{MHz}$, $-6\,\text{dB}$ reception bandwidth $f_c \times 86\%$, relative maximum sensitivity $0\,\text{dB}$

Vermon HIFU Prototype: central frequency $f_c = 1.44\,\text{MHz}$, $-6\,\text{dB}$ reception bandwidth $f_c \times 82\%$, relative maximum sensitivity $+3.5\,\text{dB}$

Imasonic HIFU Prototype: central frequency $f_c = 1.61\,\text{MHz}$, $-6\,\text{dB}$ reception bandwidth $f_c \times 55\%$, relative maximum sensitivity $+2.9\,\text{dB}$

These figures are not guaranteed to be a good estimate of the true frequency response of the transducer since the excitation spectrum generated by the lead sphere is unknown. However, since lead is a metal, the lumious energy is absorbed in a thin shell given by the skin-depth of lead. This can be expected to result in the generation of photoacoustic signals with a maxiumum spectral energy density at very high frequencies compared to the characteristic frequencies of the transducers under investigation. The photoacoustic signals generated by the lead sphere are therefore expected to exhibit a fairly flat spectrum over the range of frequencies of interest in this experiment - in which case a reasonable estimation of the reception characteristics of the

1. The design specification of the transducers are described in section 3.4 on page 72.

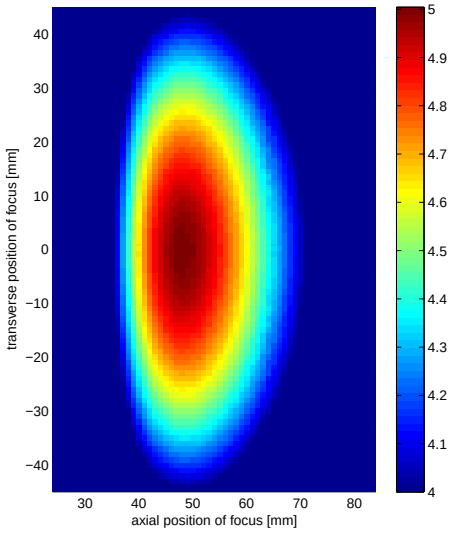

(a) Maximum linear pressure a function of focus position. The colorspace is limited below at 4 MPa to indicate the approximate useful steering range. Scale: MPa

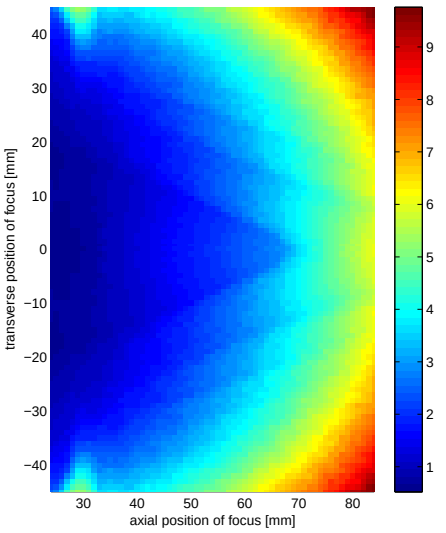

(b) Simulation of the −3 dB cross-section of the focus spot. Scale: mm^2

Figure 6.2: Simulation of key characteristics of the pressure field of the final transducer.

transducers should be obtained by the experiment. At the very least however, the experiment allows a relative comparison of the transducers reception characteristics.

The transducer's directivity on emission and reception, and thus the geometric region in which it can be used, is primarily governed by the size of the transducer elements. A design decision was made not to exceed an element width of $\lambda/2$ which was known to afford a sufficient range of steering at a depth of several centimetres. 1 MHz was considered to be the characteristic frequency of interest in any photoacoustic HIFU experiments and thus the definition of λ. There are several reasons for this choice:

1. The author was interested in developing a method for treating tumors that have not yet reached a stage at which conventional treatment procedures are considered effective or beneficial. A typical tumor size of 1.5 mm was therefore assumed which leads to photoacoustic signals with a maximum spectral energy density at approximately 1 MHz.
2. For lower frequencies, it is difficult to achieve a sufficiently high antenny gain at the focus. The risk of collateral damage on the beam path during the HIFU procedure becomes non-negligible.
3. For higher frequencies, ultrasound absorption in tissues increases signifi-

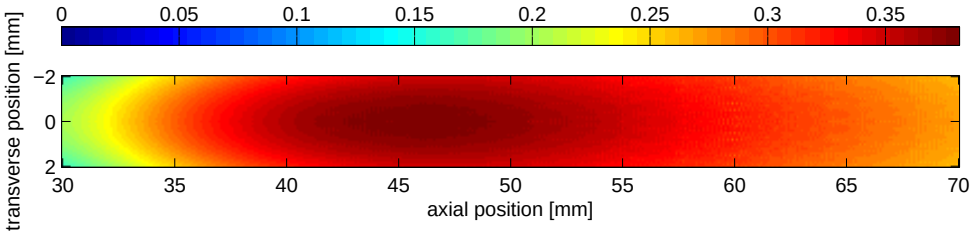

(a) Plane wave excitation 8-element prototype transducer. Scale: MPa

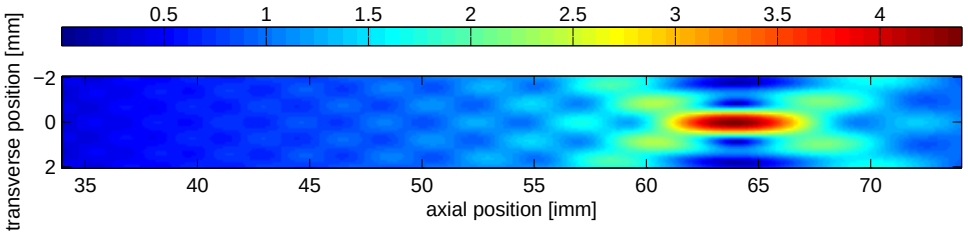

(b) Focused excitation 128-element final transducer. Scale: MPa

Figure 6.3: Simulation of the linear pressure fields of the prototype and the final transducers.

cantly which in turn increases the risk of superficial burns during HIFU treatment.

As a consequence, a maximum pitch of 0.7 mm at a minimum element number of 128 was made a design requirement. For an estimate of the resulting useful steering range of a typical transducer please refer to Figure 6.2 [2].

Heating Characteristics

During the design of the prototype transducers it was specified that a thermocouple be included close to the active elements to allow monitoring the evolution of the temperature within the transducer during HIFU procedures. By imposing a safe temperature limit, accidental thermal damage to the transducer can be avoided. Unfortunately, during construction of the Vermon HIFU prototype, it was neglected to include the thermocouple. There was therefore no non-destructive way to test that Vermon prototype transducer was conform to specifications. Given that the reception characteristics of the Imasonic HIFU prototype were comparable to those of the Vermon HIFU prototype, the remaining investigation concentrated on the first.

At the time of the evaluation of the transducer prototypes, no suitable HIFU time-reversal electronics but only a single-channel high-power amplifier was available. To attempt to predict the HIFU performance of the transducer,

2. The absolute pressure values are derived from the experiments described in the following section.

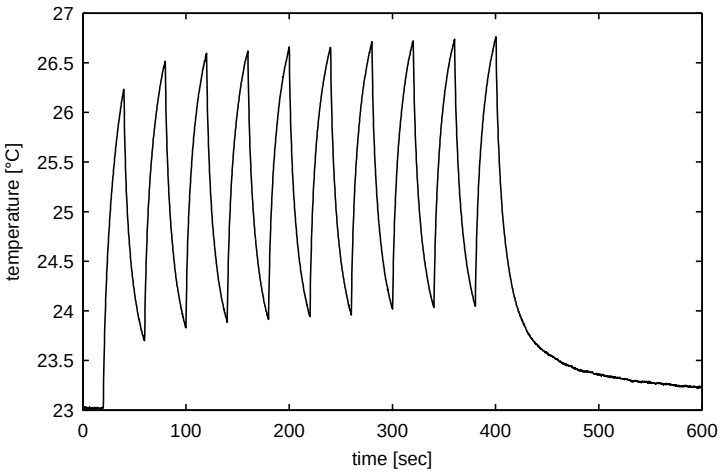

Figure 6.4: Temperature in the Imasonic prototype transducer for 10 cycles of 20 s on, 20 s off.

the field of the prototype transducer and the field of the hypothetical final transducer were simulated using the software Field II under the assumption that the individual transducer elements behaved identically in the two cases. (See Figure 6.3.)

For the case of the 8-element prototype transducer it was assumed that all elements would be connected in parallel to the single-channel amplifier resulting in a plane wave excitation. For the case of the hypothetical 128-element final transducer, it was assumed that a time-reversal electronics would be used to electronically focus the array at the depth of the geometric elevation focus. Comparison of the simulation results of the two cases allowed to determine which pressure value of the prototype transducer would allow to generate approximately 4.5 MPa with the final array. It was assumed that a linear pressure of 4.5 MPa would lead to a non-linear pressure greater than 5 MPa which is known to be sufficient to necrose tissue in a few seconds.

The prototype transducer was then driven at its central frequency of approximately 1.5 MHz with the single-channel amplifier to produce a pressure equivalent to that necessary to obtain 4.5 MPa with the final array. The duration of excitation was varied and the temperature in the transducer recorded with the thermocouple. As can be seen in Figure 6.4, even during 20 cycles of 20 seconds on, 20 seconds off, the temperature in the transducer stayed well below the limit of 65°C specified by the manufacturer. While the heat produced by a 128-element array would be 16 times larger, the rate of cooling increases with increasing internal temperature. Even if the temperature elevation were proportional to the total heat produced, a heating by 3°C with 8 elements would correspond to a temperature elevation of only 48°C which appeared manageable by active cooling if necessary.

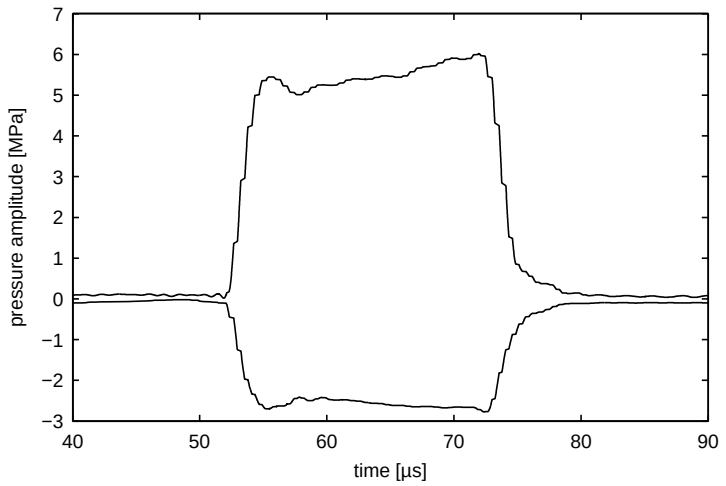

Figure 6.5: Pressure amplitude of the Imasonic HIFU transducer.

Conclusion on HIFU Prototype Transducers

The larger elevation of the HIFU prototype transducers compared to the diagnostic transducer appears to have resulted in a large sensitivity on reception. Furthermore it was found that the reception bandwidths of the HIFU prototype transducers were comparable to that of the diagnostic transducer. Even though the reception impulse response of the Vermon prototype would allow easier detection of photoacoustic structures larger than 1 mm which would be advantageous for tumour detection, it was chosen to pursue the option offered by Imasonic due to the fact that the HIFU compatibility of the Vermon HIFU prototype could not be verified at this stage.

6.2 Characterisation of the Imasonic Transducer

After connection of all 128 elements of the Imasonic HIFU transducer, it was verified that none of the parameters had deteriorated appreciably and that the final transducer was able to withstand the energies necessary for HIFU procedures.

Pressure & Thermal Characteristics

The transducer was excited at a voltage that resulted in a peak positive pressure of 5 MPa at the focus of the transducer for a duration of a few tens of microseconds. (See Figure 6.5.) After removing the hydrophone[3] to avoid damage, the temperature rise in the transducer was then measured using the

3. Hydrophone: HNA-0400 by Onda Corporation, Ca, USA.

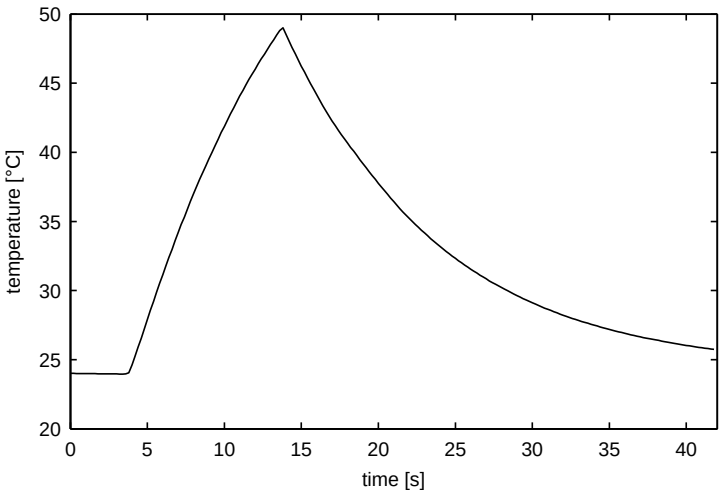

Figure 6.6: Temperature rise in the Imasonic HIFU transducer for 5 MPa at the focus.

built-in thermocouple as a function of time to verify that exposures of several seconds were feasible. Figure 6.6 shows that even for an exposure of 5 MPa the temperature in the transducer does not reach the damage threshold of 65°C recommended by the manufacturer.

Assuming constant heating due to the dissipation of power in the transducer and Newtonian cooling, the rate of temperature change is given by

$$\frac{dT}{dt} = -G_{th}\left[T\left(t\right) - T_a\right] + \frac{1}{C}P_{diss}, \tag{6.1}$$

where $T\left(t\right)$ denotes the temperature as a function of time, T_a the ambient temperature, G_{th} the thermal conductance, C the heat capacity of the transducer and $P_{diss} = RV^2$ is the electrical power dissipated in the transducer. It can be shown that the evolution of temperature is thus given by

$$T\left(t\right) = T_{eq} + \left[\left(T_0 - T_a\right) - \frac{1}{C\,G_{th}}P_{diss}\right] e^{-\frac{1}{G_{th}}t}, \tag{6.2}$$

where $T_{eq} = T_a + \frac{1}{C\,G_{th}}P_{diss}$ is the equilibrium temperature and T_0 the temperature at t_0, the time of the beginning of the heating.

If heating dominates, i.e. $T_0 - T_a \ll \frac{1}{C\,G_{th}}P_{diss}$ or equivalently $T_0 \ll T_{eq}$, the evolution of temperature may be approximated by

$$T\left(t\right) = T_a + \frac{1}{C\,G_{th}}P_{diss}\left(1 - e^{-\frac{1}{G_{th}}t}\right). \tag{6.3}$$

If additionally the heating is short compared to the characteristic time scale of cooling, i.e. $G_{th}t_{heating} = o\left(1\right)$, this may be further simplified to

$$T\left(t\right) = T_a + \frac{1}{C}P_{diss}t. \tag{6.4}$$

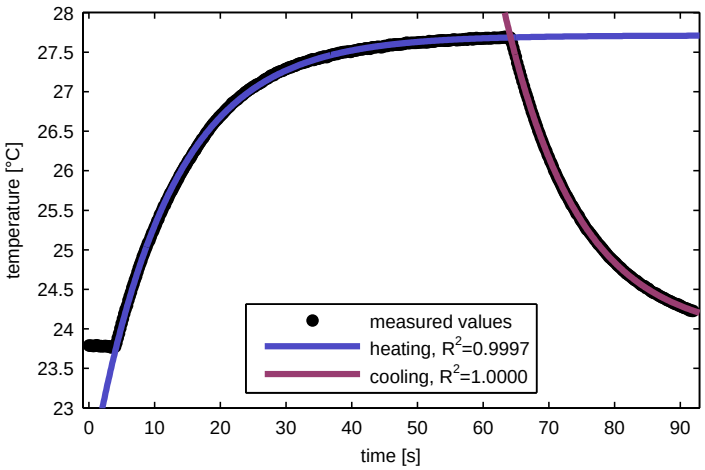

Figure 6.7: Fitting of constant heating and Newtonian cooling to temperature evolution in the Imasonic HIFU transducer. Heating for 60 s at 5 V.

If however cooling dominates, i.e. $T_0 - T_a \gg \frac{1}{C G_{th}} P_{diss}$ or equivalently $T_0 \gg T_{eq}$, the evolution of temperature may be approximated by

$$T(t) = T_{eq} + (T_0 - T_a)\, e^{-\frac{1}{G_{th}} t}. \tag{6.5}$$

Using a moderate excitation of the transducer to ensure that heating occurs on a time scale longer that the characteristic time scale of cooling, one can try to estimate the values for G_{th} and $\frac{1}{C} P_{diss}$. One fit of above heating equations to a set of temperature measurements is shown in Figure 6.7. In a large number of different experiments it was found that $G_{th} = 0.08825\,\mathrm{s}^{-1}$. It follows that the characteristic time scale for cooling of the transducer is $1/G_{th} \approx 11\,\mathrm{s}$.

By fitting the heating equations to the temperature evolution for different voltages, it is possible in principle to measure a value for R/C which in combination with the voltage would allow to predict the heating of the transducer for any type of HIFU sequence. Unfortunately, during the experiments it was found that the nominal voltage set on the amplifier of the Supersonic Imagine brain therapy system is unreliable. On three different days, the acoustic pressures at focus as well as the heating of the transducer varied for a given voltage by 100%. However, it could be shown that during a single day, $\frac{1}{C} P_{diss} \propto V^2$ (with a coefficient of determination $R^2 = 0.9999$) as would be expected. This suggests that once the issue with the amplifier is resolved, the temperature elevation in the Imasonic HIFU transducer can be reliably estimated. Depending on day, R/C was of the order of $0.015\,\mathrm{K\ V^{-2}\ s^{-1}}$.

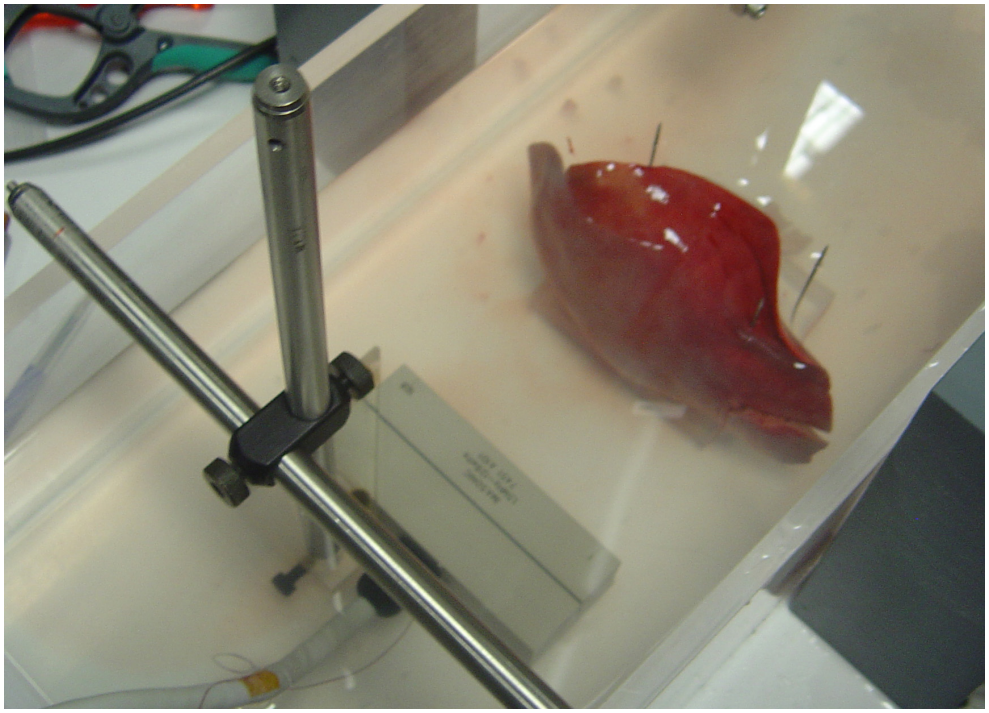

Figure 6.8: Veal liver held in front of the Imasonic HIFU transducer.

Ability to Necrose Tissue

Having confirmed that the transducer can produce 5 MPa at the focus and that its temperature stays within operating conditions, it was verified that biological tissue could be necrosed. To do so, pieces of veal liver and chicken breast were fixed in front of the transducer and the transducer focused close to the surface of the tissue as can be seen in Figure 6.8. Several lesions were produced, each within a few seconds. Examples of the lesions are shown in Figure 6.9.

6.3 Photoacoustic Guidance of HIFU

To demonstrate that photoacoustic signal can indeed be used to guide HIFU-mode ultrasound the following experiment was conducted: First, the photoacoustic signals from a phantom were acquired as in Chapter 4 on page 75 and the target's signature extracted. The signals from the target were then used to focus HIFU on an acrylic glass plate which produced a lesion that could be detected by echography. By comparing the position of the lesion with the position of the photoacoustic target, it was confirmed that photoacoustic signals can be used to guide HIFU.

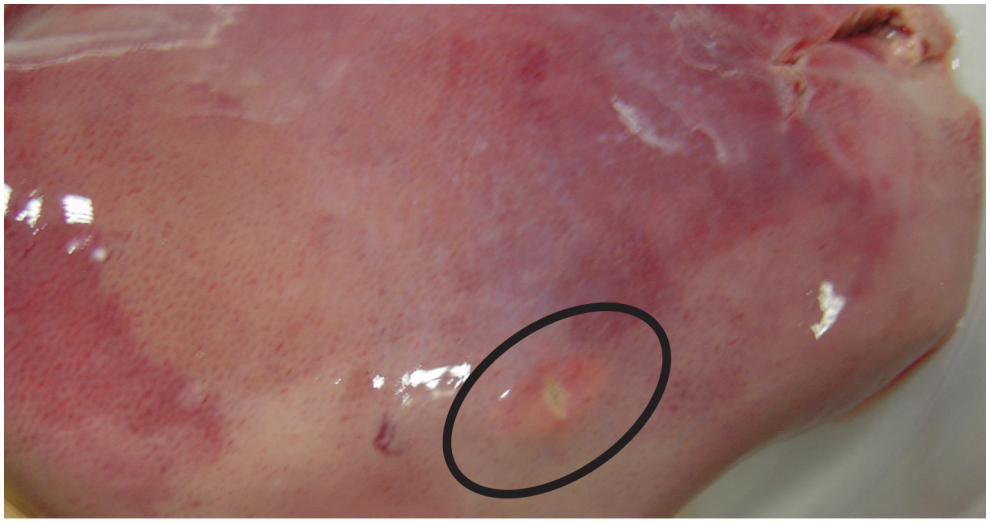

(a) Image of several HIFU lesions side by side just below the surface of a veal liver.

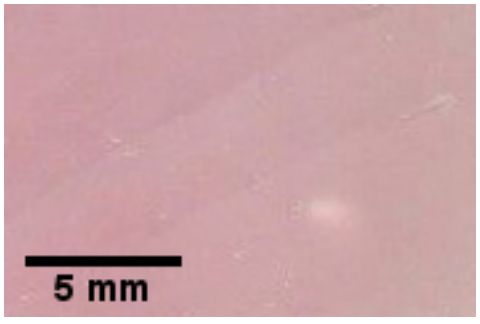

(b) Transverse cut through a single lesion in chicken breast.

(c) Longitudinal cut through a single lesion in chicken breast.

Figure 6.9: Lesions produced in fresh tissue by the Imasonic HIFU transducer.

Photoacoustic Acquisition

The experimental setup used for the first stage of the experiment, the acquisition of the photoacoustic signals, was very similar to the experimental setup described in section 4.2 on page 78. It is illustrated by Figure 6.10.

As before, the phantom consisted of a set of PVC tubes distributed quasi-randomly over an area of approximately 50 mm × 80 mm. All tubes but one were filled with a black ink solution with an absorption coefficient of $\mu_a\,(\lambda_{1=700\,\mathrm{nm}}) = 9.4\,\mathrm{cm}^{-1}$ and $\mu_a\,(\lambda_{2=750\,\mathrm{nm}}) = 8.8\,\mathrm{cm}^{-1}$. One of the tubes was filled with a green ink solution with an absorption coefficient $\mu_a\,(\lambda_{1=700\,\mathrm{nm}}) = 10.4\,\mathrm{cm}^{-1}$ and $\mu_a\,(\lambda_{2=750\,\mathrm{nm}}) = 0.4\,\mathrm{cm}^{-1}$. The set of tubes was immersed in an aquarium filled with a dispersion of 1 µm-sized polystyrene spheres which had a reduced scattering coefficient of $\mu_s' = 9.0\,\mathrm{cm}^{-1}$. The "target tube" filled with green ink was positioned 4 cm from the aquarium wall and 6 cm from the

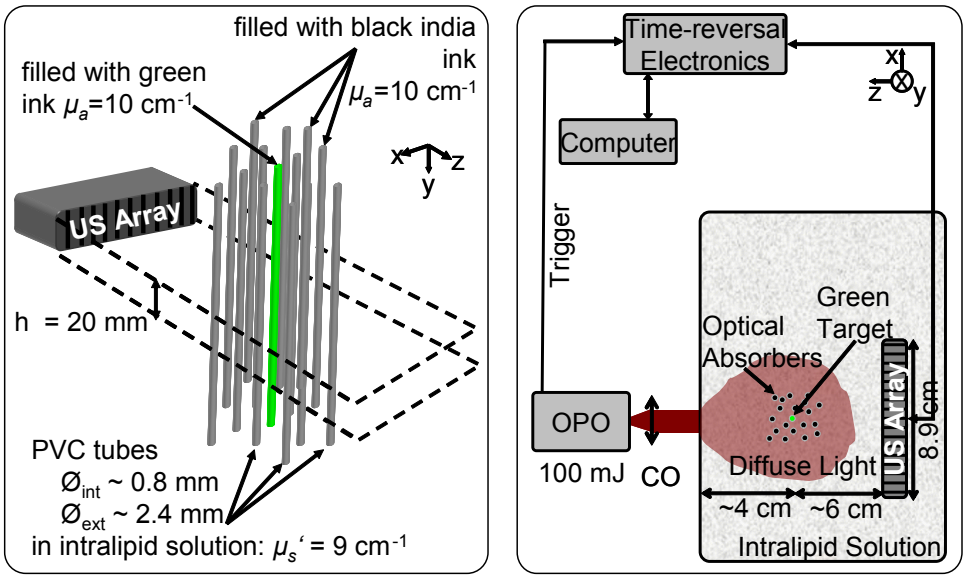

(a) (b)

Figure 6.10: Experimental setup used the acquisition of the photoacoustic signals.

ultrasound array. It was illuminated from one side with light pulses from an OPO and the photoacoustic signals were recorded on a linear array from the opposite side.

The phantom was illuminated with a collimated but otherwise unmodified beam from the OPO with a diameter of approximately 1 cm with pulses of the order of 100 mJ. The signals were detected with the Imasonic HIFU transducer and acquired on the Lecoeur time-reversal electronic with a channel multiplexer to allow acquisition on all 128 elements of the transducer. As before, the Lecoeur Open System time-reversal electronics was operated as a slave controlled by the Q-Switch trigger of the Surelite II-10.

Denoising and Target Isolation

The signals from 100 acquisitions were averaged (Figure 6.11) and bandwidth-filtered (Figure 6.12) with a Wiener filter defined with a hypothetical $SNR = 3$ of the unaveraged signals. The signals were then beamformed with a hyperbolic Radon transformation (Figure 6.13) and a regions with a large degree of dissimilarity in the envelope of the Radon transform identified using the algorithm presented in Section 5.1.

From this dissimilarity map a binary mask was derived and applied to the Radon transform of the set of signals containing the photoacoustic signals of

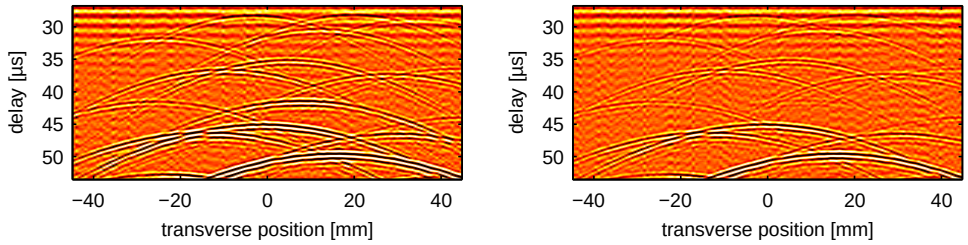

(a) $\lambda_1 = 700\,\mathrm{nm}$ (b) $\lambda_2 = 750\,\mathrm{nm}$

Figure 6.11: Photoacoustic B-scans of the phantom. Colour bar limits: ± 0.3 device units

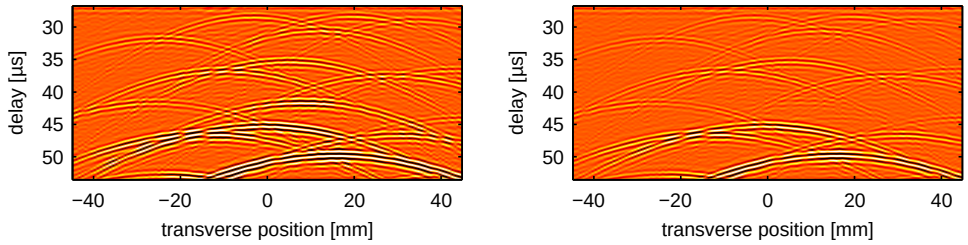

(a) $\lambda_1 = 700\,\mathrm{nm}$ (b) $\lambda_2 = 750\,\mathrm{nm}$

Figure 6.12: B-scans of the filtered photoacoustic signals of the phantom. Colour bar limits: ± 0.3 device units

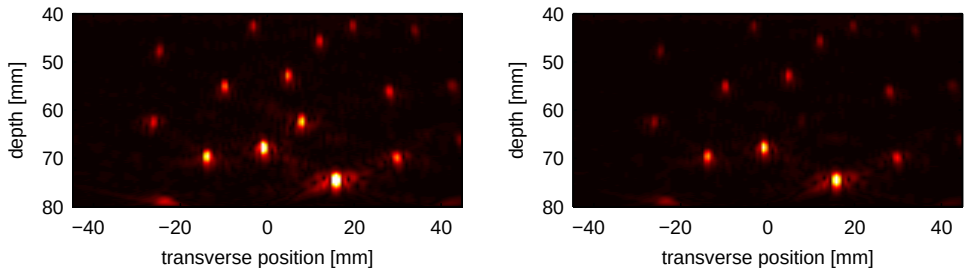

(a) $\lambda_1 = 700\,\mathrm{nm}$ (b) $\lambda_2 = 750\,\mathrm{nm}$

Figure 6.13: Radon transforms of the filtered photoacoustic signals of the phantom. The images are plotted with identical linear colour scales.

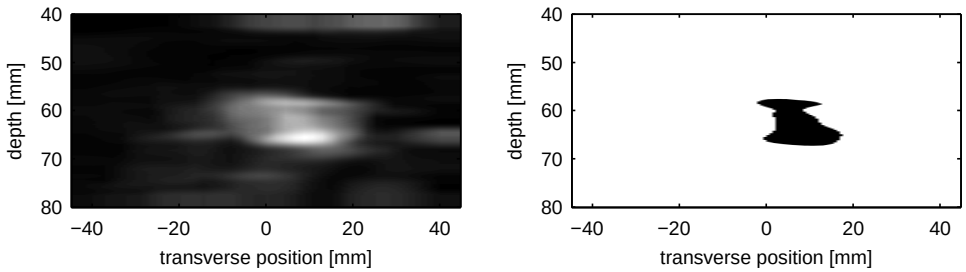

(a) Dissimilarity map of the photoacoustic signals in Radon space.

(b) Mask applied in Radon space to isolate the signals of the target.

Figure 6.14

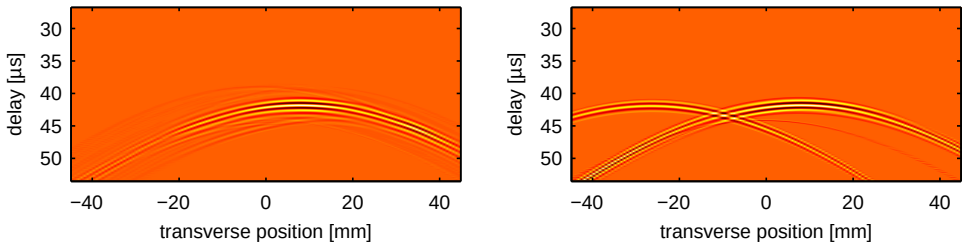

(a) Isolated photoacoustic signals of the target.

(b) Photoacoustic signals of the target and one "background tube".

Figure 6.15

the target [4]. (Figure 6.14) The masked Radon transform was then reversed by filtered back-projection to obtain a B-scan data-set containing only the information needed to focus on the target tube [5]. (Figure 6.15a)

As an alternative, a second mask was developed by hand selecting all photoacoustic signals originating from a 10 mm slice centred on the depth of the target tube. The resulting B-scan data contained the photoacoustic waveforms from the target tube and one background tube. (Figure 6.15b)

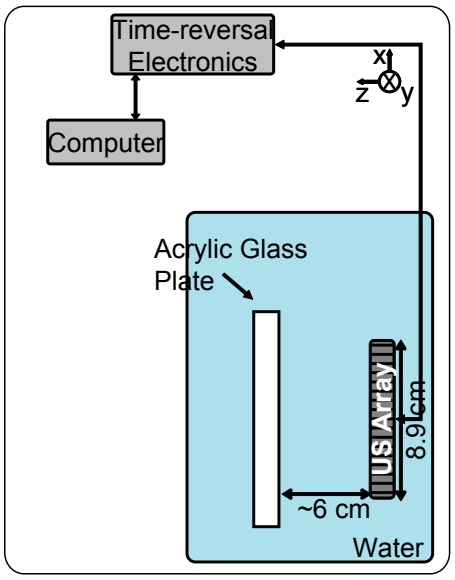

Figure 6.16: Basic experimental setup used for the work for this thesis.

Photoacoustic Guidance of HIFU by Time-Reversal

To verify that HIFU can indeed be guided by photoacoustic signals, it was attempted to demonstrate that the positions of lesions produced under photoacoustic guidance correspond exactly with the positions of the optical target. This is most easily achieved, if the lesions can be imaged by echography with the HIFU transducer. A material that allows doing so is acrylic glass which heats significantly under HIFU exposure, resulting in the formation of internal gas bubbles which cause the surface of the acrylic glass exposed to HIFU to bulge outward towards the transducer.

A acrylic glass plate was thus placed at the position of the target (see Figure 6.16) and exposed to two HIFU sequences guided by time-reversal of two different sets of photoacoustic signals. The first set of photoacoustic signals are the isolated signals of the target. Figure 6.17a is a beamformed image of the difference of the pulse-echo signals of the surface of the acrylic glass plate before and after HIFU exposure. Comparison with Figure 6.17a clearly shows that a single lesion is produced at the position of the photoacoustic target[6].

4. At the time of the experiment, the threshold applied to the dissimilarity map to create the binary mask was set manually. However, an algorithmic determination of the threshold based on the statistics of the dissimilarity map can be imagined.

5. Beyond the application of a binary mask in Radon space, no noise thresholding was applied. The noise reduction stems from the fact that in Radon space, the noise is spread over a very large region and is thus filtered to a large degree by the binary mask before inversion.

6. Please note that because the "lesions" discussed in this section are surface defects of

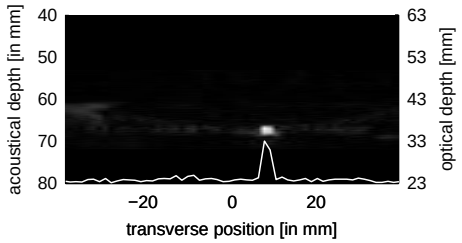

(a) Echography of lesion produced with HIFU guided by the isolated signals of the target.

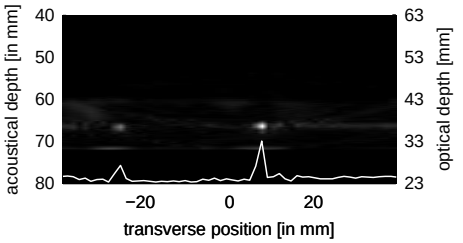

(b) Echography of the lesions produced with HIFU guided by all photoacoustic signals originating from the depth of the target.

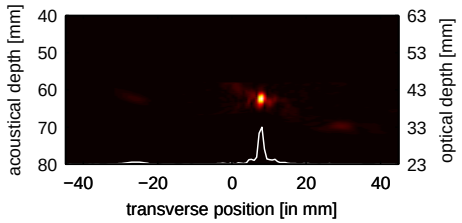

(c) Beamformed image of the isolated photoacoustic signals of the target.

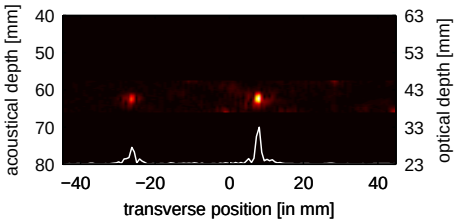

(d) Beamformed image of the photoacoustic signals originating from the depth of the target at 700 nm.

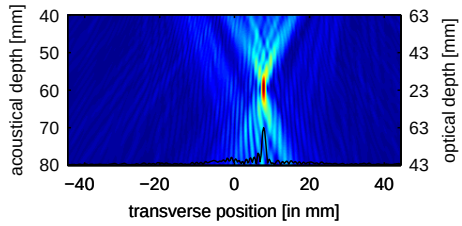

(e) Simulation of the intensity of the HIFU field when guided by the isolated photoacoustic signals of the target.

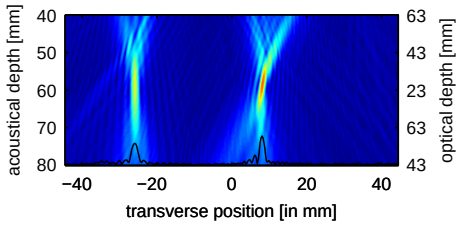

(f) Simulation of the intensity of the HIFU field when guided by all photoacoustic signals originating from the depth of the target. Note: all scales are identical to those of Figure 6.17e.

Figure 6.17

The second set of photoacoustic signals comprised the signals from all photoacoustic sources located in a 10 mm slice containing also the target acquired at 700 nm. More specifically it contains the signals of the target as well as the signals from one non-specific absorber. (See Figure 6.17d.) Figure 6.17b, the beamformed image of the difference of the pulse-echo signals of the surface of the target shows that two lesions are produced. Visual observation during the heating showed that both lesions formed simultaneously. A simulation of the acoustic intensity of the HIFU beam resulting from the two sets of photoacoustic signals is illustrated in Figures 6.17(e,f).

The fact that two lesions can be produced simultaneously at a significant distance from one another is due the particular geometry of the HIFU transducer used. In this experiment a linear HIFU array was used with elements small enough to allow the steering of the HIFU beam over a wide range of angles in the transverse plane. In general, HIFU transducers are single element transducers producing a lesion at a fixed position defined by the geometry of the transducer. However, even time-reversal arrays for therapeutic ultrasound consisting of a large number of transducers generally cannot be steered as the array used in this experiment. For example, the array used by Pernot et al. (2007) for HIFU brain therapy uses a number of plane mono-element transducers distributed over a hemi-sphere. However, since the individual transducers making up the array are large compared to the ultrasonic wavelength, the transducers are fairly directional. As a result, the array can be steered only in a small volume surrounding the geometric centre of the hemisphere.

The reason that generally large individual transducers are chosen is that the energy per surface area is a limiting factor in current HIFU technology. If the size of the individual transducers were to be reduced, a larger number of transducers would have to be used. As a result the therapeutic array would become significantly more expensive to operate as time-reversal electronics with a larger number of electronic channels would be needed. At present, time-reversal electronics with more than approximately 1000 individual channels are too expensive to consider.

6.4 Conclusion

Bossy et al. (2006) had shown that it was possible to focus ultrasound on an optical contrast. One of the great uncertainties at the outset of the work for this thesis was whether this finding would translate to HIFU-compatible devices. While in the design of HIFU transducers heat dissipation is a major consideration, factors such as bandwidth and receive sensitivity are generally not considered. The results presented in this chapter demonstrate that with purpose-built transducers it is possible to detect weak photoacoustic signals

an acrylic glass plate, no conclusions may be drawn from the volumetric shape of their echographic image. Only their positions relative to the transducer are significant.

and emit HIFU ultrasound with the same transducer. This is essential if HIFU is to be guided by time-reversal of photoacoustic waves but also simplifies focusing with traditional methods and treatment monitoring as the reference frames for therapeutic and diagnostic ultrasound are identical.

By demonstrating that there are no insurmountable technological obstacles to the implementation of photoacoustic guidance of HIFU, the results presented in this chapter open the door to further investigations into the remaining challenges.

Chapter 7

Towards *in Vivo* Applications

Contents

Chapters 4 to 6 have focused on developing solutions for some of the technological challenges for photoacoustic guidance of HIFU. However, the additional difficulties introduced by biological samples have been mentioned only in passing. This chapter presents some of the attempts that have been made in translating the method from academic phantoms to *in vivo* applications.

One of the fundamental assumptions of photoacoustic guidance of HIFU as presented in section 1.3 on page 22 is that an optical contrast exists between tumorous and healthy tissue. While it is known that such a contrast exists naturally in many cases due to the increased vascularisation of tumorous tissue, for photoacoustic guidance, it is likely that only exogenous contrast agents attached to the tumour will allow precise discrimination between the photoacoustic signals of the target and those of the natural photoacoustic background.

Three groups of the Institut Curie, specialising in medical and physical chemistry, developed in close collaboration biologically compatible, vectorised, optical contrast agents specifically for photoacoustic guidance of HIFU. Over the course of the work for this thesis the development of these contrast agents was supported and the performance of the various compounds evaluated.

7.1 Development of Contrast Agents

As has been shown in Section 2.1, there are numerous endogenous chromophores present in tissue. As a result, many tissue structures generate photoacoustic signals - a fact that is exploited by photoacoustic imaging methods. For the purposes of guiding HIFU however, it has been shown in chapters 4 and 6 that isolation of the photoacoustic signals of the target is crucial to avoid inflicting collateral damage to surrounding tissue.

The approach explored over the course of the work for this thesis was to attempt to discriminate between the photoacoustic signals of the target and those of other tissue structures by using an exogenous, spectrally selective optical contrast agent. The development of suitable contrast agents was begun in collaboration with three research groups from the Institut Curie. The Medicinal Chemistry Unit was responsible for the synthesis and functionalisation of molecular contrast agents, the Physical Chemistry Unit for the synthesis of plasmonic structures and the Intracellular Traffic, Signalling and Delivery Group provided a universal vector for targeting the contrast agents.

Choice of Contrast Agents

The difficulty of spectroscopic signal extraction deep in biological tissue, as outlined in Section 5.2, suggests the use of a contrast agent with a very steep absorption profile. This would ensure that the local light intensity as well as the absorption coefficient of the endogenous contrasts do not change appreciably between the two photoacoustic acquisitions at different optical wavelengths. Any change in the photoacoustic signal would therefore be due to the presence of a exogenous contrast agent.

Unfortunately, in the near-infrared the choice of biologically compatible optical contrast agents is fairly limited. The contrast agents that were considered can be divided into two groups: plasmonic structures and molecular dyes which were generally developed as fluorescent probes.

Figure 7.1 provides an overview of the absorption spectra of the different near-infrared contrast agents investigated. The primary selection criteria was an absorption peak between 700 and 900 nm. The molecular contrast agents considered were therefore the commercial fluorescence probe Alexa 750, Indocyanine Green (ICG), several squaraines (KSQ) and Naphtol Green. Also considered were plasmonic structures in gold, in particular gold nanorods.

To facilitate the selection of the most promising contrast agents, a figure of merit based on the spectral characteristics of the different compounds was calculated as per the formula,

$$\text{merit} = \frac{(1-\Phi)\,\epsilon}{\min\left(\lambda_{HWHM}\right)^2} \propto \frac{\text{energy lost by non-radiative relaxation}}{\left(\text{width of spectrum}\right)^2}, \quad (7.1)$$

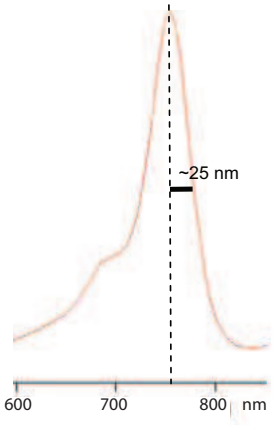

(a) Alexa Fluor 750. Illustration: Bhattacharyya et al. (2008)

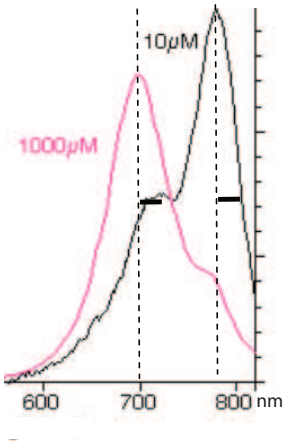

(b) Indocyanine Green. Data: Prahl (1999)

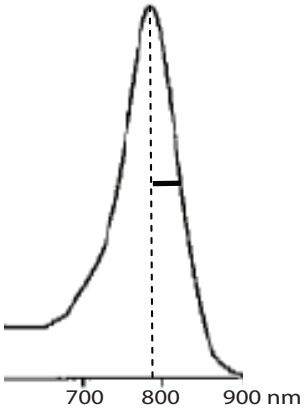

(c) KSQ-4. Illustration: Umezawa et al. (2008)

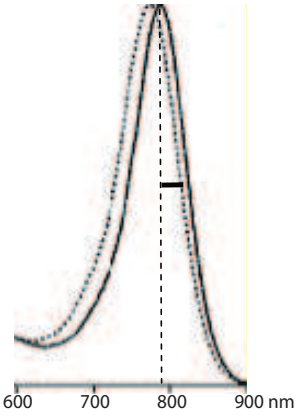

(d) KSQ-4-H. Data: Umezawa et al. (2008)

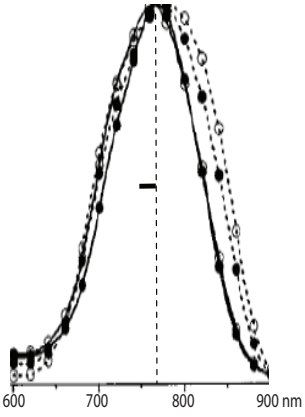

(e) KSQ-3. Illustration: Umezawa et al. (2008)

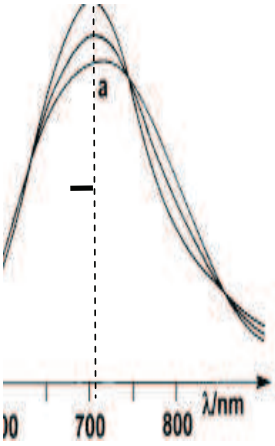

(f) Naphtol Green. Data: Kunkely and Vogler (2003)

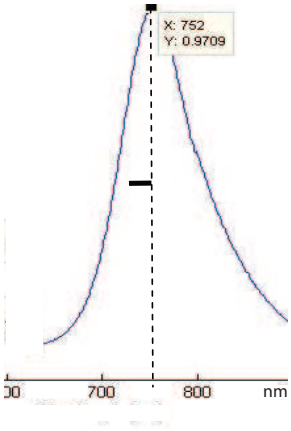

(g) Nanopartz gold nanorods, type 25-30.

Figure 7.1: Overview of different near-infrared dyes. The bold bar corresponds to 25 nm. (Illustrations slightly modified compared to their original publication.)

Contrast Agent	λ_{max} [nm]	$\Delta\lambda$ [nm]	ϵ [$M^{-1}cm^{-1}$]	Φ [%]	merit
Nanopartz 25-30	750	43	1.1×10^{10}	0	6.2×10^{6}
Alexa 750	749	24	2.4×10^{5}	12	367
ICG	778	25	1.0×10^{5}	11	154
KSQ-4-H	$787_{\dagger}$	37	$2.1 \times 10^{5}{}_{\dagger}$	$8_{\dagger}$	141
KSQ-4	787	38	$2.1 \times 10^{5}{}_{\dagger}$	8	134
KSQ-3	776	57	2.1×10^{5}	1	64
Naphtol Green	712	76	2.1×10^{4}	0.1	4

Table 7.1: Merit of different NIR dyes for photoacoustic signal isolation. Note: Values marked with $_{\dagger}$ are estimated from similar compounds. $\Delta\lambda \equiv \min(\lambda_{HWHM})$ Data: Bhattacharyya et al. (2008); Umezawa et al. (2008); Kunkely and Vogler (2003) & own measurements.

where Φ is the fluorescence quantum yield, ϵ the molar absorption coefficient and $\min(\lambda_{HWHM})$ the smallest half-maximum peak half-width. (See Table 7.1.) This merit figure selects for compounds with high conversion factors of luminous to thermal energy and a narrow absorption peak. It would be beneficial to additionally include the steepness of the absorption spectrum in the figure of merit as a criterion, however the necessary data is non-trivial to derive reliably from the plotted data available in literature.

Due to the limited information available on tumour metabolism and tissue properties, it was decided to pursue two approaches in parallel: If the limit to effective targeting of tumorous cells is found to be due to limited mobility of the contrast agent in dense tumorous tissue, a molecular contrast agent should be the best choice due to its small size. If, however, the limiting factor to effective targeting is the availability of receptors for the vector on the surface of tumorous cells, a plasmonic contrast agent should provide an advantage due to the much larger absorption per particle.

Eventhough a wide range of plasmonic structures can be tuned to provide absorption peaks in the near-infrared, it was decided to investigate gold nanorods due to the comparatively less difficult synthesis. For the molecular contrast agents the merit figure of Alexa 750 suggests the compound as the best candidate, however the chemical structure of the compound is kept confidential by the manufacturer. The possibility to vectorise Alexa 750 could therefore not be predicted reliably. This is further compounded by the fact that the product is relatively expensive which prohibits an extensive trial-and-error approach. The choice therefore fell on ICG which has the additional advantage that it is already licensed by the Food and Drug Administration (FDA) for medical diagnostic use in humans.

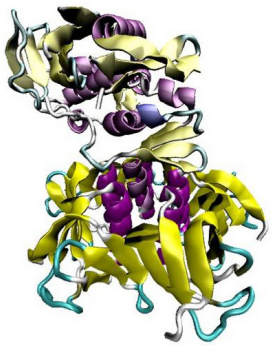

(a) Structure of Shiga Toxin.

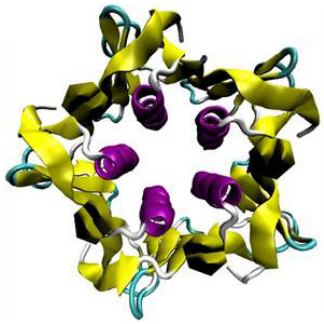

(b) Structure of subunit B of Shiga Toxin.

Figure 7.2: Illustrations: Nicolas Bogliotti

Synthesis and Vectorisation of Contrast Agents

Following the selection of suitable contrast agents, our collaborators Nicolas Bogliotti, Frédéric Schmidt and Jean-Claude Florent of The Medicinal Chemistry Unit at the Institut Curie (CNRS UMR176) and Vincent Semetey of the Physical Chemistry Unit at the Institut Curie (CNRS UMR168) developed procedures to synthesise and prepare ICG and gold nanorods for vectorisation. Vectorisation of the contrast agents with shiga toxin was carried out in collaboration with Estelle Dransart of the Intracellular Traffic, Signalling and Delivery Group (CNRS UMR144) at the Institut Curie.

Description of the Vector Johannes et al. (2002) of the Intracellular Traffic, Signalling and Delivery Group at the Institut Curie have developed a universal molecular carrier to target Gb3-receptors on the basis of the shiga toxin.

Shiga toxin is a class of toxins discovered by Shiga (1898) during his investigation of the origin of dysentery. The most common source of the toxin is the bacterium Shigella dysenteriae but other organisms also produce the compound.

Shiga toxin (STx) consists of two subunits A & B as illustrated in Figure 7.2. Subunit B binds to the Gb3-receptor on the surface of cells and is internalised. Subunit A follows the subunit B into the cell and disrupts protein synthesis in the cell. (Donohue-Rolfe et al. (1991)) Since expression of Gb3 is elevated in renal epithelial tissues, neurons of the central nervous system and the endothelium, STx has renal- and neuro-toxicity. However, it has been found that in tumorous cells, expression of Gb3 is also elevated which presents the possibility of using the non-toxic subunit B (STxB) as a universal carrier to target payloads to tumorous cells.

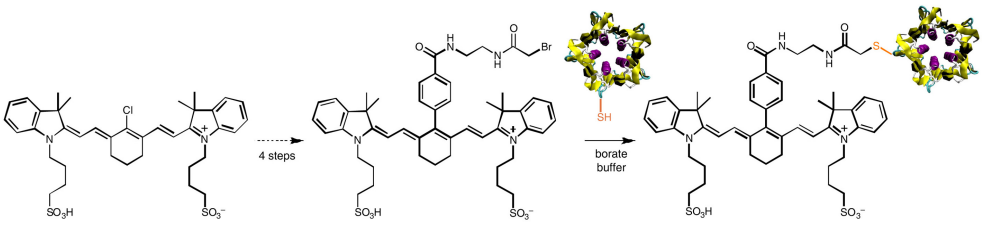

Figure 7.3: Vectorisation of ICG with STxB. Illustration (slightly modified): Nicolas Bogliotti

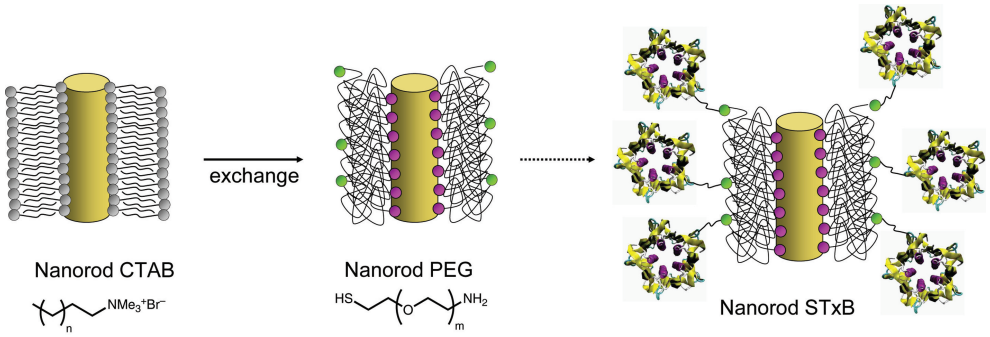

Figure 7.4: Vectorisation of gold nanorods. Illustration (slightly modified): Nicolas Bogliotti

Synthesis and Vectorisation of ICG Nicolas Bogliotti developed a modified ICG molecule which allows vectorisation of ICG with the subunit B of the shiga toxin. (Shown schematically in Figure 7.3.)

Synthesis and Vectorisation of Gold Nanorods Gold nanorods are nanometre-sized plasmonic structures which allow tuning the position of the absorption peak by changing the aspect ratio of the structure. Gold nanorods are generally synthesised by wet chemistry through anisotropic growth of gold seed particles in CTAB* micelles.

Nicolas Bogliotti and Vincent Semety have extensively investigated the parameters during synthesis which influence the spectral properties of gold nanorod solutions. To render the gold nanorods bio-compatible, the CTAB surfactant was exchanged with a PEG*. Work on vectorising the gold nanorod-PEG compound was still underway at the time of writing of this document.

Evaluation of the Properties of the Compounds

Spectral Characteristics Nicolas Bogliotti prepared solutions of a water-soluble precursor molecule to the vectorised ICG with carefully controlled concentrations. (This precursor molecule is provisionally referred to as BN65

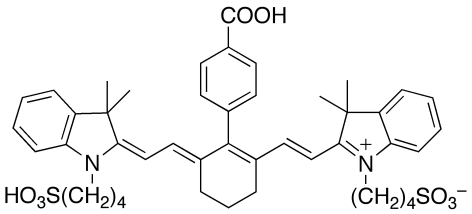

Figure 7.5: Precursor molecule to vectorised ICG. Provisionally referred to as BN65. Illustration: Nicolas Bogliotti

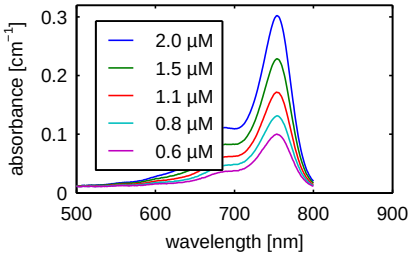

(a) Absorbance of a precursor molecule to vectorised ICG for different molar concentrations.

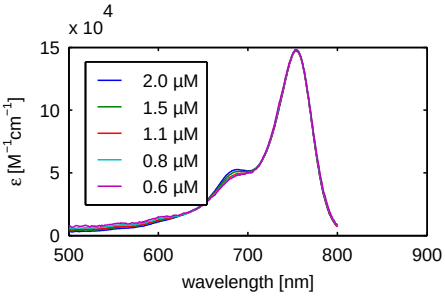

(b) Molar extinction coefficient of a precursor molecule to vectorised ICG at different molar concentrations.

Figure 7.6

and its structure is illustrated in Figure 7.5.) He measured the absorption spectra of the compound at different concentrations to allow the determination of its molar extinction coefficient. (See Figure 7.6a.)

The absorbance A_λ of a sample is defined analogously to the absorption coefficient by

$$I(z) = I_0\, 10^{-A_\lambda z}, \tag{7.2}$$

where $I(z)$ is the light intensity as a function of depth z and I_0 the initial light intensity. It follows that the absorption coefficient is related to the absorbance by

$$\mu_a = \ln(10)\, A_\lambda. \tag{7.3}$$

For molecules it is useful to define a molar extinction coefficient ϵ which quantifies the light extinction per mole of solute per litre

$$A_\lambda = c\,\epsilon, \tag{7.4}$$

where c is the molar concentration in units of mole per litre.

Analysis of the data by the author has shown that the maximum absorbance of the primary absorption peak of BN65 can be fitted with a coefficient

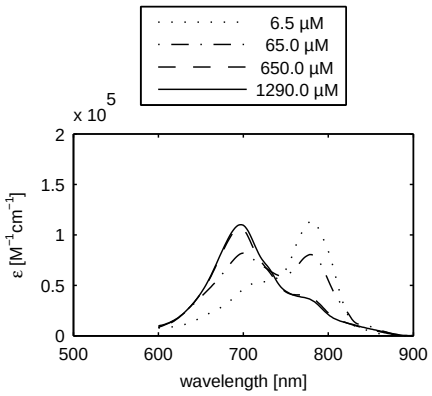

(a) Molar extinction coefficient of unmodified ICG for different molar concentrations. Data: Landsman et al. (1976)

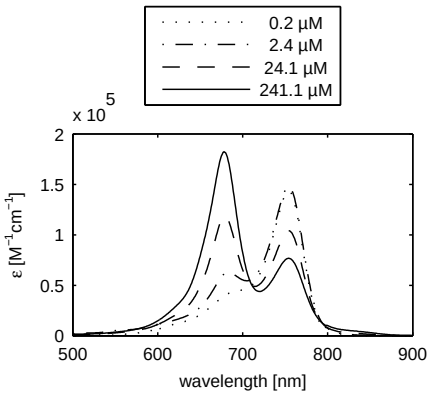

(b) Molar extinction coefficient of a precursor molecule to vectorised ICG (BN65) at different molar concentrations.

Figure 7.7

of determination $R^2 = 0.9999$ with a straight line

$$A_\lambda = \epsilon\, c + \delta, \tag{7.5}$$

where $\epsilon = 1.48 \times 10^5\,\mathrm{M}^{-1}$ is the molar extinction coefficient of the precursor BN65 in water, c its molar concentration and $\delta = 6.19 \times 10^{-3}$ presumably an offset due to a slight calibration error of the spectrometer. Figure 7.6b illustrates that correcting for the offset and the molar concentration allows collapsing the set of absorption spectra onto a single characteristic curve: the molar extinction coefficient.

For spectroscopic signal extraction it is essential to realise that the molar extinction coefficient of ICG exhibits some unusual behaviour. While for many molecules, the molar extinction coefficient is independent of concentration, for ICG this holds true only for concentrations of the order of μM or lower. For higher concentrations, the ICG molecules aggregate and a secondary absorption peak appears at lower wavelengths.

It was found that the precursor of vectorised ICG (BN65) also exhibits this behaviour. Figure 7.7 illustrates the change of the shape of the molar extinction coefficient of ICG and BN65 as a function of molar concentration.

Preliminary measurements indicate that vectorised ICG (ICG-STxB) in solution prior to injection does not exhibit this behaviour. The shape of the molecular extinction coefficient resembles that of BN65 obtained at approximately $50\,\mu$M - independent of its molar concentration [1]. This suggests that the ICG-STxB compound either has a tendency to aggregate or is stabilised by the presence of the bound vector protein.

1. This is a preliminary observation and the reason for the non-dependance on concentration of the absorption spectrum of ICG-STxB is currently under investigation.

	ICG	BN65
position of primary peak [nm]	780	754
ϵ at primary peak $\left[\mathrm{M}^{-1}\mathrm{cm}^{-1}\right]$ for $c \approx 1\,\mu\mathrm{M}$	1.14×10^5	1.48×10^5
position of minimum between peaks [nm]	746	714
position of secondary peak [nm]	697	678

Table 7.2: Summary of the key spectral parameters of unmodified ICG and BN65.

Table 7.2 summarises the key spectral parameters of unmodified ICG and BN65. It can be observed that the absorption spectrum is blue-shifted by approximately 25 nm and that BN65 is 31% more absorbent at low concentrations.

Vectorisation of ICG Estelle Dransart verified the targeting of ICG-STxB: Suspensions of cells expressing Gb3 were infused with either ICG-STxB or with unmodified ICG and unconjugated STxB. The suspensions were then washed to remove unbound molecules and imaged under a microscope with filters selecting either the intrinsic fluorecence of STxB or that of ICG.

For the cells infused with unmodified ICG and unconjugated STxB only the fluorecence signals of STxB can be observed. The ICG has been washed from the sample as can be seen in Figure 7.8.

In contrast, for the cells infused with ICG-STxB fluorecence emission of STxB and ICG can be observed after washing. Moreover, it can be observed that the vector (STxB) and its payload (ICG) are co-localised in the cells. (See Figure 7.9 on page 145.) This demonstrates that the contrast agent ICG is successfully internalised and bound in the cells by the vector.

7.2 Experiments on Biological Materials

In preparation of experiments to test the possibility of isolating the photoacoustic signals of a target marked by a vectorised, spectrally selective optical contrast agent, several experiments were carried out in parallel to the development of these contrast agents. In this section, the results of two key experiments shall be discussed.

Verification of Cellular Targeting

Having verified the efficacy of molecular targeting of ICG-STxB through the co-localisation of the fluorescence of the two components of the compound, an experiment was implemented to demonstrate the ability to discriminate between samples with and without ICG-STxB using their photoacoustic response.

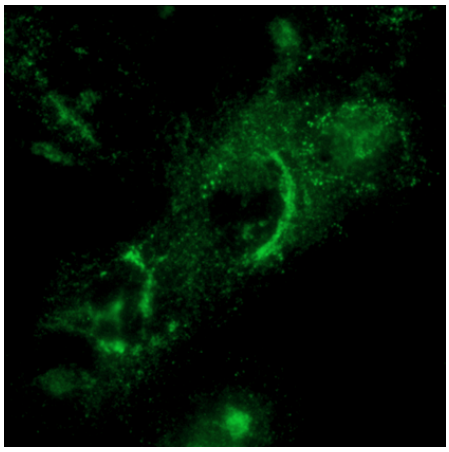

(a) Distribution of unconjugated STxB, sample 1.

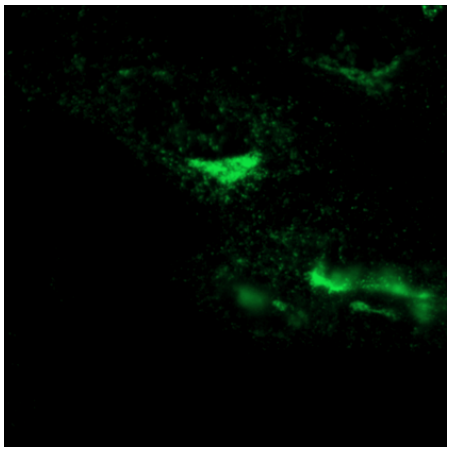

(b) Distribution of unconjugated STxB, sample 2.

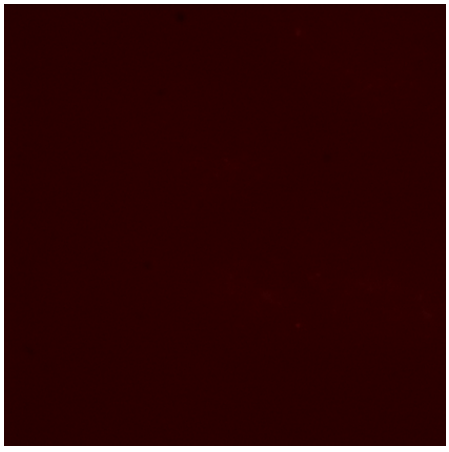

(c) Distribution of non-vectorised ICG, sample 1.

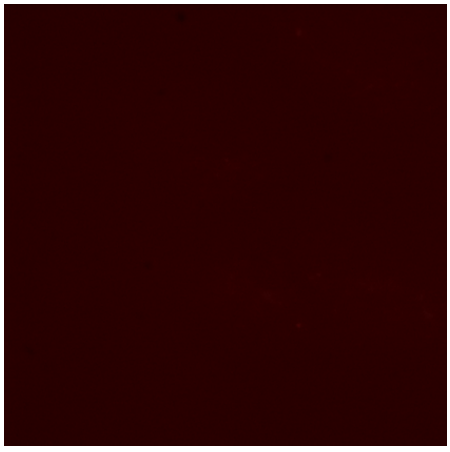

(d) Distribution of non-vectorised ICG, sample 2.

Figure 7.8: Control experiment for the verification of the co-localisation of vector and payload using unconjugated STxB (i.e. the vector is not bound to a payload) and non-vectorised ICG in two independent samples prepared with the same protocol. Illustration: Estelle Dransart

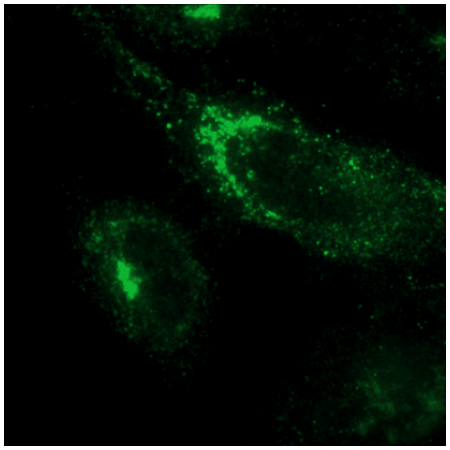

(a) Distribution of the STxB component of ICG-STxB, sample 1.

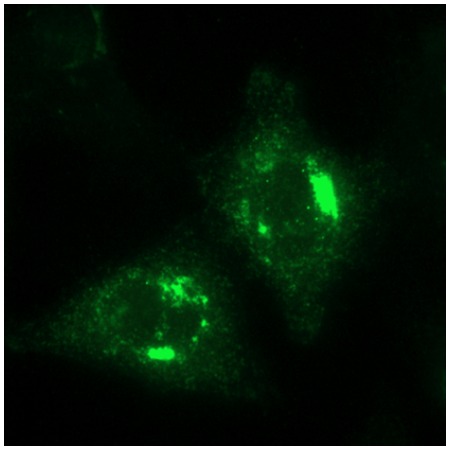

(b) Distribution of the STxB component of ICG-STxB, sample 2.

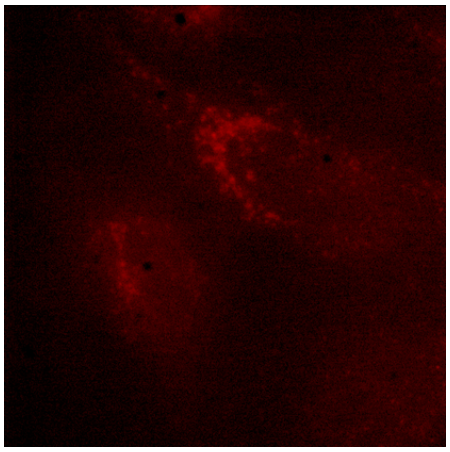

(c) Distribution of the ICG component of ICG-STxB, sample 1.

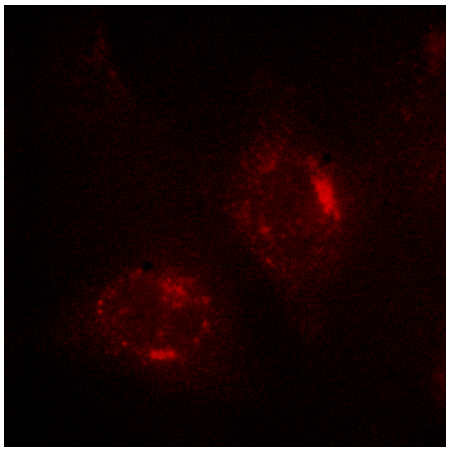

(d) Distribution of the ICG component of ICG-STxB, sample 2.

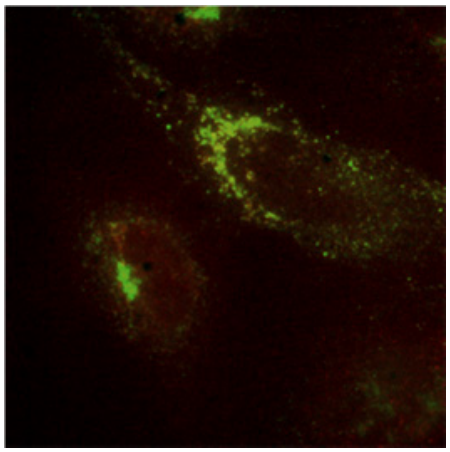

(e) Compound image of sample 1.

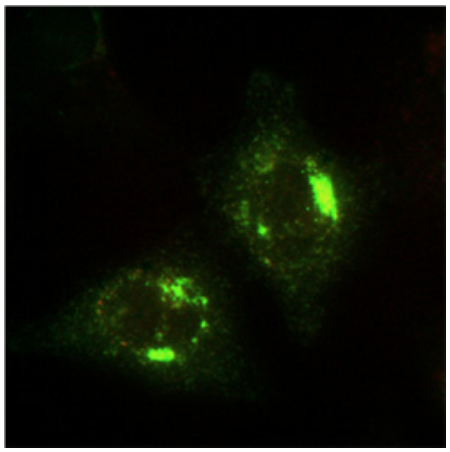

(f) Compound image of sample 2.

Figure 7.9: Experiment to verify the co-localisation of the vector (STxB) and the payload (modified ICG) of ICG-STxB in two independent samples prepared with the same protocol. Illustration: Estelle Dransart

Experimental Protocol & Setup Two populations of cells were grown *in vitro* by Marine Thiebaud of the Intracellular Traffic, Signalling and Delivery Group at the Institut Curie under the direction of Estelle Dransart. One population expressed the Gb3 receptor while the other did not. Each population was then divided into three parts and one part of each population incubated for 1 hour with either 1 μM ICG-STxB or 1 μM of the precursor BN65. One part of each population was left as control. After incubation, the samples were washed twice to remove unbound contrast agents and a cell suspension prepared with approximately 2×10^6 cells/ml in PBS*.

A set of six U-shaped capillaries with a diameter of 0.9 mm were molded into an agar gel [2]. The capillaries were then filled as follows:

1. heavily diluted solution of India ink
2. air-filled
3. unagitated suspension of cells expressing Gb3 incubated with the unvectorised precursor BN65
4. unagitated suspension of cells not expressing Gb3 but incubated with ICG-STxB
5. unagitated suspension of cells expressing Gb3 incubated with ICG-STxB
6. agitated suspension of cells expressing Gb3 incubated with ICG-STxB (The stock suspension was agitated prior to drawing a sample into the pipette which was used to inject the solution into the capillary.)

After filling the capillaries with the samples, the ends of the capillary were closed by molding a second layer of gel on top. The resulting gel was $4 \times 4 \times 4\,\mathrm{cm}^3$ with six enclosed capillaries.

The gel was then imaged echographically to determine the position of the individual capillaries and photoacoustically at several wavelengths between 700 and 900 nm. While the position of all capillaries could be clearly distinguished in the echographic image, only the capillaries 1 & 6 produced photoacoustic signals above the noise level.

Data Analysis The photoacoustic signals were beamformed and the envelope calculated. Individual masks were applied to the regions of the image corresponding to the positions of the capillaries. The standard deviation of the data of the resulting image within each mask was calculated as a measure of the photoacoustic amplitude [3].

By subtracting the noise level of the image and scaling the photoacoustic signal of capillary 6 (ICG-STxB) with the amplitude of the photoacoustic

2. To ensure a bio-compatible environment, the gel was prepared with PBS instead of water.

3. Please note that while this measure for the photoacoustic amplitude is statically stable in contrast to the maximum value, its absolute value depends on the choice of the mask. An improvement could be threshholding the data within the mask with a value related to the noise level of the acquisition and calculating e.g. the 90% quantile value.

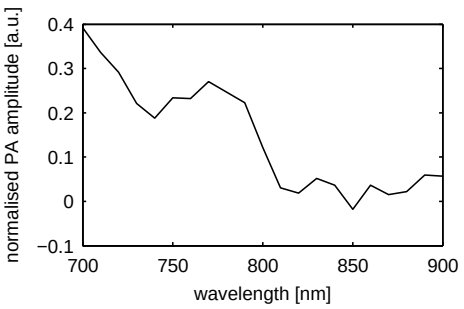

Figure 7.10: Normalised photoacoustic amplitude of capillary 6. The lower end of the range of wavelengths is limited by the useful range of the Surelite OPO used for illumination.

signals of capillary 1 (india ink) and the absorption spectrum of the india ink in this capillary (as a measure of local light fluency), a normalised photoacoustic amplitude of the cell suspension with cell expressing Gb3 incubated with ICG-STxB was obtained. (See Figure 7.10.)

Since the photoacoustic pressure is proportional to the absorbed luminous energy, the normalised photoacoustic amplitude is expected to be be proportional to the absorption coefficient $\mu_a \propto \epsilon$ of the cell suspension

$$p \propto E_{abs} \propto \mu_a I_{light} \propto \epsilon\, I_{light}, \tag{7.6}$$

where ϵ is the molar extinction coefficient of the ICG in the solution.

The experiment does not allow drawing a firm conclusion on the selectivity of the vectorisation as had been intended due to the lack of agitation of most of the cell suspensions. It appears that agitation to resuspend the cells in the buffer solution prior to drawing a sample into a pipette is essential as capillary 5 does not produce a significant photoacoustic signals despite being drawn from the same stock solution as capillary 6. Nevertheless it is clear that cells targeted with ICG-STxB produce a wavelength-dependent photoacoustic response.

Shape of the "Absorption Spectra" in Biological Environments Comparison of the normalised photoacoustic amplitude of the cell suspensions in capillary 6 (see Figure 7.10) and the absorption spectra of BN65 at low concentrations (see Figure 7.6b on page 141) shows a remarkable degree of discrepancy. However, it was found that it is possible to fit the normalised photoacoustic amplitude, $I_{PA}(\lambda)$, with a linear combination of the extinction coefficients, $\epsilon_{24.1}(\lambda)$ and $\epsilon_{241}(\lambda)$, of BN65 at molar concentrations of 24.1 μM and 241 μM respectively,

$$\begin{aligned} I_{PA}(\lambda) &= b_1 + b_2\epsilon_{24.1}(\lambda - \lambda_{shift}) + b_3\epsilon_{241}(\lambda - \lambda_{shift}), \text{ or} && (7.7)\\ &= c_1 + c_2\left[r\,\epsilon_{24.1}(\lambda - \lambda_{shift}) + (1-r)\,\epsilon(\lambda - \lambda_{shift})\right], && (7.8)\end{aligned}$$

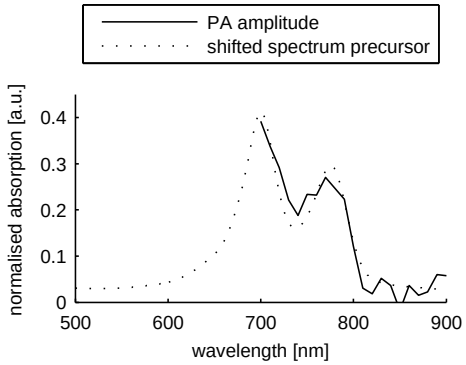

Figure 7.11: Superposition of the normalised photoacoustic amplitude with the fitted model based on a linear combination of the extinction coefficients of the unvectorised precursor BN65 at 24.1 μM and 241 μM.

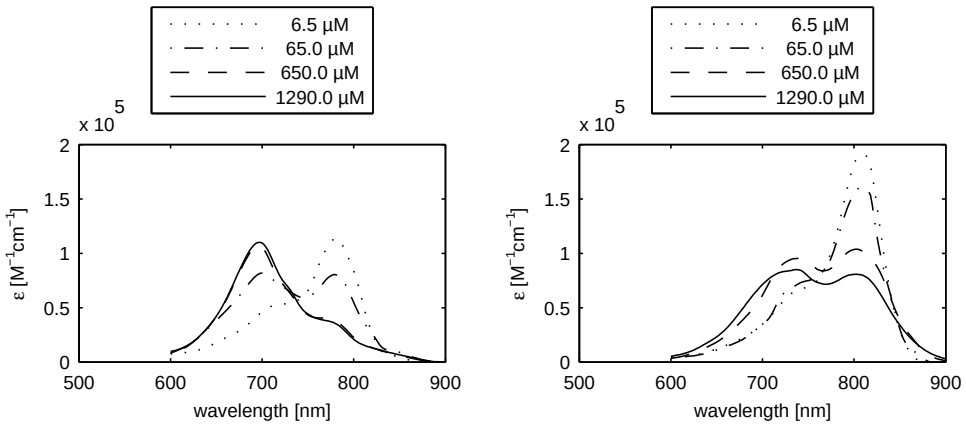

(a) Molar extinction coefficient of unmodified ICG in water for different molar concentrations. Data: Landsman et al. (1976)

(b) Molar extinction coefficient of unmodified ICG in plasma for different molar concentrations. Data: Landsman et al. (1976)

Figure 7.12

where $\{b_1, c_1, \lambda_{shift}\} \in \mathbb{R}$, $\{b_2, b_3, c_2, r\} \in \mathbb{R}^+$ and $r \leq 1$. A fit with a coefficient of determination of $R^2 = 0.9391$ is obtained for $r = 0.70 \pm 42\%$ and $\lambda_{shift} = 21.6\,\text{nm} \pm 18\%$.

The fitted value of r suggests that the true coefficient of extinction of the compound is closer to that of BN65 at a concentration of 24.1 μM than that at 241 μM. This corresponds to the results of the preliminary investigation of the spectral properties of ICG-STxB. [4]

The fitted value of λ_{shift} corresponds to a redshift of 21.6 nm of the extinc-

4. See also Section 7.1 on page 142.

tion coefficient of ICG-STxB in cells compared to the extinction coefficient of BN65 in water. A similar effect was observed by Landsman et al. (1976) who have shown that the absorption spectrum of ICG differs depending on whether it is obtained in water or in in blood plasma. The most pronounced difference is that the shape of the absorption spectrum is shifted by 30 nm towards the red. (See Figure 7.12.) The reasons given in literature for this shift is that the ICG binds to proteins in the plasma. It stands to reason that a similar effect occurs for the precursor molecule BN65 in biological environments and possibly independently of the environment for ICG-STxB as a result of the conjugation of ICG and the vector protein. However, given the differences in molecular structure between ICG and BN65 and the structures of the bound proteins, different amplitudes for the red-shift resulting from protein binding are likely for various ICG-derived molecules.

Injection with Vectorised Contrast Agents

Experimental Protocol To test whether the wavelength dependence of the photoacoustic signal could be exploited to discriminate between samples marked with an optically selective contrast agent and a sample without contrast agent, Sabrina Dehay of the Intracellular Traffic, Signalling and Delivery Group at the Institut Curie xenografted two tumours on each of four mice.

Different contrast agents were injected directly into the tumours according to the following protocol:

Animal 1, left tumour (1L): injected 15 minutes prior to sacrifice with a high concentration [5] of PEG-coated gold nanorods

Animal 1, right tumour (1R): left as control

Animal 2 died spontaneously before the protocol could be implemented

Animal 3 (3L & 3R): tumours injected 48 hours prior to sacrifice with a high concentration [6] of ICG-STxB

Animal 4, left tumour (4L): left as control

Animal 4, right tumour (4R): injected 15 minutes prior to sacrifice with a very high concentration of BN65

The tumours were excised within 15 minutes of sacrificing the animals and stored for approximately four hours in PBS. In addition, muscle samples (1M & 4M) were excised from animals 1 and 4 as additional tissue samples that should present no appreciable uptake of contrast agent.

The tumours and muscle samples were then embedded in two $4 \times 4 \times 4\,\mathrm{cm}^3$ agar gels prepared with PBS and 10%-Intralipid, resulting in a bio-compatible environment with a reduced scattering coefficient of $\mu_a \approx 5\,\mathrm{cm}^{-1}$. A small

5. The exact concentration was unknown but was the highest concentration that could be produced without provoking spontaneous aggregation.

6. The concentration of ICG-STxB was limited by the toxicity of the vector STxB.

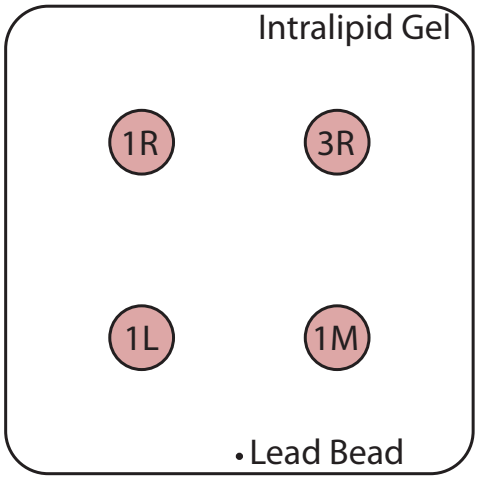

(a) Diagram of the layout of sample 1.

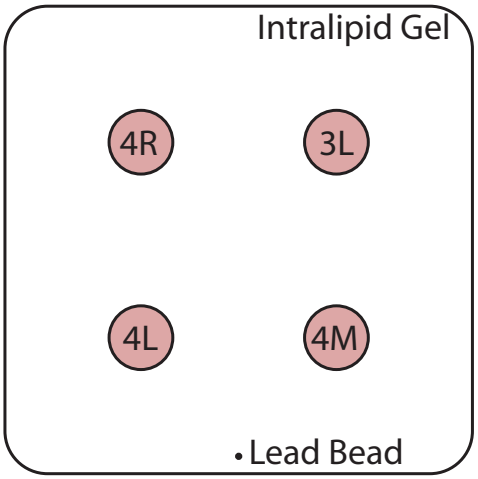

(b) Diagram of the layout of sample 2.

(c) Photo of the tumours of sample 1.

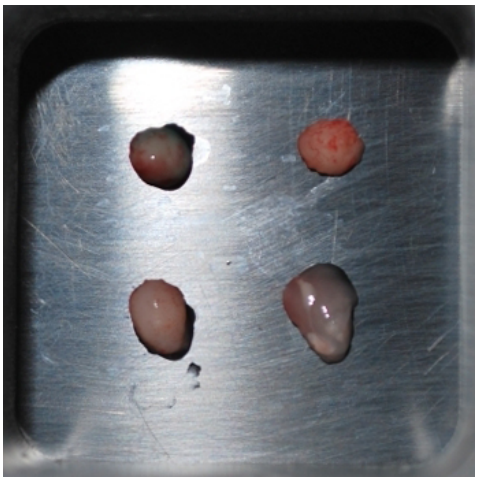

(d) Photo of the tumours of sample 2.

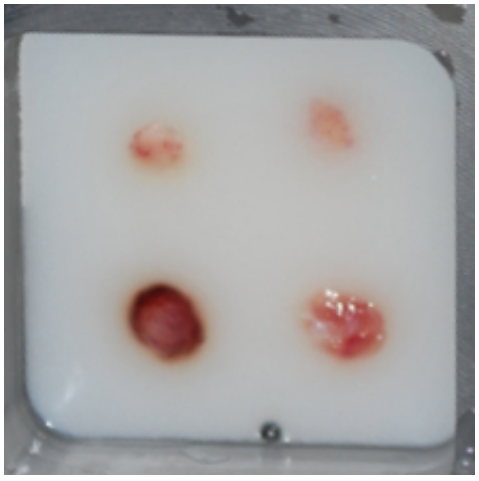

(e) Photo of the tumours of sample 1 embedded in gel before being covered with a second gel layer.

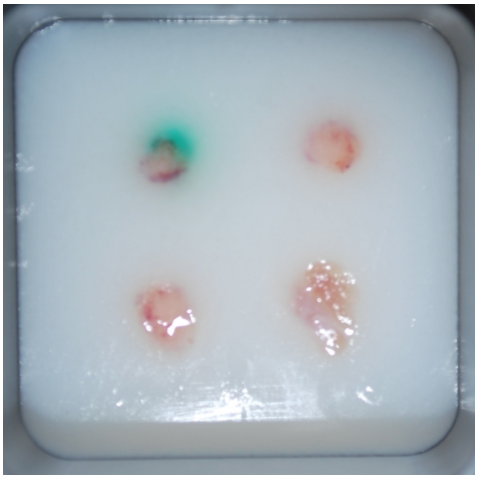

(f) Photo of the tumours of sample 2 embedded in gel before being covered with a second gel layer.

Figure 7.13

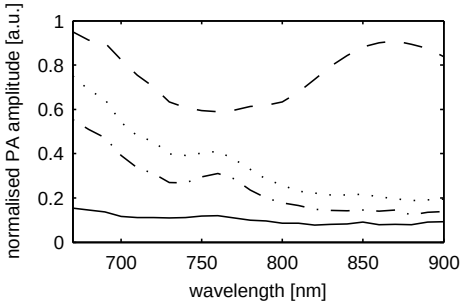

(a) Sample 1: ⋯ 1R ·−3R −−1L —— 1M

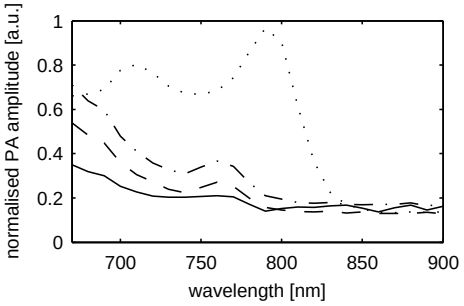

(b) Sample 2: ⋯ 4R ·−3L −−4L —— 4M (The values for 3L, 4L & 4M were scaled by a factor of 3 for better visualisation of the features of the curves.)

Figure 7.14: Normalised photoacoustic amplitude of the different tumour samples.

lead sphere was included in the phantom to serve as a probe of the local light fluency. Please refer to Figure 7.13 for a diagram of the layout and photographs of the phantom.

As in the previous section, the phantoms were imaged photoacoustically and the normalised signal amplitude of the different tumours determined. (See Figure 7.14.) For normalisation, it was assumed that the lead sphere had a constant absorption coefficient over the range of wavelengths of interest.

Features Obvious on Visual Inspection Visual inspection of the normalised photoacoustic amplitudes of the different tissue samples (see Figure 7.14) allows making several observations:

- For all signals, de-oxygenated haemoglobin remaining in the tissue after excision appears to contribute significantly to the total absorption of the tissue samples. (See also Figure 2.2 on page 30.)
- The signals produced by the muscle samples (1M & 4M), control tumours (1R & 4L) and tumours injected with ICG-STxB (3L & 3R) appear indistinguishable except for a difference in absolute signal amplitude. This difference in amplitude of the signal may be due to the high degree of vascularisation of tumourous tissue.
- The signal produced by the tumour injected with BN65 (4R) appears to present at least the characteristic absorption peak of BN65 at low concentrations . However as is to be expected for an ICG-derived molecule with a redshift due to the biological environment.
- The signal produced by the tumour injected with gold nanorods appears exhibit a relatively wide absorption peak at approximately 865 nm.

Spectral Properties of BN65 in Biological Environments In sections of this chapter the redshift of the absorption spectrum ICG in biological environments due to protein binding compared to its absorption spectrum in water is has been illustrated. Similarly it has been shown that ICG-STxB exhibits a similar redshift compared to its precursor molecule BN65 - presumably due to the presence of the bound vector protein STxB. Visual inspection of the photoacoustic signal amplitude of sample 4R shows that BN65 exhibits a redshift in biological environments similar to unmodified ICG.

To quantify the effect, the data of 4R was attempted to be fitted with the model

$$I_{PA}(\lambda) = c + c_{Hb}\epsilon_{Hb}(\lambda) + c_{BN65} r\, \epsilon_{0.2}(\lambda - \lambda_{shift}) + c_{BN65}(1-r)\, \epsilon_{241}(\lambda - \lambda_{shift}), \tag{7.9}$$

where c_{Hb} and $\epsilon_{Hb}(\lambda)$ are the molar concentration and the molar extinction coefficient of de-oxygenated haemoglobin, c_{BN65} an arbitrary scaling coeficient, and $\epsilon_{0.2}(\lambda)$ and $\epsilon_{241}(\lambda)$ the molar extinction coefficient of BN65 at molar concentrations of $0.2\,\mu$M and $241\,\mu$M respectively. Given $\{c, \lambda_{shift}\} \in \mathbb{R}$, $\{c_{Hb}, c_{BN65}, r\} \in \mathbb{R}^+$ and $r \leq 1$, a fit with a coefficient of determination of $R^2 = 0.9906$ was obtained for $\lambda_{shift} = 39.1\,\text{nm} \pm 3\%$, $c_{BN65}/c_{Hb} = 1.63 \times 10^{-3} \pm 15\%$ and $r = 0.70 \pm 6\%$.

Identification of Tissue Samples Using the remaining tissue samples, it was attempted to use their photoacoustically measured absorption characteristics to discriminate between samples containing ICG-STxB and those without. This was realised by calculating the goodness of fit of the following models:

Model 1: Absorption by de-oxygenated haemoglobin only. This is expected to fit best for muscle samples and control as any oxygen associated with haemoglobin should have been consumed by the metabolish post-sacrifice.

$$I_{PA}(\lambda) = c + c_{Hb}\epsilon_{Hb}(\lambda) \tag{7.10}$$

Model 2: To test above assumption, this model contains absorption by oxygenated and de-oxygenated haemoglobin.

$$I_{PA}(\lambda) = c + c_{Hb}\epsilon_{Hb}(\lambda) + c_{HbO_2}\epsilon_{HbO_2}(\lambda) \tag{7.11}$$

Model 3: Absorption by de-oxygenated haemoglobin and ICG-STxB. As no direct measurements of the absorption coefficient for ICG-STxB were available, the spectrum was derived from the absorption data of BN65 using the parameters fitted in the experiment on cellular targeting. (See Section 7.2.)

$$I_{PA}(\lambda) = c + c_{Hb}\epsilon_{Hb}(\lambda) + c_{ICG-STxB}\epsilon_{ICG-STxB}(\lambda) \tag{7.12}$$

R^2	Model 1	Model 2	Model 3	Model 4
1R	0.9596	0.9596	0.9718	0.9750
3R	0.9755	0.9755	0.9855	0.9862
1M	0.9320	0.9320	0.9340	0.9449
3L	0.9830	0.9830	0.9851	0.9873
4L	0.9830	0.9830	0.9836	0.9856
4M	0.9525	0.9524	0.9525	0.9513

Table 7.3: Coefficient of determination R^2 for the different models.

p-value	Model 2	Model 3	Model 4
1R	1.0000	**0.0016**	0.9997
3R	1.0000	**0.0006**	1.0000
1M	1.0000	1.0000	1.0000
3L	1.0000	**0.0138**	0.9984
4L	1.0000	0.0578	0.9727
4M	1.0000	1.0000	1.0000

Table 7.4: P-values obtained by an F-test on the residual sum of squares of the models. Model 2 and Model 3 are compared against Model 1. Model 4 is compared against Model 4. Values smaller than the acceptable significance value $\alpha = 0.05$ are printed bold.

Model 4: Analogue to model 3 but with additional absorption by oxygenated haemoglobin.

$$I_{PA}(\lambda) = c + c_{Hb}\epsilon_{Hb}(\lambda) + c_{HbO_2}\epsilon_{HbO_2}(\lambda) + c_{ICG-STxB}\epsilon_{ICG-STxB}(\lambda) \tag{7.13}$$

For above models, c and ϵ are the molar concentrations and molar extinction coefficients of the molecule indicated by their subscripts.

As the four models are nested models with different numbers of explanatory terms, the coefficient of determination R^2 is in itself no useful parameter for comparing the models: On addition of an explanatory term, R^2 would at worst stay constant, i.e. by setting the added term's scaling constant to zero. Typically however R^2 will increase slightly with each explanatory term. (See Table 7.3.)

To test whether the goodness of fit of a model with additional explanatory terms is statistically significant, a F-test may be performed on the residual sum of squares of the models. In this test the null hypothesis is that the improvement in the goodness of fit of the model with additional terms is the

result of pure chance [7]. It is rejected is the F-test results in a p-value [8] smaller than an acceptable significance value α.

To discriminate between the tissue samples an acceptable significance value of $\alpha = 0.05$ was used: it signifies that with at most a 5% chance the improvement in the goodness of fit of a model with additional explanatory terms may be purely due to chance.

As can be seen from the p-values listed in Table 7.4, this criterion correctly identifies samples 3R & 3L as containing ICG-STxB, and samples 1M, 4M &4L as lacking ICG-STxB. It also indicates that the inclusion of oxygenated haemoglobin in the models does not lead to a significant improvement - as would be expected for tissue excised several hours before the acquisition of the spectrum. However, it also results in a false positive, falsely identifying 1R as containing ICG-STxB.

It is worth noting that the tumour 1L (which was grown on the same animal at 1R) was injected with a high concentration of unvectorised gold nanorods 15 minutes prior to sacrifice. It is thus possible that the small quantity of gold nanorods that diffused into tumour 1R lead to this false positive as the spectrum of the gold nanorods was tuned to have an absorption peak in the same spectral region as ICG-STxB. For tumour 1R it would be necessary to compare coefficient of determination between a model containing haemoglobin and either ICG-STxB or gold nanorods. However, unfortunately the absorption spectrum of the gold nanorod solution could not be measured prior to injection due to logistical difficulties.

7.3 Conclusion

Over the course of the work for this thesis our collaborators at Institut Curie have made significant progress in the development of novel, vectorised optical contrast agents. The synthesis of a vectorised version of ICG has been completed and the efficacy and selectivity of targeting been verified. The synthesis and functionalisation of gold nanorods has been mastered though work on vectorising gold nanoparticles is still underway at the time of writing.

Regarding the use of these vectorised contrast agents for photoacoustic guidance of HIFU, at present even with a probe for the local light fluency (lead sphere) and a well-controlled surrounding environment (scattering agar-gel) the statstical margin of separation of tissue samples containing the contrast agent and those lacking the contrast agent appears to be fairly narrow. However, the number of tissue samples used in this experiment is insufficient to draw any firm conclusions on this issue.

7. The alternative hypothesis is that the improvement of the goodness of fit is at least partially the result of a real effect.

8. The p-value is the probability that a test statistic at least as significant as the one observed would be obtained assuming that the null hypothesis were true.

Despite the small number of tissue samples however, it would appear that at least for ICG-STxB injected at its maximum permissible concentration directly into tumours, the absorption due to ICG-STxB modifies the natural absorption spectrum of tissue sufficiently to be identifiable by statistical tests. It remains to be seen whether this holds true for systemic injection and accumulation of ICG-STxB in tumours.

Given the deficiencies of the experiment with regard to the gold nanorods, not conclusions may be drawn. It would be worthwhile however to investigate the origin of the the absorption peak of tumour 1L at approximately 865 nm. Given that the gold nanorod solutions used in the experiments are typically tuned for an absorption peak at approximately 750 nm it could be the result of pollution of the sample - or the result of the extremely high concentration of the solution injected.

Part III

Conclusions

Chapter 8

Review & Perspectives

Contents

8.1 Review of Contributions

The objective of this thesis was to explore possible improvements photoacoustics can bring to ultrasound therapy by HIFU. It was known from previous work by Bossy et al. (2006) that photoacoustic waves generated by a single optical contrast could be used to focus ultrasound via time-reversal in an acoustically complex medium. During this thesis, the challenges to photoacoustic guidance of HIFU were explored. Particular emphasis was put on the development of innovative light delivery methods, the investigation of the noise sources in the experiment and the development of algorithms for the isolation of the target's signals for time-reversal.

In a proof-of-principle experiment presented in Chapter 4 on page 75, as well as several follow-up experiments in chapters 6 and 7, it was demonstrated that it is possible to target a single, optically-selective contrast surrounded by several non-selective acoustical contrasts. This ability to discriminate between an intended target is crucial for photoacoustic guidance *in vivo* as in biological tissues a wide variety of chromophores are present which generate photoacoustic signals upon illumination. To selectively focus on a target marked with an exogenous contrast agent, it is necessary to be able to isolate its photoacoustic signals from the signals of the natural photoacoustic background.

The analysis of the proof-of-principle experiment allowed the identification of several problem complexes which present major obstacles to the implementation of the proposed method in biological tissue in general and in clinical applications in particular.

The first challenge arises from the faintness of the photoacoustic waves compared to the acoustic amplitudes generally encountered in diagnostic acoustics. It was found that noise reduction is essential to gain access to photoacoustic signals originating from sources located at depths of several centimetres in biological tissues due to the strong attenuation of the light intensity as a function of depth. In section 5.1 on page 89 several methods were developed to exploit known physical constraints on photoacoustic signals compared to the instrument noise to filter the acquired data.

A second difficulty for photoacoustic guidance of HIFU arises from the need to isolate the signals of the target from the photoacoustic background. It was found that even in well-controlled phantoms, this is a non-trivial problem due to the inhomogeneous illumination of the phantom as a function of depth. With collaborators from the Department of Applied Mathematics, first attempts at automatic target isolation algorithms were made in section 5.2 on page 107, however, it was found that further progress will require a better understanding of the characteristics of the target's signals and the photoacoustic background resulting from biological tissue.

The experiments presented in Chapter 7 on page 135 are the first steps towards towards gaining a better understanding and control of the photoacoustic signals encountered *in vivo*, in particular by use of vectorised contrast agents. It is clear that the development of vectorised contrast agents suitable for photoacoustic imaging deep in biological tissues remains a challenge despite significant advances made by several groups in the past years.

Apart from the above mentioned difficulties in signals processing, the technological limitations were explored. It was found that in particular flexible light delivery as would be required for routine clinical application is a challenge due to the high peak luminous fluencies involved. It appears however, that with a fused-end fibre bundle consisting of several hundred individual fibres, a satisfactory solution has been found. (See Section 3.2.) The use of a bundle which has one end of fused fibres and one end of individually polished fibres combines low-injection losses with a maximum flexibility for illumination of the sample as the individual fibres can be rearranged arbitrarily to best suit a given application.

A major point of uncertainty was whether the feasibility of the method would translate to HIFU-compatible acoustic devices due to the fact that HIFU-devices and diagnostic ultrasound devices have very different design constraints. It was shown in Chapter 6 on page 117 that with purpose-built HIFU transducers, it was possible to satisfy at the same time the heat-dissipation requirements to prevent overheating of therapeutic transducers as well as the requirement of high receive sensitivity to allow the detection of weak

photoacoustic signals. This encouraging finding paves the way for further work on the remaining challenges for an *in vivo* implementation of photoacoustic guidance of HIFU.

8.2 Perspectives for Future Work

One of the objectives of the work for this thesis was to ascertain where the challenges to photoacoustic guidance of HIFU lay. In many areas it has revealed more new questions that it has been able to answer. In the following the major axes requiring further work will be briefly discussed.

Improvement of the Signal-to-Noise Ratio

The acquisition of photoacoustic data with an acceptable signal-to-noise ratio from sources several centimetres deep in optically diffusive media remains a challenge. While at present data can be acquired from 6 cm in depth in optically tissue-mimicking phantoms within 10 seconds, the implementation of the method in biological tissue is likely to require further improvements to data acquisition.

By Signal Processing There are fundamentally two approaches to improving the signal-to-noise ratio of the data, a signal processing approach and a hardware approach. For homogeneous media, beamforming provides a significant improvement in SNR over data in B-scan space. It would be advantageous to be able to benefit from at least some of the beamforming-related SNR improvement with aberrated data. Unfortunately, at present this possibility is limited by the difficulty of inverting the beamforming of aberrated data after signal filtering or target isolation in beamformed-space. While it is unclear whether a hyperbolic Radon transform is strictly invertible, improvements to the filtered back-projection procedure may improve the robustness and allow extending the approach to more strongly aberrated signals. Even though such an improvement would be simple to implement with existing echographic time-reversal electronics, it appears likely that this is a mathematically non-trivial endeavour.

By Minimising Transmission Losses Another approach to improving the signal-to-noise ratio is to optimise the transmission of the electrical signal between the detector and the detection circuit. The piezo-electric elements of the Imasonic HIFU transducer used during the work for this thesis have impedances of the order of the several hundred Ohms with a significant phase angle. The impedance "matching" circuit of the Lecoeur Open System is furthermore clearly poorly adapted to standard 50 Ω or 75 Ω transmission lines.

The combination of these mismatches impedances results in a very significant transmission loss of the electrical signals generated by the piezo-electric elements on reception. It would be advantageous if the pre-amplifier of the detection circuit could be situated as close to the piezo-electric element as possible. The output impedances of the pre-amplifier and the detection circuit could then be adapted to the impedance of the transmission line to avoid transmission losses.

Pre-amplifiers located directly after the detector, fed via DC-injection are widely in use with high quality hydrophones. Use of CMUT transducer technology may facilitate the integration of the pre-amplifiers with the transducer since CMUT cells necessitate a DC voltage for pre-loading the membrane of the transducer. Furthermore the fabrication process of CMUT cells allows to design PCB circuits for pre-amplifier components with few additional steps.

With Short-Term Hardware Modifications In the short term it would be advantageous to make use of the dormant second pre-amplifier of the AD604 of the Lecoeur Open System, which would allow adding 14 dB of receive sensitivity. Furthermore, the software limitation of the receive gain to the linear region of the gain curve unnecessarily sacrifices 3 dB: in photoacoustic experiments the linearity of the gain control is of minor importance in practise. Furthermore, for the detection of tumours larger than a millimetre, it may be advantageous to increase the value of the coupling capacitor C_3 used to couple the first variable attenuator of the AD604 to the second variable attenuator. The present value of $C_3 = 1\,\text{nF}$ results in a high-pass filter with a cut-off frequency of the order of 1 MHz.

Development of Targeted Contrast Agents

While significant progress has been made by our collaborators in the development of targeted optical contrast agents, early results with a targeted ICG suggest that the compound in its current form will be unable to significantly modify the natural absorption of biological tissues. Given that part of the problem stems from the limited maximal concentration of the vector in solution, the parallel approach of targeted gold nanoparticles may yield more encouraging results. Unfortunately at present, the spectrum of the synthesised gold nanorods compares unfavourably to the spectrum of ICG.

Another possibility may be to follow an approach similar to Kim et al. (2007) and target a "container" filled with a large number of dye molecules with a single vector.

Improvements to Target Isolation Algorithms

The results of Section 5.2 and section 7.2 on page 143 show that it remains a challenge to discriminate between the photoacoustic signals of a spectrally

selective contrast agent and those of the photoacoustic background in biological tissue. The experiments of chapters 4 and 6, however, also make it clear that photoacoustic guidance of HIFU stands and falls with the reliable isolation of the photoacoustic signals of the target.

The ideal solution to this problem would be a near-infrared contrast agent with an extremely narrow absorption peak to minimise the variability of the photoacoustic background over the characteristic range of optical wavelengths. However, at present no candidate for such a contrast agent is known.

Work on the development of algorithms exploiting the apriori knowledge of the absorption spectrum of the contrast agent has been limited at present. It is likely that improvement to the current extraction algorithms are possible. An approach similar to that of Rajian et al. (2009), combining photoacoustic signals acquired before and after injection of a contrast agent, may be required for reliable target isolation.

Depending on the amount of information on the tissues surrounding the target contained in the photoacoustic signals acquired during the procedure, it may also be possible to adapt the iterative model-based inversion scheme presented in Laufer et al. (2007); Cox et al. (2009); Laufer et al. (2010). This would have the distinct advantage that no artifical probe for the local light intensity is required and greatly improve the sensitivity of the detection of exogeneous contrast agents. However, given the limited bandwidth of the transducer used in the procedure, it is unclear whether data for a sufficiently detailed forward model can be acquired.

8.3 Conclusion

The objective of this thesis was to investigate the possibility of photoacoustic guidance of HIFU. Proof-of-concept experiments have demonstrated the feasibility of the approach but several challenges were identified. Satisfactory solutions to major technological obstacles such as flexible beam-delivery and the development of HIFU transducers with sufficient receive sensitivity could be found, however, a number of difficulties related to signal processing, in particular of signals arising *in vivo*, remain. Another still very active area of research is the development of targeted optical contrast agents.

Part IV

Appendices

Appendix A

Reminder of Linear Acoustic Theory

Contents

A.1 Introduction

A sound wave is the spatial spreading of variations in the pressure and density of a medium. A description of its evolution is obtained from three fundamental principles:

1. conservation of momentum in a fluid,
2. conservation of mass in a fluid,
3. a thermodynamic statement relating changes in the three variables of state, density, pressure and entropy.

A.2 Conservation of Momentum

The conservation of momentum in a fluid is described by the Navier-Stokes equation, which is an application of Newton's second law to a continuum in

motion.

$$\underbrace{\rho\left[\frac{\partial \mathbf{v}}{\partial t}+\mathbf{v}\nabla\mathbf{v}\right]}_{\substack{\text{acceleration of a}\\ \text{moving fluid particle}}} = -\nabla p + \underbrace{\mu\nabla\mathbf{v}+\left(\zeta+\frac{1}{3}\eta\right)\nabla\left(\nabla\mathbf{v}\right)}_{\text{viscous friction}}+\mathbf{f} \tag{A.1}$$

It balances the forces due to acceleration of the fluid on the left hand side with the forces due to pressure gradients, and from internal and external sources on the right hand side. In anove equation, $p(\mathbf{r},t)$ denotes the acoustic pressure field, $\mathbf{v}(\mathbf{r},t)$ the particle velocity field, $\rho(\mathbf{r},t)$ the mass density field, μ and ζ the shear and bulk coefficients of viscosity and $\mathbf{f}(\mathbf{r},t)$ the density of external forces. A derivation of the Navier-Stokes equation can be found in any textbook on fluid dynamics, e.g. Landau and Lifshitz (1987, §15).

Generally a number of assumptions is made to simplify above equation significantly:

1. Assumption of a quasi-incompressible medium implies $\nabla\mathbf{v} = o(1)$,
2. Assumption of a non-viscous medium implies $\mu = o(1)$,
3. Assumption of subsonic fluid flow with $v \ll c$, where c is the speed of sound in the medium, implies $\frac{\partial \mathbf{v}}{\partial t} \gg \mathbf{v}\nabla\mathbf{v}$,
4. Assumption of absence of external forces, i.e. negligible gravity, implies $\mathbf{f} = o(1)$.

The assumption of a quasi-incompressible medium implies also that only small variations in the density of the medium arise, i.e. $\rho = \rho_0 + \delta\rho$ and $\rho_0 \gg \delta\rho$, where ρ_0 is the mean density of the medium and $\delta\rho$ the amplitude of density variations.

Conservation of momentum as expressed in general form by (A.1) can under above assumptions thus be approximated by

$$\rho_0\frac{\partial \mathbf{v}}{\partial t} = -\nabla p. \tag{A.2}$$

A.3 Conservation of Mass

The conservation of a quantity is commonly expressed in physics by the continuity equation

$$\frac{\partial \Psi}{\partial t} + \nabla\phi = 0, \tag{A.3}$$

where Ψ is the conserved density of the quantity and ϕ describes the flux density. Applied to a fluid, $\Psi = \rho$ and $\phi = \rho\mathbf{v}$, resulting in the continuity equation for a fluid

$$\frac{\partial \rho}{\partial t} + \nabla\left(\rho\mathbf{v}\right) = 0 \tag{A.4}$$

$$\frac{\partial \rho}{\partial t} + \mathbf{v}\nabla\rho + \rho\nabla\mathbf{v} = \tag{A.5}$$

Assuming subsonic flow, c.f. section A.2 on page 167, $\frac{\partial \rho}{\partial t} \gg \mathbf{v}\nabla\rho$ and (A.4) thus simplifies to

$$\frac{\partial \rho}{\partial t} + \rho_0 \nabla \mathbf{v} = 0. \tag{A.6}$$

A.4 Relation of Change in Variables of State

If the thermodynamic state of the medium of a sound wave is fully described by three variables of state, the mass density ρ of the medium can be expressed as a function of two other variables of state, e.g. absolute pressure P and entropy per unit mass s.

$$\rho\left(P, s\right) \tag{A.7}$$

The exact differential of the mass density, describing how a change in the mass density is related to changes in the pressure and entropy of the system, is thus given by

$$d\rho = \left(\frac{\partial \rho}{\partial P}\right)_s dP + \left(\frac{\partial \rho}{\partial s}\right)_P ds. \tag{A.8}$$

Two assumptions are commonly made to simplify (A.8):

1. assumption of a reversible process, i.e. no loss or dissipation of energy, c.f. assumption of a non-viscous medium in section A.2 on page 167,
2. assumption of an adiabatic process, i.e. with negligible heat flow to or from a fluid particle over the relevant acoustic time scale.

A reversible adiabatic process implies an isentropic process with $ds = 0$. Furthermore, one can identify $c_s = {}^1\!/\!\sqrt{\left(\frac{\partial \rho}{\partial P}\right)_s}$, where c_s is the adiabatic speed of sound. Under above assumptions (A.8) thus simplifies to

$$d\rho = \frac{1}{c_s^2} dP. \tag{A.9}$$

A.5 Wave Equation

In thermodynamics the pressure P is defined on an absolute scale, while in acoustics and fluid dynamics pressure p refers to the field of variations in the pressure relative to a mean pressure value P_0, i.e. $p\left(\mathbf{r}, t\right) \equiv P\left(\mathbf{r}, t\right) - P_0$.

Furthermore, the thermodynamic relations apply to an identified fluid particle. To allow for the possibility of flow in the medium, time derivatives of thermodynamic variables need to be taken following the fluid particle in the flow. (See This is achieved by the material derivative $\frac{D}{Dt} = \frac{\partial}{\partial t} + \mathbf{v}\nabla$, where $\mathbf{v}\left(\mathbf{r}, t\right)$ is the fluid velocity. If the fluid flow is subsonic, $\frac{\partial}{\partial t} \gg \mathbf{v}\nabla$ and the material derivative may thus be approximated by $\frac{D}{Dt} = \frac{\partial}{\partial t}$. It follows that

$$\frac{DP}{Dt} = \frac{\partial P}{\partial t} = \frac{\partial p}{\partial t}, \tag{A.10}$$

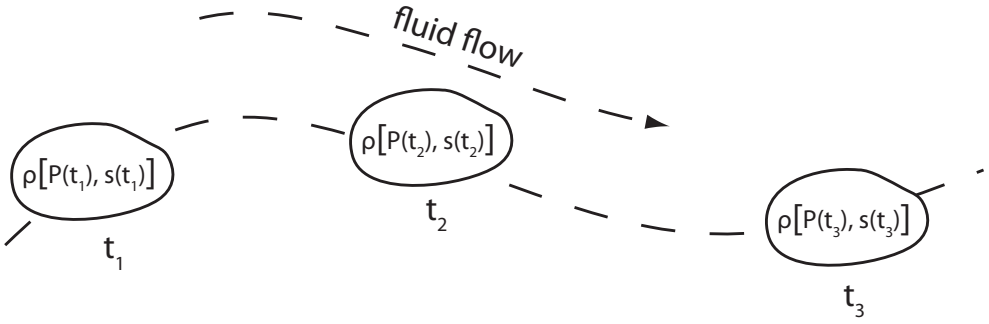

Figure A.1: Flow of a fluid particle.

since P_0 is constant by definition. Using the exact differential (A.9) the variation in the mass density and pressure of a fluid particle may thus be expressed as

$$\frac{\partial \rho}{\partial t} = \frac{1}{c_s^2}\frac{\partial P}{\partial t} \tag{A.11}$$

$$= \frac{1}{c_s^2}\frac{\partial p}{\partial t} \tag{A.12}$$

Differentiating (A.2) once with respect to space and (A.12) and (A.6) once with respect to time results in the following three equations respectively.

$$-\rho_o \frac{\partial}{\partial t}\left[\nabla \cdot \mathbf{v}\right] = \nabla^2 p \tag{A.13}$$

$$\frac{\partial^2 \rho}{\partial t^2} = \frac{1}{c_s^2}\frac{\partial^2 p}{\partial t^2} \tag{A.14}$$

$$\frac{\partial^2 \rho}{\partial t^2} + \rho_0 \frac{\partial}{\partial t}\left[\nabla \cdot \mathbf{v}\right] = 0 \tag{A.15}$$

Substituting (A.13) and (A.14) into (A.15) one obtains the linear wave equation for a non-dissipative medium:

$$\nabla^2 p - \frac{1}{c_s^2}\frac{\partial^2 p}{\partial t^2} = 0 \tag{A.16}$$

A.6 Velocity Potential

For most non-trivial problems in acoustics, it is useful to apply the fluid dynamic concept of a velocity potential to acoustics. For an irrotational fluid in a simply-connected region of space, the vector field of particle velocities $\mathbf{v}$ can be fully described by a scalar field ϕ, called the velocity potential. This can be shown as follows.

Given a vector field $\mathbf{v}$ with the properties,

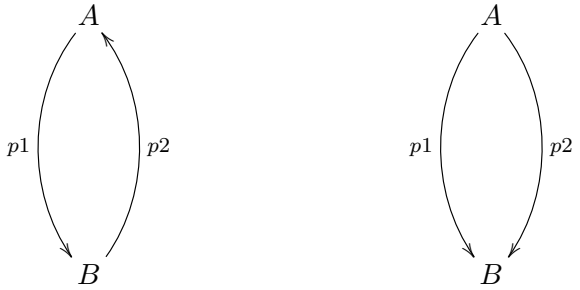

Figure A.2: Illustration of possible paths around a closed loop.

1. the field is irrotational: $\nabla \times \mathbf{v} = 0$,
2. the field has a continuous partial derivative,
3. the field occupies a simply-connected region of space [1],

the Kelvin-Stokes theorem states

$$\int_S (\nabla \times \mathbf{v})\, d\mathbf{S} = \oint_C \mathbf{v} \cdot d\mathbf{r}, \tag{A.17}$$

where S is any open surface in $\mathbb{R}^3$ and C its bounding curve.

If $\nabla \times \mathbf{v} = 0$, it follows that the line integral $\oint_C \mathbf{v} \cdot d\mathbf{r}$ around any closed loop equals zero. By defining two arbitrary points A and B on the loop C, the loop can be split into two paths, path $p1$ from A to B, and path $p2$ from B to A, as illustrated in figure Figure A.2a.

The line integral $\oint_C \mathbf{v} \cdot d\mathbf{r} = 0$ can thus be expressed as

$$\int_{A \to B \text{ along } p1} \mathbf{v} \cdot d\mathbf{r} + \int_{B \to A \text{ along } p2} \mathbf{v} \cdot d\mathbf{r} \quad = \quad 0. \tag{A.18}$$

Since a reversal of the integration limits of a line integral reverses the sign of the integrand, reversing the direction of integration along $p2$ as illustrated in Figure A.2b gives

$$\int_{A \to B \text{ along } p2} \mathbf{v} \cdot d\mathbf{r} \quad = \quad -\int_{B \to A \text{ along } p2} \mathbf{v} \cdot d\mathbf{r}. \tag{A.19}$$

Given (A.18), it follows immediately that

$$\int_{A \to B \text{ along } p2} \mathbf{v} \cdot d\mathbf{r} = \int_{A \to B \text{ along } p1} \mathbf{v} \cdot d\mathbf{r}. \tag{A.20}$$

1. A region of space is is said to be simply-connected if any simple closed path can be shrunk to a point continuously. E.g. a pillar traversing an aquarium from bottom to fluid surface breaks the single-connectedness of a fluid, while a bubble does not.

This shows that a line integral on a vector field with $\nabla \times \mathbf{v} = 0$, is independent of the path taken from a start point A to an end point B and depends only on the positions of the points A and B themselves. One can thus write

$$\int_A^B \mathbf{v} \cdot d\mathbf{r} = \phi(\mathbf{B}) - \phi(\mathbf{A}), \tag{A.21}$$

where ϕ is a single-valued scalar function of position. In the limit where A and B are separated by an infinitesimal displacement $d\mathbf{r}$, (A.21) becomes

$$\mathbf{v} \cdot d\mathbf{r} = d\phi. \tag{A.22}$$

Given that $\nabla\phi \cdot d\mathbf{r} = \frac{\partial\phi}{\partial x}dx + \frac{\partial\phi}{\partial y}dy + \frac{\partial\phi}{\partial z}dz = d\phi$,

$$(\mathbf{v} - \nabla\phi) \cdot d\mathbf{r} = 0. \tag{A.23}$$

Since $d\mathbf{r}$ is an arbitrary displacement it follows that the vector field $\mathbf{v}$ can be expressed in terms of a scalar field ϕ, called the velocity potential due to the similarity of its mathematical description to the description of other potential fields in physics:

$$\mathbf{v} = \nabla\phi \tag{A.24}$$

Equations (A.2) and (A.6) respectively can thus be expressed in terms of the velocity potential.

$$\rho_0 \frac{\partial\phi}{\partial t} = -p \tag{A.25}$$

$$\frac{\partial\rho}{\partial t} + \rho_0 \nabla^2\phi = 0 \tag{A.26}$$

Substituting a (A.25) and (A.9) suitably differentiated with respect to time into (A.26) leads to an expression of the wave equation in terms of the velocity potential:

$$\left(\nabla^2 - \frac{1}{c_s^2}\frac{\partial^2}{\partial t^2}\right)\phi = 0 \tag{A.27}$$

Appendix B

Reminder of Green's Funtion Solutions to Wave Problems

Contents

B.1 Statement and Solution of the General Problem

Statement of the General Problem

Morse and Feshbach (1953, §7.3) provide a detailed derivation of the Green's function for the scalar wave equation. Following a similar approach, it may be shown that the solution to the scalar wave equation with a particular source density $a\,q\,(\mathbf{r},t)$

$$\left(\nabla^2 - \frac{1}{c_s^2}\frac{\partial^2}{\partial t^2}\right)\phi\,(\mathbf{r},t) = a\,q\,(\mathbf{r},t)\,, \quad (\mathbf{r},t) \in \mathbb{R}^3 \times [t_0, +\infty[, \tag{B.1}$$

can be expressed in terms of the solution to the problem

$$\left(\nabla_s^2 - \frac{1}{c_s^2}\frac{\partial^2}{\partial t_s^2}\right) G\,(\mathbf{r},t|\mathbf{r_s},t_s) = b\,\delta\,(\mathbf{r}-\mathbf{r_s})\,\delta\,(t-t_s)\,, \tag{B.2}$$

where $G\,(\mathbf{r},t|\mathbf{r_s},t_s)$ gives the Green's function between the observation point denoted by $\mathbf{r}$ at time t and the source point located at $\mathbf{r_s}$ at time t_s. Assuming

causality, the solution is given by

$$\begin{aligned}\phi(\mathbf{r},t) =& \frac{a}{b}\int_{t_0}^{t} dt_s \iiint dV_s\, G\, q(\mathbf{r_s},t_s) \\ &-\frac{1}{b}\int_{t_0}^{t} dt_s \oiint d\mathbf{S_s}\left[G\nabla_s\phi(\mathbf{r_s},t_s) - \phi(\mathbf{r_s},t_s)\,\nabla_s G\right] \\ &+\frac{1}{b}\frac{1}{c_s^2}\iiint dV_s\left[\frac{\partial G}{\partial t_s}\,\phi(\mathbf{r_s},t_s) - G\,\frac{\partial\phi(\mathbf{r_s},t_s)}{\partial t_s}\right]_{t_s=t_0}\end{aligned} \tag{B.3}$$

To obtain a unique solution, Dirichlet [1] or Neumann boundary conditions or a linear combination of both must be imposed on spatial dimensions and Cauchy conditions [2] for the time dimension. It is therefore necessary to specify $\phi(\mathbf{r},t_0)$ and $\left.\frac{\partial\phi}{\partial t}\right|_{t=t_0}$.

Inspection of (B.2) shows that the source is an impulse located at $\mathbf{r}=\mathbf{r_s}$ at time $t=t_s$. G then describes the evolution of the impulse as it propagates away from $\mathbf{r}=\mathbf{r_s}$.

The first integral serves to incorporate the source term while the second and third integral take into account the spatial boundary conditions and the temporal initial conditions respectively.

Simplifying Assumptions

For an infinite medium, the second integral vanishes. Similarly under appropriate initial conditions, i.e. a medium initially in equilibrium with no initial displacement, $\phi(\mathbf{r},t=t_0)=0$, and no initial movement, $\left.\frac{\partial\phi}{\partial t_0}\right|_{t=t_0}=0$, the integral for the initial conditions vanishes.

In the case of an infinite, homogeneous medium, the wave operator exhibits translational invariance [3]. Under these condition, the first integral can be shown to be equivalent to a four-dimensional convolution operation.

---

1. Dirichlet boundary conditions specify the value of a function on a surface, i.e. $\phi(\mathbf{r_S},t)=f$ where $\mathbf{r_S}$ specifies a surface.

2. Cauchy boundary conditions specify ϕ and the normal derivative, i.e. here $\frac{\partial\phi}{\partial t}$, at $t=t_0$.

3. It is trivial to demonstrate translational invariance for the wave operator in an infinite homogeneous medium by evaluating $\Box f(\mathbf{r},t)=\Box f(\mathbf{a}+\alpha,t+\beta)$. Given the translational invariance of the linear operator, it follows that the operator's Green's function exhibits the same translational variance, $G(\mathbf{r},t|\mathbf{r_0},t_0)=G(\mathbf{r}+\alpha,t+\beta|\mathbf{r_0}+\alpha,t_0+\beta)$. If one defines $\alpha=-\mathbf{r_0}$ and $\beta=-t_0$, the expression becomes $G(\mathbf{r},t|\mathbf{r_0},t_0)=G(\mathbf{r}-\mathbf{r_0},t-t_0|0,0)=G(\mathbf{r}-\mathbf{r_0},t-t_0)$.

$$\begin{aligned}
&\frac{a}{b}\int_0^t dt_0 \iiint d\mathbf{V_0}\, G\left(\mathbf{r},t|\mathbf{r_0},t_0\right)\, q\left(\mathbf{r_0},t_0\right)\\
=&\frac{a}{b}\int_0^t dt_0 \iiint d\mathbf{V_0}\, G\left(\mathbf{r}-\mathbf{r_0},t-t_0\right)\, q\left(\mathbf{r_0},t_0\right)\\
=&\frac{a}{b}\left[G \underset{\mathbf{r}}{\otimes} \underset{t}{\otimes} q\right](\mathbf{r},t) \qquad \text{(B.4)}
\end{aligned}$$

If causality is assumed, it may be shown Morse and Feshbach (1953, §7.2,§7.3 in particular p.809, p.838) that the Green's function is given by

$$G\left(\mathbf{r}-\mathbf{r_0},t-t_0\right) = \frac{-b}{4\pi R}\,\delta\left[\frac{R}{c}-(t-t_0)\right] \qquad \text{(B.5)}$$

$$= \frac{-b}{4\pi R}\,\delta\left(t-t_0-\frac{R}{c}\right) \qquad \text{(B.6)}$$

where $R \equiv |\mathbf{r}-\mathbf{r_0}|$.

Choice of Constants

The choice of b determines how a factor of 4π arising due the spherical symmetry of the problem is distributed between the expression for the Green's function and the integral expression for ϕ. It is fundamentally of no consequence to the mathematical problem as it cancels out on substitution of the Green's function, however its sign determines the sign of the Green's function. The absolute value of a is typically chosen to be equal to that of b as to simplify the overall appearance of the expressions.

There are two common choices for the constants a and b. Morse and Feshbach (1953) define $a \equiv b \equiv -4\pi$ which simplifies the expression of the Green's function with the disadvantage of requiring a scaling of $q\left(\mathbf{r},t\right)$ by -4π to obtain the source density:

$$\left(\nabla^2 - \frac{1}{c_s^2}\frac{\partial^2}{\partial t^2}\right)\phi\left(\mathbf{r},t\right) = -4\pi\, q\left(\mathbf{r},t\right) \qquad \text{(B.7)}$$

$$\begin{aligned}
\phi\left(\mathbf{r},t\right) = &+\int_0^t dt_0 \iiint d\mathbf{V_0}\, G\left(\mathbf{r},t|\mathbf{r_0},t_0\right)\, q\left(\mathbf{r_0},t_0\right)\\
&+\frac{1}{4\pi}\int_0^t dt_0 \oiint d\mathbf{S_0}\cdot\left(G\nabla_0\phi - \phi\nabla_0 G\right)\\
&-\frac{1}{4\pi}\frac{1}{c_s^2}\iiint d\mathbf{V_0}\,\left[\frac{\partial G}{\partial t_0}\phi - G\frac{\partial \phi}{\partial t_0}\right]_{t_0=0}
\end{aligned} \qquad \text{(B.8)}$$

$$G\left(\mathbf{r}-\mathbf{r_0},t-t_0\right) = \frac{1}{R}\,\delta\left(t-t_0-\frac{R}{c}\right) \qquad \text{(B.9)}$$

In most acoustics texts the definition $a \equiv 1$ and $b = -1$ is chosen, shifting the burden of scaling to the Green's function allowing an unscaled source density $q(\mathbf{r}, t)$:

$$\left(\nabla^2 - \frac{1}{c_s^2}\frac{\partial^2}{\partial t^2}\right)\phi(\mathbf{r}, t) = q(\mathbf{r}, t) \tag{B.10}$$

$$\begin{aligned}\phi(\mathbf{r}, t) = &- \int_0^t dt_0 \iiint d\mathbf{V_0}\, G(\mathbf{r}, t|\mathbf{r_0}, t_0)\; q(\mathbf{r_0}, t_0) \\ &+ \int_0^t dt_0 \oiint d\mathbf{S_0} \cdot (G\nabla_0\phi - \phi\nabla_0 G) \\ &- \frac{1}{c_s^2} \iiint d\mathbf{V_0} \left[\frac{\partial G}{\partial t_0}\phi - G\frac{\partial \phi}{\partial t_0}\right]_{t_0=0}\end{aligned} \tag{B.11}$$

$$G(\mathbf{r} - \mathbf{r_0}, t - t_0) = \frac{1}{4\pi R}\,\delta\left(t - t_0 - \frac{R}{c}\right) \tag{B.12}$$

B.2 Recasting a Source Term Problem as an Initial Value Problem

The general Green's function solution (B.3) contains separate terms to take into account source terms, acoustic boundary conditions as well as initial value conditions. It may be shown that under appropriate conditions a source term problem for an infinite medium initially at rest,

$$\left(\nabla^2 - \frac{1}{c_s^2}\frac{\partial^2}{\partial t^2}\right)\phi(\mathbf{r}, t) = a\, q(\mathbf{r}, t), \quad (\mathbf{r}, t) \in \mathbb{R}^3 \times]-\infty, +\infty[\tag{B.13}$$

$$\phi(\mathbf{r}, t) = \frac{a}{b}\int_{t_0}^t dt_s \iiint dV_s\, G\, q(\mathbf{r_s}, t_s) \tag{B.14}$$

may be recast as an initial value problem

$$\left(\nabla^2 - \frac{1}{c_s^2}\frac{\partial^2}{\partial t^2}\right)\phi(\mathbf{r}, t) = 0, \quad (\mathbf{r}, t) \in \mathbb{R}^3 \times [t_0, +\infty[\tag{B.15}$$

$$\phi(\mathbf{r}, t) = \frac{1}{b}\frac{1}{c_s^2} \iiint dV_s \left[\frac{\partial G}{\partial t_s}\,\phi(\mathbf{r_s}, t_s) - G\,\frac{\partial \phi(\mathbf{r_s}, t_s)}{\partial t_s}\right]_{t_s=t_0}, \tag{B.16}$$

where$\phi(\mathbf{r}, t)$ and $\frac{\partial \phi}{\partial t}$ at $t = t_0$ are provided.

The conditions for this to become possible are such that solutions to the two problems result in the same acoustic pressure field. It is thus required that

$$a\int_{t_0}^t dt_s\, G\, q(\mathbf{r_s}, t_s) = \frac{1}{c_s^2}\left[\frac{\partial G}{\partial t_s}\,\phi(\mathbf{r_s}, t_s) - G\,\frac{\partial \phi(\mathbf{r_s}, t_s)}{\partial t_s}\right]_{t_s=t_0}. \tag{B.17}$$

Using a medium initially at rest with $\left.\frac{\partial \phi}{\partial t_s}\right|_{t_s=t_0}$ and a separable source term containing the derivative of a temporal Dirac function, $q(\mathbf{r},t) = \frac{\partial}{\partial t}\left(q_{\mathbf{r}}(\mathbf{r})\,\delta(t)\right)$, the equivalence condition becomes

$$a\int_{t_0}^{t} dt_s\, G(\mathbf{r},t|\mathbf{r_s},t_s)\; q_{\mathbf{r}}(\mathbf{r}_s)\; \frac{\partial}{\partial t_s}\left(\delta(t_s)\right) = \frac{1}{c_s^2}\left[\frac{\partial G}{\partial t_s}\,\phi(\mathbf{r_s},t_s)\right]_{t_s=t_0}. \quad \text{(B.18)}$$

Using the fundamental equation defining derivatives of the Dirac function $\int f(x)\;\delta^{(n)}(x)\;dx \equiv -\int f'(x)\;\delta^{(n-1)}(x)\;dx$, the temporal integration may be re-expressed as

$$-\,a\int_{t_0}^{t} dt_s\,\frac{\partial G}{\partial t_s}\,q_{\mathbf{r}}(\mathbf{r}_s)\;\delta(t_s) = \frac{1}{c_s^2}\left[\frac{\partial G}{\partial t_s}\,\phi\right]_{t_s=t_0}, \quad \text{(B.19)}$$

which evaluates to

$$-\,q_{\mathbf{r}}(\mathbf{r}_s)\;\left.\frac{\partial G}{\partial t_s}\right|_{t_s=t_0} = \frac{1}{c_s^2}\left[\frac{\partial G}{\partial t_s}\,\phi\right]_{t_s=t_0}. \quad \text{(B.20)}$$

Eliminating the common factor of $\left.\frac{\partial G}{\partial t_s}\right|_{t_s=t_0}$ and rearranging one obtains an expression for an initial value distribution for which the resulting wave field is equivalent the one obtained with the source term:

$$\phi(\mathbf{r},t_0) = -c_s^2\,q_{\mathbf{r}}(\mathbf{r}) \quad \text{(B.21)}$$

Appendix C

Principles of Optical Parametric Oscillators

Contents

The objective of this chapter is to provide the reader with an intuitive understanding of the processes at work in an optical parametric oscillator (OPO) and the factors determining major operating characteristics. For a more in depth understanding the reader is encouraged to refer to the literature cited over the course of this chapter.

C.1 Optical Parametric Processes

The term "optical parametric process" describes processes for which the initial and final quantum states of the system are identical. The system can therefore find itself only for brief periods of time at excited "virtual states". The life-time of these virtual states is determined by the uncertainty relation and is of the order of $\hbar/\delta E$ where δE is the energy difference between the virtual state and the closest real state.

The inelastic nature of these interactions requires the conservation of energy

and momentum for all optical fields

$$0 = \sum_i \omega_i \tag{C.1}$$

$$\mathbf{\Delta k} = \sum_i \mathbf{k_i} \tag{C.2}$$

$$= \sum_i \frac{n_i\,\omega_i}{c}\,\hat{\mathbf{k}}, \tag{C.3}$$

where momentum is expressed in terms of the wave number k. Each of frequency components is assigned a sign according to their phase relationships [1]. Momentum is conserved, and the efficiency of the parametric process thus optimised, when $\Delta k \to 0$. (C.2) thus describes a phase-matching criterion that must be minimised for the non-linear process of interest.

The phase matching condition $\Delta k = 0$ is difficult to achieve in practice due to an effect known as normal dispersion: the refractive index increases monotonically as a function of frequency in the transparent region of materials.

One way to overcome this challenge is to make use of birefringent materials that exhibit different refractive indexes for ordinary and extraordinary rays. By changing the orientation of the extraordinary ray with respect to the crystal's optical axis, the refractive index for the extraordinary ray may be adjusted. Many materials exhibit furthermore a temperature dependence of the degree of birefringence which may also be exploited for phase matching.

For materials that do not exhibit birefringence, quasi-phase-matching may be employed. A quasi-phase-matched medium is a crystal in which the crystal axis is periodically inverted. This leads to a periodic inversion of the polarisation of the non-linear coupling coefficient d_{eff} as a function of position which may be used to compensate for a non-zero wave-vector mismatch Δk. (Boyd (2008, §§2.3,2.4))

C.2 Optical Parametric Amplification

The principal non-linear process at work in an OPO is optical parametric amplification, also known as difference-frequency generation. Optical parametric amplification is a three-wave mixing process whereby the interaction of two waves with frequencies ω_P and ω_I with a non-linear optical medium generates a third wave at the difference frequency $\omega_S = \omega_P - \omega_I$ as illustrated by Figure C.1.

In the energy level description of the interaction, a photon of frequency ω_P is absorbed, exciting the medium to a virtual state. This virtual state then decays in a two-photon emission process which is stimulated by the presence

1. A useful convention is to denote absorbed photons with a negative sign and emitted photons with a negative sign.

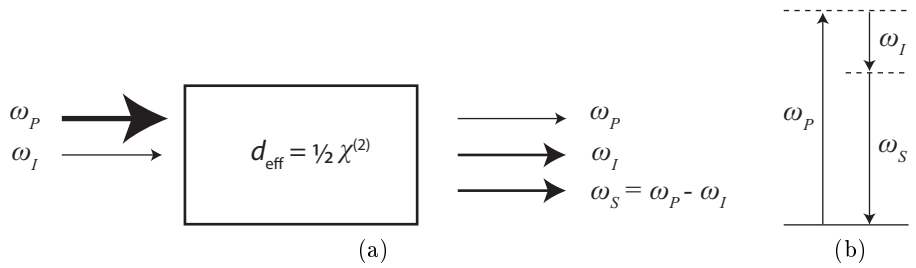

Figure C.1: Optical parametric amplification. (a) Geometry of the interaction. (b) Energy levels of the interaction.

of a "seeder" field at frequency ω_I or ω_S. With each converted photon, energy is therefore transferred from a pump beam with higher energy photons at ω_P to two beams of less energetic photons, the idler beam with ω_I and the signal beam with ω_S [2].

It may be shown (e.g. Boyd (2008, §2.9)) that in the case of intense pump beam and seeder beams, i.e. neglecting pump beam depletion, the idler beam experiences a single-pass gain

$$\frac{I_I(z=L)}{I_I(z=0)} - 1 = \sinh^2(gL) \to \frac{1}{4}\exp(2gL) \text{ if } gL \gtrsim 1, \tag{C.4}$$

$$\text{with } g = \left[\kappa_i \kappa_s^* - \left(\frac{\Delta k}{2}\right)^2\right]^{\frac{1}{2}} \text{ and } \kappa_\sigma = \frac{2i\omega_\alpha^2 d_{eff}}{k_\alpha c^2} E_p, \tag{C.5}$$

with a single pass through the crystal, where L is the crystal length, I_I the intensity of the idle beam and E_P the electric field of the pump beam. For a BBO crystal of a length of 10 mm and the typical pump beam characteristics of the Surelite II-10 laser, this results [3] in a single-pass gain of the order of 70.

C.3 Spontaneous Parametric Down-Conversion

The requirement that a seeder field be present for optical parametric amplification severely limits the ease with which the output wavelengths may be chosen. Not only must the non-linear medium be phase-matched, e.g. by rotating the crystal, but in addition the wavelength of the seeder beam must be adjusted - or alternatively contain all wavelengths of interest.

It is therefore important to note that the two-photon emission converting one photon with frequency ω_P to two photons with frequencies ω_I and ω_S described above may also occur in absence of a pre-established seeder field. In

2. For historical reasons, the beam of less energetic photons is called the idler beam, while the beam of higher energetic photons is called the signal beam.

3. Based on the data of the tables 2.1 and 2.2 of Duarte (2008, pp. 26, 28).

this case, the virtual state excited by the photon at ω_P decays spontaneously stimulated by random vacuum fluctuations in a process called spontaneous parametric down-conversion [4]. Such spontaneously created photons can then undergo further optical parametric amplification.

It should be noted however, that spontaneous parametric down-conversion is a rare process and thus much less efficient than two-photon emission stimulated by the presence of an established seeder field. To obtain a significant conversion factor of the pump beam in a single pass through a crystal, extremely high single-pass gains are required. A pulse of 100 mJ at 800 nm contains on the order of 10^{17} photons. For such a pulse to grow from a single quantum fluctuation, a single-pass gain of the same order of magnitude is therefore necessary.

Since $g \propto I_p$, this in turn requires high instantaneous pump beam intensities. According to Duarte (2008, p. 28), optical parametric amplification in the absence of an established seeder field is in practice only possible with amplified ultra-fast pulses, for which single-pass gains are of the order of 10^{31}.

C.4 Optical Parametric Oscillation

To avoid the need for extremely high pump beam intensities, the non-linear medium may be placed in an optical cavity which allows at least either the signal or the idler beam to resonate. Provided that the round-trip gain exceed the losses of the cavity, the resonant beam can oscillate and build up to large values. Such a device is called an optical parametric oscillator.

Following Boyd (2008, §2.9, in particular p. 111), for a singly-resonant cavity with a single output coupler, the resonance threshold condition is given by

$$1 = \cosh(2gL)(1 - l), \tag{C.6}$$

where l denote the round-trip losses of the cavity. For small losses, $l \ll 1$, and low gains, $2gL \gtrsim 1$, this may be expressed as

$$g^2 L^2 = 2l. \tag{C.7}$$

Since $g \propto I_P$, (C.7) defines the threshold pump beam intensity for the establishment of stable oscillation in the optical parametric oscillator as a function of the reflectivities of the cavity mirrors.

In our case, the optical parametric oscillator is pumped by a pulse of approximately 5 ns. Such a pulse has a spatial extent of 1.5 m. In a cavity 10 cm in length, this allows for 15 round-trips of the idler beam. Given the single-pass gain of 70 for the crystal in use, this leads to a cavity gain of the order of $70^{15} \approx 10^{27}$ which is several orders of magnitude greater the gain of 10^{17}

4. Alternatively: parametric fluorescence, parametric emission or optical parametric generation.

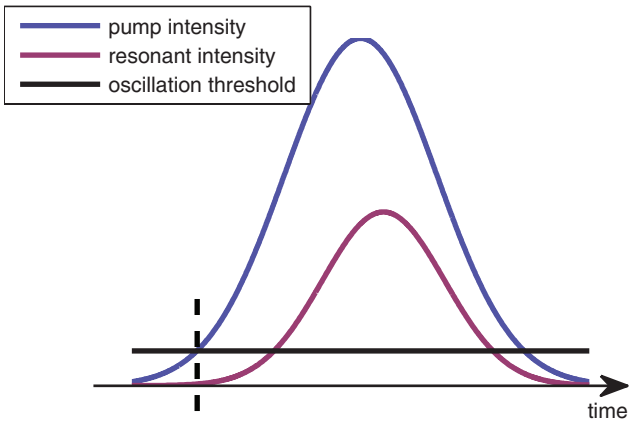

Figure C.2: Pulse shortening in optical parametric oscillators driven by pulsed pump beams

necessary to obtain a pulse of 100 mJ from a single vacuum fluctuation. The optical parametric oscillator in use in our experiment will therefore reliably "self-start", eliminating the need for a seeder beam.

For OPOs pumped by pulsed lasers, a shortening of the pulse can be observed. This is due to the fact that no oscillation and thus no generation of signal or idler occurs while the pump intensity is below the oscillation threshold of the cavity as is illustrated in Figure C.2. This leads to a delay between the onset of the pump beam and the onset of the generation of signal and idler.

Furthermore, for OPOs operating close to the oscillation threshold with nanosecond pulsed excitation, there may be insufficient time to build up stable oscillation. According to Arisholm (1999) this leads to significant pulse-to-pulse fluctuation of the energy in the signal and idler pulses generated. As resonant intensity approaches the limit where pump beam depletion occurs, these fluctuation become negligible.

Appendix D

Wiener Filters

Contents

A very accessible discussion of the basics of Wiener filtering is provided by Vaseghi (2000). Further discussion in the context of Bayesian estimation theory is available in Kay (1993) and in Trees (2001).

D.1 Derivation of a Linearly Optimised Filter Function

The fundamental problem to be solved is: given an input signal $Y(f)$ for a filter $W(f)$ producing an output signal $\hat{X}(f)$

$$\hat{X}(f) = W(f)Y(f), \tag{D.1}$$

what is the filter that produces best a desired signal $X(f)$? Given an error function $E(f)$ describing the difference between the filter output $\hat{X}(f)$ and the desired signal $X(f)$

$$\begin{aligned} E(f) =& X(f) - \hat{X}(f) && \text{(D.2)} \\ =& X(f) - W(f)Y(f) && \text{(D.3)} \end{aligned}$$

and the resulting mean square error function $MSE(f)$

$$MSE(f) = \mathsf{E}\left[|E(f)|^2\right] = \mathsf{E}\left[|X(f) - W(f)Y(f)|^2\right] \tag{D.4}$$

the problem can be formulated as the task to minimise the mean square error function with respect to the filter $W(f)$,

$$\frac{\partial MSE(f)}{\partial W(f)} = 0, \tag{D.5}$$

where $\mathsf{E}[X]$ denotes the expectation value of X over the ensemble of its generating random process.

It is convenient to reformulate the problem in terms of cross-power spectral densities [1]:

$$\begin{aligned} MSE(f) &= \mathsf{E}[E(f)E^*(f)] = P_{EE}(f) && \text{(D.7)} \\ P_{EE}(f) &= \mathsf{E}[(X - WY)(X - WY)^*] && \text{(D.8)} \\ &= P_{XX} - WP_{YX} - W^*P_{XY} + |W|^2 P_{YY} && \text{(D.9)} \end{aligned}$$

where it is implied for better readability that functions in capital letters are functions of f. If it is imposed that the signals and the filter functions must be real values in time space P_{EE} simplifies to:

$$P_{EE}(f) = P_{XX}(f) - 2W(f)P_{XY}(f) + W(f)^2 P_{YY}(f) \qquad \text{(D.10)}$$

It follows that

$$\frac{\partial MSE(f)}{\partial W(f)} = \frac{\partial P_{EE}(f)}{\partial W(f)} = -2P_{XY}(f) + 2W(f)P_{YY}(f) = 0. \qquad \text{(D.11)}$$

The filter function $W(f)$ is thus generally given by

$$W(f) = \frac{P_{XY}(f)}{P_{YY}(f)}. \qquad \text{(D.12)}$$

This type of filter is known as a Wiener filter after the work by Wiener (1949). The term "Wiener filter" describes the class of data-dependent, linear least squares error filters.

D.2 Application to the Problem of Additive Noise

To apply the above Wiener filter to the problem of additive noise one sets

$$Y(f) = X(f) + N(f) \qquad \text{(D.13)}$$

leading to

$$\begin{aligned} P_{XY}(f) &= P_{XX}(f) + P_{XN}(f) && \text{(D.14)} \\ P_{YY}(f) &= P_{XX}(f) + 2P_{XN}(f) + P_{NN}(f). && \text{(D.15)} \end{aligned}$$

1. The cross-power spectral density $P_{XY}(f)$ of two wide-sense stationary random processes X and Y is defined as :

$$P_{XY}(f) = \mathsf{E}[X(f)Y^*(f)]. \qquad \text{(D.6)}$$

If the noise $N(f)$ is uncorrelated with the original signal $X(f)$ the cross-power spectral density $P_{XN}(f)$ vanishes over the ensemble of the noise process [2]. Above equations thus simplify to

$$P_{XY}(f) = P_{XX}(f) \tag{D.16}$$
$$P_{YY}(f) = P_{XX}(f) + P_{NN}(f) \tag{D.17}$$

leading to the following filter function

$$W(f) = \frac{P_{XX}(f)}{P_{XX}(f) + P_{NN}(f)}. \tag{D.18}$$

When combined with the definition for the signal to noise ratio $SNR(f) = P_{XX}(f)P_{NN}^{-1}(f)$ the filter function can be re-expressed as

$$W(f) = \frac{SNR(f)}{SNR(f) + 1}. \tag{D.19}$$

This illustrates that the Wiener filter allows those spectral regions with a good signal to noise ratio to pass unattenuated while strongly attenuating the regions with a poor signal-to-noise ratio.

2. For correlated processes $X(f)$ and $Y(f)$, the expectation value of their product over the ensemble is non-zero. E.g. $P_{XX}(f) = \mathsf{E}\left[|X(f)|^2\right]$ if $Y(f) = X(f)$. Thus even if the phase of $X(f)$ changes from one realisation to the next, the expectation value will be greater than zero as the norm is by definition greater than zero.

In the alternative of uncorrelated processes however, even if $X(f)$ is perfectly deterministic as well as the norm of $Y(f)$, it is sufficient if $Y(f)$ has a random phase to let the product $X(f)Y(f)$ turn about the origin in the complex plane. The expectation value over the ensemble will thus vanish by collapsing to the origin in the complex plane.

Annexe E

Résumé Substantiel en Français

Contents

This chapter contains a French summary of the contents of this thesis. The main part of the thesis begins on page 1.

Introduction

(Résumé de Chapitre 1 en page 3.) Au cours des dernières décennies, les sociétés industrialisées ont connu une augmentation constante d'espérance de vie et une transformation de la pyramide des âges du profil «pyramidal » du début du 20ème siècle en un profil «champignon » ou même «pagode » dans certains cas. Une des conséquences de ce processus est une augmentation continue des taux d'incidence du cancer, puisque trois quarts des cas de cancer sont diagnostiqués chez des personnes âgées de 60 ans ou plus. Selon l'Organisation Mondial de la Santé (World Health Organisation (2009)), cancer est la principale cause de mortalité au monde. En 2004, il représentait $7,4$ million ou 13% des décès.

Avec les taux d'incidence du cancer prévisiblement à la hausse pour l'avenir, des modalités de traitement ne nécessitant pas d'environnement d'opération stérile et avec des taux de complications plus faibles seraient avantageux. Une méthode émergeante, « High Intensity Focused Ultrasound » (HIFU) ou en

français « ultrasons focalisés de haute intensité », est au seuil de la commercialisation et s'est avéré efficace, et plus important, non-invasive. Malheureusement, en ce moment les indications qui peuvent être traités avec cette nouvelle procédure sont assez limitées pour des raisons technologiques.

Au cours de ces travaux de thèse, la faisabilité d'une méthode qui pourrait éventuellement permettre d'élargir la gamme des indications qui peuvent être traités par HIFU a été explorée: plus précisément la possibilité de guider des HIFU par des signaux photoacoustiques émis par des agents de contraste exogènes. Cette méthode pourrait permettre des innovations des HIFU comme la compensation automatique de mouvement durant le traitement, le traitement de tumeurs dont la position n'est connue qu'approximativement, le ciblage moléculaire sélectif et le ciblage de tumeurs dans des environnements acoustiquement complexes comme le cerveau.

High Intensity Focused Ultrasound HIFU est un terme générique pour des méthodes chirurgicales utilisant des champs ultrasonores fortement focalisés visant à détruire une région cible en profondeur sans endommager les tissus environnants. La méthode est généralement utilisée pour l'ablation thermique des tissus, mais des modes d'utilisation non-thermiques sont possibles. L'approche HIFU est unique en ce qu'il n'est pas nécessaire d'insérer une sonde, ce qui en fait la seule technique ablative potentiellement non-invasive qui ne dépend pas de rayonnements ionisants. Dans le cadre du traitement de tumeurs, ceci est particulièrement important, car le risque d'ensemencement de cellules tumorales le long la voie d'insertion est éliminée. Les fréquences HIFU varient généralement entre plusieurs 100 kHz et quelques MHz. Selon la géométrie du transducteur et la fréquence utilisée, le foyer ultrasonore est typiquement une région en forme de grain de riz avec des dimensions 1 mm $\times$ 10 mm. Si la région à traiter est plus large, le foyer est typiquement balayé séquentiellement pour couvrir toute la région cible.

Effet Photoacoustique « L'effet photoacoustique », ou encore « l'effet thermoacoustique », décrit la conversion d'énergie radiative électromagnétique en énergie acoustique dans un milieu, par exemple, la génération de son par l'absorption de lumière. Découvert par Alexander Graham Bell en 1880, l'effet photoacoustique a été exploité systématiquement depuis les années 1970 pour la spectroscopie de gazs, par exemple pour étudier le trou d'ozone. Dans les années 1990 l'effet photoacoustique à été découvert comme moyen d'acquérir une image optique de milieux optiquement diffusant comme les tissus biologiques.

Focalisation par Renversement Temporel d'Ondes Photoacoustiques Bossy et al. (2006)ont démontré qu'il est possible d'utiliser du renversement temporel d'ondes photoacoustiques générées par un contraste optique unique dans un milieu acoustiquement aberrant pour automatiquement focaliser de

l'ultrason sur ce contraste optique. L'objectif de cette thèse était d'explorer les possibilités de la photoacoustique dans le cadre de la thérapie par HIFU.

Bases Théoriques

Propagation de la Lumière dans les Tissus (Résumé de Chapitre 2 en page 27.) Les origines de l'idée d'utiliser la lumière pour étudier l'intérieur du corps humain se trouvent dans le $19^{\text{ème}}$ siècle. Alors que le corps humain n'est manifestement pas transparent, la lueur rouge magique d'une main tenu devant une lampe dans l'obscurité montre qu'au moins une partie de la lumière peut y pénétrer. Alors que l'absorption de lumière dans les tissus est relativement faible, si des longueurs d'onde appropriées sont choisies, les tissus biologiques sont optiquement très diffusant. En conséquence, une proportion significative de la lumière utilisée pour éclairer les tissus est réfléchi et les longueurs de chemin efficace des photons dans le milieu est considérablement augmenté. La combinaison de ces deux effets conduit à une profondeur de pénétration de la lumière très limitée dans les tissus qui est de l'ordre de quelques millimètres pour la lumière balistique et de l'ordre de quelques centimètres pour la lumière multi-diffusée. Entre autres, cette pénétration faible rend l'imagerie optique directe des tissus biologiques techniquement difficile.

Pour la photoacoustique, les photons eux-mêmes n'agissent pas en tant que porteurs d'information sur le milieu, mais servent uniquement comme source d'énergie pour l'effet photoacoustique. L'information sur le milieu est porté par les ondes acoustiques générées. Par conséquent, la complexité des trajectoires des photons dans le milieu due à la diffusion n'est d'importance que dans la mesure où elle est liée à la distribution de l'énergie lumineuse dans le milieu.

La profondeur de pénétration de la lumière dans les tissus dépend essentiellement de l'absorption de lumière. Dans les tissus biologiques, deux chromophores dominent l'absorption due à leur abondance relative, l'eau et l'hémoglobine. En combinaison, ils limitent la gamme des longueurs d'onde optiques utiles à environ $700 - 900\,\text{nm}$.

Limites Médicales de l'Éclairage Lorsque des lasers sont utilisé dans un contexte de diagnostique médicale, il est particulièrement important d'assurer que l'éclairage ne cause pas de dommage aux tissus. La norme européenne NF EN 60825-1/A2 de Janvier 2006 réglemente le niveau d'exposition sans danger pour les utilisateurs de lasers afin d'éviter un des effets nocifs.

En utilisant les valeurs pour l'exposition maximale admissible définies par la norme et les caractéristiques de notre laser, on constate qu'à 800 nm l'exposition maximale admissible pour la peau est de $31\,\text{mJ cm}^{-1}$. Une impulsion de 130 mJ produite par notre laser doit donc être répartie sur une zone circulaire d'au moins $2,3\,\text{cm}$ en diamètre pour rester dans les limites d'exposition admissible. En outre, on peut montrer qu'un taux de répétition des impulsions

d'environ 10 Hz permet non seulement d'éclairer des tissus en continu, mais qu'il maximise également la puissance lumineuse moyenne qui peut être livré au tissu avec un laser produisant des impulsions d'une durée de l'ordre de nanosecondes.

L'Effet Photoacoustique Le cadre théorique utilisé pour décrire l'évolution spatio-temporelle des champs de pression et de densité dans les fluides est basée sur quatre principes fondamentaux: (1) la conservation de quantité de mouvement dans un fluide, (2) la conservation de masse dans un fluide, (3) une expression thermodynamique décrivant la relation entre des changements dans les trois variables d'état, densité ρ, pression absolue P et entropie par unité de masse s et (4) la conservation d'énergie, équilibrant l'échauffement et la diffusion thermique.

La forme la plus simple d'une équation acoustiques linéaire dans un fluide est basée sur la combinaison de ces principes avec quatre hypothèses: (1) il n'y a pas de sources acoustiques, (2) le milieu est supposé être acoustiquement homogène et de viscosité négligeable, (3) le fluide subit uniquement des transformations adiabatiques sur l'échelle de temps acoustique et (4) toutes les équations sont linéarisées aux variations de premier ordre. Sous ces hypothèses, l'équation d'onde linéaire homogène décrivant l'évolution d'un champ de pression en fonction de temps et d'espace peut être démontré

$$\left(\nabla^2 - \frac{1}{c_s^2}\frac{\partial^2}{\partial t^2}\right) p\left(\mathbf{r}, t\right) = 0, \tag{E.1}$$

où $p\left(\mathbf{r}, t\right)$ désigne le champ de pression acoustique et c_s la vitesse isentropique du son.

La théorie linéaire de le photoacoustique est basé sur les mêmes hypothèses que la théorie de l'acoustique linéaire sans sources à une exception près: l'échauffement du milieu agit comme une source d'ondes acoustiques - et donc le processus n'est plus isentropique à l'endroit de l'échauffement. Toutefois, il est toujours présumé que la propagation des ondes est adiabatique.

En définissant une fonction de chauffe $H\left(\mathbf{r}, t\right) = \frac{1}{V_0}\frac{\delta q}{dt}$ comme le taux de chaleur absorbée q par unité de volume V_0 ; sous l'hypothèse que la diffusion de chaleur est négligeable sur les échelles temporelles et spatiales pertinentes, on peut obtenir que l'équation d'onde photoacoustique

$$\left(\nabla^2 - \frac{1}{c_s^2}\frac{\partial^2}{\partial t^2}\right) p\left(\mathbf{r}, t\right) = -\frac{\Gamma}{c_s^2}\frac{\partial H}{\partial t}, \tag{E.2}$$

où Γ est le premier coefficient de Grüneisen.

Il peut être démontré que pour un milieu infini et homogène, initialement au repos, le champ de pression acoustique est donnée par

$$p\left(\mathbf{r}, t\right) = \frac{\Gamma}{c_s^2}\frac{\partial}{\partial t}\left[G \underset{\mathbf{r},t}{\otimes} H\right]\left(\mathbf{r}, t\right), \tag{E.3}$$

où G est la fonction de Green pour la dimension de l'espace considérée.

Il peut également être démontré que la fréquence de la plus haute densité d'énergie des ondes photoacoustiques est donnée par $f_{max} \sim {}^{c_s}/_{d}$, où d est la taille caractéristique de l'absorption optique. En outre, l'intensité photoacoustique I_{PA} est proportionnelle au carré de l'intensité lumineuse I_{light}: $I_{PA} \propto I_{light}^2$.

Instruments

(Résumé de Chapitre 3 en page 51.) L'objectif de ce chapitre de la thèse est de décrire en détail les composantes principales du dispositif expérimental utilisé lors des travaux de cette thèse.

Source de Lumière Pour générer l'énergie nécessaire pour l'effet photoacoustique, la combinaison d'un laser et d'un oscillateur paramétrique optique a été choisie. Cela permet une éclairage des échantillons dans une large gamme de longueurs d'onde différentes, en particulier dans la fenêtre diagnostique.

Le laser de pompe utilisé pendant les travaux de cette thèse était un Surelite II-10 par Continuum, CA, USA. Le Surelite II-10 est un laser Nd:YAG pompé par une lampe de flash, Q-switché et doublé en fréquence. La lumière produite est composé de 50% de lumière polarisée horizontalement à 1064 nm (300 mJ) et de 50% de lumière à 532 nm à polarisation verticale (300 mJ) avec durée d'impulsion $4-6$ ns. Selon Continuum (2002), le faisceau est d'environ 7 mm de diamètre et a une divergence de $0,3$ mrads.

L'OPO utilisé était un OPO Surelite Plus, un système OPO contrôlé par ordinateur avec un cristal BBO, une cavité résonnant pour l'idler et double passage du faisceau pompe. Lorsque pompé par un Surelite II-10 avec 300 mJ à 532 nm et une durée d'impulsion de $4-6$ ns, il produit environ 130 mJ combinés dans le faisceau idler et le faisceau signal, ce qui correspond à un facteur de conversion de puissance de 43%. L'impulsion du faisceau signal a une durée de $2-4$ ns et l'impulsion du faisceau idler une durée de $3-5$ ns. Les deux faisceaux, idler et signal, sont polarisés horizontalement.

Mise en Forme de Faisceau Il a été observé que la forme spatiale du faisceau signal de l'oscillateur paramétrique optique est fortement dépendant du choix de la longueur d'onde. Plus précisément, la forme de la distribution angulaire varie d'une forme gaussienne à une forme d'annaux avec des hot-spots apparaissant à différents endroits dans le faisceau. Ceci pose un problème pour la méthode explorée dans ce travail.

Une méthode pour la mise en forme de l'éclairage qui a été exploré fait usage de réseaux de microlentilles. Ces réseaux de microlentilles sont composé de lentilles avec des diamètres de l'ordre de dizaines de micromètres qui sont moulés dans un structure de treillis sur la surface d'une lame de verre. En

utilisant une montage optique adapté, des tels réseaux peuvent être utilisés pour produire des champs spatialement homogènes à partir de faisceaux de forme quasiment arbitraire. Il peut être démontré qu'en focalisant un faisceau derrière un réseau de microlentilles un spot d'éclairage homogène avec des bords raides peuvent être produites dans le plan focale. Le diamètre de la tache est donnée par $2\,d\tan(\theta)$, où d est la distance entre le réseau de microlentilles et le plan focal et θ l'angle de divergence du réseau de microlentilles.

Pour toute solution de mise en forme de faisceau, l'efficacité énergétique est un critère de performance essentiel. Un effort a été fait de comprendre l'origine des pertes de transmission non négligeables des réseaux de microlentilles. Il a été constaté que trois facteurs contribuent à un degré similaire: (1) les réflexions aux interfaces des matériaux, (2) la densité maximale d'empilement de la forme des lentilles dans un empilement compact et (3) la compacité de l'empilement des microlentilles. Il a été constaté que une transmission sans pertes n'est possible que si trois conditions sont satisfaites: (1) la forme des lentilles doit être empilable avec une densité de 1, (2) le processus de fabrication doit permettre la réalisation d'un empilement compact, (3) des traitement anti-réfléchissant doivent être utilisés.

Livraison du Faisceau Pour la facilité d'utilisation dans Des applications cliniques, la livraison du faisceau par un système flexible serait souhaitable. Un choix évident serait la livraison du faisceaux par des guides de lumière comme les fibres optiques. Toutefois, les densités d'énergie lumineuse impliqué dans l'expérience en font un problème non trivial. Trois guides de lumière différentes ont été explorés: une fibre de silice 1 mm d'épaisseur, une fibre à coeur liquide de 8 mm et un faisceau de fibres de silice fines avec extrémités fusionnées. Il a été constaté que seul ce dernier supporte les densités d'énergie mises en jeu sans détérioration évidente.

Électronique et Transducteurs à Ultrasons Les expériences présentées dans ce document ont été réalisées avec deux types d'électronique de renversement du temps différentes. Des électroniques de renversement du temps sont des systèmes séquenceur/générateur de signaux/numériseur avec des voies indépendants, entièrement programmables, contrôlé par ordinateur. Ils peuvent être utilisés pour contrôler tous les éléments d'une barrette ultrasonore en émission et réception de manière indépendante.

Pour toutes les acquisitions photoacoustique un système « Lecoeur Open System » a été utilisé. Comme ce système ne peut pas supporter les énergies nécessaires pour le HIFU, le système de thérapie cérébral prototype de Supersonic Imagine à CIERM Paris a été utilisée pour toutes les expériences HIFU.

Au cours des travaux de cette thèse principalement deux transducteurs ont été utilisés. Le premier était une sonde à 64 éléments construit par Vermon,

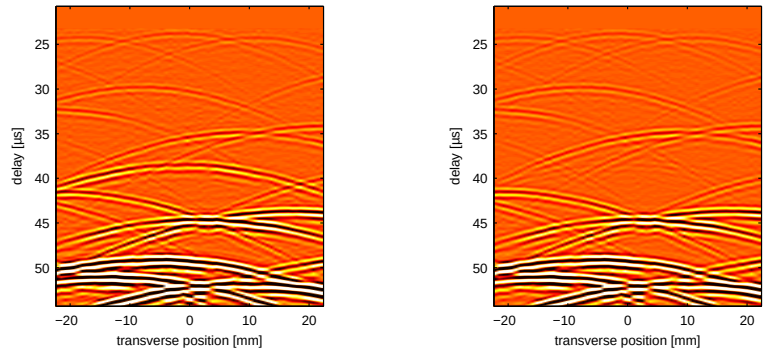

(a) $\lambda_1 = 673\,\mathrm{nm}$ (b) $\lambda_2 = 730\,\mathrm{nm}$

FIGURE E.1: Images B-scan des signaux photoacoustiques filtrées obtenu avec un fantôme. Limites de l'échelle de couleurs: ± 0.05 unités d'appareil

France, avec une fréquence centrale de $1,5\,\mathrm{MHz}$ et une bande passante pulse-écho de 65% à $-6\,\mathrm{dB}$. La sonde a un pas de $0,7\,\mathrm{mm}$ et une hauteur de $13\,\mathrm{mm}$. Elle est focalisé en élévation à $60\,\mathrm{mm}$.

Le deuxième était une barrette HIFU linéaire à 128 éléments construit par Imasonic, France, avec une fréquence centrale de $1,65\,\mathrm{MHz}$ et une bande passante pulse-écho de 45% à $-6\,\mathrm{dB}$. Elle a un pas de $0,7\,\mathrm{mm}$ et une hauteur de $20\,\mathrm{mm}$. Elle est focalisé en élévation à $64\,\mathrm{mm}$.

Preuve de Principe & Identification des Défis

(Résumé de Chapitre 4 en page 75.) Comme mentionné ci-dessus, de nombreux chromophores endogènes sont présents dans les tissus biologiques. Lors d'une exposition de tissus à des impulsions de lumière, des ondes photoacoustiques sont générées par les différentes structures tissulaires par l'effet photoacoustique. Ces ondes sont généralement exploitées pour l'imagerie photoacoustique des tissus, mais dans le cadre de ce travail, où une seule région discrète dans le tissu doit être ciblé, ce fond photoacoustique est un effet gênant.

Pour utiliser des signaux photoacoustiques pour cibler des ultrasons, les signaux en provenance de la zone cible doivent être extraits ou isolés de ce fond photoacoustique. Au cours de ce travail, il a été étudié si un agent de contraste optique à sélectivité spectrale pourrait être utilisée pour extraire les signaux d'une cible de ceux d'un fond non sélective.

Guidage d'Ultrasons avec un Contraste Optique Sélectif À la base, l'idée d'utiliser un cible optique sélectif dans un environnement non sélectif est la suivante: Supposant un milieu contient un nombre d'absorbeurs optiques discrets, dont un seul absorbe la lumière uniquement à une seule longueur

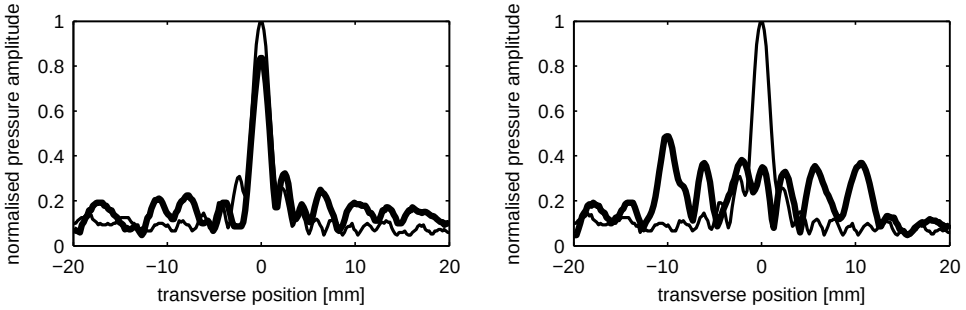

(a) Guidé par signal isolé du cible. (b) Guidé par les signaux obtenu à λ_1.

FIGURE E.2: Distributions d'amplitude de pression obtenue par guidage photoacoustique. La ligne en gras indique la répartition obtenue par guidage photoacoustique, la ligne fine est la distribution obtenue par focalisation traditionnelle par loi de retard.

d'onde λ_1, tandis que tous les autres absorbent la lumière à tous les longueurs d'onde. Si ce milieu est alors éclairé à deux longueurs d'onde différentes, λ_1 et λ_2, les ondes photoacoustiques résultant sont identiques, sauf pour un front d'onde manquante à λ_2 due au contraste optique sélectif.

Figure E.1 montre les fronts d'onde photoacoustiques enregistrées en utilisant un fantôme composé d'un ensemble de tubes en PVC dont tous sauf un ont été remplis avec une solution d'encre de chine noire. Un seul tube est rempli d'une solution d'encre verte et sert comme contraste optique sélectif.

En utilisant des algorithmes adaptés, il est possible d'extraire le front d'onde apparaissant seulement à λ_1 à $t = 38 - 42\,\mu$s. En renversant ce front d'onde temporellement et en calculant le produit de convolution avec une onde continue, de l'ultrason en mode HIFU peut être guidé vers son origine. E.2 montre les distributions d'amplitude de pression obtenues en balayant un hydrophone le long d'une ligne dans le plan du contraste optique sélective. On peut observer qu'uniquement en isolant le signal photoacoustique de la cible une bonne focalisation peut être obtenu.

Au cours des travaux présentés dans ce chapitre de la thèse, plusieurs complexes de problèmes sont devenus évidents et ont guidé les travaux suivants. (1) Le niveau de bruit de l'électronique de détection est le facteur limitant pour la profondeur maximale à laquelle des informations utiles peuvent être extraites. Des techniques de réduction de bruit avancées doivent être explorées. (2) L'isolation des signaux de la cible de ceux du font photoacoustique a été non trivial, même dans le cas du fantôme assez bien contrôlé utilisé dans les travaux présentés dans ce chapitre de la thèse. Il est clair qu'une approche différente pour l'extraction des signaux en provenance du cible sera nécessaire pour des tissus biologiques. (3) Au cours des travaux de ce chapitre de la thèse

l'électronique de renversement du temps et la sonde à ultrasons ont été conçus pour l'échographie diagnostique. Il n'est pas évident que les résultats se traduisent de façon transparente à des appareils compatibles au HIFU due au fait que lors de la conception de dispositifs les deux applications imposent souvent des exigences contradictoires. (4) Les résultats présentés dans ce chapitre de la thèse sont basées sur un fantôme très idéalisée. Il est clair que les tissus biologiques présenteront une nouvelle série de défis, en particulier en ce qui concerne la répartition de la lumière.

Réduction de Bruit & Extraction de Cible

(Résumé de Chapitre 5 en page 89.) L'analyse de l'expérience présentée dans ce chapitre de ce document a montré que le guidage photoacoustique de l'HIFU dépend essentiellement de deux facteurs clés. il est nécessaire d'être capable d'une part de détecter les signaux photoacoustique faibles de la cible et d'autre part d'isoler les signaux photoacoustique de la cible de ceux du fond photoacoustique. Ces deux défis sont liés intrinsèquement. En particulier, le meilleur algorithme d'extraction de cible est susceptible de produire des résultats insatisfaisants si la proportion de bruit dans les données à traiter est trop grand.

Contributions Déterministes au Bruit Le premier type de bruit rencontré avec le « Lecoeur Open System » sont des pics dans le signal détecté avec position et forme déterministe. Ils ont été identifiés comme des impulsions de déclenchement électronique qui contrôlent le fonctionnement du système. Par une architecture exacte des séquences d'acquisition, il est possible d'éviter des signaux fantômes à des positions critiques dans les données acquises. Quatre zones de données sont affectés: (1) les 100 premiers points et (2) les 20 derniers points d'échantillonage de tout enregistrement, (3) les 300 premiers point d'échantillonage par rapport au début d'une séquence et (4) les points $x_{bank}-2$ à $x_{bank}+150$ de tout enregistrement où x_{bank} est la taille de la rangée du mémoire d'émission.

Un deuxième type de bruit est une oscillation déterministe à 20 MHz résultant d'une infiltration de l'horloge interne dans le circuit de réception. Cela peut facilement être éliminé par filtrage de Fourier.

Filtrage Bande-Passante Optimale En plus des contributions déterministe mentionné ci-dessus, le circuit de réception de l'électronique de renversement du temps utilisé pour les expériences photoacoustiques génère du bruit aléatoire avec une bande passante d'environ $0,1$ à $12\,\mathrm{MHz}$ et une densité spectrale de puissance de forme non-triviale. Étant donné que le système de détection ne peut détecter des signaux acoustiques hors d'une bande passante de $0,1$ à $3\,\mathrm{MHz}$, il est clair qu'une réduction de bruit significatif peut être obtenu

par filtrage de bande passante. Il a été constaté qu'un filtre de Wiener définie en utilisant la densité de puissance spectrale dérivée du bruit et de la fonction de transfert du système permets une réduction du bruit d'environ 10 dB.

Transformation de Radon Hyperbolique En plus de la bande passante, les signaux photoacoustique ont une autre propriété qui permet de les distinguer du bruit: à la différence de bruit, des signaux photoacoustique proviennent d'un endroit physique. En conséquence, la forme des fronts d'onde photoacoustique n'est pas arbitraire, mais contrainte physiquement. Une approche d'exploiter ces contraintes est d'utiliser une transformation paramétrant la position de l'origine des signaux photoacoustiques. Ce type de transformation est connu sous le nom « transformation de Radon généralisée » et il est similaire à l'opération de routine de la formation d'image dans tous les appareils d'imagerie échographique connu dans la communauté acoustique en tant que « beamforming ». Les transformations de Radon sont d'intérêt dans le cadre de ce travail pour deux raisons: (1) ils permettent une réduction de bruit supplémentaire dans l'espace image et la récupération de la forme du front d'onde avec une transformation inverse approximatif et (2) ils peuvent simplifier l'extraction des fronts d'onde d'une cible dans un environnement avec de nombreuses sources photoacoustiques.

Algorithme d'Extraction de Cible Dans l'analyse de l'expérience présentée dans Chapitre 4 en page 75, plusieurs points faibles de l'algorithme d'extraction de cible utilisé pour ces expériences ont été mis en évidence. Nos collaborateurs, Vincent Jugnon et Habib Ammari du département de mathématiques appliquées, ont proposé un algorithme qui tente de remédier certains de ces problèmes:

Deux jeux de données à deux dimensions obtenues à deux différentes longueurs d'onde optiques sont divisés en un nombre de carreau. Les données de chaque carreau sont renormalisées et remis à l'échelle de façon indépendante et un facteur de dissemblance entre le même carreau aux deux longueurs d'onde est calculée. En binarisant la carte des facteurs de dissemblance un masque peut être obtenue qui permet l'isolation des régions des données qui sont différentes dans les deux acquisitions.

Il a été constaté que, bien que l'algorithme est assez efficace dans certaines situations, il a un certain nombre de faiblesses importants: (1) Tout algorithme qui s'appuie sur l'identification des variations entre deux ensembles de données est susceptible à sélectionner activement des régions où du bruit domine. (2) Si le bruit dans les carreaux est négligeable et les signaux photoacoustiques de la cible ne disparaissent pas complètement, mais changent simplement en amplitude, l'algorithme ne détecte pas de différence appréciable entre les deux signaux due à la mise à l'échelle des données. (3) L'algorithme est très sensible au mouvement des tissus.

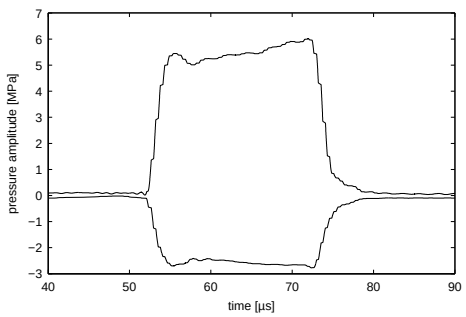

(a) Amplitude de la pression obtenu avec le transducteur HIFU d'Imasonic en version finale.

(b) Élévation de température à l'intérieur du transducteur HIFU d'Imasonic pour 5 MPa au foyer.

FIGURE E.3

Sur le Problème des Approches Spectroscopiques Il serait avantageux d'exploiter le savoir a priori sur le spectre d'absorption de l'agent de contraste attaché à la cible. Il a est démontré dans Section 2.3 que la pression acoustique est proportionnelle à l'énergie absorbée lumineux. Il peut donc paraître relativement simple à utiliser l'amplitude du signal photoacoustique pour mesurer le coefficient d'absorption de la source photoacoustique. Malheureusement, la fluence lumineuse locale en profondeur dépend des propriétés optiques du milieu que la lumière avait à parcourir pour atteindre l'endroit de profondeur ce qui rend les approches spectroscopiques techniquement difficiles.

Guidage Photoacoustique de HIFU

(Résumé de Chapitre 6 en page 117.) Lors de la tentative d'appliquer la méthode à des barrettes ultrasonores pour HIFU, il faut prendre soin que trois paramètres clé ne se détériorent pas. Le transducteur HIFU devrait être comparable ou supérieure à la barrette diagnostique en ce qui concerne la sensibilité de détection et de bande passante afin d'assurer que des signaux photoacoustiques peuvent être détectés avec la nouvelle barrette. En plus, la barrette HIFU doit être capable de résister aux énergies HIFU.

Caractérisation de Transducteurs HIFU Au cours des travaux de cette thèse, deux prototypes de transducteurs qui visaient à répondre aux exigences particulières de HIFU guidé par photoacoustique ont été développé et évalués de manière indépendante, en coopération avec Vermon, la France et Imasonic, France. Les caractéristiques de réception suivantes ont été déterminées. Sonde Vermon diagnostique: fréquence centrale $f_c = 1.30\,\text{MHz}$, bande passante en réception $f_c \times 86\%$ à $-6\,\text{dB}$, sensibilité maximale relative $0\,\text{dB}$. Prototype HIFU

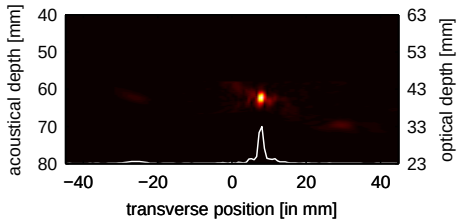

(a) Image beamformé des signaux photoacoustiques isolés de la cible.

(b) Image des signaux photoacoustique à 700 nm originant à la profondeur de la cible.

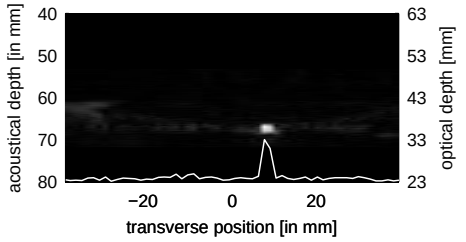

(c) Échographie de la lésion produite par HIFU guidée par les signaux isolés de la cible.

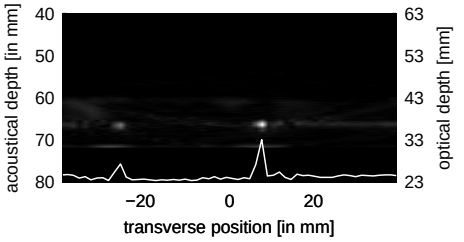

(d) Échographie des lésions produites par HIFU guidé par tous les signaux photoacoustique originant à la profondeur de la cible.

FIGURE E.4

de Vermon: fréquence centrale $f_c = 1.44\,\text{MHz}$, bande passante en réception $f_c \times 82\%$ à $-6\,\text{dB}$, sensibilité maximale relative $+3.5\,\text{dB}$. Prototype HIFU d'Imasonic: fréquence centrale $f_c = 1.61\,\text{MHz}$, bande passante en réception $f_c \times 55\%$ à $-6\,\text{dB}$, sensibilité maximale relative $+2.9\,\text{dB}$. De plus en utilisant un thermocouple interne il a été vérifiée que l'élévation de la température interne du capteur prototype d'Imasonic n'approche pas des niveaux critiques. Cela n'a pas été possible pour le prototype de Vermon car le thermocouple a été oublié au moment de la fabrication. Un transducteur équivalent au prototype d'Imasonic a donc été obtenu pour les expériences HIFU et sa performance vérifié. (Voir Figure E.3.) Il a été vérifié que des nécroses peuvent être induit avec ce transducteur dans du blanc de poulet et du foie de veau.

Guidage Photoacoustique de HIFU Pour démontrer que des signaux photoacoustiques peuvent en effet être utilisé pour guider de l'HIFU, l'expérience suivante a été effectuée: D'abord, les signaux photoacoustiques d'un fantôme ont été acquises comme en Chapitre 4 en page 75 et la signature de la cible extraite. Les signaux de la cible ont ensuite été utilisés pour focaliser de l'HIFU sur une plaque de PMMA ce qui produit des lésions sur l'exposition à l'HIFU qui peuvent être détectés par échographie. En comparant la position de des lésions avec la position de la cible photoacoustique, il a été confirmé que des signaux photoacoustiques peuvent être utilisés pour guider HIFU.

Figures E.4(a,c) montrent clairement qu'une lésion unique est produit à la position de la cible optiquement sélectives quand de l'HIFU est guidé par les signaux photoacoustiques isolés de la cible. En outre figures E.4(b,d), obtenu en guidant de l'HIFU par des données contenant non seulement la cible optique sélective, mais aussi le fond photoacoustique, illustrent une fois de plus l'importance d'une extraction de cible efficace.

Bossy et al. (2006) avaient montré qu'il est possible de focaliser de l'ultrason sur un contraste optique. L'une des grandes incertitudes au début des travaux pour cette thèse était si ce résultat restait valable avec des dispositifs compatible à l'HIFU. Alors que dans la conception de transducteurs HIFU la dissipation de chaleur est une considération importante, des facteurs tels que la bande passante et la sensibilité de réception sont généralement pas considérées. Les résultats présentés dans ce chapitre de la thèse démontrent qu'avec des transducteurs construits avec les contraintes de la photoacoustique à l'esprit, il est possible de détecter des signaux photoacoustiques faibles et emmètre de l'HIFU avec le même transducteur. Cela est essentiel si de l'HIFU doit être guidé par renversement temporel d'ondes photoacoustiques, mais simplifie également par exemple le suivi du traitement comme les cadres de référence pour les ultrasons thérapeutiques et diagnostiques sont identiques.

Vers des Applications *in Vivo*

(Résumé de Chapitre 7 en page 135.) Chapitres 4 à 6 de cette thèse mettent l'accènt sur le développement de solutions pour des défis technologiques majeurs pour la guidage d'HIFU par photoacoustique. Toutefois, les difficultés supplémentaires introduites par des échantillons biologiques ont été mentionnés qu'en passant. Ce chapitre de la thèse présente quelques-unes des tentatives qui ont été réalisés dans la transition de la méthode des fantômes académique vers des applications in vivo.

Développement d'Agents de Contraste Optiques Vectorisés Trois groupes de l'Institut Curie, spécialisant en chimie médicale et physique, ont développé en collaboration des agents de contrastes optiques, biologiquement compatibles et vectorisés, destinés à la guidage d'HIFU par photoacoustique. Au cours des travaux pour cette thèse le développement de ces agents de contraste a été soutenu et les performances des différents composés évalués.

Due à l'information limitée sur le métabolisme et les propriétés des tissus tumoraux, il a été décidé de poursuivre deux approches en parallèle, un agent de contraste moléculaires (ICG) et un agent de contraste plasmoniques (nanobatonettes d'or). (Voir Figure E.5(a,b).)

Johannes et al. (2002)ont mis au point un transporteur moléculaire universel pour cibler des récepteurs Gb3 à la base de la toxine de Shiga. La sous-unité B de la toxine Shiga (STx) est non-toxique et se lie au récepteur Gb3 à la sur-

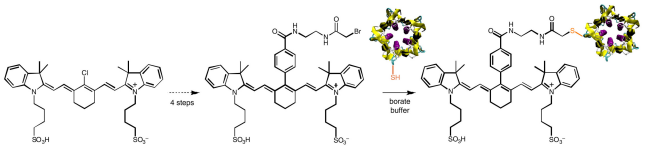

(a) Vectorisation d'ICG avec STxB. Illustration (légèrement modifié): Nicolas Bogliotti

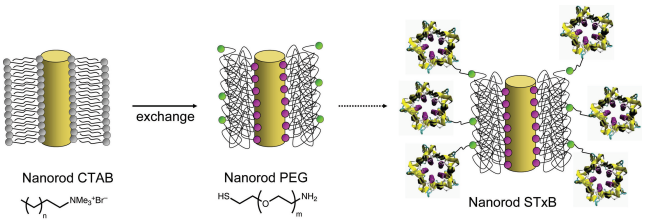

(b) Vectorisation de nano-batonettes d'or. Illustration (légèrement modifié): Nicolas Bogliotti

FIGURE E.5

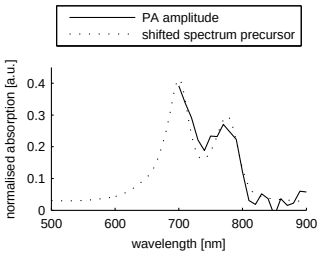

FIGURE E.6: Amplitude photoacoustique normalisée d'une suspension de cellules incubées avec ICG-STxB.

face des cellules et est internalisé. Comme l'expression de Gb3 est élevé dans de nombreuses cellules tumorales STxB peut être utilisé comme un vecteur universel pour cibler des molécules aux cellules tumorales.

Vérification du Ciblage Cellulaire En préparation d'expériences pour tester la capacité d'extraire les signaux photoacoustiques d'un cible marquée par un agent de contraste optique vectorisé, plusieurs expériences ont été menées en parallèle au développement des agents de contraste. Dans des premières expériences des cellules Gb3 positives et Gb3 négatives ont été cultivées et incubées avec ICG-STxB. Après lavage et concentration des cellules, les suspensions cellulaires ont été injectés dans les capillaires dans un gel et imagées photoacoustiquement. Il a été constaté que le spectre d'absorption des suspensions mesuré par photoacoustique présente un assez bon accord avec le spectre d'absorption d'une molécule précurseur de l'ICG-STxB. (Voir Figure E.6.)

Identification Spectroscopique d'Échantillons de Tumeurs Pour vérifier si cette dependance du longueur d'onde du signal photoacoustique pourrait être exploité afin d'isoler les signaux photoacoustiques d'une cible marquée, des des agents de contraste en cours de développement ont été injectés directement dans des tumeurs xénogreffes chez la souris. Au total, il y avait six échantillon de tumeur: deux comme contrôle, deux avec ICG-STxB, un avec un précurseur de l'ICG vectorisé et un avec des nano-batonnets d'or. Les tumeurs et deux échantillons de muscle ont ensuite été incorporé dans un gel d'agar pour être imagé par photoacoustique. Il a ensuite tenté d'identifier les échantillons de tumeurs par leur spectre photoacoustique.

Il a été constaté que, même avec une sonde pour la fluence lumineux locale et un environnement optiquement bien contrôlé, il reste difficile d'obtenir des spectres d'absorption sans ambiguïté à partir de la réponse photoacoustique d'échantillons biologiques. S'il est encore trop tôt pour tirer des conclusions définitives, mais il semblerait que, même si ICG-STxB est injecté à sa concentration maximale directement dans des tumeurs, l'absorption due à ICG-STxB est insuffisante pour modifier signicativement le spectre d'absorption naturelle des tissus. Étant donné que la concentration maximale d'ICG-STxB est limitée par la concentration de STxB dans la solution, il semblerait qu'un agent de contraste GNR-STxB (par exemple des nano-batonnets d'or vectorisées) peut être une approche plus prometteuse.

Conclusions & Perspectives

(Résumé de Chapitre 8 en page 159.) D'après les travaux antérieurs de Bossy et al. (2006), les ondes photoacoustiques générées par un contraste optique unique peuvent être utilisées pour focaliser des ultrasons par renversement temporel dans un milieu acoustiquement complexe. L'objectif des travaux de cette thèse était d'étudier les améliorations que la photoacoustique pouvait apporter à la thérapie par ultrasons focalisés de haute intensité (HIFU) et d'identifier les principaux défis d'implémentation en clinique.

Dans une expérience de validation de principe présentée dans Chapitre 4 en page 75, il a été démontré qu'il est possible de cibler des ultrasons à un niveau diagnostic sur un contraste optique à sélectivité spectrale entouré de plusieurs contrastes non-sélectifs. L'analyse de cette expérience a permis l'identification de plusieurs ensembles de problèmes qui présentent des obstacles majeurs à la mise en œuvre d'un guidage des HIFU par photoacoustique dans les tissus biologiques en général et dans un contexte clinique en particulier.

Un premier défi provient de la faiblesse de l'amplitudes des ondes photoacoustiques par rapport aux amplitudes acoustiques généralement rencontrées en acoustique pour le diagnostic. Il a été constaté que la réduction du bruit est essentielle pour avoir accès aux signaux provenant de sources photoacoustiques situées à des profondeurs de plusieurs centimètres dans des tissus biologiques, à

cause de la forte atténuation de l'intensité lumineuse avec la profondeur. Dans la section section 5.1 en page 89 plusieurs méthodes ont été développées pour exploiter les contraintes physiques connues sur les signaux photoacoustiques par rapport au bruit de l'instrument pour filtrer les données acquises.

Une deuxième difficulté pour le guidage des HIFU par photoacoustique surgit de la nécessité d'isoler les signaux provenant de la cible parmi ceux du fond photoacoustique. Avec des collaborateurs du Département de Mathématiques Appliquées de l'Ecole Polytechnique/Ecole Normale Supérieure, des premières tentatives pour developper un algorithme pour une isolation automatique des cibles ont été présentées dans la section section 5.2 en page 107.

Un point majeur d'incertitude concernait la faisabilité de la méthode avec des instruments compatibles HIFU, car les appareils d'HIFU et les appareils d'échographie ont des contraintes de conception très différentes. Il a été montré dans Chapitre 6 en page 117 qu'avec des transducteurs construits avec les contraintes de la photoacoustique et des HIFU à l'esprit, il a été possible de satisfaire à la fois aux exigences de la dissipation de la chaleur pour éviter la surchauffe des transducteurs thérapeutiques ainsi que la nécessité d'une haute sensibilité pour permettre la détection des signaux photoacoustiques faibles. Ce résultat encourageant en combinaison avec les premiers pas vers le developpement d'agents de contraste vectorisé adaptés à l'application (Chapitre 7 en page 135) ouvre la porte à la poursuite des travaux sur les défis restant pour une mise en œuvre d'un guidage photoacoustique des HIFU in vivo.

Nomenclature

Blanching of tissue describes the change of color of tissue towards a whitish appearance as a result of interrupted blood flow.

Carcinomatosis describes the medical condition where cancer has spread widely through the body.

A craniotomy is a surgical procedure in which part of the skull bone is removed to gain access to the brain.

CTAB short for Cetrimonium bromide $(C_{16}H_{33})N(CH_3)_3Br$ is a cationic surfactant widely used in synthesis of gold nanoparticles.

Diploë refers to the spongy structure found at the interior of many bones.

Elastographic imaging refers to a methods which provides a map of the elasticity parameters of the medium under investigation.

Hepatocellular carcinoma is a liver cancer. It often arises as a result of infection with hepatitis B or C or liver cirrhosis.

Ménière's disease is a symptomatic diagnosis for a disorder of the inner ear that can affect hearing and balance.

Parenchymal injury describes injury to the bulk of internal organs.

PBS is the acronym of phosphate buffered saline, a water-based solution containing sodium chloride, sodium phosphate - and depending on application potassium chloride and potassium phosphate. It is commonly used as a buffer solution for biological research.

PEG is the acronym of polyethylene glycol, a bio-compatible polymer.

A stereotactic frame is a surgical tool that can be immovably attached to the patient to provide a fixed frame of reference during a surgical procedure. This allows the surgeon to located a position identified on an image within the body.

A trocar is a surgical instrument that consists of a sharply pointed bar which is inserted into a tube to allow easier insertion of the tube into the body. It is used in minimally invasive surgery to open ports into the body.

Bibliography

Analog Devices. AD604: dual, ultralow noise variable gain amplifier. Technical Report D00540-0-4/10(F), April 2010. URL http://www.analog.com/static/imported-files/data_sheets/AD604.pdf. Cited on pages 96 and 97.

Gunnar Arisholm. Quantum noise initiation and macroscopic fluctuations in optical parametric oscillators. *Journal of the Optical Society of America B*, 16(1):117–127, January 1999. doi:10.1364/JOSAB.16.000117. Cited on page 183.

Bastien Arnal, Pernot Mathieu, and Mickael Tanter. Combined real time ultrasound-thermometry and elastography imaging during HIFU therapy : ex-vivo results. Lyon, May 2010. Cited on page 9.

J.-F. Aubry, M. Tanter, J. Gerber, J.-L. Thomas, and M. Fink. Optimal focusing by spatio-temporal inverse filter. II. experiments. application to focusing through absorbing and reverberating media. *The Journal of the Acoustical Society of America*, 110(1):48–58, July 2001. doi:10.1121/1.1377052. Cited on page 12.

Alexander Graham Bell. On the production and reproduction of sound by light. *Proceedings of the American Association for the Advancement of Science*, 29:115–136, 1881a. URL http://books.google.com/books?id=7jYLAAAAYAAJ. Cited on page 16.

Alexander Graham Bell. *Upon the production of sound by radiant energy.* Gibson Brothers, printers, Washington, 1881b. URL http://www.archive.org/details/uponproductionof00bellrich. Paper read before the National Academy of Sciences, April 21, 1881. Cited on pages 16 and 17.

G. Beylkin. Discrete radon transform. *Acoustics, Speech and Signal Processing, IEEE Transactions on*, 35(2):162–172, 1987. ISSN 0096-3518. Cited on pages 104, 105, and 107.

Sibaprasad Bhattacharyya, Shuyan Wang, Daniel Reinecke, William Kiser, Robert A. Kruger, and Timothy R. DeGrado. Synthesis and evaluation of

Near-Infrared (NIR) Dye-Herceptin conjugates as photoacoustic computed tomography (PCT) probes for HER2 expression in breast cancer. *Bioconjugate Chemistry*, 19(6):1186–1193, June 2008. doi:10.1021/bc700482u. Cited on pages 137 and 138.

Emmanuel Bossy, Khalid Daoudi, Albert-Claude Boccara, Mickael Tanter, Jean-Francois Aubry, Gabriel Montaldo, and Mathias Fink. Time reversal of photoacoustic waves. *Applied Physics Letters*, 89(18):184108–3, October 2006. doi:10.1063/1.2382732. Cited on pages 22, 23, 133, 159, 190, 201, and 203.

Emmanuel Bossy, Jean-Francois Aubry, Arik R. Funke, Mathias Fink, and Albert-Claude Boccara. Guiding of HIFU beams towards optical contrast agents by time-reversal of photoacoustic waves. URL `http://dx.doi.org/10.1121/1.2934200`, July 2008. Conference presentation at Acoustics '08 (ASA & SFA) in Paris. Cited on pages 76 and 77.

Robert W. Boyd. *Nonlinear Optics, Third Edition*. Academic Press, 3 edition, April 2008. ISBN 0123694701. Cited on pages 57, 180, 181, and 182.

Cancer Research UK. CancerStats. URL `http://info.cancerresearchuk.org/cancerstats/index.htm`, July 2010. Cited on pages 4 and 25.

Constantin Chilowsky and Paul Langevin. Procédés et appareils pour la production de signaux sous-marins dirigés et pour la localisation à distance d'obstacles sous-marins, 1916. French Patent. Cited on page 6.

D J Coleman, F L Lizzi, J Driller, A L Rosado, S Chang, T Iwamoto, and D Rosenthal. Therapeutic ultrasound in the treatment of glaucoma. i. experimental model. *Ophthalmology*, 92(3):339–346, March 1985. ISSN 0161-6420. URL `http://www.ncbi.nlm.nih.gov/pubmed/3991121`. PMID: 3991121. Cited on page 7.

Continuum. Operation and maintenance manual for Surelite lasers, 2002. Rev. J. Cited on pages 52, 53, 54, 56, and 193.

C. C. Coussios, C. H. Farny, G. Ter Haar, and R. A. Roy. Role of acoustic cavitation in the delivery and monitoring of cancer treatment by high-intensity focused ultrasound (HIFU). *International Journal of Hyperthermia*, 23(2): 105–120, 2007. doi:10.1080/02656730701194131. Cited on page 9.

B. T. Cox, S. R. Arridge, and P. C. Beard. Estimating chromophore distributions from multiwavelength photoacoustic images. *Journal of the Optical Society of America A*, 26(2):443–455, February 2009. doi:10.1364/JOSAA.26.000443. Cited on page 163.

Jacques Curie and Pierre Curie. Développement, par pression, de l'électricité polaire dans les cristaux hémièdres à faces inclinées. *Comptes rendus hebdomadaires des séances de l'Académie des sciences*, 91:294–295, 1880. URL `http://gallica.bnf.fr/ark:/12148/bpt6k30485.image.f296.pagination.langEN`. Cited on page 6.

Adam De La Zerda, Cristina Zavaleta, Shay Keren, Srikant Vaithilingam, Sunil Bodapati, Zhuang Liu, Jelena Levi, Bryan R. Smith, Te-Jen Ma, Omer Oralkan, Zhen Cheng, Xiaoyuan Chen, Hongjie Dai, Butrus T. Khuri-Yakub, and Sanjiv S. Gambhir. Carbon nanotubes as photoacoustic molecular imaging agents in living mice. *Nat Nano*, 3(9):557–562, 2008. ISSN 1748-3387. doi:10.1038/nnano.2008.231. Cited on page 21.

Eric Delabrousse, Rares Salomir, Alain Birer, Christian Paquet, François Mithieux, Jean-Yves Chapelon, François Cotton, and Cyril Lafon. Automatic temperature control for MR-guided interstitial ultrasound ablation in liver using a percutaneous applicator: Ex vivo and in vivo initial studies. *Magnetic Resonance in Medicine*, 63(3):667–679, 2010. doi:10.1002/mrm.22328. Cited on page 10.

M.L. Denbow, I.H. Rivens, I.J. Rowland, M.O. Leach, N.M. Fisk, and G.R. ter Haar. Preclinical development of noninvasive vascular occlusion with focused ultrasonic surgery for fetal therapy,. *American Journal of Obstetrics and Gynecology*, 182(2):387–392, February 2000. ISSN 0002-9378. doi:10.1016/S0002-9378(00)70229-8. Cited on page 9.

Arthur Donohue-Rolfe, David W. K. Acheson, and Gerald T. Keusch. Shiga toxin: Purification, structure, and function. *Reviews of Infectious Diseases*, 13:S293–S297, April 1991. ISSN 01620886. URL `http://www.jstor.org/stable/4455885`. Cited on page 139.

F. J. Duarte. *Tunable Laser Applications, Second Edition.* CRC Press, 2 edition, August 2008. ISBN 1420060090. Cited on pages 57, 181, and 182.

T. Durduran, R. Choe, J. P. Culver, L. Zubkov, M. J. Holboke, J. Giammarco, B. Chance, and A. G. Yodh. Bulk optical properties of healthy female breast tissue. *Physics in Medicine and Biology*, 47(16):2847–2861, 2002. ISSN 0031-9155. URL `http://www.iop.org/EJ/abstract/0031-9155/47/16/302/`. Cited on pages 31 and 32.

R.O. Esenaliev, A.A. Karabutov, and A.A. Oraevsky. Sensitivity of laser optoacoustic imaging in detection of small deeply embedded tumors. *IEEE Journal of Selected Topics in Quantum Electronics*, 5(4):981–988, August 1999. ISSN 1077260X. doi:10.1109/2944.796320. Cited on page 21.

F. J. Fry and J. E. Barger. Acoustical properties of the human skull. *The Journal of the Acoustical Society of America*, 63(5):1576–1590, May 1978. doi:10.1121/1.381852. Cited on page 11.

W. J. Fry, W. H. Mosberg, J. W. Barnard, and F. J. Fry. Production of focal destructive lesions in the central nervous system with ultrasound. *Journal of Neurosurgery*, 11(5):471–478, September 1954. ISSN 0022-3085. doi:10.3171/jns.1954.11.5.0471. Cited on page 7.

J. Gateau, L. Marsac, M. Pernot, J.-F. Aubry, M. Tanter, and M. Fink. Transcranial ultrasonic therapy based on time reversal of acoustically induced cavitation bubble signature. *Biomedical Engineering, IEEE Transactions on*, 57(1):134–144, 2010. ISSN 0018-9294. doi:10.1109/TBME.2009.2031816. Cited on page 15.

B. Gelebart. *Réfléctrance résolue dans le temps et dans l'espace appliquée à l'étude de tissus biologiques*. PhD thesis, Université de Paris-Nord, Paris, 1998. Cited on page 33.

H. Gohr and Th. Wedekind. Der Ultraschall in der Medizin. *Journal of Molecular Medicine*, 19(2):25–29, January 1940. doi:10.1007/BF01772492. Cited on page 6.

L. C. Henyey and J. L. Greenstein. Diffuse radiation in the galaxy. *The Astrophysical Journal*, 93:70, January 1941. ISSN 0004-637X. doi:10.1086/144246. Cited on page 33.

K. Hynynen. The threshold for thermally significant cavitation in dog's thigh muscle in vivo. *Ultrasound in Medicine & Biology*, 17(2):157–169, 1991. ISSN 0301-5629. doi:10.1016/0301-5629(91)90123-E. Cited on page 9.

Steven Jacques. Optical absorption of melanin. URL `http://omlc.ogi.edu/spectra/melanin/index.html`, 1998. Cited on pages 30 and 31.

Ludger Johannes, Eric Tartour, Bruno Goud, and Wolf Herve Fridman. Universal carrier for targeting molecules to gb3 receptor expressing cells. URL `http://www.freepatentsonline.com/EP1229045A1.html`, August 2002. European Patent Application. Cited on pages 139 and 201.

A. Karabutov, N. B. Podymova, and V. S. Letokhov. Time-resolved laser optoacoustic tomography of inhomogeneous media. *Applied Physics B: Lasers and Optics*, 63(6):545–563, December 1996. doi:10.1007/BF01830994. Cited on page 19.

Steven M. Kay. *Fundamentals of Statistical Signal Processing: Estimation Theory*, volume 1. Prentice Hall, US edition, May 1993. ISBN 0133457117. Cited on page 185.

Gwangseong Kim, Sheng-Wen Huang, Kathleen C. Day, Matthew O'Donnell, Rodney R. Agayan, Mark A. Day, Raoul Kopelman, and Shai Ashkenazi. Indocyanine-green-embedded PEBBLEs as a contrast agent for photoacoustic imaging. *Journal of Biomedical Optics*, 12(4):044020–8, July 2007. doi:10.1117/1.2771530. Cited on page 162.

Robert A. Kruger. Photoacoustic ultrasound. *Medical Physics*, 21(1):127, 1994. ISSN 00942405. doi:10.1118/1.597367. Cited on pages 18, 19, and 22.

Robert A. Kruger, Kenyon K. Kopecky, Alex M. Aisen, Daniel R. Reinecke, Gabe A. Kruger, and William L. Kiser. Thermoacoustic CT with radio waves: A medical imaging paradigm. *Radiology*, 211(1):275 –278, April 1999. URL `http://radiology.rsna.org/content/211/1/275.abstract`. Cited on page 20.

Horst Kunkely and Arnd Vogler. Photolysis of naphthol green b in aqueous solution. photoreduction of Fe(III) induced by Ligand-to-Metal charge transfer excitation. *Zeitschrift für Naturforschung*, 58(b):922–924, June 2003. URL `http://znaturforsch.com/ab/v58b/s58b0922.pdf`. Cited on pages 137 and 138.

C. Lafon, J. Y. Chapelon, F. Prat, F. Gorry, J. Margonari, Y. Theillère, and D. Cathignol. Design and preliminary results of an ultrasound applicator for interstitial thermal coagulation. *Ultrasound in Medicine & Biology*, 24(1): 113–122, January 1998. ISSN 0301-5629. doi:10.1016/S0301-5629(97)00203-2. Cited on page 10.

Lev Davidovich Landau and Evgeny Mikhailovich Lifshitz. *Fluid Mechanics, Second Edition: Volume 6*. Butterworth-Heinemann, 2 edition, January 1987. ISBN 0750627670. Cited on page 168.

M. L. Landsman, G. Kwant, G. A. Mook, and W. G. Zijlstra. Light-absorbing properties, stability, and spectral stabilization of indocyanine green. *J Appl Physiol*, 40(4):575–583, April 1976. URL `http://jap.physiology.org/cgi/content/abstract/40/4/575`. Cited on pages 142, 148, and 149.

Jan Laufer, Dave Delpy, Clare Elwell, and Paul Beard. Quantitative spatially resolved measurement of tissue chromophore concentrations using photoacoustic spectroscopy: application to the measurement of blood oxygenation and haemoglobin concentration. *Physics in Medicine and Biology*, 52:141–168, January 2007. ISSN 0031-9155, 1361-6560. doi:10.1088/0031-9155/52/1/010. Cited on page 163.

Jan Laufer, Edward Zhang, Gennadij Raivich, and Paul Beard. Three-dimensional noninvasive imaging of the vasculature in the mouse brain using a high resolution photoacoustic scanner. *Applied Optics*, 48(10):D299–D306, April 2009. doi:10.1364/AO.48.00D299. Cited on pages 20 and 21.

Jan Laufer, Ben Cox, Edward Zhang, and Paul Beard. Quantitative determination of chromophore concentrations from 2D photoacoustic images using a nonlinear model-based inversion scheme. *Applied Optics*, 49(8):1219–1233, March 2010. doi:10.1364/AO.49.001219. Cited on page 163.

T. A Leslie and J. E Kennedy. High intensity focused ultrasound in the treatment of abdominal and gynaecological diseases. *International Journal of Hyperthermia*, 23(2):173–182, 2007. doi:10.1080/02656730601150514. Cited on page 9.

Changhui Li and Lihong V Wang. Photoacoustic tomography and sensing in biomedicine. *Physics in Medicine and Biology*, 54(19):R59–R97, October 2009. ISSN 0031-9155. doi:10.1088/0031-9155/54/19/R01. Cited on pages 20 and 21.

Meng-Lin Li, Jung-Taek Oh, Xueyi Xie, Geng Ku, Wei Wang, Chun Li, Gina Lungu, George Stoica, and Lihong V. Wang. Simultaneous molecular and hypoxia imaging of brain tumors in vivo using spectroscopic photoacoustic tomography. *Proceedings of the IEEE*, 96(3):481–489, 2008. ISSN 0018-9219. doi:10.1109/JPROC.2007.913515. Cited on page 21.

Petter Lindstrom. Prefrontal ultrasonic irradiation - a substitute for lobotomy. *AMA Arch Neurol Psychiatry*, 72(4):399–425, October 1954. doi:10.1001/archneurpsyc.1954.02330040001001. Cited on page 7.

Dalong Liu and Emad S. Ebbini. Real-time 2D imaging of thermal and mechanical tissue response to focused ultrasound. In Kullervo Hynynen and Jacques Souquet, editors, *9th International Symposium on Therapeutic Ultrasound: ISTU 2009*, volume 1215, pages 57–61, Aix-en-Provence (France), March 2010. AIP. doi:10.1063/1.3367197. URL `http://link.aip.org/link/?APC/1215/57/1`. Cited on page 8.

F L Lizzi, D J Coleman, J Driller, L A Franzen, and F A Jakobiec. Experimental, ultrasonically induced lesions in the retina, choroid, and sclera. *Investigative Ophthalmology & Visual Science*, 17(4):350–360, April 1978. ISSN 0146-0404. URL `http://www.iovs.org/cgi/content/abstract/17/4/350`. PMID: 640782. Cited on page 7.

F.L. Lizzi, D.J. Coleman, J. Driller, L.A. Franzen, and M. Leopold. Effects of pulsed ultrasound on ocular tissue. *Ultrasound in Medicine & Biology*, 7(3): 245–247, 249–252, 1981. ISSN 0301-5629. doi:10.1016/0301-5629(81)90035-1. Cited on page 7.

John G. Lynn and Tracy J. Putnam. Histology of cerebral lesions produced by focused ultrasound. *The American Journal of Pathology*, 20(3):637–649, May 1944. ISSN 0002-9440. PMID: 19970769 PMCID: 2033152. Cited on pages 6 and 11.

Srirang Manohar, Susanne E. Vaartjes, Johan C. G. van Hespen, Joost M. Klaase, Frank M. van den Engh, Wiendelt Steenbergen, and Ton G. van Leeuwen. Initial results of in vivo non-invasive cancer imaging in the human breast using near-infrared photoacoustics. *Optics Express*, 15(19):12277–12285, 2007. doi:10.1364/OE.15.012277. Cited on page 21.

F Marquet, M Pernot, J-F Aubry, G Montaldo, L Marsac, M Tanter, and M Fink. Non-invasive transcranial ultrasound therapy based on a 3D CT scan: protocol validation and in vitro results. *Physics in Medicine and Biology*, 54(9):2597–2613, May 2009. ISSN 0031-9155. doi:10.1088/0031-9155/54/9/001. Cited on pages 14 and 15.

Konstantin Maslov, Hao F. Zhang, Song Hu, and Lihong V. Wang. Optical-resolution photoacoustic microscopy for in vivo imaging of single capillaries. *Optics Letters*, 33(9):929–931, May 2008. doi:10.1364/OL.33.000929. Cited on page 20.

T. H. Maugh. Photoacoustic spectroscopy: New uses for an old technique. *Science*, 188(4183):38–39, April 1975. ISSN 0036-8075. doi:10.1126/science.188.4183.38. Cited on page 18.

Russell Meyers, William J. Fry, Frank J. Fry, Leroy L. Dreyer, Donald F. Schultz, and Robert F. Noyes. Early experiences with ultrasonic irradiation of the pallidofugal and nigral complexes in hyperkinetic and hypertonic disorders. *Journal of Neurosurgery*, 16(1):32–54, January 1959. ISSN 0022-3085. doi:10.3171/jns.1959.16.1.0032. Cited on page 7.

Serge Mordon. Les lasers: risques et prévention, 2007. Presentation Notes. Cited on page 34.

Philip McCord Morse and Herman Feshbach. *Methods of Theoretical Physics*. McGraw-Hill Science/Engineering/Math, 1 edition, June 1953. ISBN 007043316X. Cited on pages 173 and 175.

Alexander A. Oraevsky. Laser-based optoacoustic imaging in biological tissues. In *Proceedings of SPIE*, volume 2134A, pages 122–128, August 1994. doi:10.1117/12.182927. URL `http://spie.org/x648.html?product_id=182927`. Cited on page 18.

Alexander A. Oraevsky, Steven L. Jacques, and Frank K. Tittel. Measurement of tissue optical properties by time-resolved detection of laser-induced transient stress. *Applied Optics*, 36(1):402–415, January 1997. doi:10.1364/AO.36.000402. Cited on page 19.

Alexander A. Oraevsky, Steven L. Jacques, and Rinat O. Esenaliev. Optoacoustic imaging for medical diagnosis. URL `http://www.google.com/patents/about?id=PGAWAAAAEBAJ`, November 1998. Cited on page 19.

C. K. N. Patel, E. G. Burkhardt, and C. A. Lambert. Spectroscopic measurements of stratospheric nitric oxide and water vapor. *Science*, 184(4142): 1173–1176, June 1974. doi:10.1126/science.184.4142.1173. Cited on page 17.

Mathi Pernot. *Nouvelles techniques de thérapie ultrasonore et de monitoring.* PhD thesis, Université Paris 7, Paris, October 2004. Cited on pages 13 and 14.

Mathieu Pernot, Jean-Francois Aubry, Mickael Tanter, Anne-Laure Boch, Fabrice Marquet, Michele Kujas, Danielle Seilhean, and Mathias Fink. In vivo transcranial brain surgery with an ultrasonic time reversal mirror. *Journal of Neurosurgery*, 106(6):1061–1066, September 2007. doi:10.3171/jns.2007.106.6.1061. Cited on pages 12, 13, 14, and 133.

PD Phillips, S Smith, O von Ramm, and F Thurstone. Sampled aperture techniques applied to b-mode echoencephalography. *Acoustical Holography*, 6:103–120, 1975. Plenum Press Plenum Publishing Corporation. Cited on page 11.

Scott Prahl. Optical absorption of hemoglobin. URL `http://omlc.ogi.edu/spectra/hemoglobin/index.html`, 1999. Cited on pages 29, 30, 31, and 137.

Justin R. Rajian, Paul L. Carson, and Xueding Wang. Quantitative photoacoustic measurement of tissue optical absorption spectrum aided by an optical contrast agent. *Optics Express*, 17(6):4879–4889, March 2009. doi:10.1364/OE.17.004879. Cited on pages 114 and 163.

Lord Rayleigh. *The Theory of Sound.* Macmillan and co., 1877. Cited on page 6.

Lord Rayleigh. The photophone. *Nature*, 23(586):274–275, January 1881. ISSN 0028-0836. doi:10.1038/023274a0. Cited on page 16.

Allan Rosencwaig. Photoacoustic spectroscopy of biological materials. *Science*, 181(4100):657–658, August 1973. ISSN 00368075. URL `http://www.jstor.org/stable/1736952`. Cited on page 18.

Allan Rosencwaig. Theory of the photoacoustic effect with solids. *Journal of Applied Physics*, 47(1):64, 1976. ISSN 00218979. doi:10.1063/1.322296. Cited on pages 16 and 17.

Allan Rosencwaig and Allen Gersho. Photoacoustic effect with solids: A theoretical treatment. *Science*, 190(4214):556–557, November 1975. ISSN 00368075. URL `http://www.sciencemag.org/content/vol190/issue4214/index.dtl`. Cited on page 17.

A. A. Said, T. Xia, A. Dogariu, D. J. Hagan, M. J. Soileau, E. W. Van Stryland, and M. Mohebi. Measurement of the optical damage threshold in fused quartz. *Applied Optics*, 34(18):3374–3376, June 1995. doi:10.1364/AO.34.003374. Cited on page 66.

E Sapin-de Brosses, J-L Gennisson, M Pernot, M Fink, and M Tanter. Temperature dependence of the shear modulus of soft tissues assessed by ultrasound. *Physics in Medicine and Biology*, 55(6):1701–1718, March 2010. ISSN 0031-9155. doi:10.1088/0031-9155/55/6/011. Cited on page 9.

D. J. Segelstein. *The Complex Refractive Index of Water*. MSc thesis, University of Missouri, Kansas City, 1981. As reported at: http://omlc.ogi.edu/spectra/water/abs/index.html. Cited on page 29.

Kiyoshi Shiga. Über den Erreger der Dysenterie in Japan. *Zentralblatt für Bakteriologie, Microbiologie und Hygiene*, 23:599–600, 1898. Vorlaufige Mitteilung. Cited on page 139.

C Simon, P Vanbaren, and E S Ebbini. Two-dimensional temperature estimation using diagnostic ultrasound. *IEEE Transactions on Ultrasonics, Ferroelectrics, and Frequency Control*, 45(4):1088–1099, 1998. ISSN 0885-3010. doi:10.1109/58.710592. PMID: 18244264. Cited on page 8.

M. Tanter, J.-F. Aubry, J. Gerber, J.-L. Thomas, and M. Fink. Optimal focusing by spatio-temporal inverse filter. i. basic principles. *The Journal of the Acoustical Society of America*, 110(1):37–47, July 2001. doi:10.1121/1.1377051. Cited on page 12.

Charles R. Thomas, Caleb H. Farny, Constantin C. Coussios, Ronald A. Roy, and R. Glynn Holt. Dynamics and control of cavitation during high-intensity focused ultrasound application. *Acoustics Research Letters Online*, 6(3):182–187, July 2005. doi:10.1121/1.1901744. Cited on page 9.

Jean-Louis Thomas, François Wu, and Mathias Fink. Time reversal focusing applied to lithotripsy. *Ultrasonic Imaging*, 18(2):106–121, April 1996. ISSN 0161-7346. doi:10.1006/uimg.1996.0006. Cited on page 11.

Harry L. Van Trees. *Detection, Estimation, and Modulation Theory: Detection, Estimation, and Linear Modulation Theory*, volume 1. WileyBlackwell, October 2001. ISBN 0471095176. Cited on page 185.

Keitaro Umezawa, Daniel Citterio, and Koji Suzuki. Water-soluble NIR fluorescent probes based on squaraine and their application for protein labeling. *Analytical Sciences*, 24(2):213, February 2008. ISSN 0910-6340. doi:10.2116/analsci.24.213. Cited on pages 137 and 138.

Shahram Vaezy, Roy Martin, Udo Schmiedl, Michael Caps, Shari Taylor, Kirk Beach, Steve Carter, Peter Kaczkowski, George Keilman, Scott Helton, Wayne Chandler, Pierre Mourad, Matthew Rice, Ronald Roy, and Lawrence Crum. Liver hemostasis using high-intensity focused ultrasound. *Ultrasound in Medicine & Biology*, 23(9):1413–1420, 1997. ISSN 0301-5629. doi:10.1016/S0301-5629(97)00143-9. Cited on page 9.

Shahram Vaezy, Xuegong Shi, Roy W. Martin, Emil Chi, Peter I. Nelson, Michael R. Bailey, and Lawrence A. Crum. Real-time visualization of high-intensity focused ultrasound treatment using ultrasound imaging. *Ultrasound in Medicine & Biology*, 27(1):33–42, January 2001. ISSN 0301-5629. doi:10.1016/S0301-5629(00)00279-9. Cited on page 8.

Shahram Vaezy, Vesna Zderic, Riyad Karmy-Jones, Gregory J. Jurkovich, Carol Cornejo, and Roy W. Martin. Hemostasis and sealing of air leaks in the lung using High-Intensity focused ultrasound. *The Journal of Trauma: Injury, Infection, and Critical Care*, 62(6):1390–1395, June 2007. ISSN 0022-5282. doi:10.1097/01.ta.0000215942.42423.6c. Cited on page 9.

H. J. van Staveren, C. J. M. Moes, J. van Marle, S. A. Prahl, and M. J. C. van Gemert. Light scattering in Intralipid-10% in the wavelength range of 400–1100 nm. *Applied Optics*, 30(31):4507–4514, 1991. Cited on page 78.

R. L. P. van Veen, H. J. C. M. Sterenborg, A. Pifferi, A. Torricelli, and R. Cubeddu. Optical absorption of fat. URL `http://omlc.ogi.edu/spectra/fat/`, 2004. Cited on page 30.

Saeed V. Vaseghi. *Advanced Signal Processing and Noise Reduction*. John Wiley & Sons, 2 edition, September 2000. ISBN 0471626929. Cited on page 185.

ML Viengerov. New method of gas analysis based on tyndall-roentgen optoacoustic effect. *Doklady Akademii Nauk SSSR*, 19:687–8, 1938. ISSN 0002-3264. Cited on page 17.

Lihong V. Wang and Hsin-i Wu. *Biomedical Optics: Principles and Imaging*. Wiley-Interscience, May 2007. ISBN 0471743046. Cited on page 33.

Lihong V. Wang, Xuemei Zhao, Haitao Sun, and Geng Ku. Microwave-induced acoustic imaging of biological tissues. *Review of Scientific Instruments*, 70 (9):3744, 1999. ISSN 00346748. doi:10.1063/1.1149986. Cited on page 20.

Shiou-Han Wang, Chen-Wei Wei, Shiou-Hwa Jee, and Pai-Chi Li. Photoacoustic temperature measurements for monitoring of thermal therapy. In Alexander A. Oraevsky and Lihong V. Wang, editors, *Photons Plus Ultrasound: Imaging and Sensing 2009*, volume 7177, pages 71771S–11, San Jose, CA, USA, February 2009. SPIE. URL `http://link.aip.org/link/?PSI/7177/71771S/1`. Cited on page 21.

Xueding Wang, Yongjiang Pang, Geng Ku, Xueyi Xie, George Stoica, and Lihong V Wang. Noninvasive laser-induced photoacoustic tomography for structural and functional in vivo imaging of the brain. *Nat Biotech*, 21(7): 803–806, July 2003. ISSN 1087-0156. doi:10.1038/nbt839. Cited on page 21.

D. White, J. Clark, D. White, J. Campbell, K. Bahuleyan, A. Kraus, and R. Brinker. The deformation of the ultrasonic field in passage across the living and cadaver head. *Medical and Biological Engineering and Computing*, 7(6):607–618, November 1969. doi:10.1007/BF02551731. Cited on page 11.

D. N. White, J. M. Clark, J. N. Chesebrough, M. N. White, and J. K. Campbell. Effect of the skull in degrading the display of echoencephalographic b and c scans. *The Journal of the Acoustical Society of America*, 44(5): 1339–1345, November 1968. doi:10.1121/1.1911266. Cited on page 11.

Nobert Wiener. *Extrapolation, interpolation, and smoothing of stationary time series with engineering applications*. Technology Press of Massachusetts Institute of Technology, August 1949. ISBN 978-0-262-23002-5. Cited on page 186.

Joseph Woo. A short history of the development of ultrasound in obstetrics and gynecology. URL `http://www.ob-ultrasound.net/history1.html`, 1998. Cited on pages 5 and 7.

World Health Organisation. Fact sheet no 297: Cancer. URL `http://www.who.int/mediacentre/factsheets/fs297/en/`, February 2009. Cited on pages 3 and 189.

Oz Yilmaz. *Seismic Data Analysis*. Society Of Exploration Geophysicists, 2 edition, January 2001. ISBN 1560800941. Cited on page 105.

Özdogan Yilmaz. Velocity-Stack processing. *Geophysical Prospecting*, 37(4): 357–382, 1989. doi:10.1111/j.1365-2478.1989.tb02211.x. Cited on page 105.

Vesna Zderic, Grant E. O'Keefe, Jessica L. Foley, and Shahram Vaezy. Resection of abdominal solid organs using High-Intensity focused ultrasound. *Ultrasound in Medicine & Biology*, 33(8):1251–1258, August 2007. ISSN 0301-5629. doi:10.1016/j.ultrasmedbio.2007.02.010. Cited on page 9.

Hao F Zhang, Konstantin Maslov, George Stoica, and Lihong V Wang. Functional photoacoustic microscopy for high-resolution and noninvasive in vivo imaging. *Nat Biotech*, 24(7):848–851, July 2006. ISSN 1087-0156. doi:10.1038/nbt1220. Cited on page 20.